IMPACT OF DEGLACIATION ON STRESS AND IMPLICATIONS FOR SEISMICITY AND HYDROCARBON EXPLORATION

A DISSERTATION

SUBMITTED TO THE DEPARTMENT OF GEOPHYSICS

AND THE COMMITTEE ON GRADUATE STUDIES

OF STANFORD UNIVERSITY

IN PARTIAL FULFILLMENT OF THE REQUIREMENTS

FOR THE DEGREE OF

DOCTOR OF PHILOSOPHY

Balz Grollimund

October 2000

I certify that I have read this dissertation and that in my opinion it is fully adequate, in scope and quality, as a dissertation for the degree of Doctor of Philosophy.

_____

Mark D. Zoback (Principal Advisor)

I certify that I have read this dissertation and that in my opinion it is fully adequate, in scope and quality, as a dissertation for the degree of Doctor of Philosophy.

_____

Amos M. Nur

I certify that I have read this dissertation and that in my opinion it is fully adequate, in scope and quality, as a dissertation for the degree of Doctor of Philosophy.

_____

Norm Sleep

Approved for the University Committee on Graduate Studies:

_____

Abstract

The retreat of major ice sheets in North America, northern Eurasia and Antarctica caused an immense isostatic disequilibrium of the lithosphere-asthenosphere system. As a result, formerly glaciated areas started to uplift and lithospheric bending occurred near ice margins. While it is well known that the ongoing post-glacial uplift has continued until present-day, so has the associated flexure of the lithosphere which has altered the stress state in the surroundings of the former ice sheet. One of the principal goals of this dissertation has been to map out, and explain the stress field in the Norwegian offshore areas, a prominent hydrocarbon region in the vicinity of a former ice sheet. In another study, I investigated the influence of lithospheric flexure on the anomalously high seismicity in the New Madrid Seismic Zone, central United States.

In Norway, I have compiled data on stress orientation, pore pressure and least principal stress from approximately 400 wells offshore Norway. Well-defined regional variations are observed in all three parameters. Incorporation of precise stress orientation data from drilling-induced tensile borehole wall fractures shows that the orientation of maximum horizontal stress rotates in the vicinity of the former ice margin and does not correspond to the large-scale plate driving direction. I show that this rotation is due to lithospheric flexure caused by deglaciation. Regional variations of the magnitude of the least principal stress and pore pressure also appear to support the hypothesis that the stress field offshore Norway has been strongly affected by deglaciation.

The comparison of the observed stress data with two-dimensional models of lithospheric flexure in the northern North Sea, and later three-dimensional models of the entire Norwegian margin, suggest that late Quaternary melting of the Fennoscandian ice sheet strongly influences the in situ stress field offshore Norway. The modeling shows that viscoelastic behavior within the lithosphere is required to explain the observed stresses. The models further suggest that the viscous portions of the lithosphere have viscosities on the order of 10^{22} to 10^{23} Pa s in the northern North Sea. Towards the northeast, on the Mid-Norwegian margin, lithospheric viscosities seem to be slightly higher.

The locations of estimated overpressure, due to the poroelastic response to glacially-induced stress changes, coincide with areas of observed overpressures which shows that the glacially-induced stress changes in fact had an impact on the reservoir pore pressure. The magnitude of the modeled overpressure is however smaller than observed overpressures, which suggests that additional mechanisms, such as rapid sedimentation, also contribute to the observed overpressures. The model results can also be used to assess temporal leaking

potential changes of important reservoir faults in the Norwegian offshore area. The fault analysis reveals that most hydrocarbon fields in the northern North Sea were potentially subjected to leakage during Weichselian interglacials.

In New Madrid, I have modeled the interaction between large-scale plate driving forces, lithospheric structure and the stresses induced by bending of the lithosphere as a result of glacial loading and unloading in central North America. The modeling shows that the removal of the Laurentide ice sheet that covered large parts of the northern United States until ~20,000 years ago changed the stress field in the vicinity of New Madrid and caused seismic strain rates to increase by about 3 orders of magnitude. The modeling predicts that the high rate of seismic energy release observed during late Holocene time is likely to remain essentially constant for the next few thousand years. We believe that seismicity is localized in the New Madrid area, because stress changes due to deglaciation are amplified by the anomalous lithospheric structure associated with an ancient Precambrian rift.

Acknowledgments

Finally, after 4 years of hard work I have finished my Ph.D. thesis! As exciting as it is to be so close to getting a Ph.D., I would have never gotten this far without the help of many people. First and foremost, I was very fortunate to have Mark Zoback as my advisor. He initiated the project and within a couple of days after my arrival at Stanford I was hooked to the "really cool" subject of how glaciers might have affected the oil fields in the North Sea. Ever since, he has provided invaluable scientific, moral, and financial support that was crucial for the success of my Ph.D. On my way through Graduate School, I always benefited from his inspiration, interest and trust in my work. Despite his at times very tight schedule he always found time for discussions or to read manuscripts, even at a preliminary stage. Beyond research, he provided a warm and friendly atmosphere within the research group which was fundamental for the beginning of my relationship with Lourdes, I can never thank enough for that!

Many thanks to Bjørn Larsen who was critical in the initiation of this project. The people at the research center of Norsk Hydro ASA in Bergen, Norway generously sponsored the entire project and provided a wealth of data which was absolutely essential for my research. Special thanks go to Linn Arnesen, Nils Telnæs, Tor Harald Hansen, Chris Dart and Nils Kageson Loe for always being there to help me getting the data I needed and for giving valuable input through critical discussions of my research. I would also like to thank the people at Hydro's document center for patiently processing my endless requests for more data.

Many people in the School of Earth Science helped me with my research: My committee members Amos Nur, Paul Segall, Norm Sleep, and Jack Dvorkin witnessed the evolution of my project from the oral exam through annual reviews and finally the defense. Along this way, they provided insight and useful comments. David Pollard be thanked for his spontaneous acceptance to chair my defense. I always enjoyed the discussions with Shelley Kenner who was able to understand my at times frustrating experiences with the many potential pitfalls of numerical modeling. Jean Chéry helped me improve my models during his one year visit at Stanford and I always enjoyed the relaxing lunch breaks with a "fellow post-lunch coffee drinker". Research also requires a solid administrative support and that I certainly had with Agnes, Linda, Laurie and Jeannette. Special thanks to Jeannette who did everything possible to assist me with bureaucracy problems.

Of course, being able to relax is absolutely necessary to gain new momentum to carry on with research. I thank Andres, Adrian, Denise, Martin, Christine, Christoph, Francesca,

and all my other Swiss friends for the many enjoyable and truly relaxing stays in Switzerland. I also thank my office mates for making my stay at Stanford.a pleasant experience. I always enjoyed the many runs across the dish with Martin and Thomas that often helped to get some distance from pressing research problems. Very special thanks to my dear friends Dave and Lourdes (the two other Musketeers) who were always there for me. I had a lot of fun with you guys!

My best friend and now wife Lourdes deserves my deepest thankfulness for all the understanding, patience and support she has given me throughout the last 1 1/2 years. She always knew how to comfort me when things did not go as expected and shared all the joy in moments of success.

And last but certainly not least my family in Switzerland. My parents in particular, who always gave me their full support, both morally and financially throughout the many years of my education.

Table of Contents

Abstract iv

Acknowledgments vi

List of Tables xi

List of Illustrations xii

Chapter 1: Impact of deglaciation on stress and implications for seismicity and hydrocarbon exploration: Introduction

1.1 Introduction 2

1.2 The structure and contents of this thesis 3

1.2.1 The observed stress field offshore Norway (Chapter 2) 4

1.2.2 The influence of glaciation/deglaciation on the northern North Sea (Chapter 3) 6

1.2.3 Three-dimensional models of glaciation offshore Norway (Chapter 4) 7

1.2.4 Impact of glacially-induced stress changes on hydrocarbon exploration offshore Norway (Chapter 5)8

1.2.5 Seismicity in the New Madrid area (Chapter 6) 9

Chapter 2: Stress orientation, pore pressure and least principal stress offshore Norway

2.1 Abstract 12

2.2 Introduction 12

2.3 Orientation of the maximum horizontal stress (SHmax) 15

2.4 Magnitude of the least principal stress (S3) 18

2.5 Pore pressure (Pp) 24

2.6 Discussion 29

2.6.1 Possible sources of spatial stress variations 29

2.6.2 The influence of deglaciation on stress 34

2.6.3 The influence of deglaciation on pore pressure 35

2.7 Conclusions 36

Chapter 3: Post glacial lithospheric flexure and induced stresses and pore pressure changes in the northern North Sea

3.1 Abstract 39

3.2 Introduction 39

3.3 Observed stress in the northern North Sea 41

3.4 Flexural stresses 45

3.4.1 Analytical model for glacial loading 48
3.4.2 Analytical model for glacial unloading 50
3.4.3 Numerical model of the entire loading-unloading cycle 52
3.5 Prediction of pore pressure from glacial unloading 59
3.6 Conclusions 61

Chapter 4: Three-dimensional models of glacially-induced stresses offshore Norway
4.1 Abstract 63
4.2 Introduction 63
4.3 Three-dimensional numerical models 66
4.3.1 Data to constrain the models 66
4.3.2 Modeling the in-situ stress field in the northern North Sea (the “North Sea model”) 68
4.3.3 Modeling the in-situ stress field on the Mid-Norwegian Margin (the ‘Mid-Norway model’)92
4.3.4 Comparison of model results to uplift rates 109
4.4 Discussion 114

Chapter 5: Impact of glacially-induced stress changes on hydrocarbon exploration offshore Norway
5.1 Abstract 118
5.2 Introduction 118
5.3 The evolution of stress magnitudes 119
5.4 Predicted pore pressure changes 127
5.5 Predicted sealing/leaking behavior of faults 131
5.6 Conclusions 143

Chapter 6: Did deglaciation trigger intraplate seismicity in the New Madrid seismic zone?
6.1 Abstract 145
6.2 Introduction 145
6.3 The model 147
6.4 Model results 153
6.4.1 Different implications of the structural heterogeneity 153
6.4.2 The influence of the chosen lithospheric viscosities 160
6.4.3 The influence of interglacials 163
6.5 The change of seismicity with time 169
6.6 Discussion 172

6.7 Conclusions 174

Appendix A 175

Appendix B 178

References 181

List of Tables

Table 1.1:Number of wells used for the stress compilation.....4
Table 4.1:Rheological parameters of the three-dimensional models.....67
Table 4.2:Fault orientations used in the sealing/leaking analysis.....125
Table 5.1:Rheological parameters and initial stress state of the New Madrid models....146

List of Illustrations

1.1.: Illustration of how a glacial cycle affects vertical lithospheric deformation and associated mass flux in the underlying asthenosphere after Nansen (1921). 2

1.2.: Stress data coverage. 5

1.3.: Map view of stress and pore pressure in the North Sea. 6

1.4.: Comparison of modeled to observed stress orientations in the vicinity of the northern North Sea. 8

1.5.: Modeled seismic strain rates in the central United States. 9

2.1.: Data coverage for the North Sea. 13

2.2.: Data coverage for the Mid-Norwegian margin. 14

2.3.: Compilation of S_{Hmax} orientations in the Norwegian sector of the North Sea from the analyses of breakouts and tensile fractures. 16

2.4.: Compilation of S_{Hmax} orientations on the Mid-Norwegian margin from the analyses of borehole breakouts.1 7

2.5.: Typical examples of compiled S_3, S_v and pore pressure depth profiles.....20

2.6.: Lateral variation of the least principal stress normalized by the vertical stress (S_3/S_v) for different depth slices in the North Sea.....22

2.7.: Lateral variation of the least principal stress normalized by the vertical stress (S_3/S_v) for different depth slices on the Mid-Norwegian margin. 24

2.8.: Lateral variation of overpressure for different depth slices in the North Sea.....26

2.9.: Lateral variation of overpressure for depths between 1500 m and 3000 m on the Mid-Norwegian margin. 28

2.10.: Lateral variation of overpressure for depths between 3500 m and 4000 m on the Mid-Norwegian margin. 29

2.11.: Map of available S_{Hmax} orientations in northern Europe resulting from the compilation in Chapter 2, by using data from the World Stress Map (WSM) database. 31

2.12.: Possible stress generating mechanisms and their potential effect on Norway and adjacent areas (from Fejerskov and Lindholm, 2000).....32

2.13.: Predicted stress perturbation for deglaciation on an elastic lithosphere with an initially isotropic stress state. 35

3.1.: Overview map.of western Norway and the northern North Sea. 40

3.2.: Observed stress and pore pressure in the northern North Sea. 42

3.3.: Map view of stress and pore pressure in the North Sea. 44

3.4.: Illustration about how flexural stresses affect the stress field. 46
3.5.: Viscoelastic model for flexural stresses as a result of ice loading. 49
3.6.: Elastic model for flexural stresses as a result of ice melting. 51
3.7.: Setup of the 2D numerical model and assumed ice sheet history. 53
3.8.: Predicted stress from numerical model with a single loading-cycle. 55
3.9.: Predicted stress from numerical model with multiple loading-cycles. 56
3.10.: Predicted pore pressure change from glaciation-deglaciation. 60
4.1.: Estimates for the lithospheric thickness in Fennoscandia from studies of post-glacial uplift, compiled by Wolf (1993). 65
4.2.: Location map of 3D Norway models. 67
4.3.: Setup of the numerical models showing element sizes and modeled rheological layering of the lithosphere. 70
4.4.: Extent and thickness of the modeled ice sheet for the North Sea model. 71
4.5.: Modeled S_{Hmax} orientation for the best fitting North Sea model. 73
4.6.: Comparison of modeled and observed S_{hmin}/S_v. 74
4.7.: Modeled S_{Hmax} orientation for North Sea models with varying viscosities. 75
4.8.: Modeled S_{Hmax} orientation for the North Sea model with a purely elastic lithosphere. 82
4.9.: Modeled S_{Hmax} orientation for North Sea models with only one viscoelastic layer below the upper crust. 82
4.10.: Temporal change of ice extent for different ice models. 85
4.11.: Modeled S_{Hmax} orientation for North Sea models with varying ice sheet evolutions. 88
4.12.: Modeled S_{Hmax} orientation for the North Sea model assuming that ridge push significantly influences the stress field in the North Sea. 91
4.13.: Extent and thickness of the modeled ice sheet for different stages of the Mid-Norway model. 93
4.14.: Modeled S_{Hmax} orientation for the Mid-Norway model with the same lithospheric and asthenospheric viscosities as the best-fit North Sea model. 94
4.15.: Comparison of modeled and observed S_{hmin}/S_v for the Mid-Norway model. 96
4.16.: Modeled S_{Hmax} orientation for the Mid-Norway models with varying viscosities. 97
4.17.: Modeled S_{Hmax} orientation for the Mid-Norway model with a purely elastic lithosphere. 103
4.18.: Modeled S_{Hmax} orientation for Mid-Norway models with varying ice sheet evolutions. 104

4.19.: Modeled S_{Hmax} orientation for the Mid-Norway model assuming that ridge push significantly influences the stress field along the Mid-Norwegian margin.....108

4.20.: Map of apparent uplift rates in Fennoscandia (Ekman, 1996). 109

4.21.: Modeled uplift from the best-fitting North Sea model. 111

4.22.: Modeled uplift from the Mid-Norway model. 112

4.23.: Modeled shoreline tilt ≈20 km north of Bergen compared to shoreline tilt measurements (Kaland, 1984). 113

4.24.: Modeled shoreline tilt in the Trondheimfjord area compared to shoreline tilt measurements (Kjemperud, 1986). 114

5.1.: Temporal evolution of S_{Hmax}/S_v and S_{hmin}/S_v in the North Sea.....122

5.2.: Temporal evolution of S_{Hmax}/S_v and S_{hmin}/S_v in Mid-Norway.....126

5.3.: Overpressure in the North Sea. 127

5.4.: Overpressure in Mid-Norway. 130

5.5.: Calculated ΔPp_{crit} for Visund, assuming ice model 3. 133

5.6.: Structural map of the Visund field showing the major fault. 135

5.7.: Calculated ΔPp_{crit} for Visund, assuming ice model 5 with a varying, pre-Weichselian ice sheet.1 35

5.8.: Structural map of the Fram field showing the major faults. 137

5.9.: Calculated ΔPp_{crit} for Fram, assuming ice model 3 with a constant, pre-Weichselian ice sheet. 138

5.10.: Calculated ΔPp_{crit} for Fram, assuming ice model 5 with a varying, pre-Weichselian ice sheet. 139

5.11.: Structural map of the Oseberg field showing the major faults. 140

5.12.: Calculated ΔPp_{crit} for Oseberg, assuming ice model 3 with a varying, pre-Weichselian ice sheet.1 41

5.13.: Calculated ΔPp_{crit} for Oseberg, assuming ice model 5 with a varying, pre-Weichselian ice sheet. 142

6.1.: Map of the NMSZ and Crustal heterogeneities below the area.....146

6.2.: The portion of the central United States that has been modeled. 148

6.3.: The three different lithospheric models tested. 150

6.4.: Initial stress state and boundary conditions of the NMSZ model. 151

6.5.: Predicted present-day seismic strain rates for Model 1 at a depth of 12,000 m. ...154

6.6.: Predicted present-day seismic strain rates for Model 2 at a depth of 12,000 m. ...157

6.7.: Predicted present-day seismic strain rates for Model 3 at a depth of 12,000 m. ...159

6.8.: Predicted present-day seismic strain rates for Model 3 at a depth of 12,000 m, with

an increased lower crustal viscosities.....160

6.9.: Predicted present-day seismic strain rates for Model 3 at a depth of 12,000 m, with increased lower crustal and lithospheric mantle viscosities.....161

6.10.: Predicted present-day seismic strain rates for Model 3 at a depth of 12,000 m, with increased lower crustal and lithospheric mantle viscosities.....162

6.11.: Temporal change of ice extent for different ice models.....164

6.12.: Predicted present-day seismic strain rates for ice model 1.....165

6.13.: Predicted present-day seismic strain rates for ice model 2.....166

6.14.: Predicted present-day seismic strain rates for ice model 3.....167

6.15.: Seismicity in the NMSZ as a function of time. 171

Chapter 1

IMPACT OF DEGLACIATION ON STRESS AND IMPLICATIONS FOR SEISMICITY AND HYDROCARBON EXPLORATION:

INTRODUCTION

1.1 Introduction

It has long been recognized that ancient ice sheets had a major impact on present-day crustal movements. Based on a comprehensive study of glacial records in Fennoscandia, Nansen (1921) developed a relatively detailed model on how the Fennoscandian ice sheet caused a crustal depression below the center of the ice sheet. His model included a viscous substratum underneath the “flexible sheet of solid rock” (lithosphere), which implies that crustal movements continue even after the completion of ice melting and possibly until present-day (Figure 1.1).

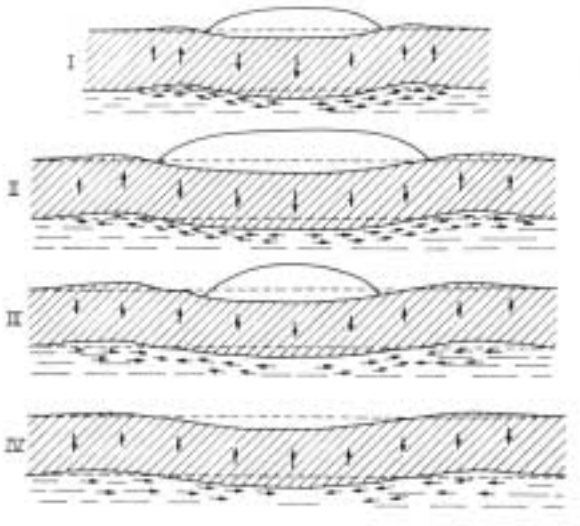

Figure 1.1: Illustration of how a glacial cycle affects vertical lithospheric deformation and associated mass flux in the underlying asthenosphere after Nansen (1921). Importantly, the illustration considers a time-delayed response of the lithosphere-asthenosphere system to the imposed ice load.

Since the 1960’s numerous authors have developed more sophisticated models of glacial loading (e.g. McConnell, 1968; Peltier, 1974; Cathles, 1975). Such models, in combination with observations of post-glacial uplift, were used to constrain the earth’s rheology including mantle viscosities and the flexural rigidity, i.e. thickness of the lithosphere. Fjeldskaar (1997) developed a relatively detailed model of glacial uplift for Fennoscandia suggesting a lithospheric thickness of less than 50 km in southwestern Norway.

Despite, the large number of models investigating uplift (vertical displacement), stress changes due to glacial loading and loading have not been considered until relatively recently. Stein et al. (1979) saw a possible relationship between deglaciation and the

transition from normal faulting earthquakes on Baffin Island, northeastern Canada, to thrust faulting events in the Baffin Bay. They speculated that this laterally changing stress state might be due to bending of the lithosphere, associated with post-glacial rebound. Adams (1989), suggested that the melting North American ice sheet significantly affected the stress state along the former ice margin causing a number of paleo-seismic events, and Hasegawa and Basham (1989) found a spatial correlation between the occurrence of seismicity and post-glacial uplift. More recent studies, including three-dimensional models of plate flexure due to glacial loading, suggest that the existence of ice sheets significantly affected the stress state within the lithosphere and might still partly explain the observed present-day seismicity in Canada and Fennoscandia (e.g. Wu et al., 1999). However, these models were constrained by a very limited amount of questionable stress data and thus more of a speculative nature.

The purpose of this Ph.D. was to get a better idea on how exactly plate flexure due to glacial loading and unloading can affect the stress field within the earth by utilizing reliable stress information with a high spatial resolution. It turns out that the effects of ice loading and unloading significantly altered the stress field along the Norwegian coast. This finding has immense consequences for the exploration and production of hydrocarbons which takes place in large parts of the Norwegian offshore areas. A similar study of deglaciation in the eastern United States shows that the yet unexplained, anomalously high seismicity in the New Madrid area (both paleo-events and more recent seismicity) can be related to stress changes, caused by glacial-related bending of the lithosphere.

1.2 The structure and contents of this thesis

The thesis consists of five main chapters: Chapters 2 through 5 investigate the stress field offshore Norway, starting with the compilation of stress data (Chapter 2). In Chapter 3, I used the compiled stress data to constrain some relatively simple, two-dimensional models of plate flexure, in order to assess the speculated importance of deglaciation in the northern North Sea. Based on the knowledge gained in Chapter 3, in Chapter 4 I rigorously reproduce the observed stresses with three-dimensional models, covering most of the Norwegian margin. In Chapter 5, I used the knowledge gained from the previous chapters to investigate the implications of the modeled stresses for hydrocarbon exploration. In Chapter 6 I extend the study of glaciation related stress changes to the New Madrid Seismic Zone in the United States, where the onset of high seismicity roughly coincided with the melting of the Laurentide ice sheet.

1.2.1 The observed stress field offshore Norway (Chapter 2)

The rigorous testing of models of lithospheric flexure associated with glacial loading requires a reliable stress data set, including stress orientations and magnitudes with a sufficient spatial coverage to detect possible stress changes due to deglaciation. Thanks to the unlimited access to wellbore information at the in-house data base of Norsk Hydro ASA in Bergen, Norway, I was able to obtain a comprehensive stress data set covering large parts of the Norwegian offshore areas, including the northern North Sea and the Mid-Norwegian margin.

The resulting data set is based on the analysis of least principal stress (S_3), pore pressure (P_p), and vertical stress (S_v) data from more than 400 wells offshore Norway (Figure 1.2, Table 1.1).

Table 1.1: Number of wells used for the stress compilation

	North Sea	**Mid-Norwegian margin**
Total nr. of wells	447	114
Wells containing S_3 data	324	70
Wells containing P_p data	385	104
Wells containing S_v data	444	97

Well-defined regional variations are observed in S_3, and P_p but the vertical stress shows no significant lateral changes. Incorporation of precise stress orientation data from drilling-induced tensile borehole wall fractures along with higher quality breakout data from the World Stress Map database (WSM) (Zoback, 1992) shows that the S_{Hmax} orientation is approximately E-W between 60ºN and 62ºN but tends to be NNW-SSE south of 58ºN, similar to the average stress direction seen throughout Great Britain and continental northwest Europe. This stress rotation suggests the influence of stresses due to lithospheric flexure caused by deglaciation. Regional variations of the magnitude of the least principal stress and pore pressure also appear to support the hypothesis that the stress field in this region has been strongly affected by deglaciation. Lowered horizontal stresses are found in proximity of the coast, but the horizontal stresses are higher at larger distances from the coastline. Further north, between 64ºN and 66ºN the orientation of the maximum horizontal stress consistently strikes WNW-ESE. In this area, the least principal stress and pore pressure are spatially more uniform than in the North Sea suggesting that deglaciation-related spatial stress changes are small.

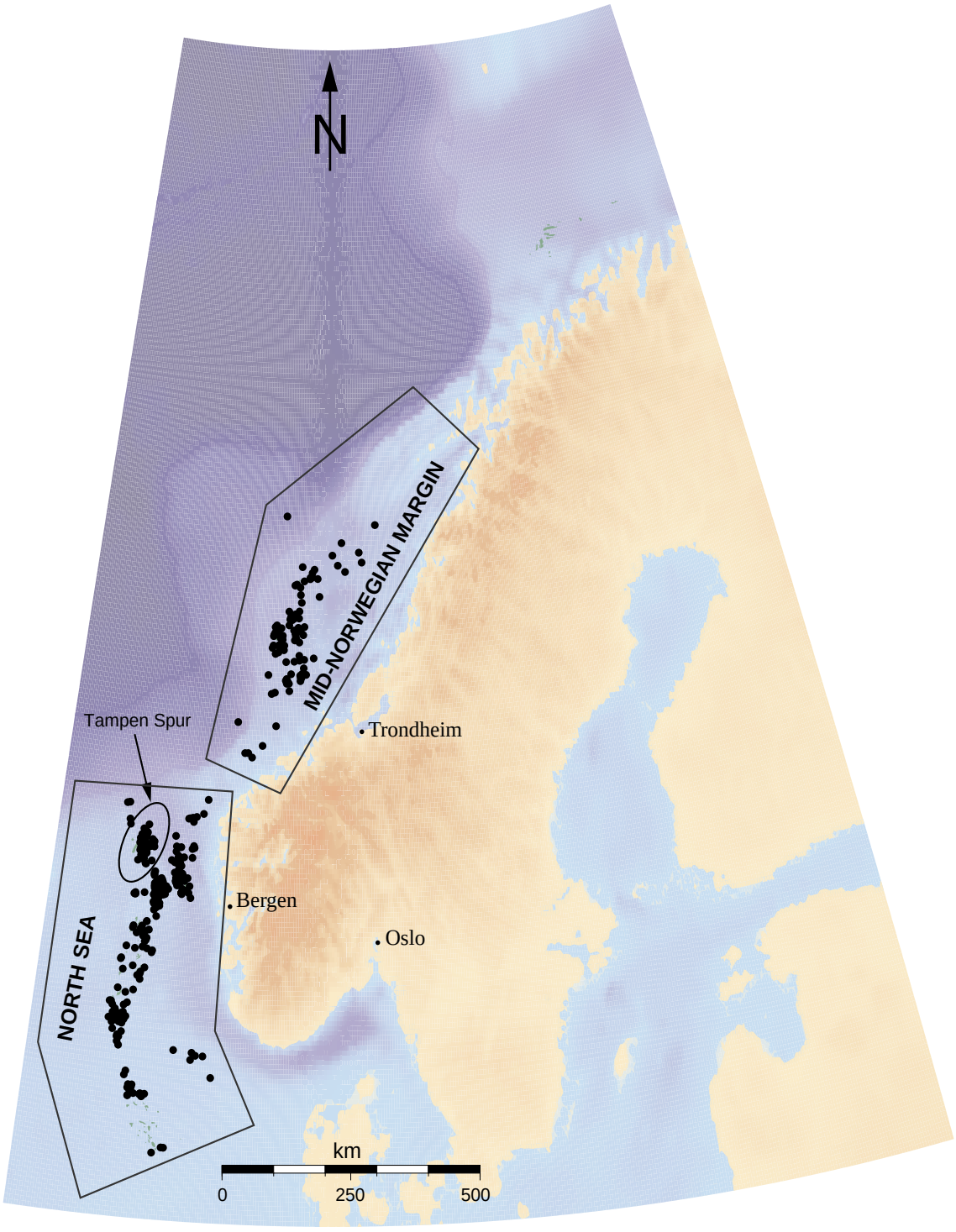

Figure 1.2: Stress data coverage. The map shows the locations of all the wells that were used in the stress analysis (S_3, P_p, S_v), presented in Chapter 2.

1.2.2 The influence of glaciation/deglaciation on the northern North Sea (Chapter 3)

The stress information obtained in Chapter 2, enabled me to rigorously test the influence of deglaciation on the local stress field. If deglaciation was a main source of present-day stress variations offshore Norway, the model should be able to at least partially reproduce the observed stress field. The model should additionally be capable of matching the observed uplift data, the traditional way of constraining models of post-glacial rebound.

The purpose of Chapter 3 was to assess the speculated importance of deglaciation in the northern North Sea by comparing the stress data from Chapter 2, to two-dimensional models of plate flexure. In the northern North Sea, the lateral transition from high horizontal stresses at large distances from the coast to lowered horizontal stresses towards the coast is most pronounced (Figure 1.3).

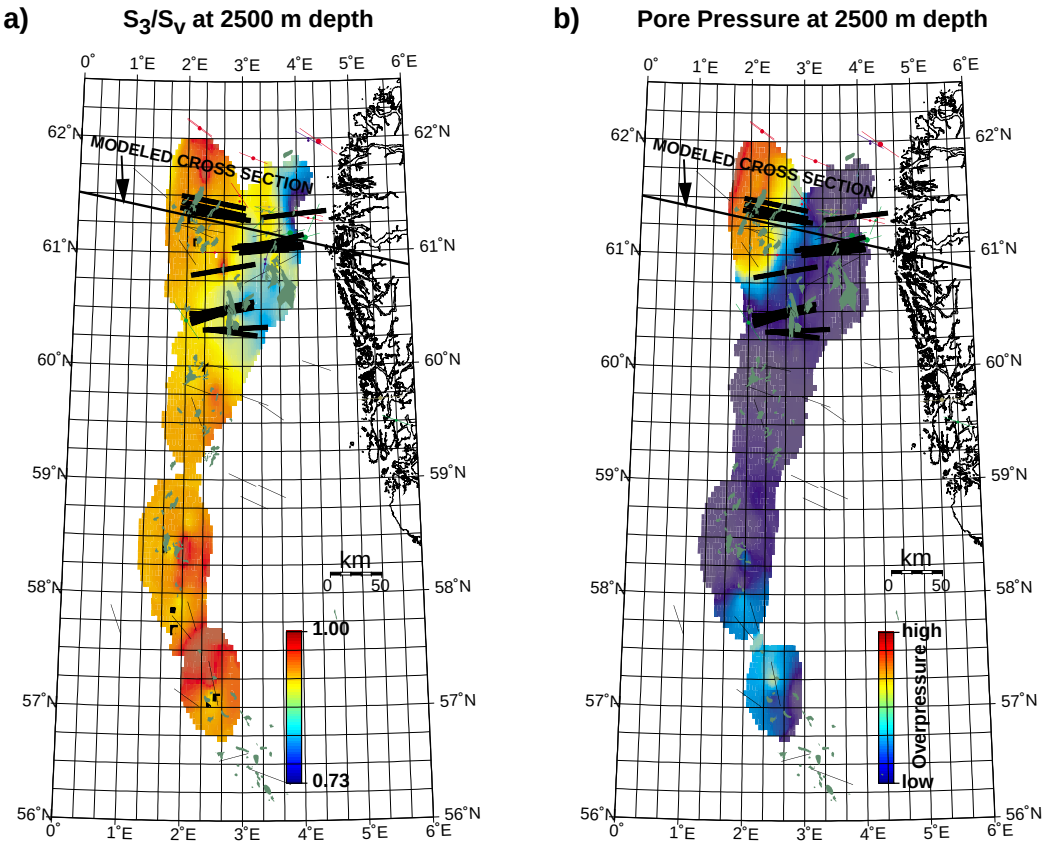

Figure 1.3: Map view of stress and pore pressure in the North Sea. The figure also shows the location of the models studied in Chapter 3. The modeled cross section is located in the northern North Sea, where the lateral transition from high to low stresses and pore pressures is most pronounced.

Two-dimensional, analytical and numerical models of plate flexure suggest that these observed lateral stress variations are the result of deglaciation, superimposed on a regional stress field dominated by ridge push. The results of the numerical models are also consistent with measurements of apparent uplift rate. The pore pressure in the northern North Sea roughly follows the stress trend, i.e. high overpressures where horizontal stresses are high (Tampen Spur) and close to hydrostatic pore pressures east of the Viking Graben where stresses are decreased. This close relationship of pore pressure and horizontal stress suggests that they have the same source. We have modeled the pore pressure change expected from the poroelastic response to deglaciation. The results show that strong overpressures in the Tampen Spur appear to be only partly caused by deglaciation and flexure. Other sources of overpressure, such as compaction disequilibrium also play an important role.

1.2.3 Three-dimensional models of glaciation offshore Norway (Chapter 4)

The purpose of Chapter 4 was to rigorously reproduce the observed stresses along the entire Norwegian margin, using three-dimensional models of plate flexure. The stress data from Chapter 2 helped to constrain the three-dimensional finite element models investigating the effects of glacial melting and the associated flexuring of the lithosphere on the local stress field offshore Norway. The comparison of the model results with the observed stresses suggests that the late Quaternary melting of the Fennoscandian ice sheet strongly influences the in situ stress field along the entire Norwegian margin (see Figure 1.4). Viscoelastic behavior within the lithosphere is required to explain the observed stresses. The model results suggest lithospheric viscosities on the order of 10^{22} to 10^{23} Pa s in the northern North Sea, and slightly higher viscosities on the Mid-Norwegian margin. In addition to the good fit with stress data, the three-dimensional models presented in Chapter 4 are compatible with available uplift data which further supports their validity.

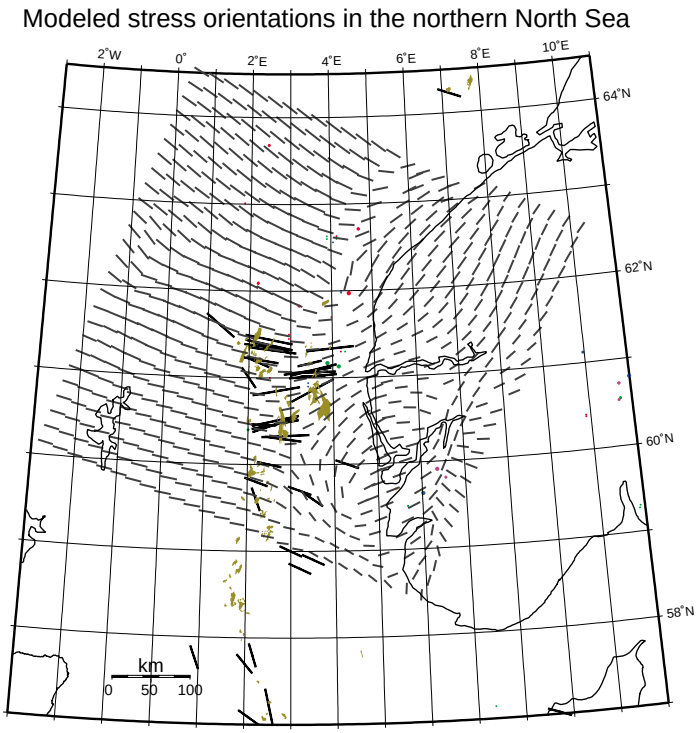

Figure 1.4: Comparison of modeled to observed stress orientations in the vicinity of the northern North Sea. The modeled stress orientations (blue lines) match the stress observations (black lines) extremely well, which suggests that deglaciation is a major stress contributor in the area.

1.2.4 Impact of glacially-induced stress changes on hydrocarbon exploration offshore Norway (Chapter 5)

The Three-dimensional models of lithospheric bending associated with glacial loading and unloading from Chapter 4 provided the evolution of the stress field in the Norwegian offshore areas. In Chapter 5, I have used this knowledge of temporal and lateral stress changes in the Norwegian sector of the North Sea, and on the Mid-Norwegian margin to estimate pore pressure changes due to the poroelastic response to glacially related stress changes. The locations of modeled overpressure coincide with areas of observed overpressures which shows that the glacially-induced stress changes had an impact on the reservoir pore pressure. The magnitude of the modeled overpressure is however smaller than observed overpressures, which suggests that additional mechanisms, such as rapid sedimentation, also contribute to the observed overpressures. The temporally changing stress field leads to frequent reactivations of reservoir faults during the course of the Pleistocene glaciations. As a result, hydrocarbon fields in the Norwegian offshore areas might have been exposed to multiple periods of extensive fault leakage.

1.2.5 Seismicity in the New Madrid area (Chapter 6)

The purpose of Chapter 6 was to extend the knowledge gained in previous chapters, to explain the occurrence of seismicity in the New Madrid seismic zone. This intraplate region has been subjected to an anomalously high seismicity which lead to three M>7 events in 1811-1812. Paleoseismic investigations suggest that seismic activity increased during Holocene time, so a possible relationship to the melting of the Laurentide ice sheet seems obvious.

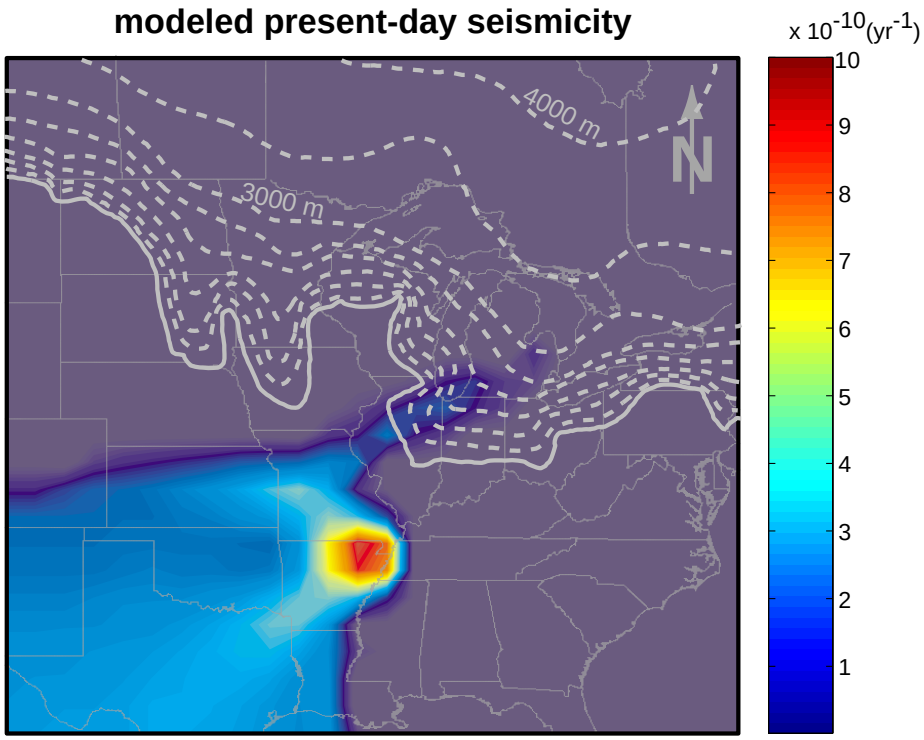

Figure 1.5: Modeled seismic strain rates in the central United states as a result of deglaciation. The model shows that deglaciation causes high seismic strain rates in the vicinity of the New Madrid seismic zone.

We have used a three-dimensional model, similar to the models in Chapter 4, to investigate the interaction between large-scale plate driving forces, lithospheric structure and the stresses induced by bending of the lithosphere as a result of glacial loading and unloading in the New Madrid seismic zone and surrounding regions. The modeling shows that the removal of the Laurentide ice sheet that covered large parts of the northern United States until ~20,000 years ago changed the stress field in the vicinity of New Madrid and caused seismic strain rates to increase by about 3 orders of magnitude. This suggests, that the 1811-1812 earthquake sequence, and the previous large earthquakes throughout the

Holocene, have in fact been triggered by retreat of the Laurentide ice shield. The modeling predicts that the high rate of seismic energy release observed during late Holocene time is likely to remain essentially constant for the next few thousand years which implies high seismic hazard for this anomalous intraplate region.

Chapter 2

STRESS ORIENTATION, PORE PRESSURE AND LEAST PRINCIPAL STRESS OFFSHORE NORWAY

Parts of this chapter will be published with Mark D. Zoback, David J. Wiprut, and Linn Arnesen as co-authors (Accepted for publication in Petroleum Geoscience as of March 2., 2000).

2.1 Abstract

We have compiled data on stress orientation, pore pressure and least principal stress from approximately 400 wells offshore Norway. Well-defined regional variations are observed in all three parameters. Incorporation of precise stress orientation data from drilling-induced tensile borehole wall fractures shows that the orientation of maximum horizontal stress is approximately E-W between 60ºN and 62ºN but tends to be NNW-SSE south of 58ºN, similar to the average stress direction seen throughout Great Britain and continental northwest Europe. We believe this rotation is due to the superposition of plate-driving stresses with those associated with lithospheric flexure caused by deglaciation. Regional variations of the magnitude of the least principal stress and pore pressure also appear to support the hypothesis that the stress field in this region has been strongly affected by deglaciation. Further north, between 64ºN and 66ºN the orientation of the maximum horizontal stress consistently strikes WNW-ESE. In this area, the least principal stress and pore pressure are spatially more uniform than in the North Sea suggesting that deglaciation-related spatial stress changes are small.

2.2 Introduction

In recent years it has become clear that knowledge of the in-situ stress field is important to address problems as diverse as wellbore stability, hydrocarbon migration, and fluid flow through fractured reservoirs. Having good knowledge about the in-situ stress field and its spatial variations is also crucial to understand geodynamic processes such as ridge push or deglaciation and their influence on the evolution of an area such as the North Sea, or the Mid-Norwegian margin. To date, knowledge of stress in these areas is mostly limited to stress orientations, whereas studies of stress magnitudes have been limited to specific hydrocarbon reservoirs. The aim of this chapter was therefore to provide a comprehensive understanding of stress in the Norwegian offshore areas, including spatial variations of orientations and magnitudes. More specifically, we concentrated on the North Sea (Figure 2.1), and on the Mid-Norwegian Margin (Figure 2.2) because the stress data coverage is sufficient in these areas. We left out the Barents Sea because the limited amount of wells, distributed over a large area do not provide enough data.

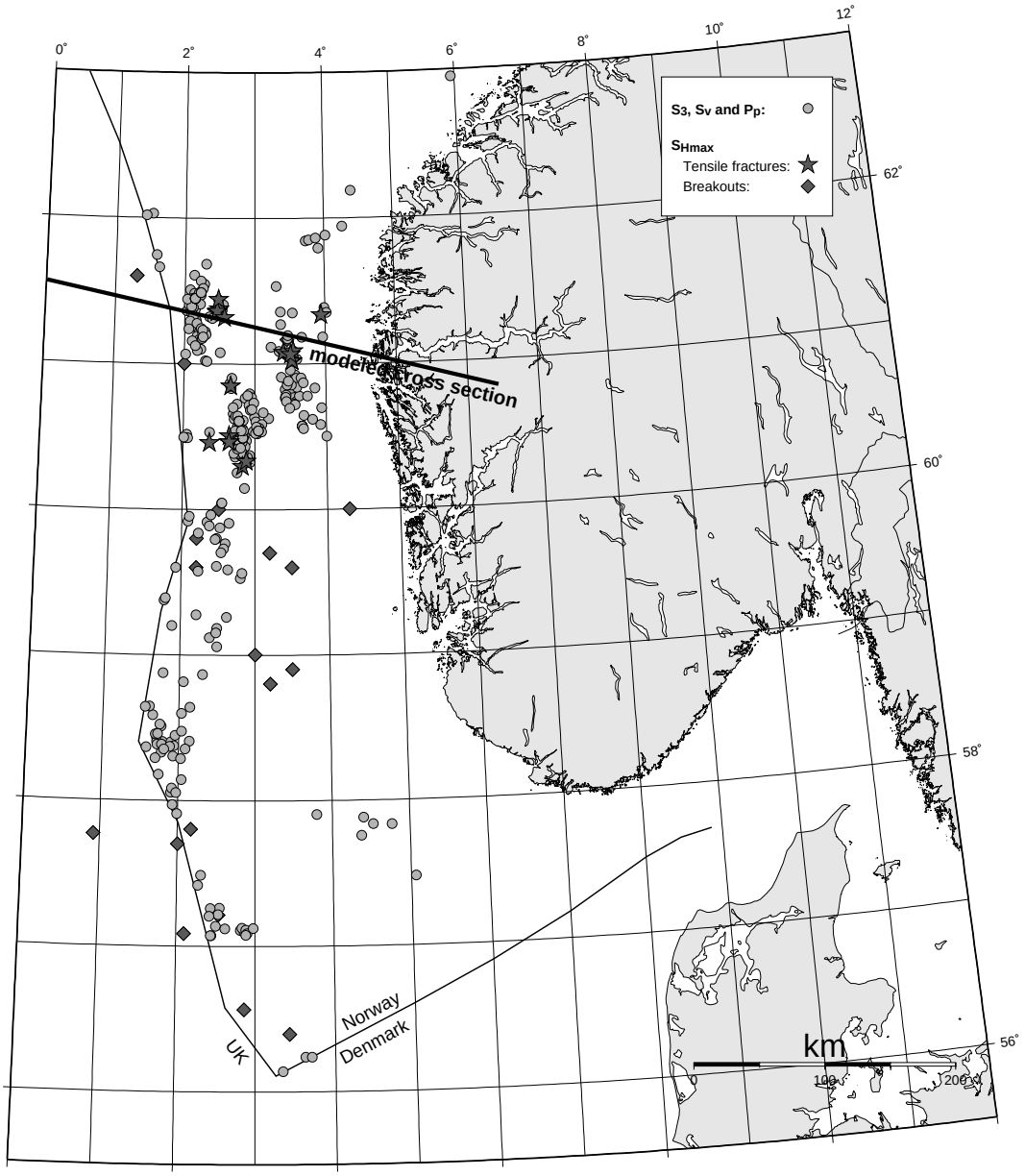

Figure 2.1: Data coverage for the North Sea. Grey circles: boreholes with leak-off test (S_3), density log (S_v), and pore pressure data. The data coverage is noticeably better north of 60ºN than further to the south. The stars indicate the location of boreholes for which Wiprut & Zoback (1998) used tensile fractures to deduce the orientation of S_{Hmax}. The diamonds are the locations of S_{Hmax} measurements from breakouts. The modeled cross section refers to the model shown in Figure 2.13.

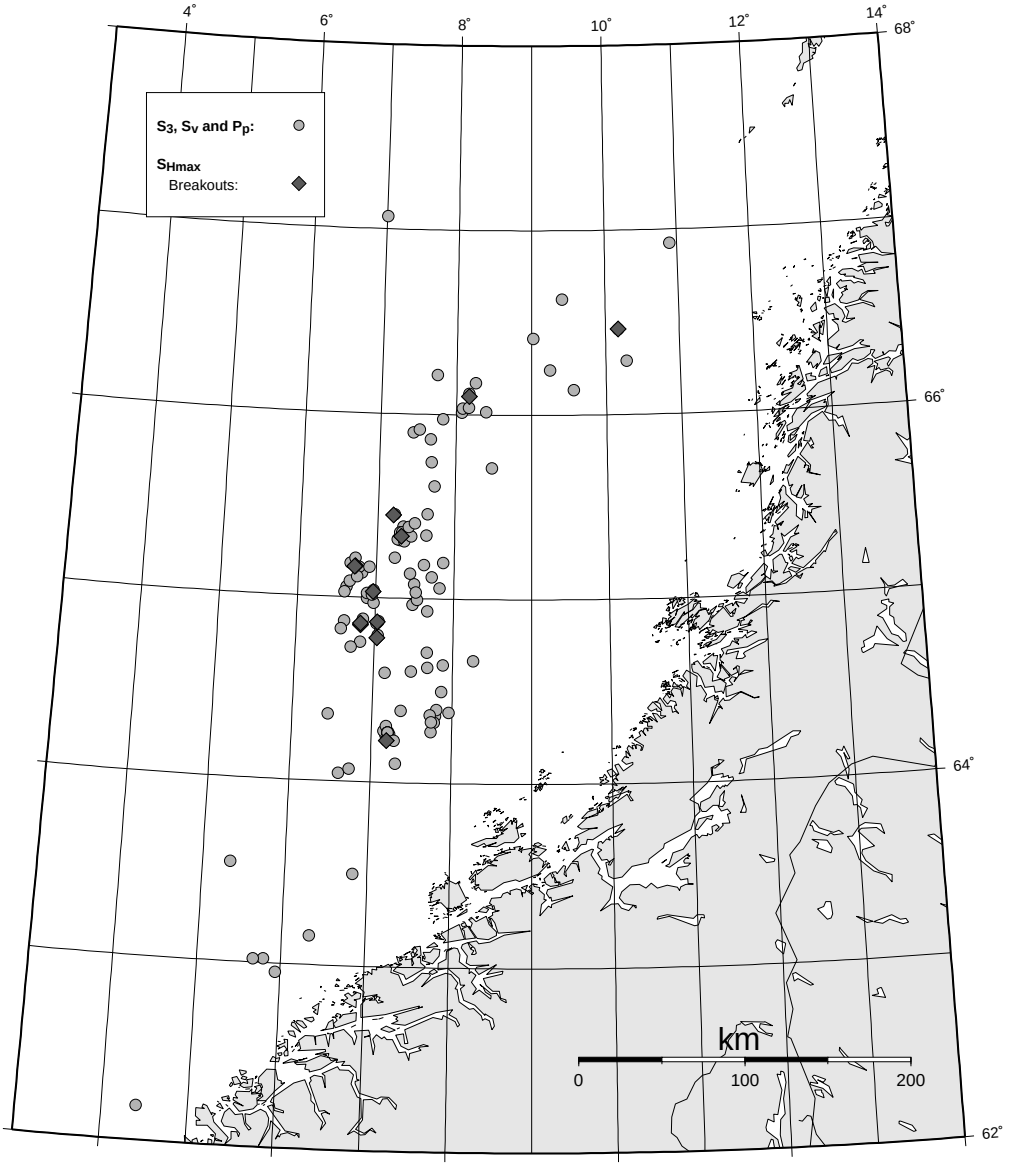

Figure 2.2: Data coverage for the Mid-Norwegian margin. Grey circles: boreholes with leak-off test (S_3), density log (S_v), and pore pressure data. The data coverage is best between 64ºN and 66ºN. The diamonds are the locations of S_{Hmax} measurements from breakouts. No tensile fracture analysis exists for this area.

The World Stress Map (WSM) project (Müller et al. 1992; Zoback 1992) has accumulated a large data base on the orientation of the maximum horizontal stress (S_{Hmax}) including data for the North Sea (Figure 2.1) and Mid-Norway (Figure 2.2). We have used the data from the WSM together with S_{Hmax} orientations obtained from tensile fractures along the wellbore wall to compile a map of S_{Hmax} orientations.

Numerous authors have analyzed leak-off tests to determine the least principle stress

(S_3) for specific hydrocarbon fields (e.g. Borgerud & Svare 1995; Jorgensen & Bratli 1995), but a comprehensive analysis of S_3 throughout the North Sea and Mid-Norway has been lacking to date. As pore pressure (P_p) is closely related to stress and affects the faulting behavior of rock, in this study we have gathered S_3 and P_p information from approximately 400 wells, covering most of the Norwegian sector of the North Sea, and Mid-Norway, which enabled us to systematically track magnitudes and spatial changes of S_3 and P_p.

2.3 Orientation of the maximum horizontal stress (S_{Hmax})

A number of studies have investigated the stress field offshore Norway by using borehole breakout data to determine the orientation of S_{Hmax} (e.g. Fejerskov 1996; Gölke & Brudy 1996). The breakout data give a good picture of the large scale changes in stress orientations. However, breakout data are potentially contaminated by keyseating (abrasion of the wellbore wall in deviated wells caused by drill string rotation) and as a result the data often reflect the borehole orientation rather than the stress field. Unfortunately, keyseating can occur even at borehole deviation angles of less than 5 degrees from vertical, so a large portion of the breakout data can be affected by keyseating. To clean up the existing breakout database, we excluded all breakouts with azimuths within 10 degrees of the borehole deviation direction).

Figure 2.3 shows the revised breakout data together with S_{Hmax} orientations inferred from drilling induced tensile fractures for the North Sea. The bold lines display the S_{Hmax} orientations by Wiprut & Zoback (1998) as inferred from drilling induced tensile fractures. Drilling induced tensile fractures are more reliable to determine the orientation of S_{Hmax} because they are identified from image logs which precludes data contamination of any kind. Importantly, S_{Hmax} orientations from tensile fractures typically show no depth dependence and have a standard deviation of ±10 degrees for an entire well (Wiprut & Zoback 1998). Unfortunately, no S_{Hmax} orientations from tensile fractures are available for the Mid-Norwegian margin and all S_{Hmax} orientations on the Mid-Norwegian margin (Figure 2.4) are obtained from borehole breakouts.

Earthquake focal plane mechanisms can also be used to determine S_{Hmax} orientations (e.g. Bungum et al. 1991). However, focal plane solutions give only a rough estimate of the in-situ stress field, since one has to assume that the principal stress axes form an angle of 45 degrees with the rupture plane. Also, the focal plane solutions offshore Norway are not

well determined since all the seismographs are onshore and the depth resolution is poor. For these reasons we excluded S_{Hmax} orientations inferred from earthquakes. However, S_{Hmax} orientations from earthquakes generally agree with the borehole measurements.

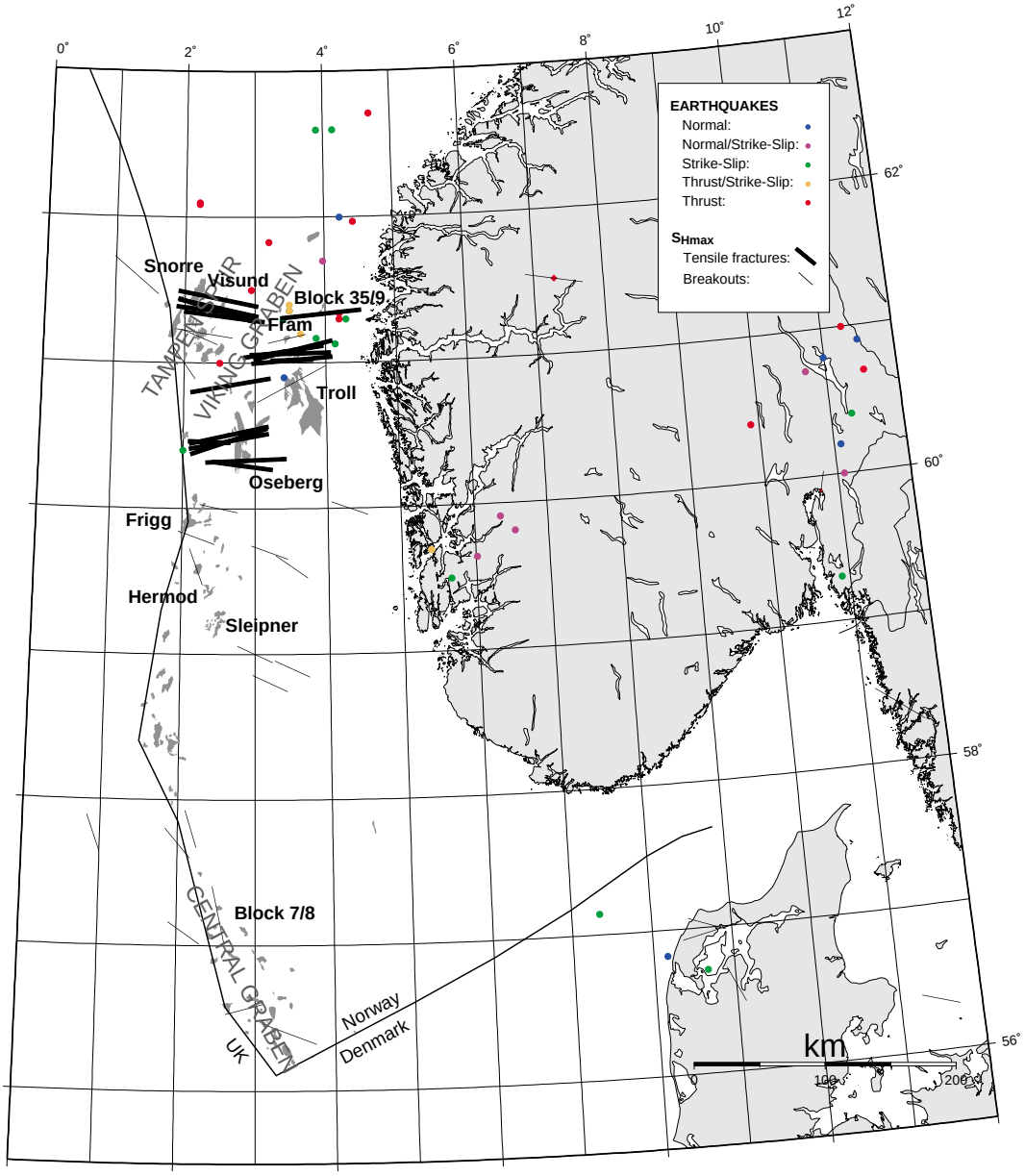

Figure 2.3: Compilation of S_{Hmax} orientations in the Norwegian sector of the North Sea from the analyses of breakouts and tensile fractures. The data show that between 60ºN and 62ºN S_{Hmax} strikes WNW-ESE west of the Viking Graben and rotates to a WSW-ENE striking direction towards the Norwegian coast. Between 59ºN and 60ºN S_{Hmax} is WNW-oriented. South of 58ºN the S_{Hmax} directions are not as well defined as further north but have an average strike of NNW-SSE. Also, the figure shows an increased occurrence of earthquakes north of 60ºN.

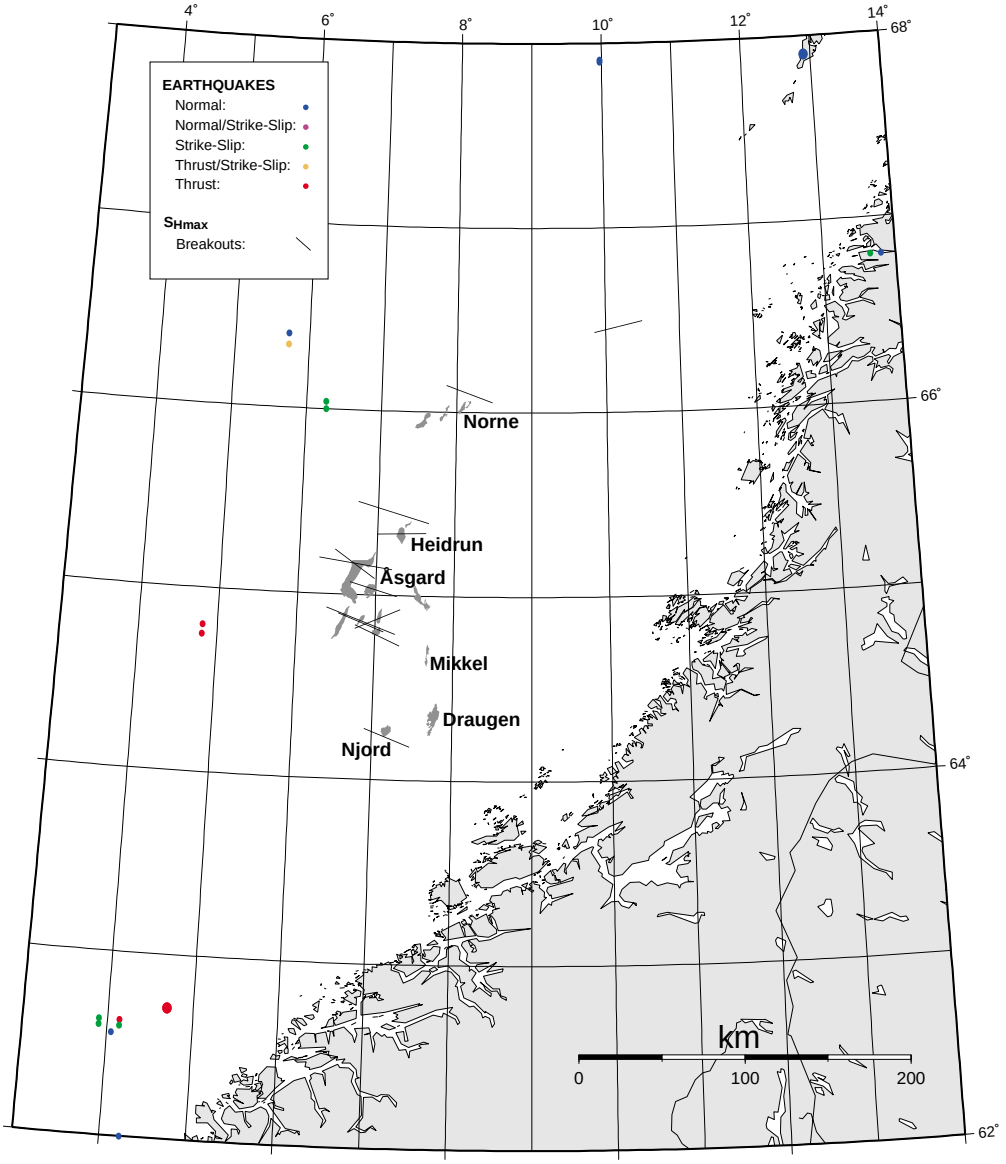

Figure 2.4: Compilation of S_{Hmax} orientations on the Mid-Norwegian margin from the analyses of borehole breakouts. The data show that between 64ºN and 66ºN S_{Hmax} strikes WNW-ESE without noticeable variations. Data coverage does not allow the investigation of a possible stress rotation towards the coast.

Figure 2.3 displays the compilation of available S_{Hmax} orientations from borehole breakouts and drilling induced tensile fractures in the North Sea. The area between 60ºN and 62ºN has the best data coverage and roughly shows an E-W direction of S_{Hmax}. A closer examination reveals that S_{Hmax} rotates from an azimuth of ≈100º west of the Viking Graben, to ≈80º closer to the coast. South of 60ºN, S_{Hmax} tends to rotate clockwise to an average direction of ≈115º and seems to be independent of longitude. South of 59ºN the

data coverage is very sparse. The breakout data available for the Central Graben area roughly show a NW striking S_{Hmax}-orientations that are subjected to a large scatter.

On the Mid-Norwegian margin (Figure 2.4) the orientation of S_{Hmax} is WNW-ESE with almost no variations. Unfortunately, the available data only cover a relatively small area, i.e. a possible rotation of S_{Hmax} towards the coast can not be resolved. All S_{Hmax} orientations on the Mid-Norwegian margin are obtained from borehole breakouts and therefore not as reliable as the North Sea data set. Nevertheless, the orientations are very consistent, thereby suggesting that the quality of the measurements is sufficient.

It is noteworthy that S_{Hmax} orientations offshore Norway show no systematic changes with depth. Further, at least for the area between 60ºN and 62ºN, and between 64ºN and 66ºN S_{Hmax} orientations are laterally very consistent and follow clear trends rather than random variations which implies that the data quality is high enough to reflect changes in the tectonic stress field, and that such changes exist. Finally, the stress orientation data suggest that the stress field in the northern North Sea deviates from the NNW-striking orientation of S_{Hmax} that is observed almost throughout northwest Europe (Müller et al. 1992).

2.4 Magnitude of the least principal stress (S_3)

Another valuable source of stress data are leak off tests (LOT) which give the approximate magnitude of the least principal stress (S_3). A LOT is performed by pressurizing the uncased section of a borehole until fractures open and begin to take in fluid. By plotting the pressure as a function of mud volume pumped into the hole, a deviation from a linear trend indicates the onset of fracture opening and gives a rough estimate for the least principle stress, assuming that the tensile strength of rock is negligible; a good assumption if preexisting fractures exist. S_3 is fairly well known for a number of oil fields (e.g. Borgerud & Svare 1995; Jorgensen & Bratli 1995). However, a consistent analysis of LOTs throughout the entire North Sea was lacking. Thus, we analyzed LOT's from every borehole displayed in Figures 2.1 and 2.2 to improve the knowledge of regional trends of the S_3 magnitude at a relatively high resolution.

Assuming that one of the principal stress axes is vertical, the overburden stress (S_v) derived from integrated density logs corresponds to another principal stress magnitude. By looking at S_3 normalized by S_v (S_3/S_v), we can partly determine the stress regime a certain area is exposed to. In addition to being characteristic of the stress regime the use of S_3/S_v eliminates the effects of varying water depth on stress at a given depth below sea level. If S_3/S_v is significantly lower than unity, the faulting regime according to Andersonian

faulting theory (Anderson 1951) is normal faulting. Conversely, if S_3/S_v is close to unity the faulting regime is more compressive, i.e. strike-slip or even reverse faulting. High S_3/S_v ratios (≈1) can also represent a near isotropic stress state which may be the case at shallow depths (< 1000 m) where the viscous behavior of the unconsolidated Plio-Pleistocene sediments leads to an almost immediate relaxation of any imposed differential stress. This explains why S_3 on Figure 2.5 is always very close to S_v at depths shallower than 1000 m. However, analysis of the full stress tensor in the Visund field (Wiprut & Zoback 1998) shows that at depths greater than 2000 m below mean sea level (MSL) the stress state is strongly anisotropic and some faults in the area are close to failure. Similar studies of wellbore failure also show high stress anisotropies in Fram and Oseberg (pers. com. D. Wiprut 2000). Further, the spatially consistent S_{Hmax} orientations (Figures 2.3 and 2.4) requires horizontal stress anisotropy and the frequently observed drilling induced tensile fractures, (used to constrain many S_{Hmax} orientations on Figure 2.3), form only under an appreciable horizontal stress anisotropy (Moos & Zoback 1990). All together, these observations provide strong evidence for high stress anisotropies at depths greater than 2000 m. Thus, it seems reasonable to assume that S_3/S_v close to unity suggests high horizontal stresses.

We have utilized the following methodology to obtain S_3/S_v ratios for depths between 1500 m and 3000 m at increments of 500 m. First we analyzed leak-off tests for 324 vertical exploration wells in the North Sea, and 70 wells offshore Mid-Norway. We ignored data from production wells to prevent the influence of S_3 changes due to production-related pore pressure draw down. The obtained S_3-values were classified into good and poor measurements. A good measurement, has a well-defined leak-off pressure and the pressure buildup during the test exceeds the formation breakdown pressure. In the case of the poor measurements, leak-off pressures are not well defined or were not reached at all. Additionally, in some rare cases we obtained S_3 from minifrac tests which are more reliable than LOT's because only small isolated sections of the formation are pressurized in multiple cycles (e.g. Figure 2.5d). We used integrated density logs to obtain S_v for every well containing S_3 data although the obtained S_v with depth profiles do not vary much throughout large portions of the Norwegian offshore area. Subsequently, we plotted the obtained S_3-values, together with S_v as a function of depth. In cases where one well did not provide enough data we merged nearby wells. Figure 2.5 shows examples of such stress versus depth plots. We then fit a line through the S_3 data by hand, giving the preference to good LOT measurements and Minifrac tests if available. As, LOT's tend to overestimate S_3 (e.g. Gaarenstroom et al. 1993) we gave preference to lower S_3 estimates if multiple values were available (e.g. Figure 2.5f). As can be seen on Figure 2.5, not every well provides S_3-data

for the entire depth range but the combination of all available wells allows a very good data coverage of the entire depth range between 1,500 m and 3,000 m. To map spatial changes of stress we have plotted S_3/S_v at the previously mentioned depths for areas with satisfactory data coverage (Figures 2.6 and 2.7).

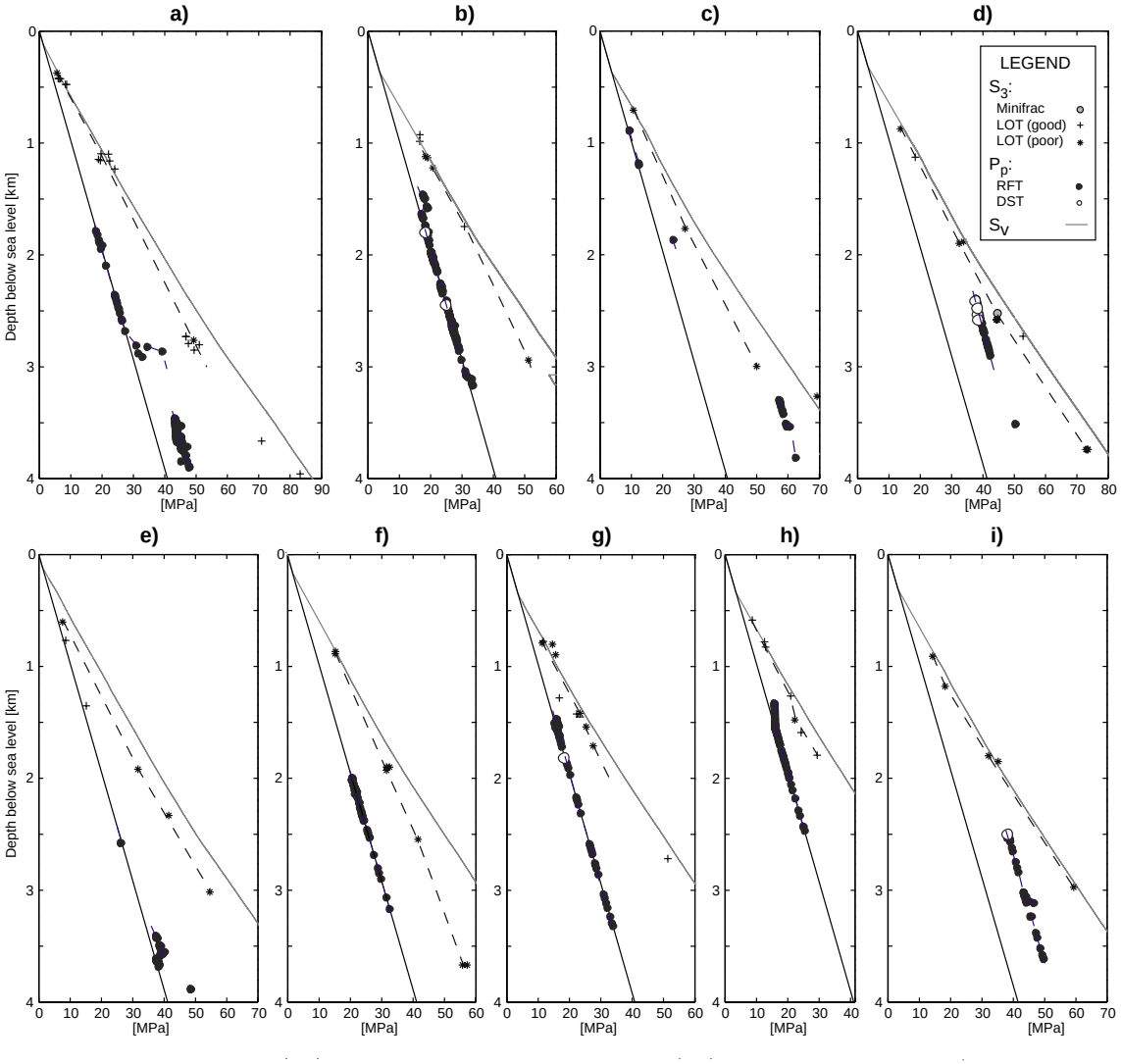

Figure 2.5: The different panels (a-i) show typical examples of compiled S_3, S_v and pore pressure data as a function of depths used in the analysis.

To estimate the error associated with the S_3/S_v values we need to consider the uncertainties of the S_3 and S_v measurements. We mentioned earlier that LOT's are only an approximate measure of S_3 since they can be affected by several factors such as a poor cement bond at the casing shoe, and a finite tensile strength of the formation. However, Figure 2.5 shows that the LOT's define clear trends of S_3 with depth and are subjected to a maximum scatter of ≈±2 MPa. The S_v estimations from integrated density logs are very

accurate and overlap for nearby wells. Thus, it is fair to assume that S_v does not scatter more than ±0.5 MPa. Using equation 2.1 from basic error propagation theory, the error of S_3/S_v can be estimated.

$$\Delta(\mathbf{S}_3/\mathbf{S}_v) = \left|\frac{\Delta \mathbf{S}_3}{\mathbf{S}_3}\right| + \left|\frac{\Delta \mathbf{S}_v}{\mathbf{S}_v}\right| \qquad \text{Eqn. 2.1}$$

$\Delta(S_3/S_v)$ is the uncertainty of S_3/S_v. ΔS_3 and ΔS_v are the scatter associated with the measurements of S_3 and S_v respectively. $\Delta(S_3/S_v)$ varies with depth since it depends on S_3 and S_v. For a depth of 3000 m, $\Delta(S_3/S_v)$ is approximately 0.05 but gradually increases towards the surface and reaches a value of 0.1 at 1500 m. Also, the data coverage shown on Figure 2.1 is best between 60ºN and 62ºN and decreases towards the south, so the values illustrated in Figures 2.6 and 2.8 tend to be more reliable in the Viking Graben area with a decreasing reliability towards the south. Similarly, in Mid-Norway (Figure 2.2) the values displayed in Figures 2.7, 2.9 and 2.10 are most reliable around 65ºN as this is the area with the best data coverage.

In the North Sea, at a depth of 1500 m MSL (Figure 2.6a) no clear pattern of lateral stress variation can be observed. However, a zone of relatively low S_3/S_v values (≈0.83) starts to develop around 61.5ºN and 4ºE. The rest of the Norwegian North Sea exhibits fairly high S_3/S_v ratios between 0.9 and 1, except for the area surrounding the Frigg field (see Figure 2.3 for locations) which shows slightly reduced S_3/S_v ratios of <0.9. A clearer picture unfolds at 2000 m MSL (Figure 2.6b), where S_3/S_v ratios consistently drop close to the coast reaching values of as low as 0.78 in Block 35/9. Towards the west S_3/S_v gradually increases across the Viking Graben and exhibits values close to unity in the Tampen Spur area. The transition from low S_3/S_v values in Block 35/9 to the highest S_3/S_v ratios in the Tampen Spur occurs over a horizontal distance of ≈100 km. Further to the south S_3/S_v is mostly high and rarely drops below 0.9. At 2500 m MSL (Figure 2.6c) the S_3/S_v-distribution looks very similar to 2000 m MSL. However, the zone of decreased S_3/S_v seems to extend further to the west in the Oseberg region. In the southern parts of the Norwegian Sector (south of 60˚N) S_3/S_v is generally higher than at 2000 m MSL and never falls below 0.95. The stress distribution at 3000 m MSL has a decreased reliability, because the amount of S_3-data is reduced for this depth slice. Nevertheless, the horizontal stress changes at 3000 m MSL are comparable to the shallower depth slices with high S_3/S_v values (0.9-1) in the west and decreased S_3/S_v closer to the coast. A marked decrease of S_3/S_v occurs in the Oseberg area but around Block 35/9 S_3/S_v is higher than at shallower depth.

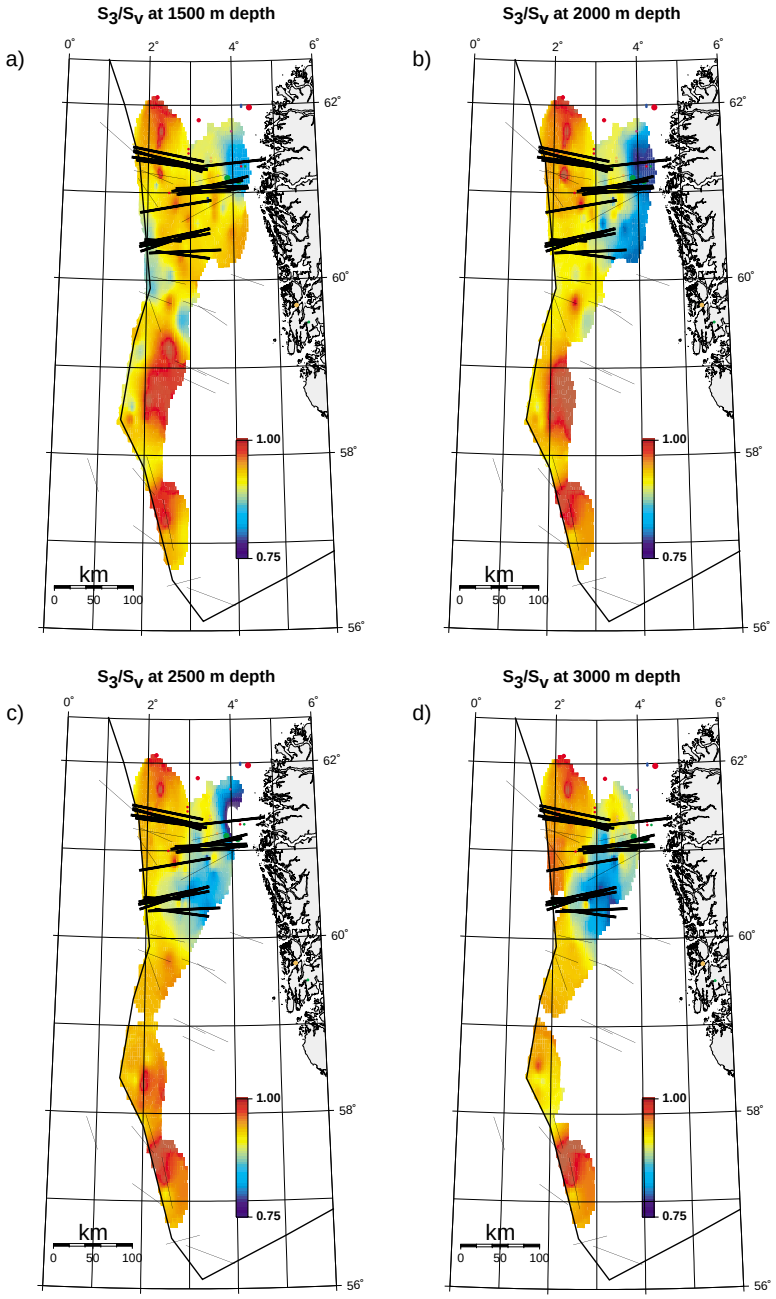

Figure 2.6: Lateral variation of the least principal stress normalized by the vertical stress (S_3/S_v) for different depth slices in the North Sea. S_3 is derived from leak-off tests and S_v comes from integrated density logs. The figure shows that S_3/S_v is consistently low close to the Norwegian coast and increases towards the west (perpendicular to the coast line). The black lines indicate S_{Hmax} orientation from Figure 2.3.

In summary, S_3/S_v is consistently high (0.9-1) at distances larger than ≈100 km from the coast at all depths indicating a strike-slip or even reverse faulting stress state. Closer to the coast (between 60ºN and 62ºN where data are available), S_3/S_v drops to values as low

as 0.73 in Block 35/9 at a depth of 2500 m MSL which suggests that the stress state is strike-slip or even normal faulting. Importantly, lines of equal S_3/S_v run roughly parallel to the coast line, which gives some indications as to what causes these lateral stress variations (see discussion section). Earthquake focal plane mechanisms confirm the transition from reverse faulting offshore to strike-slip or even normal faulting towards the coast for the area between 61ºN and 62ºN (Lindholm et al. 1995).

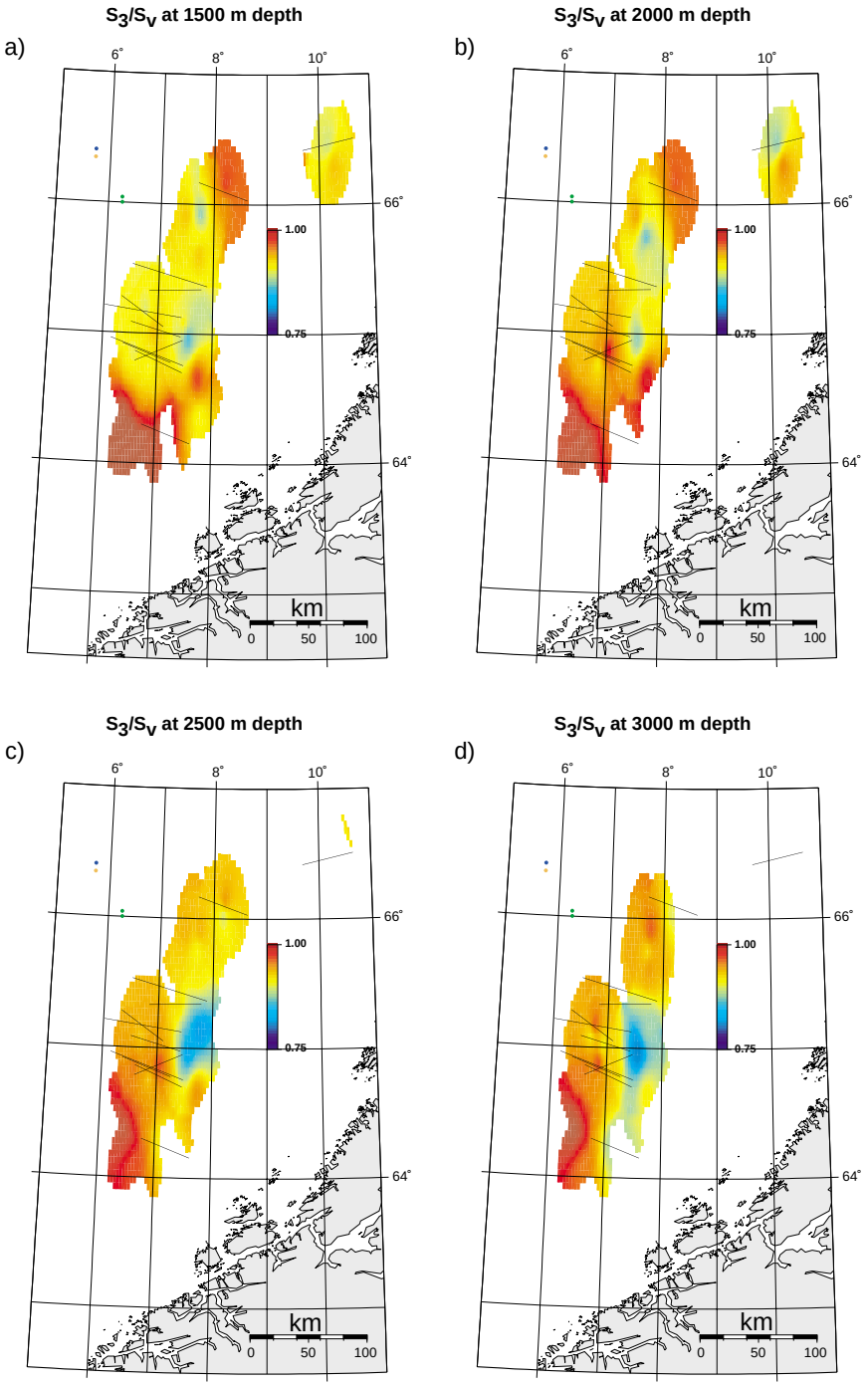

Figure 2.7: (previous page) Lateral variation of the least principal stress normalized by the vertical stress (S_3/S_v) for different depth slices on the Mid-Norwegian margin. S_3 is derived from leak-off tests and S_v comes from integrated density logs. The figure shows that spatial changes of S_3/S_v are not as obvious as in the North Sea. At least for depths below 2000 m S3/Sv seems to show a tendency to decrease towards the coast. The black lines indicate S_{Hmax} orientation from Figure 2.4.

In Mid-Norway, the spatial changes of the least principal stress are not as clear as in the North Sea. Figure 2.7a shows that at a depth of 1500 m MSL S_3/S_v is mostly between 0.9 and 1 except for a small area at 65ºN and 7.5ºE where S_3/S_v drops to 0.85. A zone of consistently high stress ($S_3/S_v \approx 1$) is located south of 64.5ºN and west of 7ºE. At 2000 m depth (Figure 2.7b) the stress distribution looks very similar but west of 7ºE S_3/S_v is slightly higher than at 1500 m depth. A more consistent pattern unfolds at 2500 m depth (Figure 2.7c) where most of the area shows S_3/S_v values of approximately 0.95 but a distinct zone of lowered S_3/S_v develops around 65ºN and 8ºE. At 3000 m (Figure 2.7d) this zone extends further to the south such that S_3/S_v is below 0.9 east of 7ºE and south of 65.3ºN. Even at this depth the zone of very high S_3/S_v in the southwest corner still exists.

In summary, the spatial distribution of S_3/S_v offshore Mid-Norway is not as clear as in the North Sea. At depths of 2,500 m, and 3,000 m the data indicate a transition to lowered S_3/S_v towards the coast, as observed in the North Sea but the data does not get close enough to the coast to fully resolve a possible stress change. Above 2,500 m the observed stress variations are almost within the error bounds which suggests that there are no significant spatial changes in stress at these depths.

In contrast to S_3 and S_v it is much harder to get reliable values for the magnitude of the maximum principal stress (S_1) and analyses of the full stress tensor from wellbore failure are needed. To date, only two studies of the full stress tensor inferred from wellbore failure exist for the studied area (Wiprut & Zoback 1998; Brudy 1998). Unfortunately, both of these papers deal with fields on the Tampen Spur, so it is impossible to directly track lateral changes of S_1 outside the Tampen Spur. Nevertheless, the results of the two studies are consistent and give values for S_1/S_v between 1.2 and 1.35. Combined with the leak off data ($S_3/S_v \approx 0.95$) this results in a strike-slip or almost reverse faulting stress regime in the Tampen Spur.

2.5 Pore pressure (P_p)

To identify the stress field it is crucial to know the pore pressure since stress and pore pressure are closely related via poroelastic responses (e.g. Engelder & Fischer 1994). Also, the faulting behavior of rock depends on the stress state and the pore pressure. Thus, we

have compiled pore pressure (P_p) data from 385 exploration wells in the Norwegian sector of the North Sea, and another 104 wells from the Mid-Norwegian margin. We ignored data from production wells to prevent the influence of production-related pore pressure draw down. The pore pressures are derived from repeat formation tests (RFT), which are routinely performed at reservoir depth. An RFT is carried out by measuring the fluid pressure necessary to prevent flow into or out of the formation. Additionally, a limited number of P_p values come from drill stem tests. Almost all P_p-measurements are made in sandstones so the subsequent analysis resembles P_p as observed in sandstones. We produced maps of overpressure (P_p-$P_{hydrostatic}$) for different depth slices in the same way as for S_3/S_v ratios to track changes of P_p both laterally and with depth. The error associated with the P_p measurements used in this analysis is negligible. However, the methodology of showing regional trends of P_p (Figures 2.8, 2.9, and 2.10) does not resolve P_p-variations within a specific hydrocarbon reservoir. For reasons of data confidentiality we can not provide absolute P_p-values in these figures.

At depths shallower than 1500 m MSL the pore pressure is hydrostatic throughout the Norwegian sector of the North Sea, which is not surprising since the pore fluids are likely to be in hydraulic communication with the sea floor. A small zone of moderate overpressure starts to develop south of 58ºN at 1500 m MSL (Figure 2.8a). The pore pressures in the remaining parts of the Norwegian sector are however close to hydrostatic. At 2000 m MSL (Figure 2.8b) a distinct zone of hard overpressure starts to develop in the Tampen Spur. Additionally, a small zone of overpressure exists in the vicinity of Block 35/9. The previously mentioned zone of overpressure at 1500 m MSL south of 58ºN still exists at 2000 m MSL. However, the majority of the Norwegian sector exhibits pore pressures close to hydrostatic at 2000 m MSL. At 2500 m MSL (Figure 2.8c) the zone of hard overpressure in the Tampen Spur area is even more pronounced. In contrast to 2000 m MSL at 2500 m MSL the zone of elevated pore pressures around Block 35/9 has disappeared and except for the Tampen Spur area most of the Norwegian sector exhibits hydrostatic pore pressures. Figure 2.8d shows that the Tampen Spur still is strongly overpressured at 3000 m MSL. However, further south in the vicinity of the Frigg and Hermod fields a very strong overpressure can be observed. Also, the area south of 59˚N generally displays a slight overpressure at 3000 m MSL. Still, large parts of the Norwegian sector show pore pressures close to hydrostatic, including the areas surrounding the Troll and Oseberg fields.

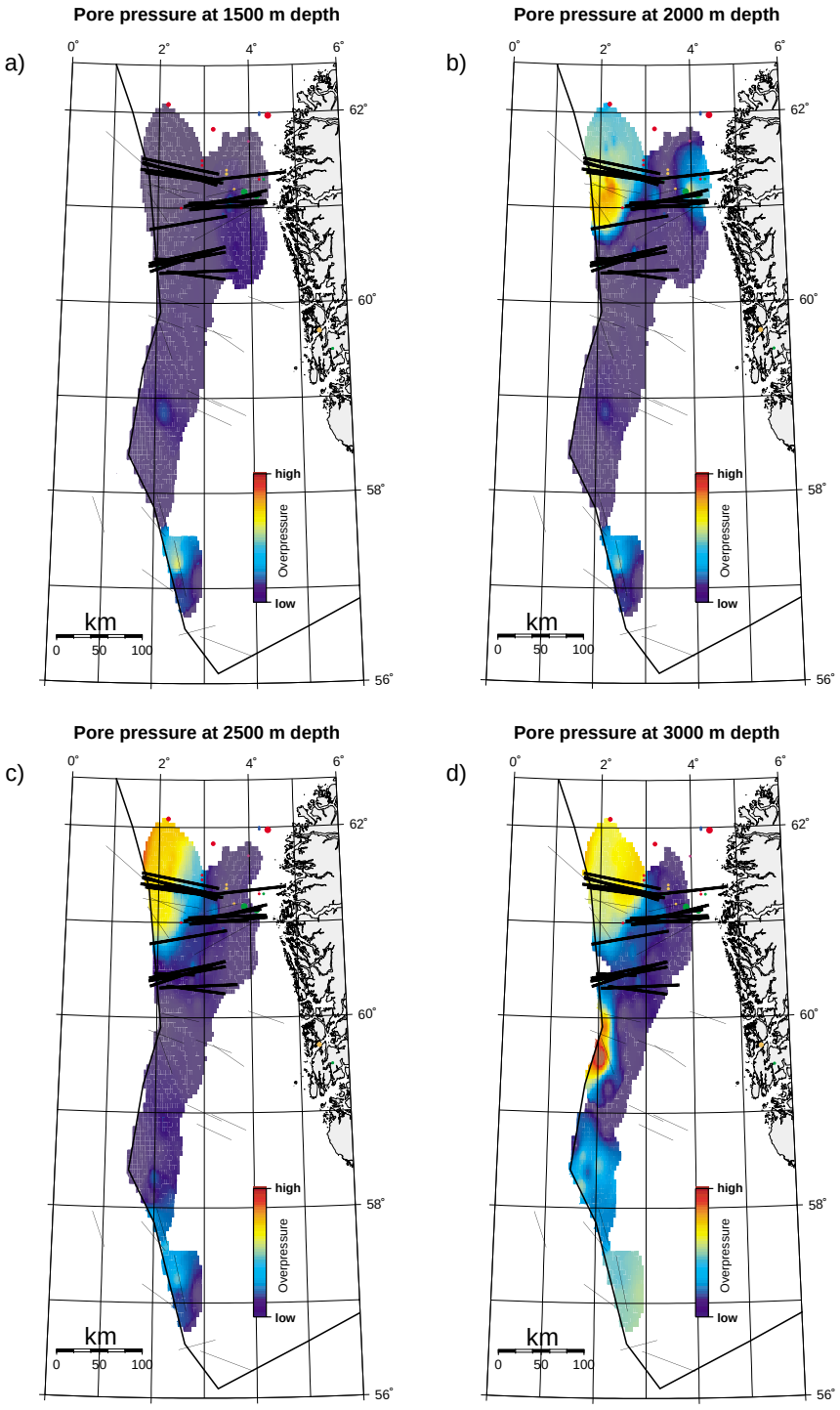

Figure 2.8: Lateral variation of overpressure for different depth slices in the North Sea. The overpressure is mostly derived from RFT-logs and in some cases from drill stem tests. The figure shows that the pore pressure is mostly hydrostatic but highly overpressured west of the Viking Graben (Tampen Spur). Slight overpressure also occurs south of 58ºN. The black lines indicate S_{Hmax} orientations from Figure 2.3.

In summary, pore pressures are mostly hydrostatic throughout the Norwegian part of the North Sea to a depth of 2500 m MSL with the exception of the Tampen Spur, Blocks 35/9, and 7/8. The Tampen Spur shows the most marked pore pressure increase, whereas the overpressure in Block 35/9 is small and limited to a relatively small depth interval.

Figures 2.9 and 2.10 show the results of the pore pressure analysis for the Mid-Norwegian margin. Figure 2.9a shows that the pore pressures are mostly hydrostatic at a depth of 1500 m, with the exception of a small area at 66.5ºN and 8ºE with a slight overpressure. At 2000 m depth pore pressure measurements are relatively rare (Figure 2.9b) but where available they indicate hydrostatic pore pressures with an indication for higher pore pressures north of 65.5ºN. At 2500 m (Figure 2.9c) the zone with slight overpressure north of 65.5ºN still exists and a second zone of overpressure develops south of 64.5ºN around 7ºE. It is hard to tell whether this overpressured area connects to the moderately overpressured reservoirs at 63ºN and 6ºE. According to Figure 2.9d the spatial distribution of pore pressures at a depth of 3000 m is comparable to the one at 2500 m but with a tendency to higher pore pressures. Additionally, at a latitude of 65ºN a zone of moderate overpressure forms. As hydrocarbon reservoirs offshore Mid-Norway are at greater depths, pore pressure measurements are available even for a depth of 4000 m. Figure 2.10a displays the high overpressures in certain areas at a depth of 3500 m. Nevertheless, even at this depth the pore pressure is still mainly hydrostatic around 65ºN. At 4000 m depth (Figure 2.10b) most of the areas west of 7ºE are severely overpressured and north of 65.5ºN the zone of overpressure reaches further east until 7.5ºE. No hydrostatic pore pressures can be found at this depth.

In summary, the pore pressure analysis shows mostly hydrostatic pore pressures down to 2000 m. Deeper down several zones of overpressure evolve leading to a distinct pattern of severe overpressures roughly west of 7ºE with a sharp transition to lowered overpressures towards the coast.

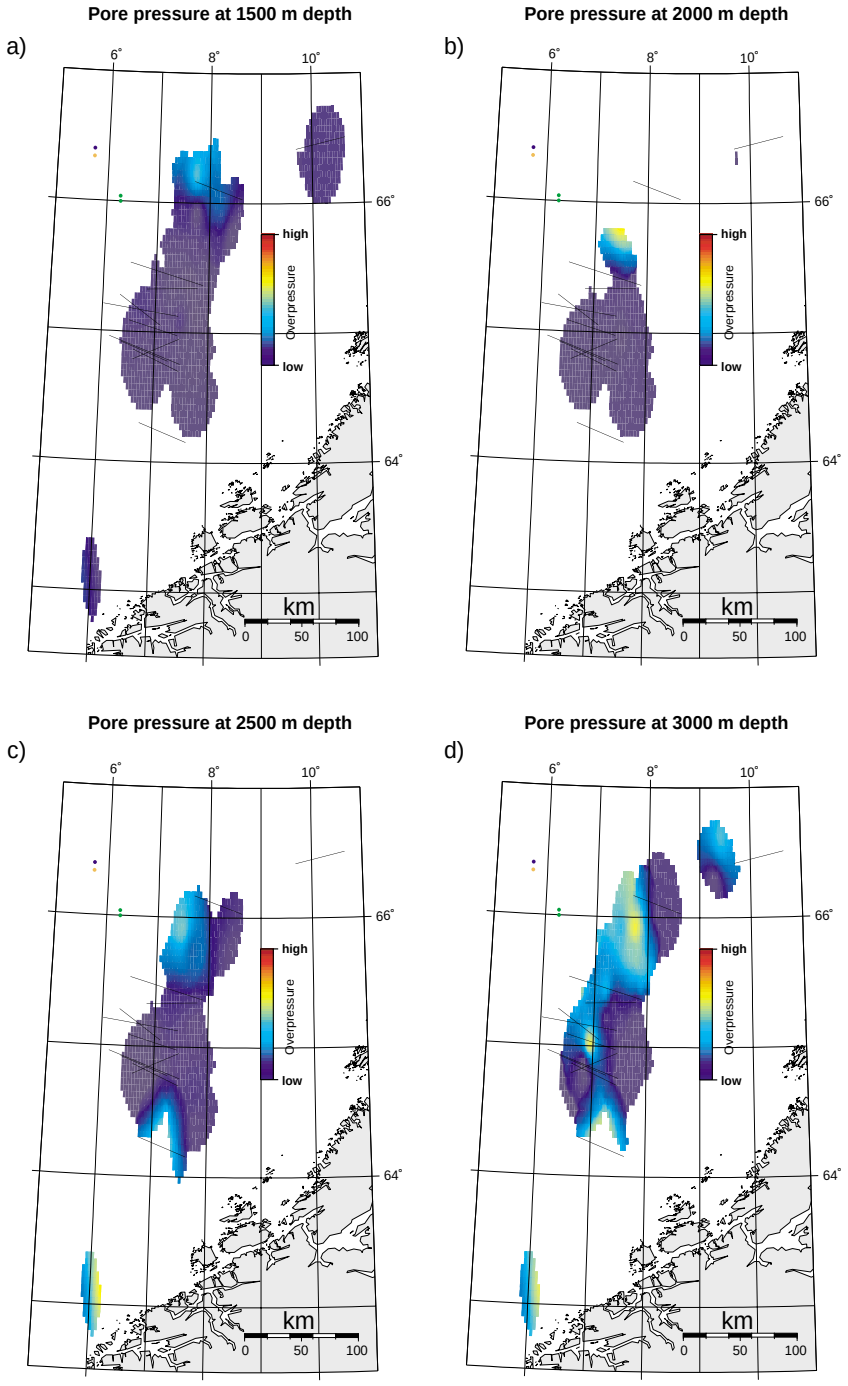

Figure 2.9: Lateral variation of overpressure for depths between 1500 m and 3000 m on the Mid-Norwegian margin. The overpressure is mostly derived from RFT-logs and in some cases from drill stem tests. The figure shows that the pore pressure is mostly hydrostatic with some zones of moderate overpressure. The black lines indicate S_{Hmax} orientations from Figure 2.4.

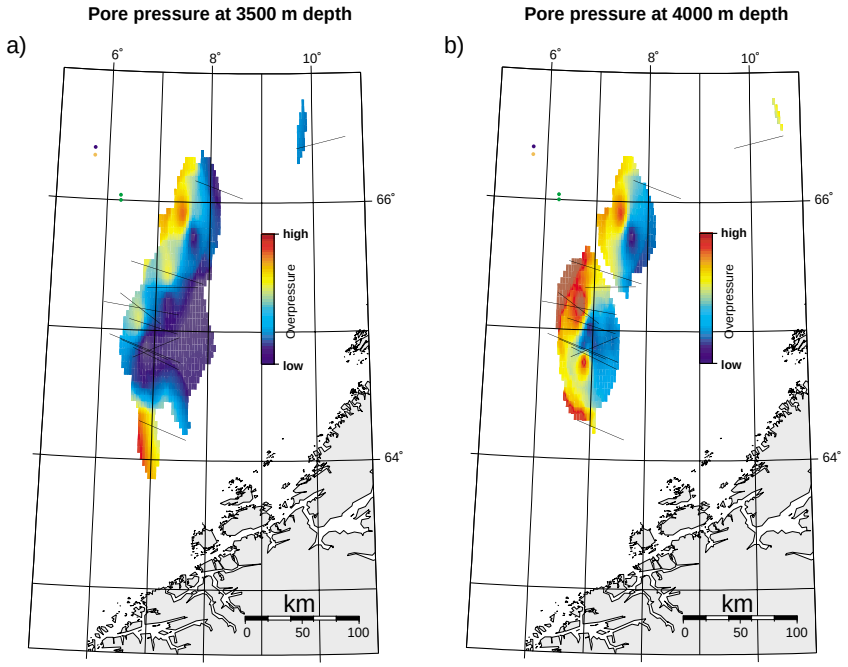

Figure 2.10: Lateral variation of overpressure for depths between 3500 m and 4000 m on the Mid-Norwegian margin. The overpressure is mostly derived from RFT-logs and in some cases from drill stem tests. The figure shows that severe overpressure can be found west of 7ºE south of 65.5ºN and west of 7.5ºE north of 65.5ºN. The black lines indicate S_{Hmax} orientations from Figure 2.4.

2.6 Discussion

By comparing the orientations of S_{Hmax} with S_3/S_v between 60ºN and 62ºN (Figures 2.3 and 2.6), it is striking that S_{Hmax} generally rotates where S_3/S_v is low. Roughly speaking, the area east of the Viking Graben (e.g. Oseberg, Troll, 35/9) shows anomalous S_{Hmax} orientations (≈80˚ instead of the regionally typical >100˚) and S_3/S_v drops to less than 0.8 in the same region. This close spatial relationship between the S_{Hmax} rotation and the S_3/S_v decrease suggests that both are caused by the same mechanism.

2.6.1 Possible sources of spatial stress variations

Stein et al. (1989) have discussed a number of possible sources of stress perturbations for the Baffin Bay region in northeastern Canada, which is comparable to the Norwegian coast since both are formerly glaciated, passive continental margins.

Ridge push

Numerous authors have pointed out the importance of ridge push as a large scale stress source along the Norwegian margin (Müller et al. 1992; Lindholm et al. 1995). Since the crust cools down and becomes denser as it moves away from the Mid Atlantic Ridge, gravitational sliding occurs and causes increased horizontal stresses in the direction of plate motion. The consistent orientation of the maximum horizontal stress (S_{Hmax}) in western Europe (striking NW-SE to NNW-SSE) suggests a uniform stress field caused by ridge push and the collision of the Eurasian plate with the African plate (e.g. Grünthal and Stromeyer).

Figure 2.11 shows that a large portion of available orientations of the maximum horizontal stress in northern Europe are also consistent with the ridge push direction. For example, stress orientations in England, the southernmost North Sea, and in Denmark consistently strike to the north-northwest, which agrees with the regional ridge push direction. The northwest trending S_{Hmax} orientations in southern Sweden also match the expected ridge push direction.

Thus, ridge push is likely to be the source of the general S_{Hmax} orientation in northern Europe. However, the stress field in western Fennoscandia can not be explained by ridge push alone. The increased occurrence of earthquakes, along with large variations in S_{Hmax} orientations, and the observation of all possible faulting styles (normal, strike-slip and even thrust faulting) within small areas (e.g. off the coast of southwestern Norway, northern Sweden), indicate that the local stress field is affected by an additional mechanism. Expected stresses as a result of ridge push do not include such lateral stress variations on the order of 100 km (e.g. Lister, 1975; Forsyth and Uyeda, 1975).

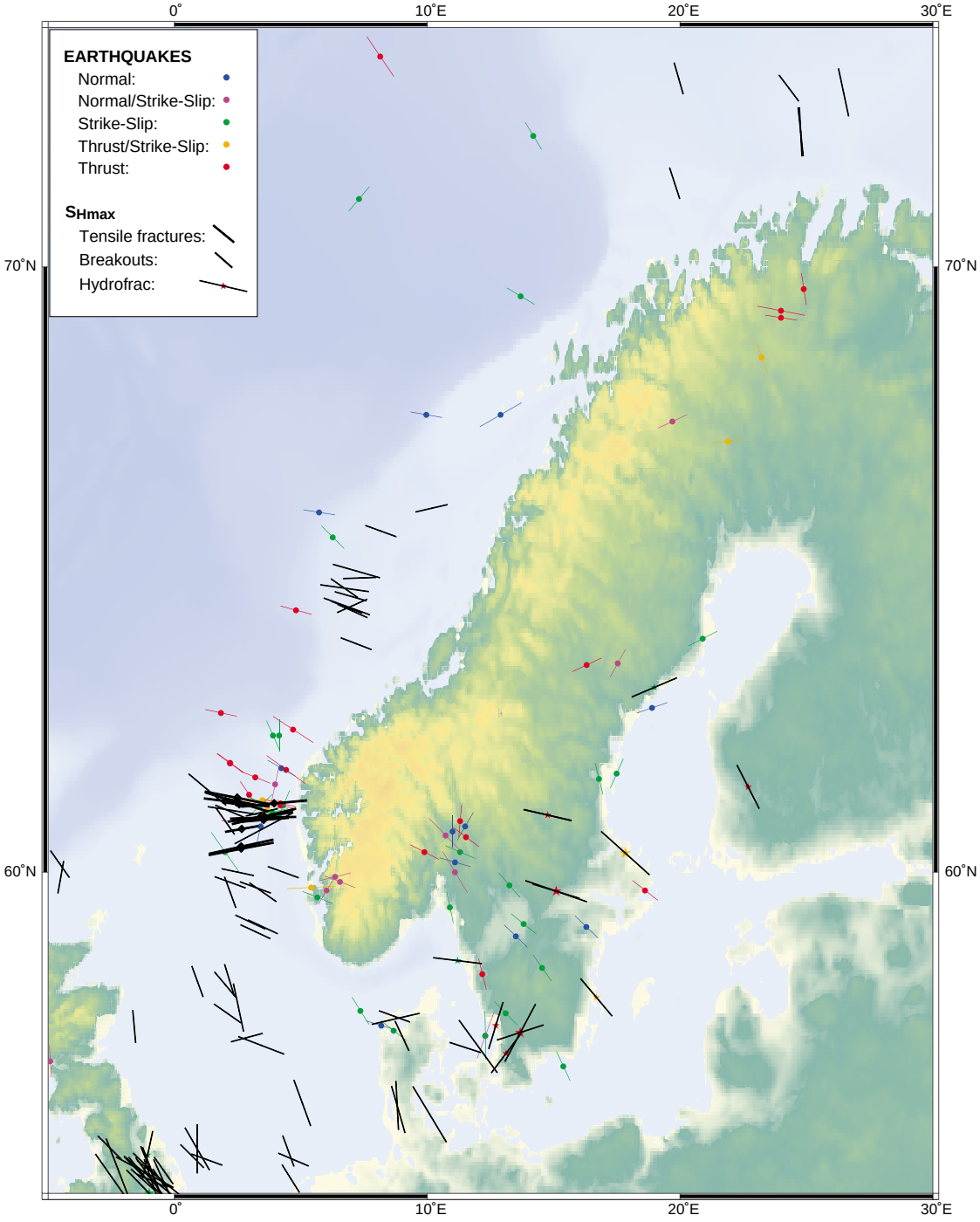

Figure 2.11: Map of available S_{Hmax} orientations in northern Europe resulting from the compilation in Chapter 2, by using data from the World Stress Map (WSM) database. The map includes stress orientations inferred from focal plane mechanisms (colored lines), borehole breakouts (gray lines), drilling-induced tensile fractures (black lines) and hydraulic fractures (dark gray lines with colored star).

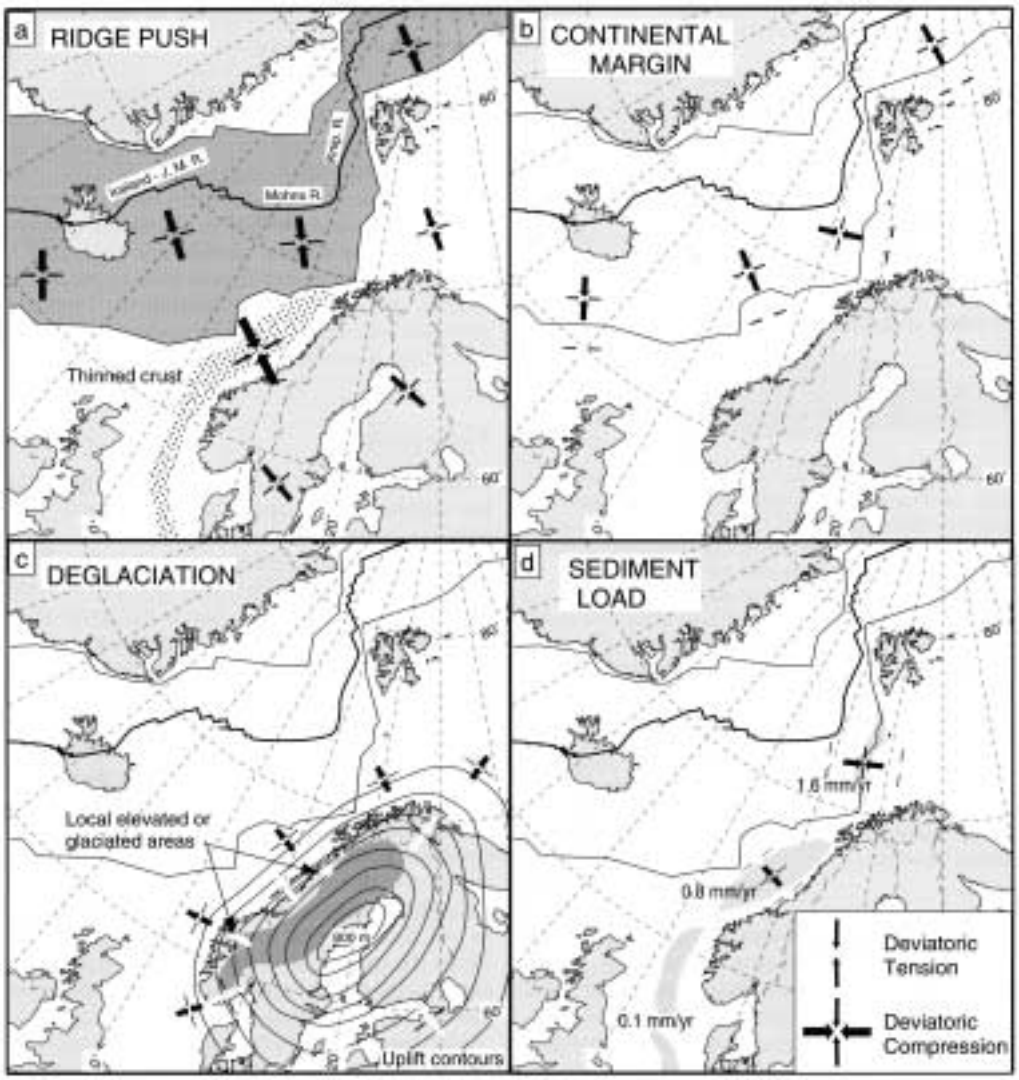

Figure 2.12: Possible stress generating mechanisms and their potential effect on Norway and adjacent areas (from Fejerskov and Lindholm, 2000).

Spreading stresses

A possible explanation for local stress perturbations, unexplained by ridge push, are spreading stresses near the continental slope. Artyushkov (1973) showed that the transition between the thin/dense oceanic crust and the thick/light continental crust causes a horizontal stress anisotropy. The continental crust tends to spread out towards the oceanic crust which decreases horizontal stresses within the continental crust while increasing them in the oceanic crust. Stein et al. (1989) used a numerical model to show that spreading stresses can change horizontal stresses by up to 50 MPa near the surface. Their model also shows that spreading stresses only affect an area within ≈100 km from the continental slope.Figure 2.12b illustrates the areas which might be affected by spreading stresses. The

comparison with Figure 2.11 reveals that anomalous S_{Hmax} orientations (different than ridge push direction) are mostly located at distances of more than 100 km from the continental margin. Thus, spreading stresses can not explain the perturbed stress field associated with anomalous S_{Hmax} orientations, and increased seismicity. Except, some earthquakes in the immediate vicinity of the continental slope might in fact be due to the spreading effect.

Sediment loading

A further source of stress perturbation might be the rapid sedimentation that took place during the Tertiary and especially during the Plio-Pleistocene along the Norwegian margin. Sediment thicknesses of up to 1 km accumulated during Tertiary times, causing a significant load on the lithosphere (Doré 1992). If a passive margin is subjected to a large amount of sediment deposition, the weight of the accumulated sediments can lead to local lithospheric bending. As a result, horizontal stresses increase below the sediments, in the uppermost parts of the lithosphere. Conversely, sediment loading lowers the horizontal stresses near the boundaries of the sedimentary basin. Many passive margins, such as the western Labrador Sea, the Gulf of Mexico, and the southern Barents Sea, are subjected to high sedimentation rates, so local stress variations should be observed in these areas. But, Stein et al. (1989) showed that the stress changes associated with sediment loading are drastically reduced, if viscoelastic behavior within the lithosphere is considered. Their finding is supported by the observation that heavily sedimented margins do not correlate with high seismicity. Consequently, sediment loading is probably only a secondary source of stress perturbations, restricted to areas with extremely high sedimentation rates combined with a thin lithosphere, which serves to amplify the effect.

Figure 2.12d shows that the North Sea is only subjected to a small amount of current sedimentation (≈0.1 mm/year). So, based on the argumentation presented above sediment loading hardly affects the stress state in the North Sea. Off the coast of Mid-Norway the sedimentation rates are considerably higher (≈0.8 mm/year) and so sedimentation might have a larger impact there. However, according to Figure 2.11 there is no indication for a perturbed stress field in the area of high sedimentation offshore Mid-Norway (i.e. no local rotation of S_{Hmax}, and no seismicity). With sedimentation rates of ≈1.6 mm/year, sediment loading might significantly influence the stress field in the southern Barents Sea, but no stress data is available to prove this.

2.6.2 The influence of deglaciation on stress

The most likely source of stress variations along the Norwegian coast is lithospheric flexure associated with the melting of the late Weichselian ice sheet. In fact, areas with increased seismicity, and/or anomalous S_{Hmax} orientations tend to coincide with the location of the former ice sheet front. Also, post-glacial faulting activity in northern Norway, and northern Sweden (e.g. Muir Wood, 1989; Lagerbäck, 1990) shows that the stress field was significantly perturbed, immediately following the completion of ice melting.

Assuming that the stress field was laterally uniform before the onset of ice melting, the isostatic response due to deglaciation and the resulting lithospheric flexure leads to a horizontal stress decrease in areas which were formerly covered by ice and to a horizontal stress increase at shallow depth away from the former ice sheet. If the lateral ice sheet extent at 15 000 years before present after Mangerud et al. (1979) is representative for most of the ice sheet's history, the Tampen Spur is expected to have increased horizontal stress magnitudes. Conversely, the region east of the Viking Graben would be subjected to a stress decrease. Figure 2.13 shows expected stress perturbations as a result of deglaciation for an elastic lithosphere (Turcotte & Schubert 1982). This analytical model assumes that the shape of the ice sheet can be described by a step function and that the ice sheet was 1 km thick.

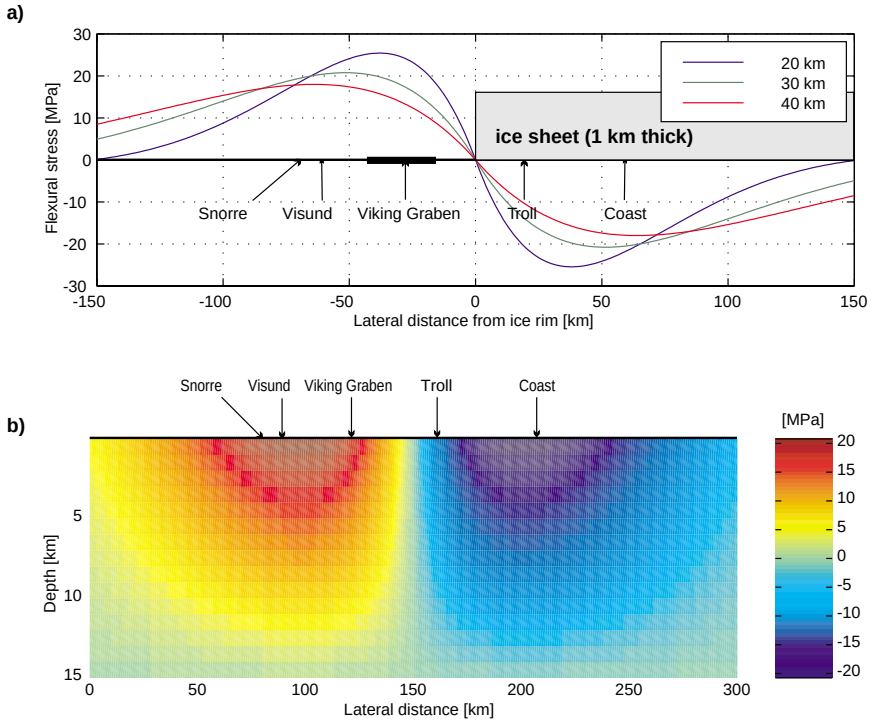

Figure 2.13: (previous page) Predicted stress perturbation for deglaciation on an elastic lithosphere with an initially isotropic stress state. Figure 2.13a shows predicted stress perturbations at the surface for different effective elastic thicknesses of the lithosphere. For lithospheric thicknesses between 30 and 40 km the maximum stress increase is ≈20 MPa and occurs in the fields of the Tampen Spur (e.g. Snorre, Visund). Similarly the maximum stress decrease is ≈-20 MPa and is located in proximity of the coast. Figure 2.13b shows predicted stress changes for an elastic lithospheric thickness of 30 km as a function of depth. Stress perturbations decrease monotonically to a depth that corresponds to half the plate thickness (15 km). Below this depth the stress perturbation would be similar but with opposite signs.

Figure 2.13a shows predicted stress perturbations in east-west direction at the surface for different effective elastic lithospheric thicknesses. The model shows that for effective elastic thicknesses between 30 and 40 km the half-wavelength of the stress variation is around 100 km, which matches the observed stress variation between 60ºN and 62ºN. For the fields in the Tampen Spur (e.g. Snorre, Visund) the model predicts an east-west stress increase on the order of 20 MPa near the surface. Since this stress increase is perpendicular to the ice sheet margin it leads to a more pronounced orientation of S_{Hmax}. Closer to the coast the east-west stress is predicted to decrease by about 20 MPa, possibly leading to the observed rotation of S_{Hmax}. Figure 2.13b shows that the predicted stress perturbation decreases with depth and disappears at a depth corresponding to half the effective lithospheric thickness. However, these predicted stress perturbations are upper bounds, since we assume that no spatial stress perturbations exist before the onset of ice melting. Further, gravity and uplift data show that the rebound is incomplete (Ekman & Makinen 1996), so the lithosphere is not subjected to the full amount of bending yet. Nevertheless, the lateral extent, and roughly the magnitudes agree with the observed stress variations. Finally, it is striking that the area between 60ºN and 62ºN as the region of the largest horizontal stress variations shows a remarkably increased seismic activity (Figure 2.3), which strongly suggests that whatever mechanism causes the previously described stress variations is also responsible for triggering the earthquakes in this province.

2.6.3 The influence of deglaciation on pore pressure

By comparing Figures 2.6 and 2.7 with Figures 2.8 and 2.9 high pore pressures roughly coincide with high values of S_3/S_v. For example, the Tampen Spur as an area with high S_3/S_v ratios exhibits severe overpressure, whereas decreased stresses closer to the coast (e.g. Block 35/9) are associated with low, close to hydrostatic pore pressures. This close relationship between stress and pore pressure suggests that they are connected via a close cause-effect relation. Engelder & Fischer (1994) have shown that S_3 drops in response to pore pressure draw down in numerous hydrocarbon provinces. As a result of such a

poroelastic response S_3 within the hydrocarbon reservoir decreases by ≈70% of the associated pore pressure drop. Since S_3 seems to follow the pore pressure, the high observed S_3 in the Tampen Spur could be induced by high pore pressures. However, if that was the case stress magnitudes south of 61ºN should be lower than observed because the pore pressure is mostly hydrostatic. But, if pore pressure-changes influence S_3, S_3-changes might in turn have an effect on the pore pressure. So, maybe at least part of the high observed pore pressures in the Tampen Spur result from a poroelastic response to the increase of horizontal stresses. In other areas (e.g. south of the Tampen Spur or around 65ºN) where horizontal stresses are equally high as in the Tampen Spur, the induced pore pressure increase might have simply leaked away. Consequently, the high pore pressures in the Tampen Spur might be partially the result of a poroelastic response to increased stress magnitudes due to deglaciation. Closer to the coast where deglaciation is expected to decrease horizontal stress, poroelasticity would lead to subhydrostatic pore pressures, which does not match the observation of more or less hydrostatic P_p. However, a stress decrease also tends to cause faulting, which in turn increases permeability (Barton et al. 1995). As a result of increased permeability the pore fluids communicate with the sea floor and no subhydrostatic pore pressure can develop.

Several other processes such as under-compaction and hydrocarbon maturation have certainly influenced pore pressures in the North Sea (Caillet et al. 1991) and offshore Mid-Norway. For instance, zones of moderate overpressure occur south of 58ºN in the Norwegian sector and close to the Norwegian coast at 61.2ºN, where deglaciation does not lead to a horizontal stress increase, and therefore can not be explained by a poroelastic response to deglaciation.

2.7 Conclusions

We conclude that in-situ stress and pore pressure offshore Norway are regionally consistent and follow well defined spatial trends. The most marked change of stress occurs between 60ºN and 62ºN. In this area the horizontal stresses are relatively low close to the coast and increase further offshore at distances greater than ≈100 km from the coast. This change of stress magnitude is accompanied by a rotation of S_{Hmax} of ≈20º. A simple model of elastic plate flexure suggests that the observed stress variations are the result of deglaciation. The pore pressure is close to hydrostatic in most of the Norwegian North Sea except for the area west of the Viking Graben, north of 61ºN where large overpressures exist at depths greater than 1500 m. Likewise, on the Mid-Norwegian margin the pore pressure tends to increase towards the west, i.e. away from the coast. These high pore pressures

offshore Norway might be partly caused by deglaciation.

Acknowledgments

We would like to thank Norsk Hydro for generously providing the data and financial support for this study.

Chapter 3

POST GLACIAL LITHOSPHERIC FLEXURE AND INDUCED STRESSES AND PORE PRESSURE CHANGES IN THE NORTHERN NORTH SEA

This chapter will be published with Mark D. Zoback as co-author (Accepted for publication in Tectonophysics as of July 17., 2000).

3.1 Abstract

We have compiled data on the least principal stress, overburden, pore pressure and stress orientation for 92 wells in the northern North Sea. These data show that the least principal stress is close to the overburden in the Tampen Spur indicating high horizontal stress in this area. Closer to the coast, i.e. east of the Viking Graben the least principal stress drops significantly. Along with this spatial change in stress magnitudes, the orientation of the maximum horizontal stress rotates from ≈100˚ in the Tampen Spur to ≈80˚ around block 35/9. Analytical and numerical models of plate flexure suggest that these observed lateral stress variations are the result of deglaciation, superimposed on a regional stress field dominated by ridge push.

The pore pressure in the northern North Sea roughly follows the stress trend, i.e. high overpressures where horizontal stresses are high (Tampen Spur) and close to hydrostatic pore pressures east of the Viking Graben where stresses are decreased. This close relationship of pore pressure and horizontal stress suggests that they have the same source. We have modeled the pore pressure change expected from the poroelastic response to deglaciation. The results show that strong overpressures in the Tampen Spur appear to be only partly caused by deglaciation and flexure. Other sources of overpressure, such as compaction disequilibrium also play an important role.

3.2 Introduction

Many previous studies have investigated the effect of glaciation on the lithosphere (e.g. Walcott, 1970; Peltier, 1976; James and Bent, 1994; Wu, 1997). Most of these studies for Fennoscandia were based on uplift data (e.g. Fjeldskaar, 1997), on the occurrence of earthquakes (e.g. Wolf, 1987; Klemann and Wolf, 1998; Johnston et al., 1998, Wu et al., 1999), or on the analysis of gravity anomalies (Ekman and Makinen, 1996) which allowed them to come up with estimates for certain parameters such as the asthenospheric viscosity and lithospheric thickness. Direct investigation of the influence of glaciation-deglaciation on the mechanics of the crust-mantle system requires knowledge of the in-situ stress field within the crust. Rough estimates for the stress state in the crust of Fennoscandia come from the analysis of earthquake focal plane mechanisms (Bungum, 1989; Gregersen et al., 1991; Lindholm et al., 1995). However, to accurately investigate possible stress changes caused by lithospheric flexure, it is necessary to have direct stress measurements to calibrate and test the models. Fortunately, the northern North Sea contains numerous hydrocarbon wells which can provide appreciable data for such an analysis. In this study, we used data from

92 wells located between 61˚N and 62˚N (Figure 3.1).

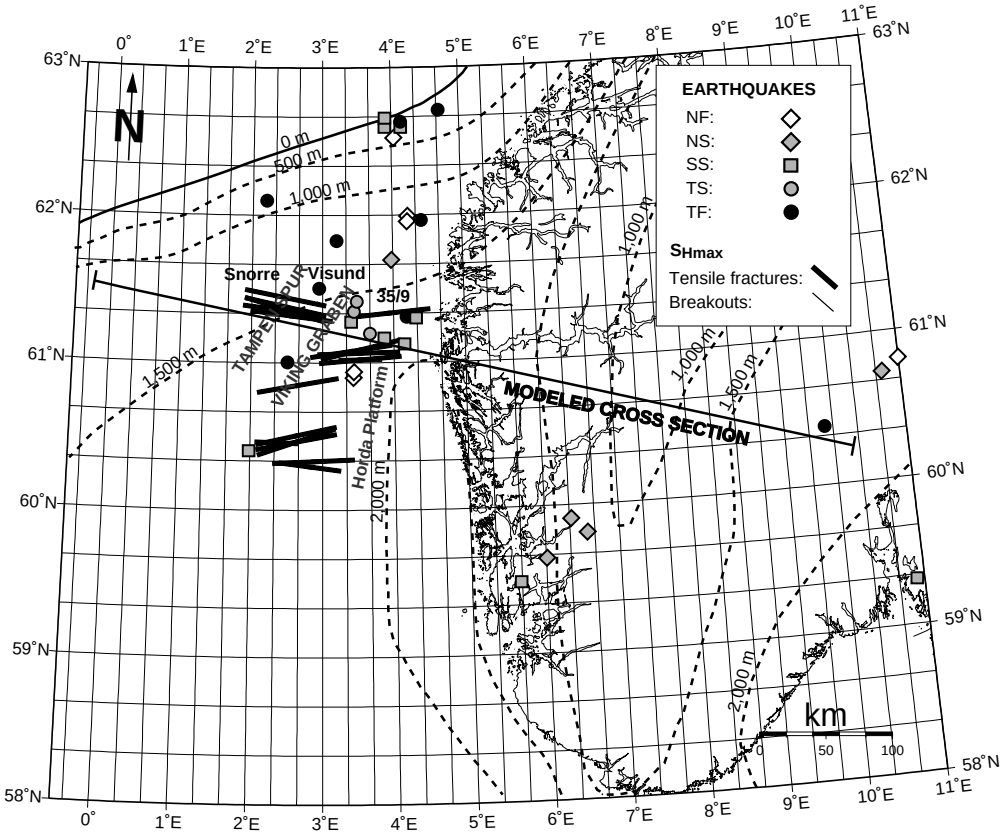

Figure 3.1: Overview map.of western Norway and the northern North Sea. The bold lines show S_{Hmax} orientations inferred from drilling induced tensile fractures (Wiprut and Zoback, 1998) and the narrow black lines illustrate S_{Hmax} orientations from borehole breakouts. S_{Hmax} rotates from ≈100˚ west of the Viking Graben to ≈80˚ closer to the coast. The circles, squares and diamonds show locations of earthquakes with their respective faulting regime. The dashed lines are isolines of ice sheet thickness for the maximum extent 20,000 years ago from Andersen (1981). The light grey areas illustrate the lateral extents of known hydrocarbon fields.

The northern North Sea is an ideal area to investigate flexural stresses due to deglaciation. We used borehole breakout data from the World Stress Map project (Müller et al., 1992; Zoback, 1992) and drilling induced tensile fractures (Wiprut and Zoback, 1998) to monitor the orientation of the maximum horizontal stress (S_{Hmax}). Figure 3.1 shows that the azimuth of S_{Hmax} changes from >100˚ west of the Viking Graben to ≈80˚ on the east side of the Viking Graben, indicating that the stress field in the northern North Sea is subjected to significant spatial variations possibly related to post glacial flexure. Other indications of flexural stress perturbations in the northern North Sea are the increased earthquake activity in this area (Figure 3.1), and the variations of stress magnitudes as described below.

3.3 Observed stress in the northern North Sea

In this study we focus on the relatively detailed data collected along the cross section shown in Figure 3.1, although stress data have been compiled throughout the Norwegian sector of the North Sea (Grollimund et al., in press). We have compiled leak-off tests (LOT) to determine the magnitude of the least principal stress (S_3), and density logs to calculate the vertical stress (S_v). A LOT is performed by pressurizing a short, uncased section of a well until a hydraulic fracture opens and begins to take fluid. By plotting the pressure as a function of mud volume pumped into the hole, a deviation from a linear trend indicates the onset of fracture opening and gives a rough estimate for S_3. To be independent of depth, we used the normalized least principal stress (S_3/S_v) to characterize the stress field and its spatial variations. If S_3/S_v approaches 1, then S_3 is close to S_v which by definition characterizes a reverse faulting environment, according to Anderson faulting theory (Anderson, 1951). Of course, another possibility for $S_3/S_v \approx 1$ is an almost isotropic stress state. However, at least for depths > 5 km numerous earthquakes in the northern North Sea suggest a stress state close to failure of the crust, thus precluding an isotropic stress state. Furthermore, the stress analysis of Wiprut and Zoback (1998) shows that a high horizontal stress anisotropy exists in the Visund field. Accordingly, $S_3/S_v \approx 1$ most probably indicates high horizontal stresses, i.e. strike-slip to reverse faulting in the northern North Sea, whereas decreased S_3/S_v imply lower horizontal stresses, i.e. strike-slip to normal faulting. Thus, we believe S_3/S_v is a good general indicator of the magnitude of horizontal stress.

For this analysis, we used data from wells from the hydrocarbon fields in the Tampen Spur (e.g. Snorre, Gulfaks, Visund), and other fields east of the Viking Graben (e.g. Fram, block 35/9). Some wells didn't have a sufficient number of leak-off tests to allow S_3 to be estimated with depth. For such cases, we merged data from nearby wells, assuming that the stress field is relatively uniform between the wells. Data points which do not lie exactly on the cross section were projected perpendicular onto it.

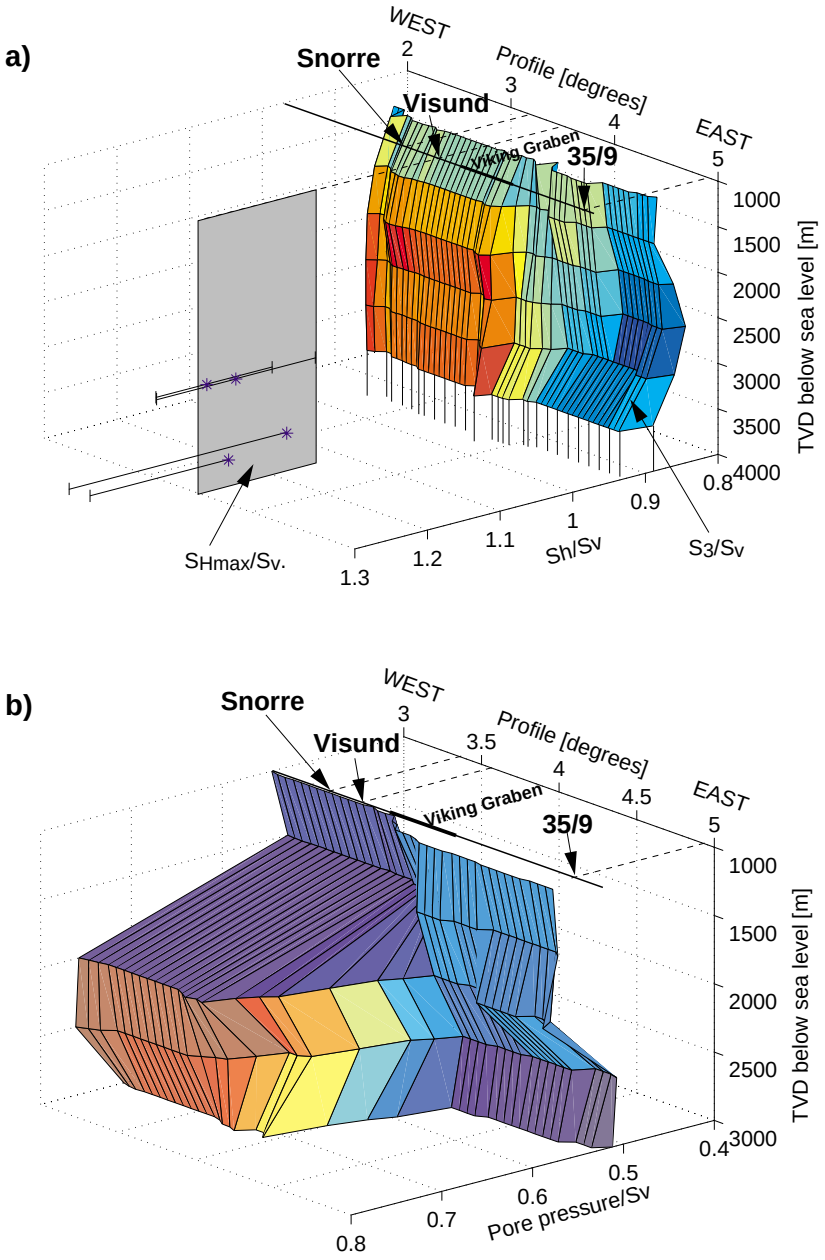

Figure 3.2: Observed stress and pore pressure in the northern North Sea. In Figure 3.2a the colored surface shows spatial variations of S_3 as inferred from leak-off test, normalized by S_v from integrated density logs. S_3/S_v is close to 1 in the fields of the Tampen Spur (Snorre, Visund) but decreases towards the coast. The maximum decrease occurs at a depth of 2500 m. The blue asterisks show S_{Hmax}/S_v and are obtained from the analysis of the full stress tensor from wellbore failure in Visund (Wiprut and Zoback, 1998) and suggest a strike-slip to almost reverse faulting stress state in the Visund field. In Figure 3.2b the colored surface shows spatial variations of P_p mostly from RFT-logs and from drill stem tests, normalized by S_v from integrated density logs.The plot shows that in Snorre and Visund formations are severely overpressured at depths greater than 1500 m. Closer to the coast, P_p is close to hydrostatic down to 3000 m.

Using basic error propagation, the uncertainty associated with S_3/S_v $\Delta(S_3/S_v)$ is equal to the sum of the relative errors of S_3 and S_v. The relative errors are defined as $\Delta S_3/S_3$ for the least principal stress, and $\Delta S_v/S_v$ for the vertical stress. While the determination of S_v is very precise (ΔS_v=0.5 MPa), the S_3 estimates have a maximum error of ±2 MPa (Grollimund et al., in press). As S_v and S_3 increase with depth the relative error decreases with depth and consequently $\Delta S_3/S_v$ is on the order of ±0.1 at a depth of 1000 m and ±0.05 at a depth of 3000 m.

Figure 3.2a shows the results of the S_3/S_v-analysis along part of the cross section illustrated in Figure 3.1 as a function of depth below sea level. In the Tampen Spur S_3/S_v is close to 1 at depths greater than 1000 m MSL. Towards the coast S_3/S_v drops to ≈0.8 at a depth of ≈2500 m MSL. At depths shallower than 1000 m MSL no change of S_3/S_v is observable along the entire cross section. The transition from high S_3/S_v ratios in the Tampen Spur towards decreased values closer to the coast occurs in the vicinity of the Viking Graben, over a horizontal distance of ≈100 km. The lateral distance of the stress change will be important later on, to estimate the lithospheric thickness. With respect to the error, even if S_3/S_v has an uncertainty of ≈0.05 at a depth of 2,500 the observed spatial variation is 0.2 or even higher slightly to the north (Figure 3.3a). As a result, the observed spatial stress variation is above the noise level associated with the stress measurements.

In summary, the northern North Sea consists of two main stress provinces, (1) the Tampen Spur with high S_3/S_v ratios indicating high horizontal stresses, i.e. a strike-slip to reverse faulting stress state, and (2) the area between the Viking Graben and the coast with decreased S_3/S_v ratios (≈0.8) suggesting decreased horizontal stresses, i.e. strike-slip to normal faulting. Additionally, Wiprut and Zoback (1998) have estimated the magnitude of S_{Hmax} from the analysis of wellbore failure in the Visund field. For depths between 2000 m and 3000 m MSL they predict S_{Hmax} magnitudes that are considerably higher than S_v (S_{Hmax}/S_v≈1.25) (Figure 3.2a), supporting a strike-slip to almost reverse faulting stress regime.

To interpret the stress field it is crucial to know the pore pressure (P_p) as stress and pore pressure are closely related. Also, the faulting behavior of rock depends on the stress state and the pore pressure (e.g. Jaeger and Cook, 1979). P_p data comes from the same boreholes as the S_3 and the S_v measurements. The majority of pore pressures are derived from repeat formation tests (RFT), which are routinely performed at reservoir depth. An RFT is carried out by measuring the fluid pressure necessary to prevent flow into or out of the formation. Additionally, drill stem tests provide a limited number of P_p measurements. Similar to the S_3 analysis, we display pore pressure normalized by S_v (P_p/S_v). For typical S_v with depth profiles in the northern North Sea, P_p/S_v ratios of ≈0.5 indicate approximately hydrostatic

pore pressures. P_p/S_v-values higher than 0.5 indicate overpressured formations.

The errors associated with the pore pressure measurements are very small (≈0.2 MPa). As a consequence, $\Delta(P_p/S_v)$ is on the order of ±0.04 at shallow depth and decreases to values of less than 0.02 at depths of 2500 m or below which compared to the observed variations of P_p/S_v is negligible.

Figure 3.2b shows P_p/S_v as a function of depth along the same cross section as Figure 3.2a. To a depth of 2500 m MSL, P_p/S_v hardly exceeds 0.5, which implies that the pore pressure is hydrostatic to this depth. The slight increase in P_p/S_v towards the coast at shallow depth is not the result of higher P_p but rather of a decreased overburden due to increased water depth. However, between 2000 m and 3000 m MSL a distinct zone of overpressure develops west of the Viking Graben with P_p/S_v of up to 0.8. At the same depth P_p is still close to hydrostatic between the Viking Graben and the coast, with the exception of a slightly overpressured zone at a depth of 2000 m MSL.

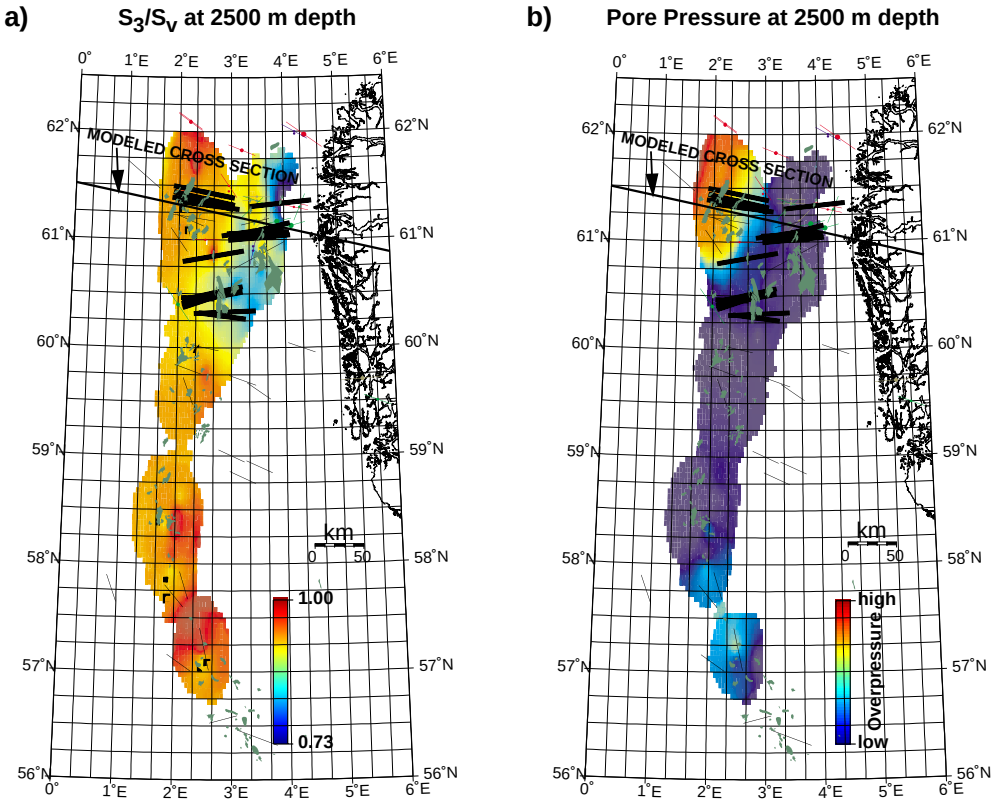

Figure 3.3: Map view of stress and pore pressure in the North Sea. Figure 3.3a shows the least principal stress normalized by the overburden (S_3/S_v) for a depth of 2500 m. The figure shows that S_3/S_v is consistently low close to the coast and increases towards the west (perpendicular to the coast line). Figure 3.3b shows the pore pressure normalized by the overburden (P_p/S_v) at a depth of 2500 m. The pore pressure is mostly hydrostatic but highly overpressured west of the Viking Graben (Tampen Spur). Slight overpressure also occurs in the southern North Sea.

The lateral stress variations described above are not limited to the northern North Sea but are rather a large scale phenomenon that can be observed throughout the North Sea. I.e. S_3/S_v is generally approaching unity at distances greater than 100 km from the coast (e.g. in the Tampen Spur) but is decreased in the vicinity of the coast (Figure 3.3a). Conversely, with the exception of the Tampen Spur P_p is mostly hydrostatic (Figure 3.3b).

3.4 Flexural stresses

As a next step, we attempt to explain the observed stress variations in the northern North Sea. We will use the following sign convention: positive stress for compression and negative stress for tension.

Several authors have pointed out the influence of ridge push on the regional stress field along the entire Norwegian margin (e.g. Gregersen et al., 1991; Müller et al., 1992). Since the crust cools down and becomes denser as it moves away from the Mid Atlantic Ridge, gravitational sliding occurs and causes high stresses in the direction of increasing plate age and thickness (e.g. Forsyth and Uyeda, 1975; Parsons and Richter, 1980; Bott and Kusznir, 1984). Ridge push uniformly increases stress over large areas. However, Figures 3.1-3.3 show that the observed stress changes in the northern North Sea occur over a horizontal distance of ≈100 km which suggests that an additional stress source affects the local stress field.

Goelke (1996) modeled stress perturbations as a result of the interaction between ridge push and a laterally heterogeneous crustal structure. However, another typical cause of such stress variations within short distances is bending of the lithosphere due to the isostatic response to loads imposed on the surface of the lithosphere. Thus, in this paper we investigate lithospheric flexure as an alternative mechanism to explain the local stress perturbations observed in the northern North Sea. The Baltic ice sheet that also covered parts of the northern North Sea until ≈15,000 years ago (e.g. Mangerud, 1979; Andersen, 1981; Lundqvist, 1986) represented a significant load on the lithosphere. Assuming an ice sheet thickness of 1000 m or more, an imposed vertical load of ≈10 MPa would result. Another possibility for such a load is the accumulation of sediments which were deposited in the northern North Sea, especially during the Tertiary (Dore, 1992). However, according to Stein et al. (1989) sedimentation occurs over a very long period (millions of years) and the associated flexure stresses most likely disappeared as a result of creep processes within the crust. Conversely, the melting of the ice sheet as a relatively recent phenomenon and consequently the crust had no time to relax the induced bending stresses. Therefore, for the remainder of this paper we will only consider the perturbation of stresses in the northern

North Sea that are the result of glacial loading and unloading.

By assuming that glacial loading and unloading is the major source of lateral stress perturbations in the northern North Sea we do not rule out the importance of ridge push on the local stress field. In fact, the observed stresses in Section 3.3 may be the result of the superposition of glacial loading/unloading, and far-field stresses (ridge push). As mentioned earlier, ridge push uniformly changes the magnitude of stress so the observed spatial stress variations must be caused by another stress source (e.g. deglaciation). Consequently, we can not use a model that only includes glacial loading and unloading to fully reproduce the stress observations from Section 3.3 but the model should be able to mimic the spatial change in stress. Therefore, we can neither use the model to reliably predict stress at a specific location nor can we claim that the match of the model with a specific stress observation validates the model. Instead, the model is useful to explain lateral changes of stress and such changes can in turn be used to test the model.

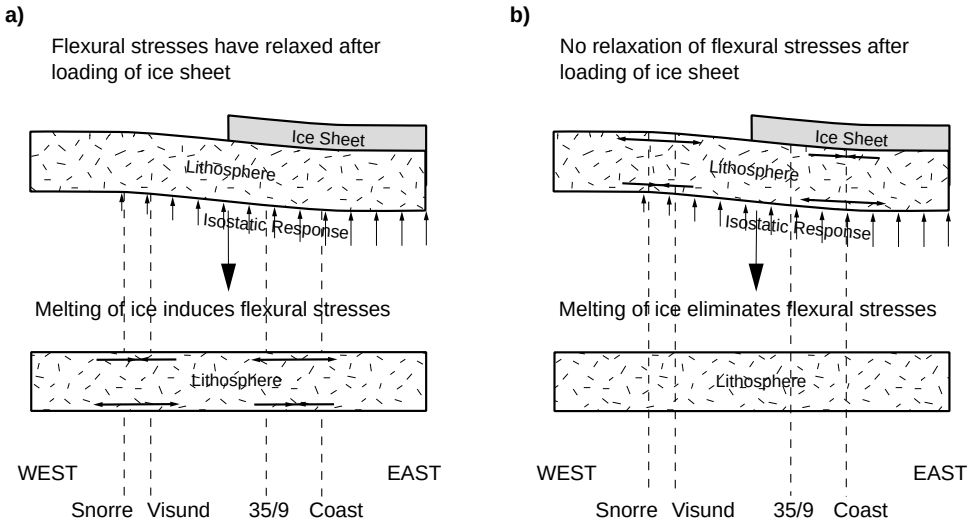

Figure 3.4: Illustration about how flexural stresses affect the stress field. Figure 3.4a assumes that bending stresses relax during the existence of the ice sheet. Subsequent melting leads to extension under the former ice sheet and compression further offshore with increasing amplitude as the rebound goes on. In the case of Figure 3.4b it is assumed that relaxation processes are insignificant during the duration of glaciation. After ice melting stresses are still compressive under the former ice sheet and extensive further offshore but decrease as the rebound goes on.

Figure 3.4 illustrates two simplified end-member models on how glacial loading cycles are expected to perturb the local stress field, assuming that the entire lithosphere behaves as a rheologically uniform plate (Stephansson, 1988, Stein et al., 1989). In the case of Figure 3.4a the ice sheet existed for a long enough time for the lithosphere to relax the induced bending stresses. For this assumption, subsequent melting of the ice sheet leads to

extension under the former ice sheet and compression away from it, at shallow depth. At the base of the lithosphere the stress perturbations are inverted, i.e. compression under the former ice sheet and extension away from it. For this case the magnitude of the stress perturbation increases as the lithospheric rebound progresses. Stein et al. (1989) use this assumption to explain the transition from reverse faulting earthquakes offshore Baffin Bay to normal faulting earthquakes along the coast. Stephansson (1988) proposes the opposite assumption. That is, none of the bending stresses relax during the existence of the ice sheet (Figure 3.4b). For this case, we would expect increased stresses under the former ice sheet and a stress decrease further offshore, at shallow depth. The stress perturbation decreases during the lithospheric rebound and completely vanishes after the rebound is complete.

In addition to the bending stresses discussed in the previous paragraph, the change from a bent lithosphere before ice melting to a flat lithosphere after complete rebound causes a net shortening in both models illustrated in Figure 3.4. This effect does not cause variations in horizontal stress magnitudes either spatially or with depth but instead leads to a uniform horizontal stress increase throughout the entire lithosphere.

Both end-member models are able to explain the observed decrease in horizontal stress at shallow depth (<5 km) towards the coast as illustrated in Figures. 3.2a and 3.3a). The model illustrated in Figure 3.4b requires that the ice sheet front was predominantly located in proximity of the coast to explain the decreased horizontal stresses east of the Viking Graben. On the western side of the Viking Graben this model appropriately suggests a horizontal stress increase as lithospheric bending tapers off. Conversely, for the model illustrated in Figure 3.4a the ice front must have been mainly located in the vicinity of the Viking Graben to fit the stress observations by actively increasing the horizontal stresses west of the Viking Graben and decreasing them towards the coast. More recently, Wu et al. (1999) used a three-dimensional model of deglaciation with a rheologically uniform lithosphere to predict an increase of thrust faulting seismicity roughly underneath the former ice sheet.

Realistically, the lithosphere is strongest in the upper crust as elevated temperatures at great depths enable stress relaxation as a result of creep processes. Consequently, the observed stresses most likely reflect a combination of both end-member models, i.e. the lower part of the lithosphere relaxes while the upper part stores the imposed bending stresses. We will revisit this issue in Section 3.4.3 by using a finite element model to combine a purely elastic upper crust with a viscoelastic lower crust and lithospheric mantle in order to study the interaction between different rheologies. First, we will investigate under what conditions a single layer lithosphere is capable of reproducing the observed stresses to set the stage for the multi-layer model in Section 3.4.3.

3.4.1 Analytical model for glacial loading

We have used a simple analytical model derived by Nadai (1963) for the bending of a viscoelastic slab under a distributed load to explore the effects of different lithospheric thicknesses (T) and relaxation times (τ) on the response of bending stresses within a single-layer lithosphere to ice loading, i.e. this glacial loading model sets the stage for the unloading model in Section 3.4.2. In this model, the lithosphere has a Maxwell-viscoelastic rheology and a constant thickness. The viscoelastic lithosphere is underlain by a fluid substratum which allows the lithosphere to be in isostatic equilibrium. The boundaries of the model are subjected to the condition that the first derivative of the deflection is zero. See Appendix A for a formal description of the model.

For this simple model we are assuming that the ice sheet grew instantaneously at the beginning of the Pleistocene, i.e. 2 million years ago, and that it always had the same extent as 15,000 years ago. In the numerical model, we will use a more refined ice model as compiled by Andersen and presented by Denton and Hughes (1981) based on the mapping of ice front features. For now we model the ice sheet as a 1 km thick block that covered the entire Horda Platform and ended east of the Viking Graben where ice front features are very abundant (Andersen, 1981), suggesting that the ice sheet remained at this stage during large portions of its existence. A transition in the magnitude of shale compaction across the Viking Graben (Hansen, 1996) further supports the assumption that the ice front was predominantly located near the Viking Graben. Obviously, during its existence the ice sheet was subjected to cycles of growth and retreat. In this section, we are not interested in the exact ice sheet history but rather in a rough estimate of its overall effect on the lithosphere which can be mimicked well enough by a constant reference ice sheet extent. However, in Section 3.4.3 we will also consider cyclic ice loading.

All of the models considered in this paper are subject to the assumption that the ice sheet geometry can be considered as two-dimensional but the Fennoscandian ice sheet is characterized by a complicated, three-dimensional geometry. This simplification certainly adds some uncertainty to the stress predictions. However, as the fit of the model results to the data (both spatial stress changes and uplift) in Section 3.4.3 will show, the two-dimensional approach seems to be satisfactory for roughly estimating the influence of deglaciation in the northern North Sea. A more detailed analysis of stress in the northern North Sea, will require three-dimensional models of glacial loading and unloading.

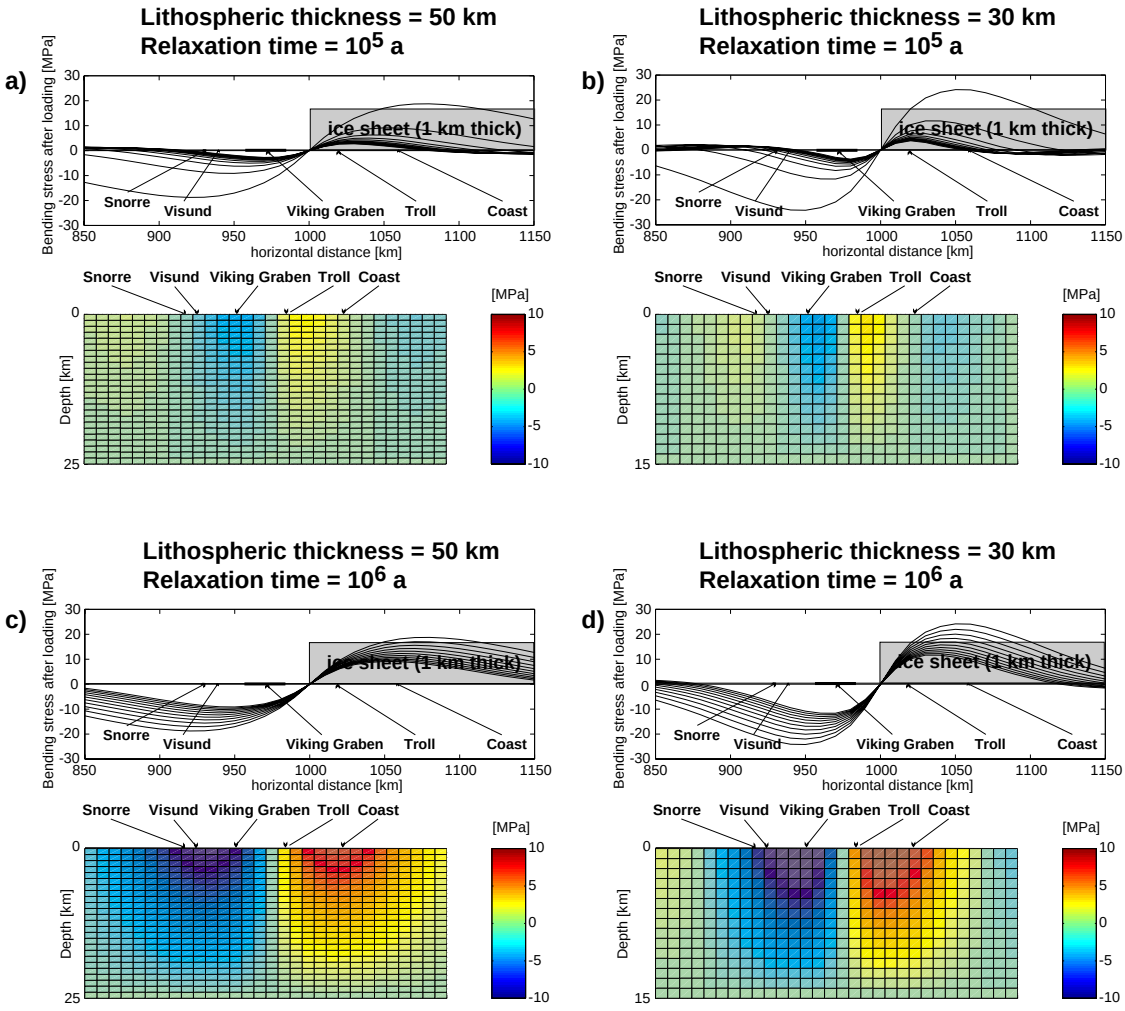

Figure 3.5: Viscoelastic model for flexural stresses as a result of ice loading. The lithosphere is modeled as a viscoelastic layer underlain by a fluid substratum. The model assumes loading of the lithosphere for 2 Ma by an ice sheet with 1 km thickness. The upper graph for each subplot shows expected bending stresses at the surface for different time slices with an increment size of 200,000 years (decreasing magnitude with time). The lower graph illustrates the bending stresses as a function of depth predicted for 2 Ma after the onset of ice loading. Compressive stresses are positive.

Figure 3.5 shows modeled stress perturbations for different lithospheric thicknesses and relaxation times. We assumed values of T=50 km and T=30 km as they result in stress perturbations with wavelengths comparable to the observations (Figures. 3.2 and 3.3). Table 1 lists the other model parameters. The upper graphs for each subplot show bending stresses at the surface with different lines representing different time slices. The line with the largest magnitude displays the instantaneous response after growing of the ice sheet. Subsequent lines represent the time evolution of the bending stresses with an increment size of 200,000 years. The lower part of each subplot shows modeled stress perturbations as a

function of depth, after 2 Ma of ice loading. Figure 3.5a and b show that for $\tau=10^5$ years most of the bending stresses that were induced by the growing of the ice have relaxed almost entirely after a relatively short period. Certainly, 2 Ma into the existence of the ice sheet remaining stress magnitudes are not higher than 3 MPa for T=50 km and 4 MPa for T=30 km respectively. As a result of the block-shaped ice sheet, the bending stresses are antisymmetric with respect to the ice front. Also, note that the wavelength of the stress perturbations depend on T as well as on time, i.e. the wavelength of the stress perturbation always decreases with time and that higher T cause larger wavelengths. Even for a higher $\tau=10^6$ years (Figure 3.5c, d), which is probably more realistic, a large portion of the induced stress perturbation relaxes. In the case of T=50 km (Figure 3.5c) the stress perturbation decreases by up to 20 MPa west of Snorre and the remaining stresses are not higher than 10 MPa. For T=30km and τ=1 Ma the remaining stress variations are up to 13 MPa but are more confined laterally than for T=50km.

According to this simplistic model, large parts of the stress perturbations induced by glacial loading have disappeared before the melting of the ice sheet even for a relatively high τ of 1 Ma. Thus, this glacial loading model favors the assumption made in Figure 3.4a that most of the bending stresses from the loading process have relaxed during the existence of the ice sheet.

3.4.2 Analytical model for glacial unloading

In this section we will now attempt to model the present-day stress perturbation due to deglaciation. Based on the arguments presented above, we assume that the bending stresses induced by glacial loading were significantly reduced before the ice sheet started to melt. Since the melting of the last ice sheet occurred relatively recently (≈15,000 years ago) we further assume that the lithospheric response to glacial unloading was fully elastic and the ice sheet has a rectangular shape (see Figure 3.6). The resulting horizontal stress perturbations after the complete rebound of the lithosphere are displayed in Figure 3.6. Note, that the different lines in Figure 3.6 represent different lithospheric thicknesses rather than time slices as in Figure 3.5. The model predicts an E-W stress increase in the fields of the Tampen Spur and decreased horizontal stresses in proximity of the coast. The amplitude of the stress perturbation is on the order of 20 MPa, depending on the assumed value of T. As mentioned earlier, the observed stress decrease occurs over a horizontal distance of ≈100 km. The result for T=30 km best matches this observed wavelength and T=40 km still gives a satisfactory fit to the lateral extent of the observed stress drop, whereas T=20 km clearly results in a too short stress pulse.

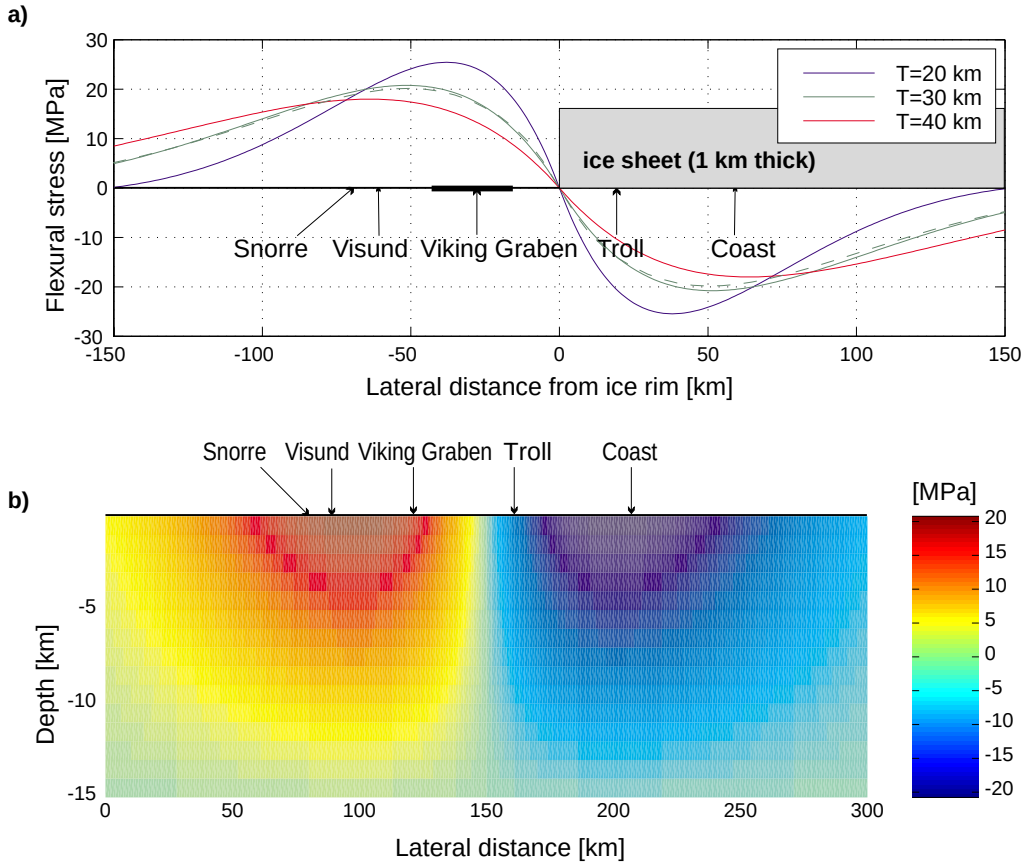

Figure 3.6: Elastic model for flexural stresses as a result of ice melting. The lithosphere is modeled as an elastic layer underlain by a fluid substratum. The model assumes that no bending stresses existed before the ice sheet started to melt. The upper graph shows predicted present day bending stresses at the surface for different effective elastic thicknesses of the lithosphere (T). The lower graph illustrates bending stresses as a function of depth for T=30 km. Compressive stresses are positive.

In summary, the comparison of observed data and the elastic unloading model suggest an effective elastic thickness of 30 to 40 km on a time scale of ≈10,000 years for the lithosphere in the northern North Sea, which agrees well with the findings of Fjeldskaar (1997) who proposes T<50 km. However, the amplitudes of the predicted stress perturbations (≈20 MPa) are upper bounds, since we have to assume that the bending stresses due to glacial loading, as modeled in Section 3.4.1, fully relaxed prior to ice melting, and that the lithospheric rebound after glacial unloading is complete. The analysis of gravity data shows that the rebound is only completed by ≈80% (Ekman and Makinen, 1996).

With these analytical models we only investigated the perturbation of bending stresses in proximity of the ice sheet edge. By doing so, we expect a tendency from high to low horizontal stresses towards the coast which is compatible with the observed focal plane

mechanisms indicating a transition from reverse/strike-slip to strike-slip/normal faulting towards the coast (e.g. Lindholm et al., 1995). However, the modeled stress perturbation is spatially constrained and negligible at distances larger than 100-150 km from the ice front. In fact, underneath the center of the former ice sheet, i.e. further onshore, earthquakes and movements of postglacial faults suggest a thrust faulting stress state (e.g. Muir Wood, 1989), which is compatible with the net shortening of the lithosphere as mentioned in Section 3.4.

3.4.3 Numerical model of the entire loading-unloading cycle

Clearly, by analytically modeling the lithosphere as a single layer we ignored the fact that the lithospheric rheology varies with depth. For example, the assumption that the entire lithosphere, even at shallow depth, relaxes deviatoric stresses might be overly simplified. Also, the analytical models are incapable of including time-varying ice sheet geometries. For these reasons we used the finite element technique to first model a full ice loading-unloading cycle with varying ice sheet geometries and later include cyclic ice loading, on a rheologically more realistic lithosphere.

Figure 3.7a shows the basic setup of the two-dimensional numerical model. It covers the cross section illustrated in Figure 3.1, which corresponds to a lateral extent of 600 km. With depth, the model consists of a 20 km thick elastic upper crust, made up of 5 km of sediments and 15 km of basement, and a 15 km thick viscoelastic lower crust to account for ductile processes that occur at this depth. The depth of the transition to the ductile layer (lower crust) is based on estimates from studies of geothermal gradients (Dragoni et al., 1993). We assign the lower crust a viscosity of 10^{22} Pa s which Strehlau and Meissner (1987) infer for a feldspar/pyroxene-dominated, wet lower crust. The lithospheric mantle is 15 km thick and has a viscosity of 10^{23} Pa s. The lithosphere system is underlain by an asthenosphere which is modeled as a semi-infinite viscous substratum with a viscosity that results in the best match with the observed land uplift (3×10^{19} Pa s). More specifically, at the lithosphere-asthenosphere interface we apply a pressure that is proportional to the vertical deflection. The proportionality constant corresponds to the density restoring force (k) which we introduced in the analytical models (see Appendix A). The purpose of this load is to give the lithosphere the ability to reach isostatic equilibrium after ice loading, and to obtain lithospheric rebound following the onset of ice melting. Additionally, we apply a pressure that is proportional to the rate of vertical deflection on the lithosphere-asthenosphere interface. The proportionality constant is the viscosity of the asthenosphere. Thus, the asthenosphere prevents the lithosphere from deforming instantaneously after ice emplacement but with time the viscous resistance of the asthenosphere decreases and the

density restoring force starts to compensate for the ice load until the viscous resistance disappears and isostatic equilibrium is reached. Ice melting causes the same effect but in the opposite direction. Our implementation of the asthenosphere ignores rheological stratifications of the sub-lithospheric mantle.

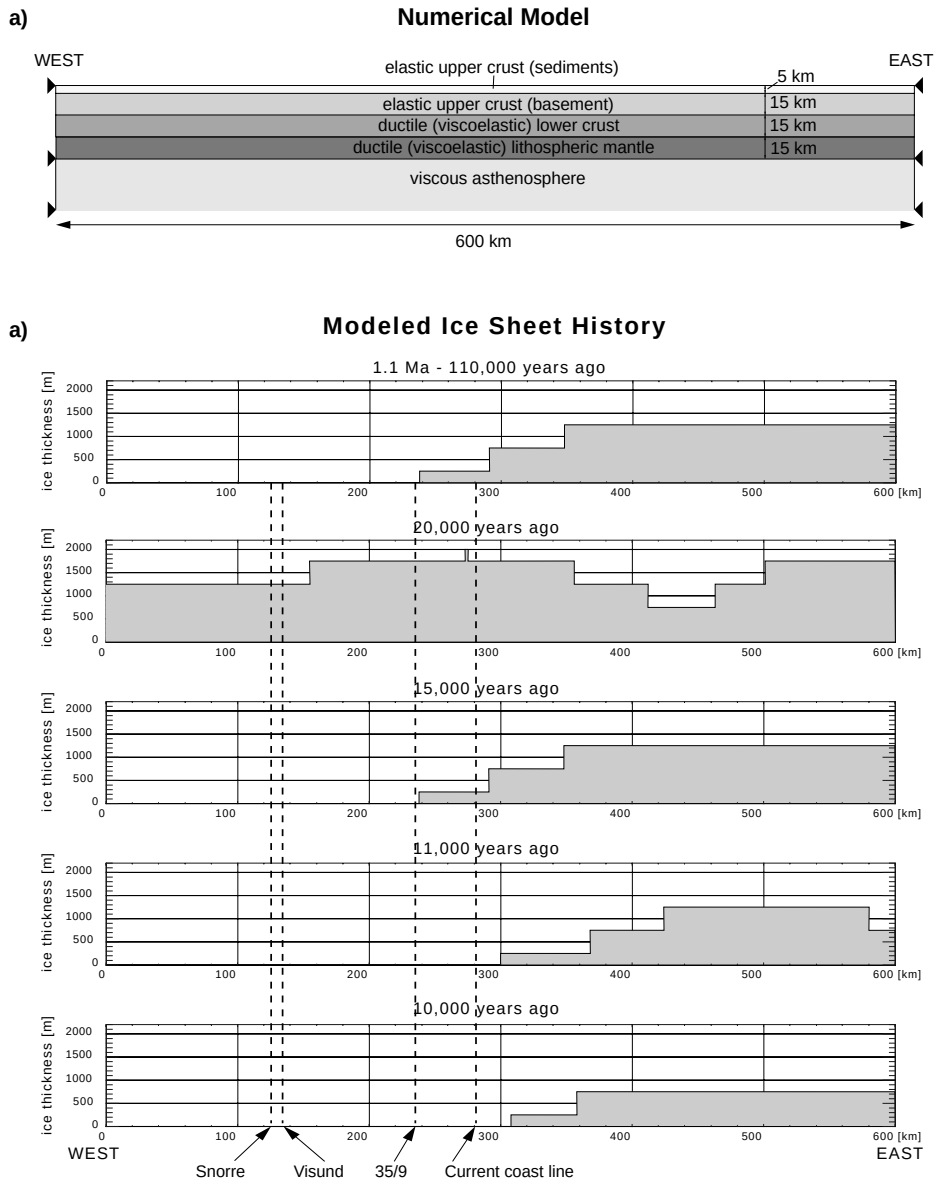

Figure 3.7: Setup of the numerical model and assumed ice sheet history. Figure 3.7a shows the rheologies of the model. The upper crust is elastic and divided into sediments and basement. The basement has a higher density than the sediments. The lower crust and the upper mantle are assumed to be Maxwell-viscoelastic to account for time-dependent irreversible deformation. The asthenosphere is modeled as a viscous semi-infinite substratum. Figure 3.7b shows the modeled ice sheet geometry. The ice sheet grows 1.1 Ma years ago and has a constant extent until 110,000 years ago. Then it grows to its maximum extent (20,000 years ago) and subsequently melts. The ice sheet is assumed to be melted entirely 9000 years ago.

The modeled lithosphere consists of bilinear 4-node elements which means that strain within an element changes linearly in both directions. The model has a lateral resolution of 1 km in the center, and 2 km towards the ends while the vertical resolution is 1 km for the upper crust, and 1.5 km for the lower crust and the lithospheric mantle. Thus, the model is resolved by 40 elements vertically, and 350 elements horizontally resulting in a total number of 14,000 elements. Even the sediment part of the upper crust which is the thinnest rheological unit vertically consists of 5 element layers. The model assumes plane strain perpendicular to the modeled cross section, and the ends of the cross section are fixed horizontally but are allowed to move vertically.

Before we use the numerical model for a full loading cycle we wanted to check whether element sizes and boundary conditions were chosen appropriately. We reproduced the results of the analytical unloading model with a lithospheric thickness of 30 km. As the lithospheric thickness of the numerical model is 50 km we scale Young's Modulus (E) such that the flexural rigidity (D) of the numerical model corresponds to the flexural rigidity of the analytical model. The dashed line in Figure 3.6 displays the flexural stress obtained from the numerical solution, demonstrating that the elastic response of the numerical model has a maximum error of ≈1 MPa.

The model with one full loading cycle starts 1.1 Ma ago with an isotropic stress state, i.e. S_{Hmax} and S_{hmin} are equal to S_v. By assuming an initially isotropic stress state we are ignoring the fact that the crust might have been prestressed, e.g. as a result of ridge push. However, the assumption of initially isotropic stresses allows us to focus on the stress changes deglaciation may have induced. Figure 3.7b illustrates the temporal evolution of the modeled ice sheet. 1.1 Ma ago we let the ice sheet grow to its lateral extent and thickness at 15,000 years ago and let the ice geometry unchanged for one million years until 110,000 years ago. This phase of the model aims to mimic the Pleistocene cold climate with frequent ice sheet advances and retreats. The ice sheet extent from 15,000 years ago is probably a good average of the ice sheet's geometry during this phase as supported by shale compaction and the great abundance of ice front features. Between 110,000 years ago and 20,000 years ago the ice sheet grows to its maximum extent. Subsequently it follows the relatively well documented retreat (Mangerud, 1979; Andersen, 1981; Lundqvist, 1986) illustrated in Figure 3.7b. 9000 years ago the ice sheet has fully disappeared and we monitor the model until the present time.

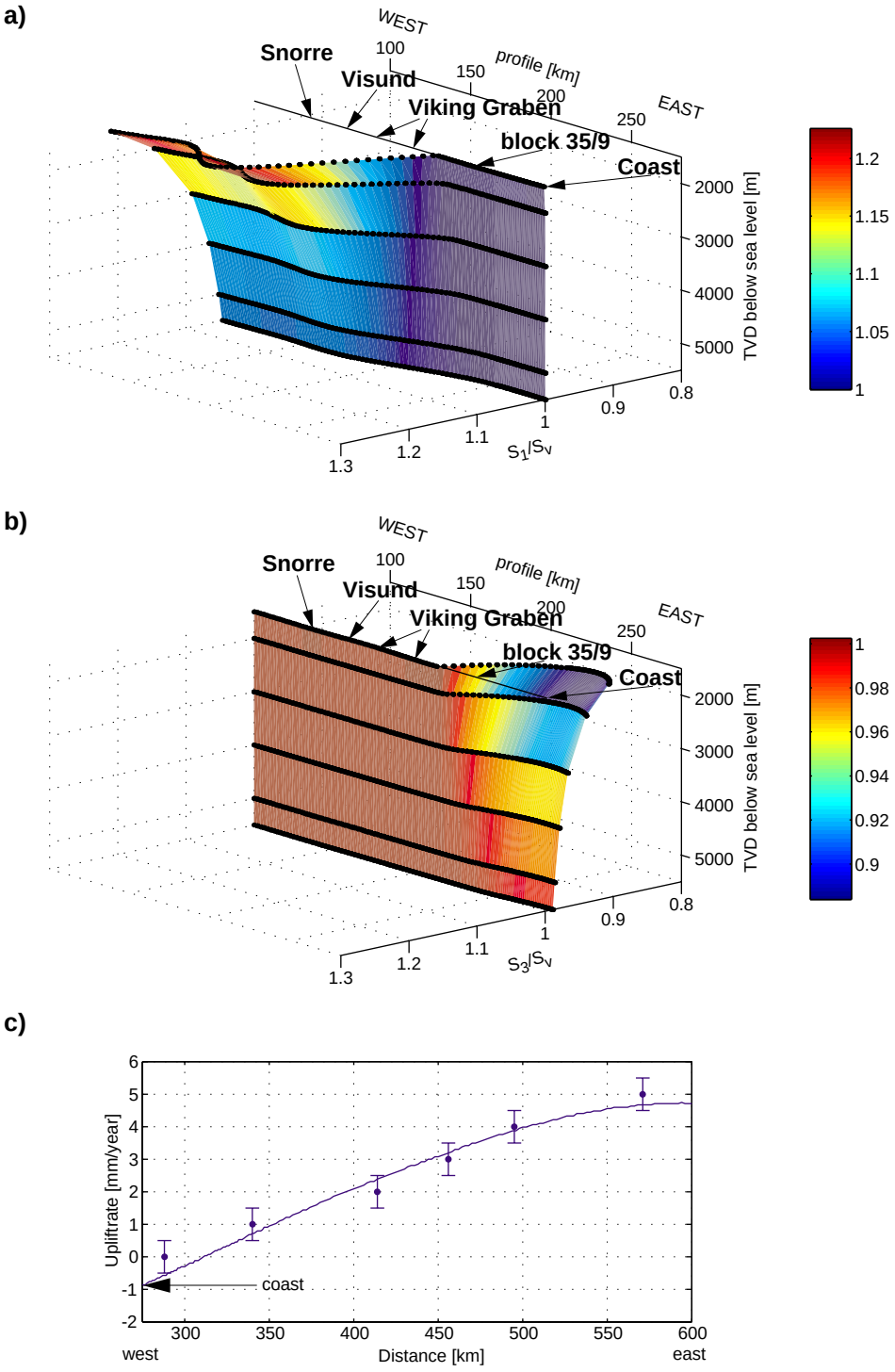

Figure 3.8: Predicted stress from numerical model with a single loading-cycle. The colored surfaces show the predicted spatial variations of S_1/S_v and S_3/S_v for the present. The observed stress decrease towards the coast is reproduced by the model. However, west of the Viking Graben the model underpredicts the observed stresses, which suggests that ridge push also contributes to the horizontal stresses. Figure 3.8c compares the modeled uplift rate to estimates from mareograph and precision leveling data.

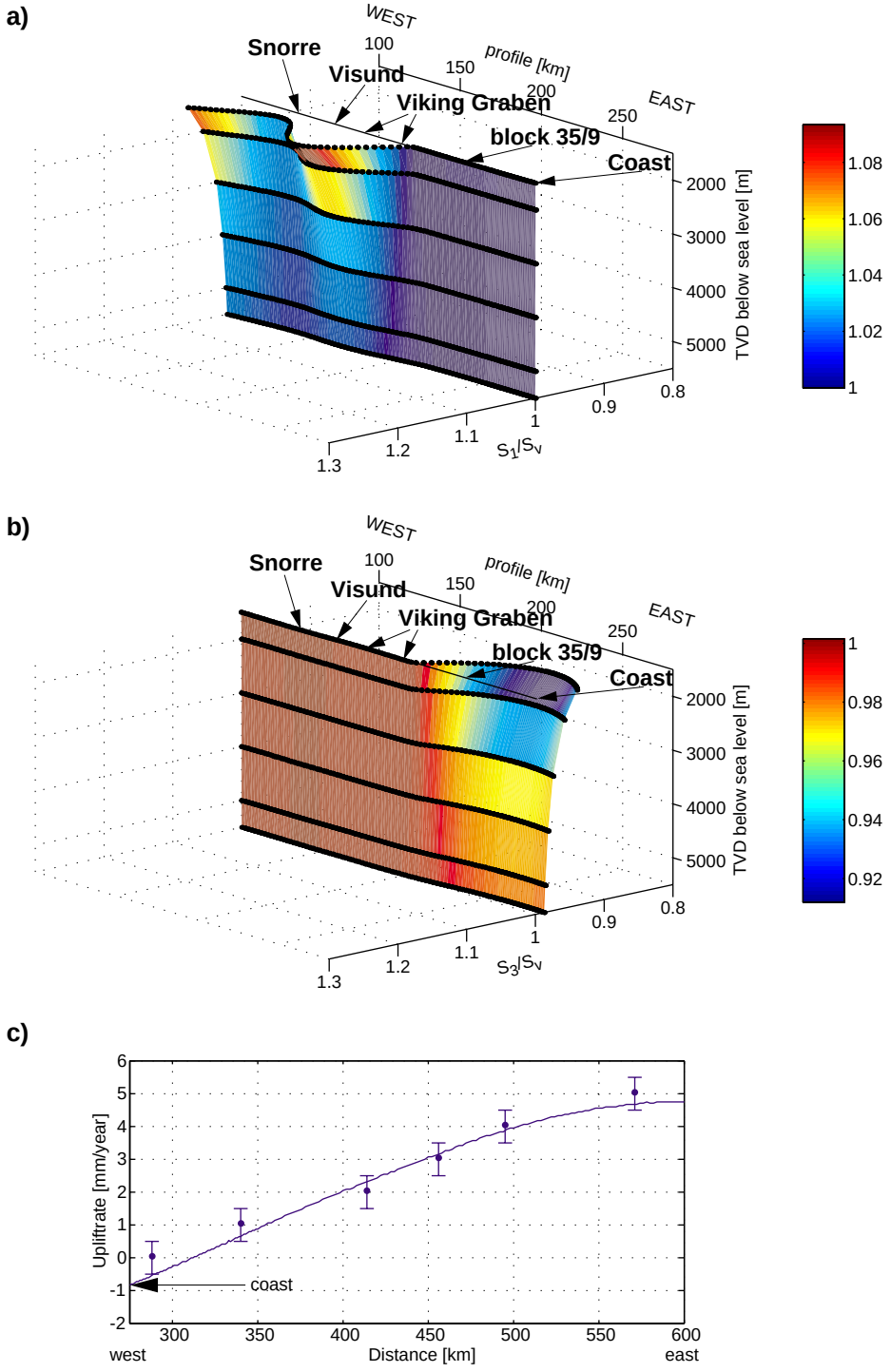

Figure 3.9: Predicted stress from numerical model with multiple loading-cycles. The colored surfaces show the predicted spatial variations of S_1/S_v and S_3/S_v for the present. The observed stress decrease towards the coast is reproduced by the model. Compared to the single loading cycle model stress perturbations are smaller but show the same patterns. Figure 3.9c compares the modeled uplift rate to estimates from mareograph and precision leveling data.

The sediments in the northern North Sea are fairly unconsolidated to a depth of ≈1000 m. Unconsolidated sediments are incapable of supporting differential stress. Therefore, we expect that imposed bending stresses are only taken up by rock units at depths greater than 1000 m. As a result, the surface of the model corresponds to a real depth of ≈1000 m. Consequently, we shifted the modeled results with depth, e.g. 2000 m depth in Figure 3.8 corresponds to 1000 m model depth.

The predicted present day stress perturbations along the profile line in the northern North Sea are displayed in Figures 3.8a and 3.8b. First, it is important to note that the numerical model predicts increased horizontal stresses in the western part of the northern North Sea, including the Tampen Spur and lowered horizontal stresses in proximity of the coast. This agrees well with the observed drop of horizontal stresses towards the coast (Figure 3.2a) and also with the results of the analytical unloading model. But, for the numerical model we did not have to make any assumptions for the stress state before the onset of ice melting as in the analytical unloading model (Section 3.4.2). Further, the entire upper crust is purely elastic and therefore can not relax deviatoric stresses at all.

Instead, the transition from lowered horizontal stresses in the proximity of the coast to higher horizontal stresses further offshore is the result of creep deformation that takes place in the lower crust during the ice sheet's existence. The lower crust and lithospheric mantle horizontally extend underneath the ice sheet. As a result of the coupling between the lower and the upper crust, the lower crust transmits the horizontal extension to the upper crust which leads to the observed and modeled horizontal stress decrease in proximity of the coast at shallow depth. Away from the former ice sheet, a similar effect causes the present-day increase of the horizontal stresses. In other words, the ductile part of the lithosphere behaves similar to the end member model illustrated in Figure 3.4a, while the upper crust follows the assumption made in Figure 3.4b. The numerical model shows that the coupled behavior of the two end-member models shown in Figure 3.4 give a good fit to the stress observations. The resulting modeled present-day stresses are comparable to what is expected from the assumption made in Figure 3.4a but for a slightly different reason.

More specifically, compared to the analytical model, i.e. the assumption made in Figure 3.4a, the amplitudes of the stress perturbations are smaller. The predicted S_1/S_v (Figure 3.8a) is high on the west side of the Viking Graben and has a maximum value of 1.22 in the vicinity of the Visund field at relatively shallow depth. This matches the S_1/S_v estimates from wellbore failure of Wiprut and Zoback (1998) for the Visund field very well (S_1/S_v between 1.2 and 1.3). Closer to the coast (i.e. east of the Viking Graben), S_1 is equal to S_v which would lead to a normal faulting stress regime. Predicted values for S_3/S_v (Figure 3.8b) are close to 1 west of the Viking Graben and drop to minimum values of 0.88 in the

region of block 35/9. As mentioned previously, our models ignore the influence of ridge push which introduces some uncertainty to the predicted stress values. Our most reliable predictions are with respect to spatial stress changes which are unaffected by ridge push. The lateral extent of the predicted changes in horizontal stress match the measured stresses, with maxima in the Tampen Spur and minima in proximity of block 35/9.

Figure 3.8c compares the modeled uplift rates with estimates obtained from mareograph and precise leveling data (Ekman, 1996) from the coast towards the center of the ice sheet. To compare the model results to the observations we subtracted a eustatic correction of 1.15 mm/year (Nakiboglu and Lambeck, 1991) from the model results. The model achieves a good fit to the uplift measurements. Except in proximity to the coast where the modeled uplift rates fall slightly outside the error bounds of the measurement. A possible reason for this discrepancy is the two-dimensional geometry of the model which implies that the ice sheet front was always oriented perpendicular to the modeled cross section. Figure 3.1 shows that this is not the case for the maximum ice sheet extent.

We also considered an ice model that consists of ten ice loading cycles with a periodicity of 10^5 years based on oxygen isotope curves obtained from deep sea drilling (Shackleton et al., 1984). Otherwise the model is identical to the single loading cycle-model described above. Compared to the model with a single loading cycle (Figure 3.8) the horizontal stress perturbations are lower. S_1/S_v reaches a maximum of 1.1 and S_3/S_v varies between 1 and 0.91 (Figure 3.9, a and b). Even if the magnitudes of the stress perturbation are lower than in the single loading cycle-model the general pattern of the stress perturbations is identical showing a transition from high horizontal stresses, compatible with the observed strike-slip/thrust faulting earthquakes west of the Viking Graben to lower horizontal stresses as evidenced by strike-slip/normal faulting earthquakes between the Viking Graben and the coast. The predicted uplift rates (Figure 3.9c) are almost identical for both models.

In both numerical models, the zone of decreased horizontal stress beneath the former ice sheet is limited to within 100-150 km of the ice sheet front. Closer to the center of the ice sheet the modeled horizontal stress perturbations diminish. As mentioned earlier, the stress state obtained from earthquakes and postglacial fault movements is predominantly thrust faulting near the center of the ice sheet which is compatible with the model results. The induced stress perturbations decrease with depth, which is a typical feature for bending stresses. However, the predicted horizontal stresses are slightly to low. A possible explanation for this underprediction of horizontal stress is the fact that we ignore ridge push as a stress source. As mentioned earlier, ridge push uniformly increases horizontal stress over large areas so the observed stresses result most likely from the superposition of

glacially induced stress perturbations as modeled in this paper and spatially uniform tectonic stresses. Additionally, the stress estimates of our model can be affected by the two-dimensional approach which introduces additional uncertainties, so the discrepancy between the modeled and observed stresses may result from neglecting ridge push or can be an artifact of the two-dimensional approach.

Also, note that the modeled upper crust has a purely elastic rheology, lacking the possibility to undergo brittle deformation. We chose the purely elastic rheology because we wanted to keep the model as simple as possible without complicating it unnecessarily. The fact that we can model the observed stresses without accounting for brittle failure indicates that the observed in-situ stress variations are mostly the result of the previously described interaction between the ductile lower crust and the strong, elastic upper crust.

3.5 Prediction of pore pressure from glacial unloading

Comparing Figure 3.2a and Figure 3.2b it is evident that the pore pressure is somehow related to stress. The highest pore pressures occur in the Tampen Spur, where S_3/S_v is close to 1, indicating high horizontal stresses. Conversely, east of the Viking Graben the pore pressure is mostly hydrostatic and S_3/S_v drops to ≈0.8 in the same region. In the previous sections we have established that the increased horizontal stresses in the Tampen Spur are likely to be caused by glaciation-deglaciation and therefore developed very recently (since 20,000 years ago). So, perhaps part of the overpressure in the Tampen Spur results from the poroelastic response to the stress increase that was induced by deglaciation.

To test this hypothesis, we calculated the change in the modeled 1st stress invariant ($\Delta\sigma_m$) between the onset of the model and present, which corresponds to the change of the isotropic part of the stress tensor and is a measure for the volume change a certain rock mass was exposed to. $\Delta\sigma_m$ is related to a change in pore pressure (ΔP_p), via Skempton's coefficient (B), where B varies between 0 and 1. For B=1 the change in P_p is equal to $\Delta\sigma_m$ and for B=0 any change in $\Delta\sigma_m$ doesn't affect the pore pressure.

Figure 3.10 shows the predicted ΔP_p as a result of glaciation-deglaciation for B=0.8, which is an upper bound for realistic values of B and typical for shales. Reservoir sands with high porosities typically have B-values of ≈0.5. We chose a relatively high B-value since we wanted to get an upper bound on how deglaciation influences the pore pressure.

The highest modeled ΔP_p of 3.5 MPa occurs where the horizontal stress increases the most, which is west of the Viking Graben in the vicinity of the Snorre and Visund fields. In the Snorre field ΔP_p is predicted to be around 3.5 MPa and in Visund it drops to 2.8 MPa. Closer to the coast, e.g. in block 35/9 ΔP_p is negative so we would actually expect a P_p

decrease, leading to subhydrostatic pore pressures in proximity of the coast. If we compare these P_p predictions to the observed P_p-values shown in Figure 3.2b, it becomes obvious that the predicted P_p-increase in Snorre (3.5 MPa) and Visund (2.8 MPa) are much smaller than measured overpressures, which reach up to 15 MPa in the Tampen Spur. Conversely, we don't observe subhydrostatic pore pressures around block 35/9 as predicted by the model.

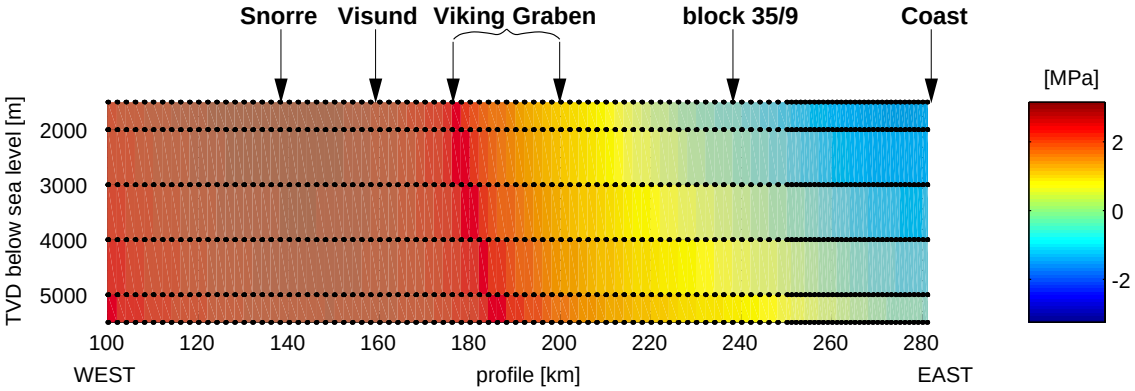

Figure 3.10: Predicted pore pressure change from glaciation-deglaciation. The figure shows the potential for a change in pore pressure as a result of poroelastic response to deglaciation for B=0.8. The predicted pore pressure increase is highest in the vicinity of the Snorre field with increases of 3.5 MPa. Closer to the coast, P_p remains almost constant or slightly decreases.

A possible explanation for the higher than predicted pore pressures in the Tampen Spur are additional sources of overpressure, such as under-compaction. If the overburden due to sedimentation increases faster than pore fluids can diffuse away the pore pressure increases. Caillet et al. (1991) modeled P_p-increases resulting from this effect for the Tampen Spur. For Visund they predict overpressures of around 7 MPa at 2500 m depth and 12 MPa for a depth of 3000 m. However, measured pore pressures are typically around 5 MPa higher. After adding the overpressure of 2.8 MPa due to deglaciation to the under-compaction prediction, we actually get closer to the observed pore pressures. The same applies to the Snorre field where the combined overpressure from under-compaction and deglaciation gets very close to the observed pore pressures. Therefore, the overpressures in the Tampen Spur seem to be the result of both, under-compaction and poroelastic response to bending stresses induced by glaciation-deglaciation.

Concerning the predicted P_p-decrease close to the coast, we have to take into account that in this area stresses are strongly decreased which tends to cause faulting, and consequently increases permeability (e.g. Barton et al., 1995). As a result of increased permeability the pore fluids communicate with the sea floor and no subhydrostatic pore

pressure can develop.

An alternative explanation for the low P_p close to the coast is the stress decrease that deglaciation induced. The P_p can never exceed S_3 since this would lead to fracturing of the formation and as a result the fluids would escape to the surface. The stress decrease due to deglaciation might have brought S_3 down to the existing pore pressure at the time when the stress decrease took place and parts of the fluids leaked away, leading to a P_p reduction. Possibly, the expected P_p decrease due to poroelasticity from Figure 3.10 was superimposed onto this effect, leading to the close to hydrostatic pore pressures at present. Conversely, in the Tampen Spur where stresses remained high, the high overpressures were contained.

3.6 Conclusions

Observed stress data in the northern North Sea shows a transition from high horizontal stresses in the Tampen Spur to decreased stresses towards the coast. Modeling of flexural stresses due to glaciation-deglaciation shows that this lateral stress variation is likely to be the result of this process. The regionally consistent orientation of S_{Hmax} as well as the underprediction of stress magnitudes by the flexural models suggests that ridge push also significantly contributes to the stress state in the northern North Sea. The wavelength of the stress perturbation implies that the effective elastic lithospheric thickness in the northern North Sea ranges between 30 and 40 km on a time scale comparable to deglaciation (≈10,000 years).

Concerning the model it shouldn't be forgotten that we limited ourselves to a two-dimensional approach which has the advantage of simplicity. However, by doing so we have to assume that the changes in ice sheet thickness are largest parallel to the modeled cross section. Figure 3.1 shows that this is not true for the maximum ice sheet extent 20,000 years ago. Nevertheless, the modeling shows that deglaciation is a possible source of overpressure in the Tampen Spur. However, part of the observed overpressure must have been caused by another source such as compaction disequilibrium resulting from rapid sedimentation.

Acknowledgments

We would like to thank Norsk Hydro for generously providing the data and financial support for this study.

Chapter 4

THREE-DIMENSIONAL MODELS OF GLACIALLY-INDUCED STRESSES OFFSHORE NORWAY

This chapter will be submitted with Mark D. Zoback as co-author to Journal of Geophysical Research.

4.1 Abstract

It is well known that the melting of the Fennoscandian ice sheet caused significant uplift of the formerly glaciated areas, and associated bending of the lithosphere. In this work we evaluate the role of lithospheric flexure resulting from post-glacial rebound as a possible source of regional stress variations in the northern North Sea and on the Mid-Norwegian Margin. We use stress information derived from earthquake focal plane mechanisms and from a variety of borehole measurement techniques to constrain spatial variations of stress. We have used these stress data to constrain finite element models to investigate the effects of glacial melting and the associated flexuring of the lithosphere on the local stress field offshore Norway. The comparison of the model results with the observed stresses suggests that the late Quaternary melting of the Fennoscandian ice sheet strongly influences the in situ stress field offshore Norway. Viscoelastic behavior within the lithosphere is required to explain the observed stresses. The model results suggest that the lower portions of the lithosphere have viscosities on the order of 10^{22} to 10^{23} Pa s in the northern North Sea and slightly higher viscosities on the Mid-Norwegian margin.

4.2 Introduction

Passive continental margins at high latitudes, are frequently associated with anomalously high seismicity. Two well studied examples are the passive margin of eastern Canada (e.g. Stein et al., 1989; Hasegawa and Basham, 1989), and the Norwegian margin (e.g. Bungum et al., 1991). Stein et al. (1979) proposed a model in which the increased seismicity is due to flexural stresses generated by the removal of ice sheets. The influence of ice melting would explain why increased passive margin seismicity is restricted to high latitudes which makes this model very appealing. To rigorously test the hypothesized influence of ice removal on passive margin seismicity, knowledge of the in-situ stress field, including stress orientations, magnitudes and lateral changes, is crucial. The Norwegian margin is a perfect laboratory for investigating the influence of ice removal on the local stress field because offshore drilling operations associated with hydrocarbon exploration provide an extensive stress data set (Grollimund et al., in press).

South of the Norwegian Margin, in northwestern Europe, the orientation of the maximum horizontal stress (S_{Hmax}) strikes consistently northwest to north-northwest (Müller et al., 1992) and a strike-slip/normal faulting regime ($S_v \approx S_{Hmax} > S_{hmin}$) is generally observed. Geodynamic models show that this consistent S_{Hmax} orientation results from the interaction between sea floor spreading at the Mid-Atlantic ridge and the collision of

the Eurasian plate with the African plate (Grünthal and Stromeyer, 1992). However, off the coast of Norway the stress field appears to be regionally perturbed as S_{Hmax} orientations change markedly (Figure 4.2). For example, S_{Hmax} roughly strikes east-west at 61ºN and 3ºE but almost north-south around 57ºN and 2ºE. Additionally, investigation of stress magnitudes reveals significant changes of the least principal stress over relatively small distances (see Chapter 2), i.e. high magnitudes are observed at distances greater than roughly 100 kilometers from the coast but in proximity of the coast, stress magnitudes are greatly reduced. This transition from high to low stress magnitudes towards the Norwegian coast is confirmed by earthquake focal plane mechanisms which are mostly reverse faulting far from the coast but strike-slip or even normal faulting closer to the coast. Stein et al. (1989) and Walcott (1970) have shown that such spatial stress variations can be the result of flexural stresses associated with deglaciation. In this study we wanted to test whether all the observed stress variations offshore Norway are possibly the result of lithospheric bending due to glacial loading and what lithospheric properties would be necessary to reproduce the observed stresses with the flexure model.

Another possible constraint for the earth's rheology, are uplift data and shoreline tilt measurements that have been used extensively to constrain models of post-glacial rebound. Figure 4.1 shows estimates of lithospheric thickness ($T_{lithosphere}$) for Fennoscandia obtained from models of post-glacial rebound, constrained by various kinds of uplift data. McConnell (1968) suggested a lithospheric thickness of 120 km. Cathles (1975), and Anundsen and Fjeldskaar (1983) came up with an estimated $T_{lithosphere}$ of ≈70 km. The estimate for $T_{lithosphere}$ = 110 km by Wolf (1986) is based on an equilibrium model and therefore represents an upper bound. The estimate of Lambeck et al. (1990) for $T_{lithosphere}$ between 100 and 150 km is considerably higher than Fjeldskaar's finding of $T_{lithosphere}$≈ 40 km (Fjeldskaar and Cathles, 1991). More recently, Fjeldskaar estimates $T_{lithosphere}$ between 20 km and 50 km (Fjeldskaar, 1997). A more detailed discussion of lithospheric thickness estimates can be found in Wolf (1993). In summary, the lithospheric thickness in Fennoscandia is poorly constrained and estimates vary depending on the data sets against which the models were calibrated. Lateral changes in lithospheric thickness might also explain the discrepancies between the estimates of different authors. Breuer and Wolf (1995) suggest that the lithospheric thickness varies laterally near Spitsbergen and Fjeldskaar (1997) proposes a decrease in lithospheric thickness from central Fennoscandia towards western Norway.

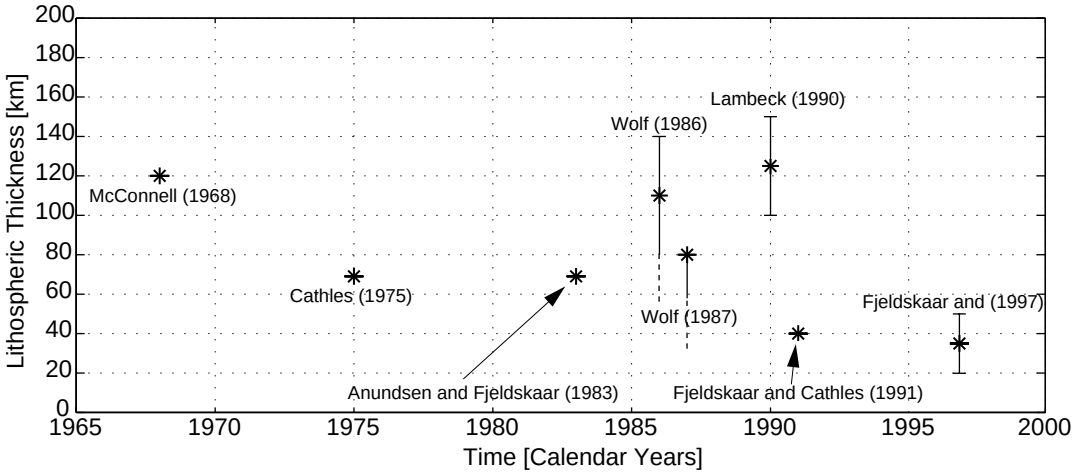

Figure 4.1: Estimates for the lithospheric thickness in Fennoscandia from studies of post-glacial uplift, compiled by Wolf (1993).

Most models of post-glacial rebound have considered the lithosphere as purely elastic, ignoring the possibility for intra-lithospheric, viscous deformation. This is a good approximation for the purpose of reproducing post-glacial uplift because modeled uplift is mostly governed by sub-lithospheric rheologies. However, Klemann and Wolf (1998) suggest that viscous behavior within the lithosphere might be crucial for modeling stress changes associated with post-glacial rebound. In fact, the results of our models demonstrate that the observed stress patterns can only be explained if the lower lithosphere undergoes permanent, viscous deformation during the ice sheet's existence.

Global models of post-glacial rebound show that post-glacial uplift is influenced by deformation processes even at great depths, possibly down to the core-mantle boundary (e.g. Peltier, 1985). However, the purpose of our models is to reproduce the relatively small scale stress variations in the vicinity of the former ice sheet front. These local stress variations are most likely unaffected by viscosity variations at great depth, but rheological behavior at more shallow depth is more important. For this reason, we have adopted a relatively simple model representation of the sub-lithospheric units, as described in Section 4.3.2, while focusing on a detailed representation of lithospheric rheologies. The good match of our model results with the observations, both stress and uplift, indicates that our approach is adequate.

4.3 Three-dimensional numerical models

To investigate the effect of ice loading on the stress field offshore Norway, we used two three-dimensional finite element models including realistic ice sheet geometries, and lithospheric rheologies. The location and spatial extent of the two models are shown in Figure 4.2. The first model covers southwestern Norway and the northern North Sea and will be referred to as the 'North Sea model'. The second model covers an area further north, including central Norway and the corresponding offshore area, the so called Mid-Norwegian Margin. We will subsequently refer to this model as the 'Mid-Norway model'. All the model results, and the observed stress magnitudes presented in this Chapter correspond to a depth of 3000 m.

4.3.1 Data to constrain the models

As mentioned earlier, we use in-situ stress measurements to constrain the models. Figure 4.2 shows all the available S_{Hmax} orientations from the analysis of wellbore failure, and from earthquakes. Additionally, magnitudes of the least principal stress from the analysis of leak off tests in Chapter 2 can be used to constrain our modeling. Our strategy was to run the models for a variety of reasonable rheological parameters to see whether it is possible to imitate the observed stresses. Later, we also tested the impact of the chosen ice evolution on the model results.

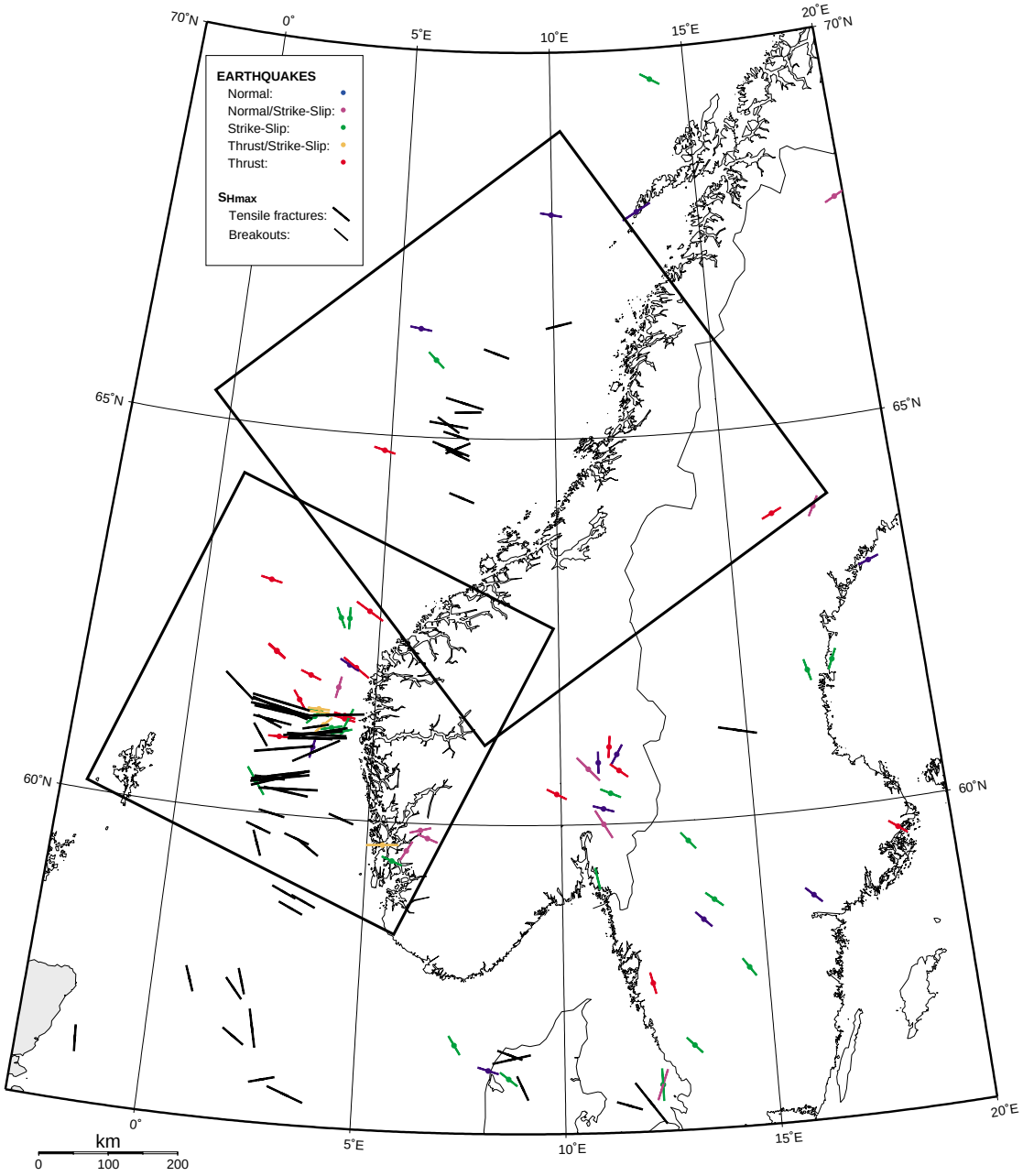

Figure 4.2: Location map. The map shows the horizontal extent of the two numerical models along with stress orientation data. The smaller rectangle in the south marks the extent of the 'North Sea model', and the larger rectangle outlines the location of the 'Mid-Norway model'. Black lines indicate the orientation of S_{Hmax} from borehole measurements and colored lines are S_{Hmax} orientations inferred from earthquakes.

4.3.2 Modeling the in-situ stress field in the northern North Sea (the "North Sea model")

The spatial extent of the 'North Sea model' is outlined by the lower rectangle in Figure 4.2 and corresponds to an area of 250,000 km^2. The model reaches to a depth of 50 km and is centered on the northern North Sea which contains the most valuable stress data to constrain the model. We use 21,025 8-node trilinear brick elements (strain within an element changes linearly in all three directions) assuming a flat layer geometry. Amelung and Wolf (1994) show that the flat earth assumption is valid for models of glacial isostasy even for the Laurentide ice sheet which was much larger than the Fennoscandian ice sheet. 15,625 elements cover the area illustrated in Figure 4.2. The remaining 5,400 elements form a 300 km wide zone surrounding the area of interest to minimize boundary effects. The 15,625 center elements each measure 20 km horizontally and 2 km vertically (Figure 4.3).

The upper crust is 20 km thick and has an elastic-plastic rheology. We assume linear elasticity for the elastic domain and perfect plasticity if the stress state exceeds the Mohr Coulomb failure criterion with a coefficient of friction of 0.6 and a close to zero cohesion, which is a good representation of upper crustal rheology (Byerlee, 1978; Zoback and Healy, 1992). Equation 4.1 describes the Mohr Coulomb failure envelope in absence of cohesion.

$$(\mathbf{S}_1 - \mathbf{P_p}) = (\mathbf{S}_3 - \mathbf{P_p})(\sqrt{\mu^2 + 1} + \mu)^2 \qquad \text{Eqn. 4.1}$$

S_1 and S_3 are the maximum and minimum total principal stresses, P_p is the pore pressure and μ is the coefficient of friction. In order to incorporate pore pressure we are working with effective stresses which are the difference between total stress and pore pressure assuming that the pore pressure is hydrostatic. Also, failure according to Mohr Coulomb depends on both the deviatoric and the hydrostatic part of the stress tensor. Consequently, we have to include body forces resulting from gravity in the model. The initial stress state before ice sheet growth is described in Equation 4.2 where S_v is the vertical stress, S_{hmin} is the minimum horizontal stress, ρ is the density, g is gravity, and z is depth. McGarr (1988) suggests this isotropic stress state as a good estimate in absence of tectonic forces.

$$\mathbf{S_v} = \mathbf{S_{Hmax}} = \mathbf{S_{hmin}} = \rho \mathbf{g z} \qquad \text{Eqn. 4.2}$$

The instantaneous application of gravity in our model affects the stress state. Thus, we need

to prestress the model before we apply gravity in order to obtain stress conditions which satisfy Equation 4.2. More specifically, the application of gravity leads to $S_v = \rho g z$ (as in Equation 4.2) but it only increases the horizontal stresses by $(\nu/(1-\nu))\rho g z$. Thus, in order to obtain the proper initial stress state, we have to prescribe the missing horizontal stresses. This procedure also allows to include the tectonic contribution to the stress field (ridge push) by simply adding the tectonic stress to the prescribed horizontal stresses.

Underneath the upper crust lies a 14 km-thick Maxwell viscoelastic layer representing the lower crust. The lithospheric mantle is 16 km thick and assumed to behave according to Maxwell viscoelasticity as well. We use the viscosities of the lower crust, and the lithospheric mantle as free parameters in order to calibrate the model results until they fit the stress observations (for details see section on influence of chosen viscosities on page 75). Similar to the model described in Section 3.4.3, we include the asthenosphere by applying appropriate boundary conditions at the bottom of the lithosphere, thereby neglecting possible sub-lithospheric stratifications of the mantle. More specifically, at each bottom node of the model we apply a vertical force to account for isostasy ($F_{isostatic}$) according to Equation 4.3.

$$\mathbf{F}_{\mathbf{isostatic}} = -\mathbf{k}\mathbf{A}\mathbf{u}_{\mathbf{z}} \qquad \text{Eqn. 4.3}$$

k is the density restoring factor as described in Chapter 3 and Appendix A, A is the area surrounding the node, and u_z is the vertical displacement of the node. The purpose of this load is to give the lithosphere the ability to reach isostatic equilibrium after ice loading and to obtain lithospheric rebound following ice melting. An additional upward-directed force has to be applied at the bottom of the lithosphere to compensate the weight of the lithospheric overburden and is equal to the vertical stress at the base of the lithosphere times A. This “overburden” force prevents the model from subsiding unrealistically after the application of gravity. Lastly, we have to apply a force that is proportional to the rate of vertical displacement to account for the viscous resistance of the asthenosphere as described in Chapter 3.

Table 4.1 lists the rheological parameters we used for the numerical models. We are aware that a power creep law including temperature (Kirby, 1983; Carter and Tsenn, 1987) would be a better representation of the ductile part of the lithosphere. However, we believe the benefit of having a very accurate representation of the in-situ rock rheology does not compensate for including the uncertainty of two additional parameters per layer. Because we simply include the asthenosphere as a boundary condition, its behavior is described by two parameters (k and the proportionality constant for the viscous resistance).

Table 4.1: Rheological parameters of the three-dimensional models.

Depth unit	ρ (kg/m^3)	E (GPa)	ν	η (Pa s)	μ	C_0 (MPa)
Upper crust	2,700	56	0.25	-	0.6	0.1
Lower crust	2,700	71	0.25	varies	-	-
Lithospheric mantle	3,200	100	0.25	varies	-	-

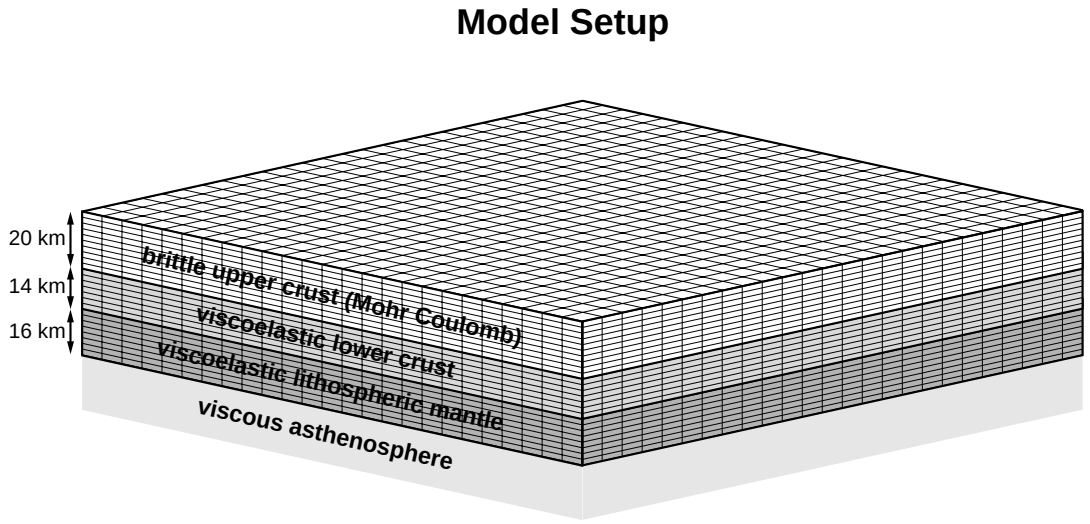

Figure 4.3: Setup of the numerical models showing element sizes and modeled rheological layering of the lithosphere. In this figure we only display the 15,625 elements in the center of the model, omitting the 5,400 elements surrounding the area of interest.

In order to include the ice sheet, we compiled published data on ice sheet extents and thicknesses for different ice stages (Mangerud et al., 1979; Andersen, 1981; Lundqvist, 1986). The North Sea model includes four ice stages as illustrated in Figure 4.4. The maximum ice extent (20,000 years ago) covers the entire North Sea. A remarkable evidence for the existence of this huge ice shield are erratic blocks of Scandinavian origin that were deposited on the Shetland Islands (Hoppe, 1974). The ice extent 15,000 years ago can be regarded as representative for most of the ice sheet's existence during the Pleistocene, which is supported by high shale compaction in certain areas (Hansen, 1996), that coincide with the 15,000 years ago ice extent. According to these observations, we start ice loading 2 million years ago with the 15,000 years ago ice sheet extent (Figure 4.4b) and maintain this load until 110,000 years ago. Subsequently, we grow the ice sheet to its maximum extent (Figure 4.4a) and keep this load until 20,000 years ago. During the last 20,000 years we gradually melt the ice sheet back according to Figure 4.4 until 9,000 years ago when the

entire ice sheet has disappeared and finally let the lithosphere equilibrate until present-day. For the remainder of Chapter 4 we will use the above described ice evolution as “reference” ice model (see also Figure 4.10). In a later section on page 84, we will also test the impact of different ice evolutions on the model results.

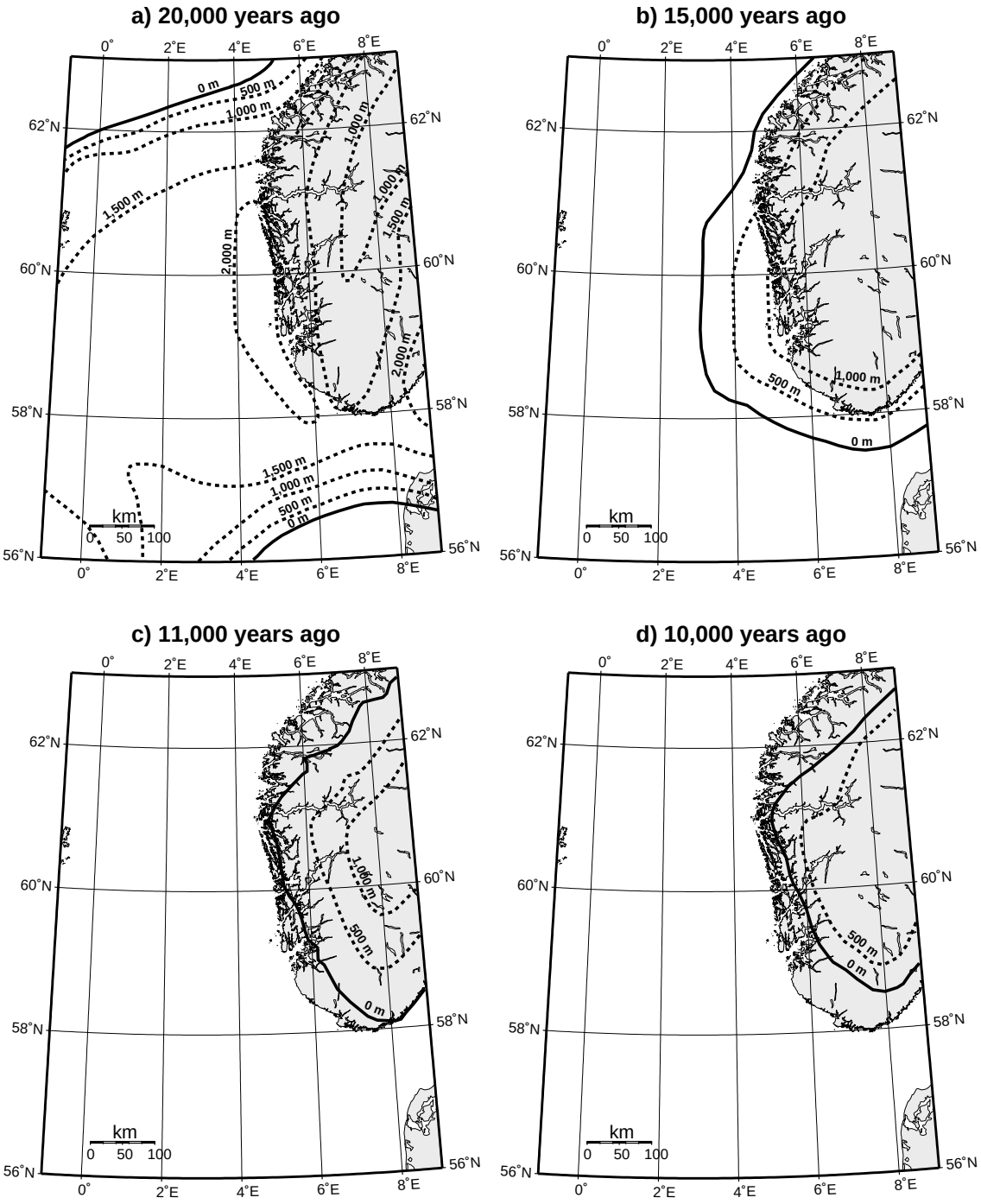

Figure 4.4: (previous page) Extent and thickness of the modeled ice sheet for different

stages of the North Sea model. figure a) shows the maximum ice sheet extent that existed 20,000 years ago. The ice extent at 15,000 years ago (Figure 4.4b) is the reference ice extent that is representative for most of the ice sheet's existence during the Pleistocene.

To test the model results we compare the present-day predictions of stress to the observed in-situ stresses from Chapter 2. All the model results presented in this paper are present-day predictions.

Results of the best-fitting North Sea model

Figure 4.5 compares observed S_{Hmax} orientations with the results of the best fitting model. The best fitting North Sea model has a lower crustal viscosity of 10^{22} Pa s, and a lithospheric mantle viscosity of 10^{23} Pa s. These viscosities agree with values based on estimations of a linearized power creep law for a wet Variscan continental crust (Strehlau and Meissner, 1987). The asthenospheric viscosity is poorly constrained by stress measurements but a comparison with measurements of uplift rate and shoreline tilt yields a viscosity of $5x10^{19}$ Pa s which agrees with the findings of (Fjeldskaar, 1997). In addition to this best-fitting model, I will discuss the stress predictions from models with different viscosities later in this chapter on page 75.

Generally, the model shows that deglaciation causes S_{Hmax} orientations to be close to perpendicular to the ice sheet margins at distances of > 100 km from the coast. Closer to the coast the S_{Hmax} orientations tend to align with the coastline at least north of 61.5ºN. Further south, the complex ice sheet geometry during the maximum extent causes a complicated pattern of stress orientations. More specifically, at a latitude of 61ºN the model reproduces the roughly E-W striking S_{Hmax} orientation and perfectly mimics the smooth S_{Hmax} rotation from ≈ 100º at 2.5ºE to ≈ 85 at 3.5ºE. Further south, around 60ºN and 2.5ºE the model exactly matches the observed S_{Hmax} orientations. The only discrepancy is located at 60ºN and 4.5ºE where the model deviates from the single stress observation by almost 90º. However, this particular stress measurement is obtained from a breakout analysis using caliper logs. This kind of stress measurement has several potential error sources such as keyseating and the measurement might reflect the orientation of the borehole rather than stress direction (Plumb and Hickman, 1985). Nevertheless, with few exceptions the 'North Sea model' fits the stress orientation data extremely well.

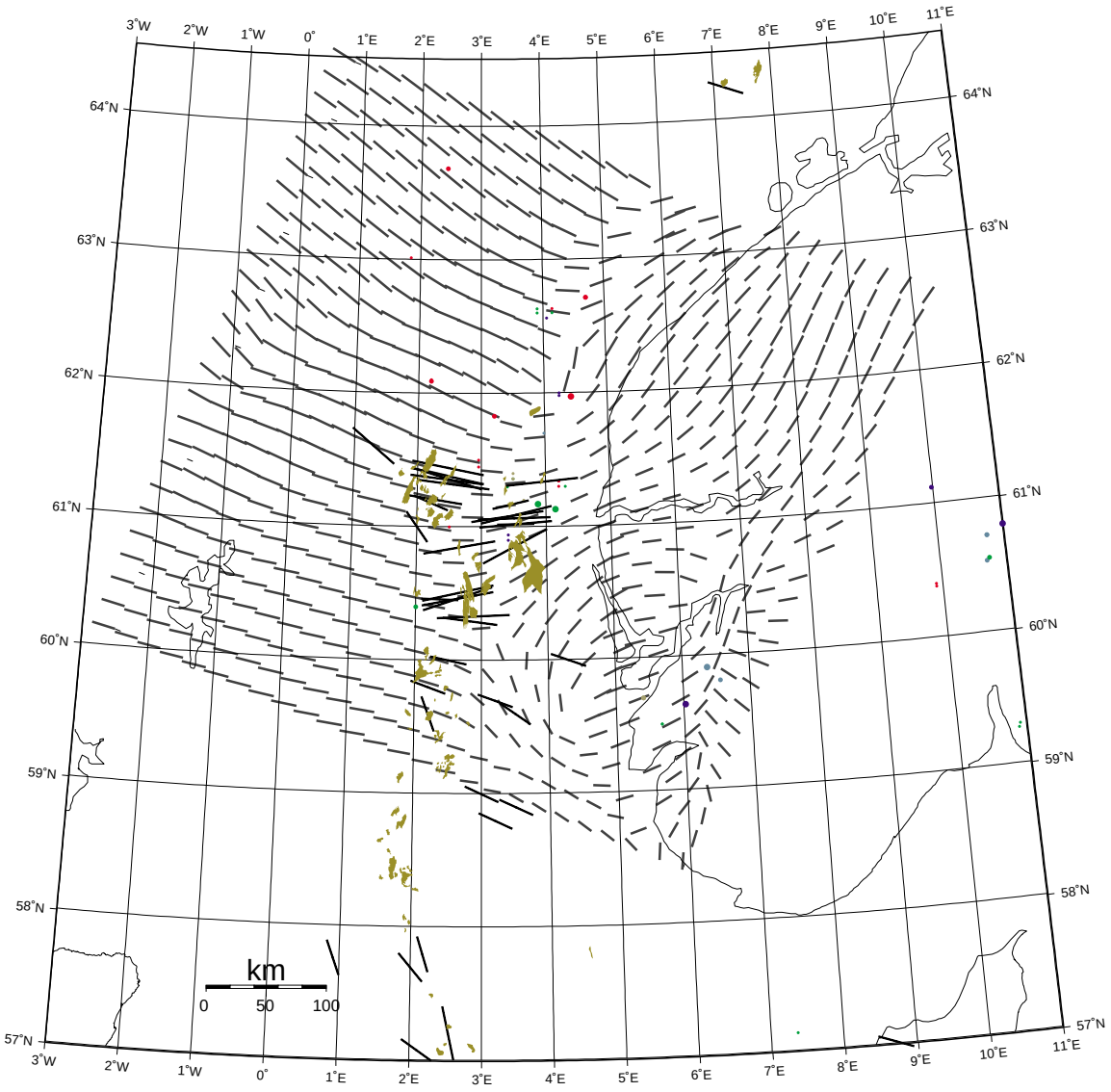

Figure 4.5: Modeled S_{Hmax} orientation for the best fitting North Sea model at a depth of 3000 m. The grey lines show the modeled results of S_{Hmax} which can be compared to the borehole measurements (black lines). The model fits the observations extremely well, suggesting that deglaciation causes the observed spatial stress variations and that the model rheology represents the lithosphere.

a)

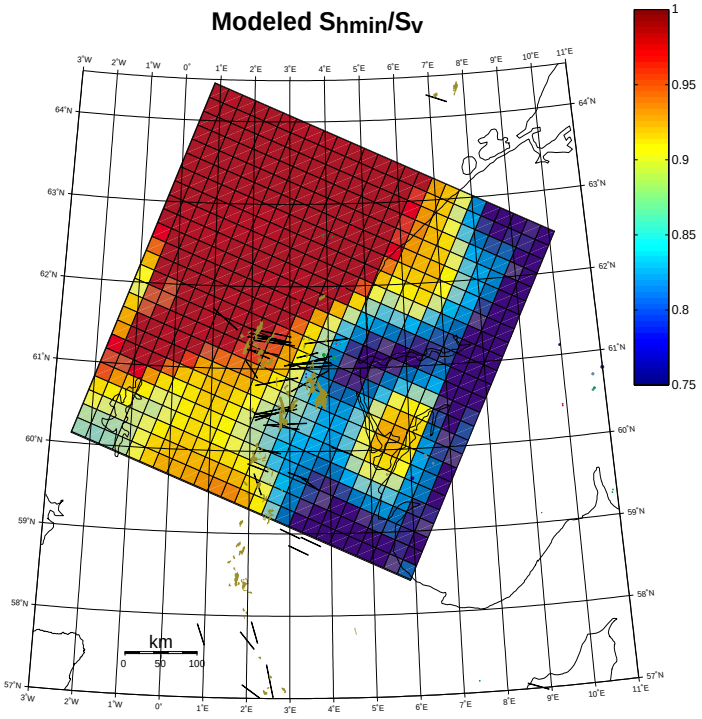

b)

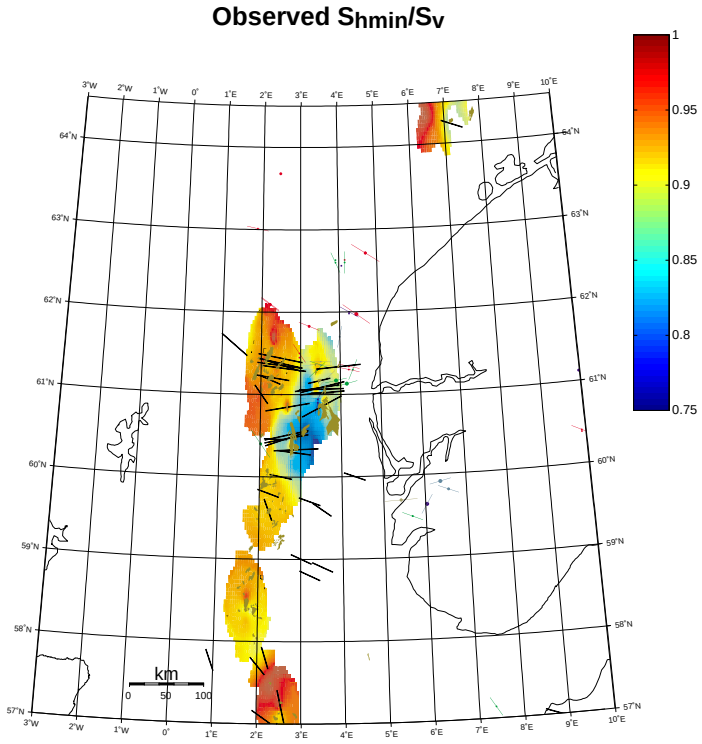

Figure 4.6: Comparison of modeled and observed S_{hmin}/S_v. Figure a) shows the modeled S_{hmin}/S_v for the best-fitting model at a depth of 3000 m. Figure 4.6b shows observed S_{hmin}/S_v from leak off tests for comparison. The model reproduces the observed drop of S_{hmin}/S_v towards the coast and is also able to capture the spatial variations of S_{hmin}/S_v.

Figure 4.6 compares the model results to observed least horizontal stress data. Largely, modeled and observed S_{hmin}/S_v are high at distances > 100 km from the coast and decrease towards the coast. However, south of 61ºN the geometry of the maximum ice sheet extent complicates the spatial stress pattern as S_{hmin}/S_v is < 1 even at large distances from the coastline. More specifically, around 61ºN modeled S_{hmin}/S_v drop from unity at 2ºE to 0.75 at 4.5ºE which roughly agrees with the observations. More to the south, at approximately 60.5ºN the model along with the observations show that the zone of decreased S_{hmin}/S_v reaches as far west as 2ºE. South of 60ºN the model suggests that S_{hmin}/S_v starts to drop around 2.5ºE which agrees with the observations. As for the S_{Hmax} orientations, the model fit to the S_{hmin}/S_v observations is satisfactory in that the model is able to roughly capture the pattern of spatial variations as well as the magnitudes of stress. Importantly, S_{hmin}/S_v values are high where the azimuth of S_{Hmax} is greater than 90º but lower S_{hmin}/S_v coincide with S_{Hmax} orientations that tend to have an azimuth smaller than 90º. This correlation between S_{Hmax} orientations with respect to the coast and stress magnitudes could be used to qualitatively asses stress magnitudes for areas where only S_{Hmax} orientations are available.

Influence of chosen lower crust and lithospheric mantle viscosities

In order to find the viscosity values which lead to the best fitting model, as described in the previous section, I had to search the parameter space by testing a variety of viscosity values until a satisfactory match between the model results and the stress observations was achieved. I varied the lower crustal viscosity (η_{lc}) from 10^{21} Pa s to 10^{23} Pa s, and the lithospheric mantle viscosity (η_{lm}) from 10^{21} Pa s to 10^{24} Pa s, testing most of the possible combinations between η_{lc} and η_{lm}. Additionally, I considered two models with no lithospheric mantle (only one viscoelastic layer below the upper crust), and another model assuming purely elastic behavior throughout the lithosphere.

Figure 4.7: (next pages) Modeled S_{Hmax} orientation for North Sea models with varying viscosities. The grey lines show the modeled results of S_{Hmax} which can be compared to the borehole measurements (black lines). For all these models we assumed the "reference" ice evolution as described in Section 4.3.2.

a)

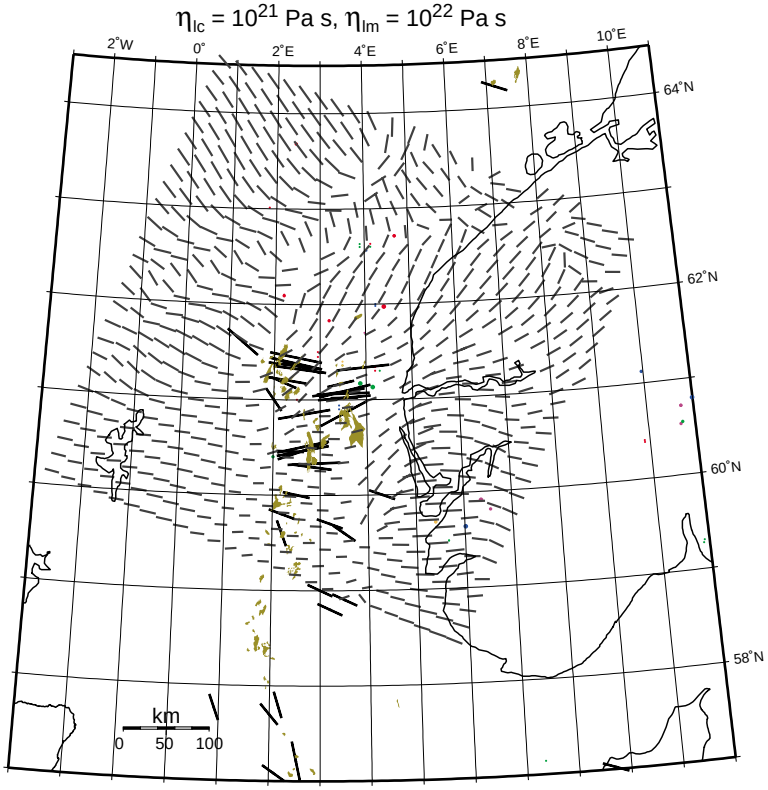
$\eta_{lc} = 10^{21}$ Pa s, $\eta_{lm} = 10^{22}$ Pa s
2°W
0°
2°E
4°E
6°E
8°E
10°E
64°N
62°N
60°N
58°N
km
0 50 100

b)

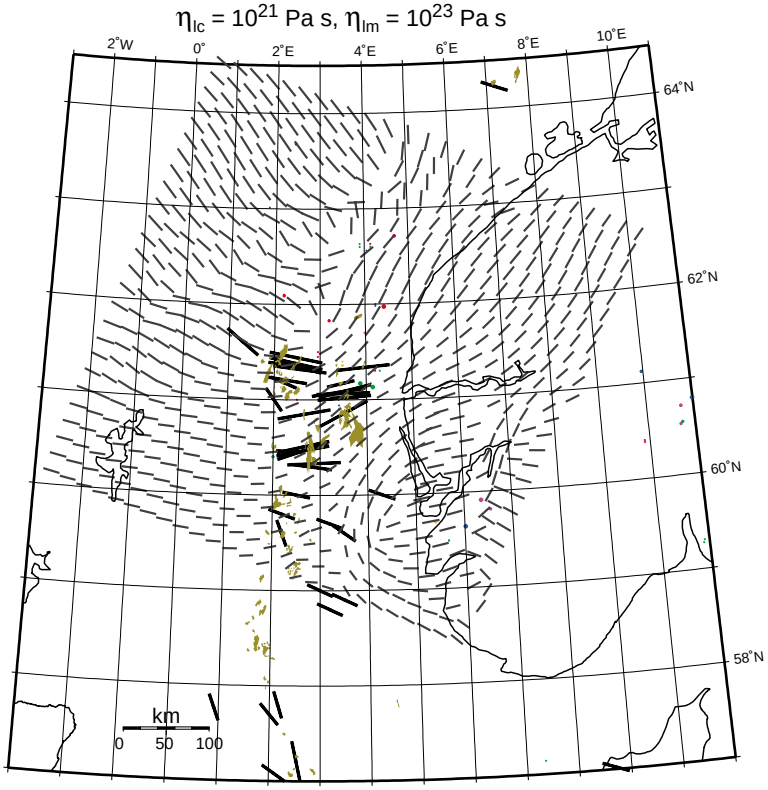
$\eta_{lc} = 10^{21}$ Pa s, $\eta_{lm} = 10^{23}$ Pa s
2°W
0°
2°E
4°E
6°E
8°E
10°E
64°N
62°N
60°N
58°N
km
0 50 100

c)

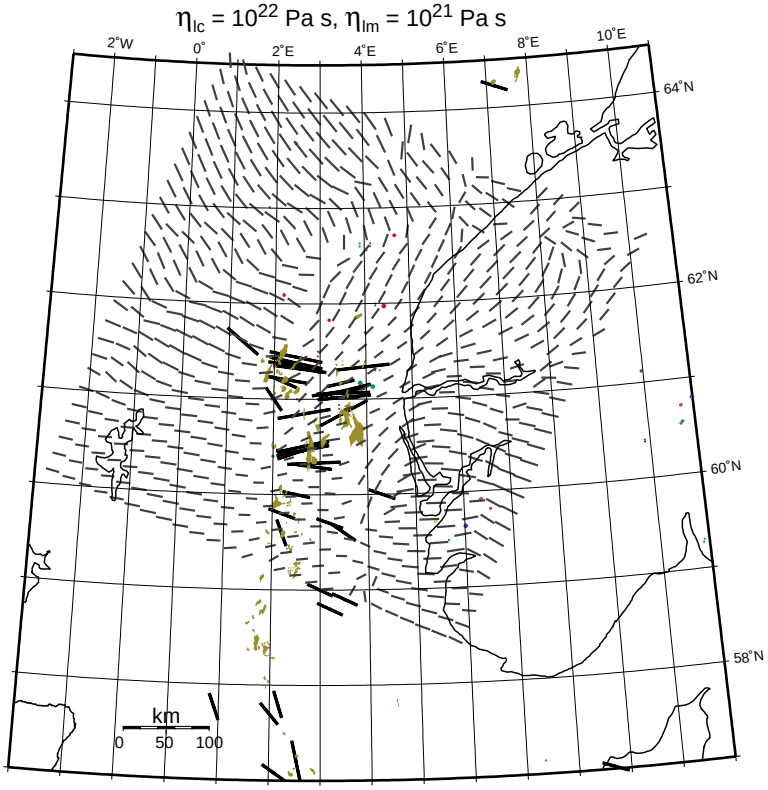
η_{lc} = 10^{22} Pa s, η_{lm} = 10^{21} Pa s
2°W
0°
2°E
4°E
6°E
8°E
10°E
64°N
62°N
60°N
58°N
km
0 50 100

d)

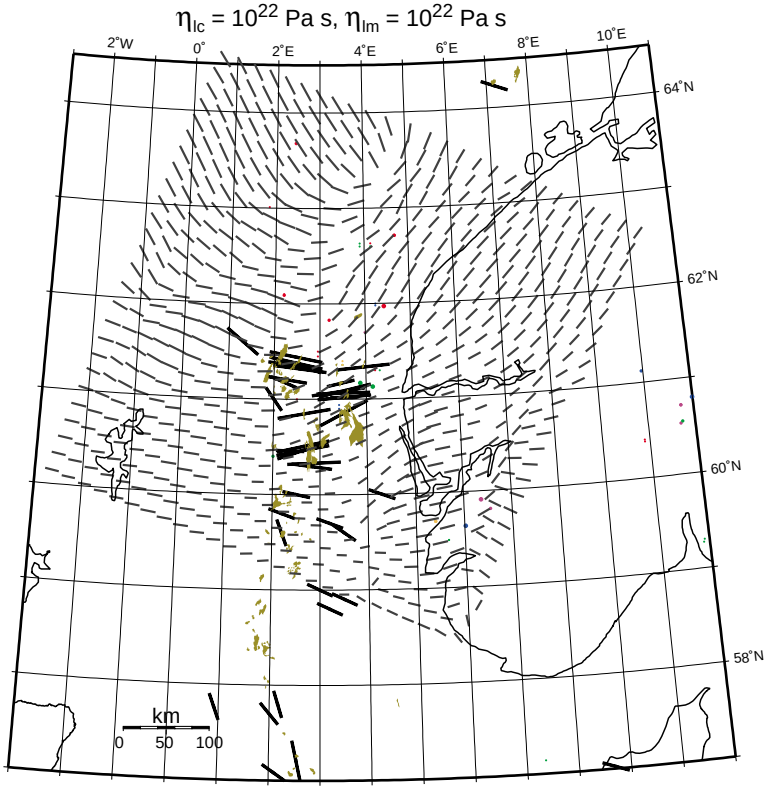
η_{lc} = 10^{22} Pa s, η_{lm} = 10^{22} Pa s
2°W
0°
2°E
4°E
6°E
8°E
10°E
64°N
62°N
60°N
58°N
km
0 50 100

e)

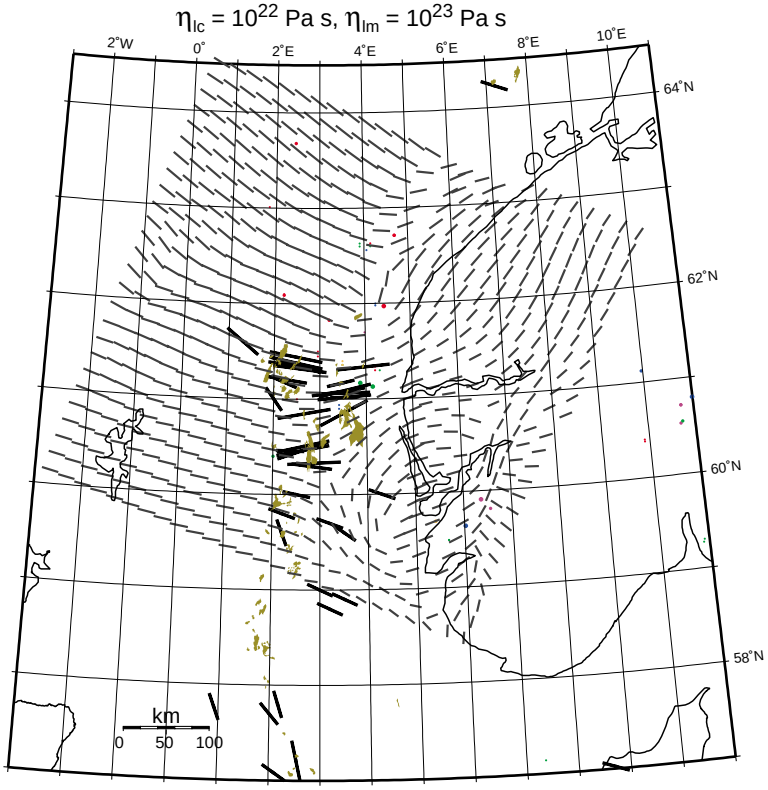
η_{lc} = 10^{22} Pa s, η_{lm} = 10^{23} Pa s
2°W
0°
2°E
4°E
6°E
8°E
10°E
64°N
62°N
60°N
58°N
km
0 50 100

f)

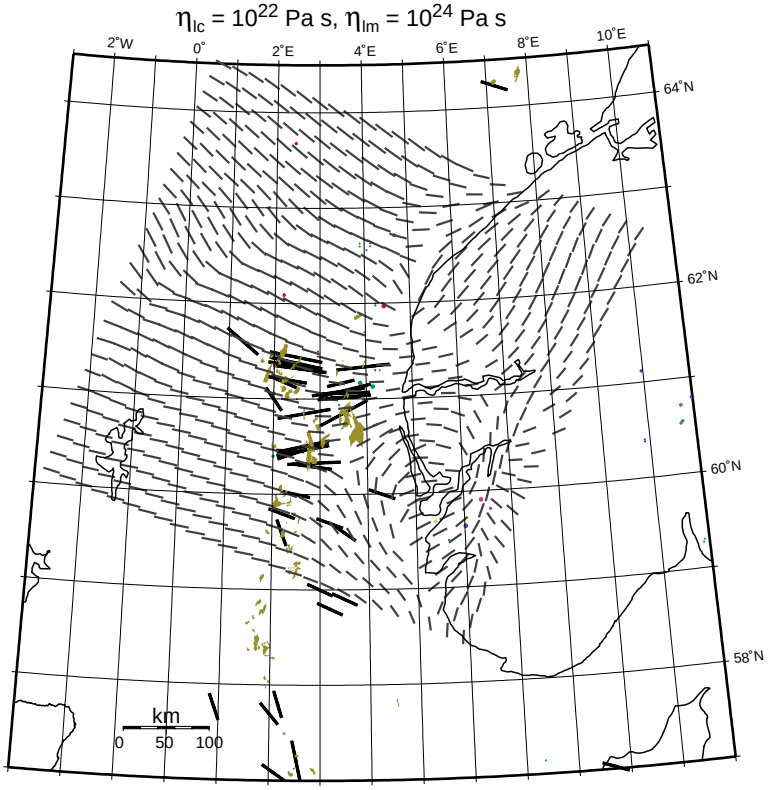
η_{lc} = 10^{22} Pa s, η_{lm} = 10^{24} Pa s
2°W
0°
2°E
4°E
6°E
8°E
10°E
64°N
62°N
60°N
58°N
km
0 50 100

g)

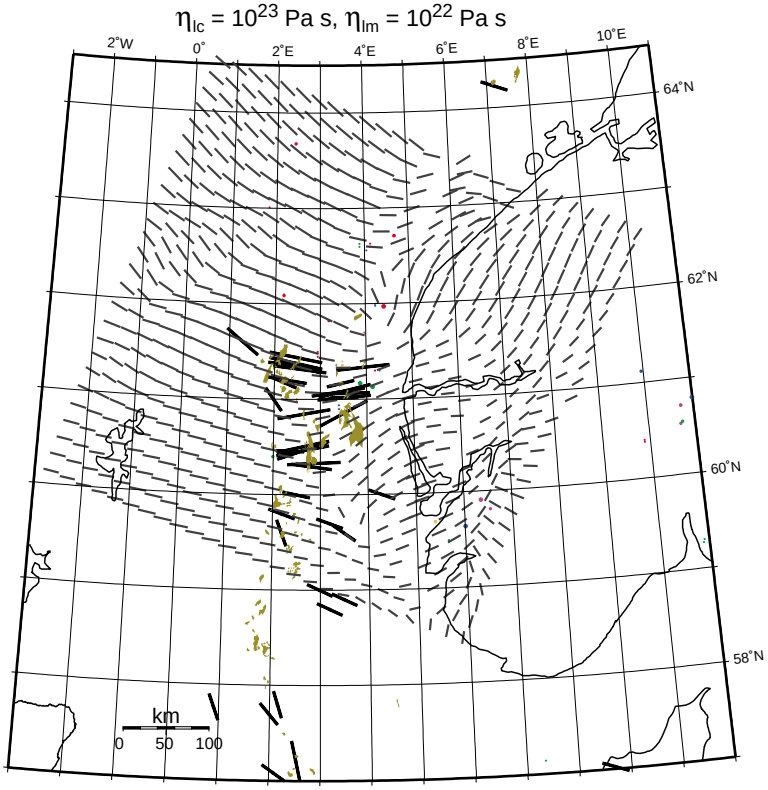
η_{lc} = 10^{23} Pa s, η_{lm} = 10^{22} Pa s
2°W
0°
2°E
4°E
6°E
8°E
10°E
64°N
62°N
60°N
58°N
km
0 50 100

h)

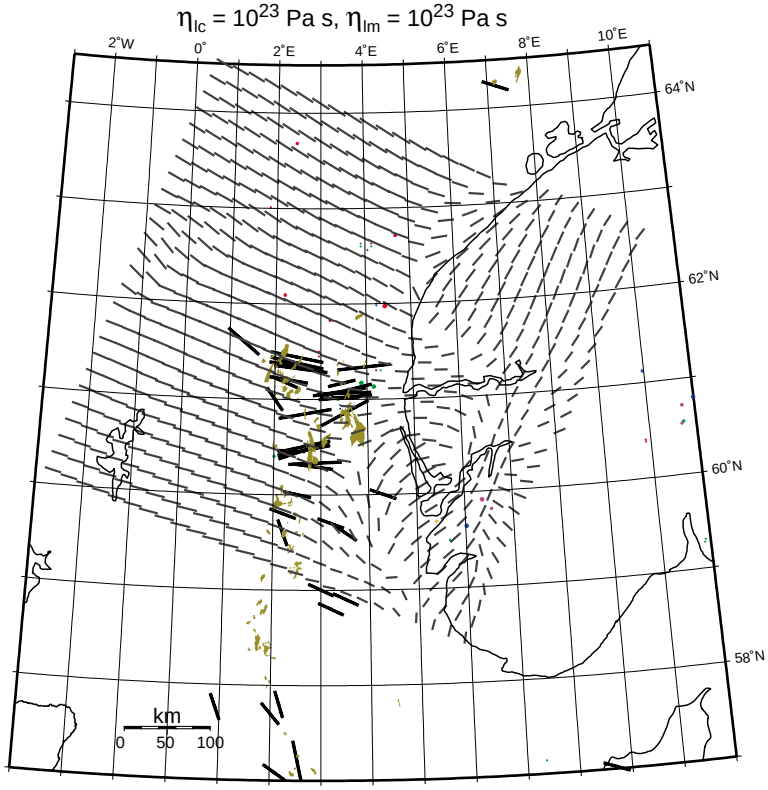
η_{lc} = 10^{23} Pa s, η_{lm} = 10^{23} Pa s
2°W
0°
2°E
4°E
6°E
8°E
10°E
64°N
62°N
60°N
58°N
km
0 50 100

i)

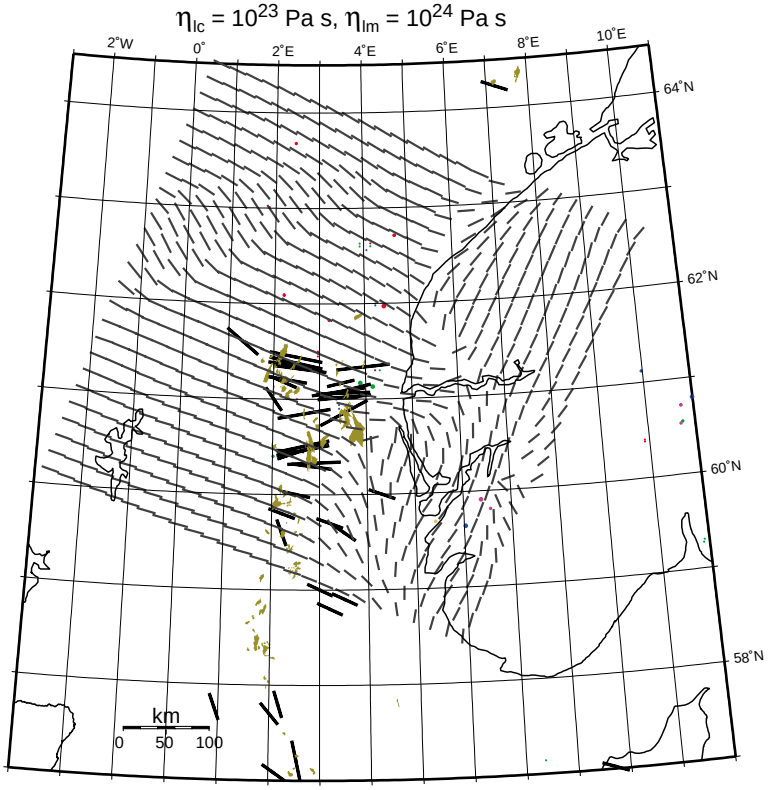

At a first glance, Figure 4.7 shows that all of the models tested predict roughly east-west striking S_{Hmax} orientations in the northern North Sea (61ºN, 3ºE) and most of the models agree that S_{Hmax} strikes approximately WNW-ESE near the three stress measurements at 59ºN and 3ºE. Furthermore, to a certain degree all models predict a clockwise rotation of S_{Hmax} towards the northwestern end of the model. However, a closer inspection reveals many differences between the model results and the well resolved S_{Hmax} observations in the northern North Sea which makes it relatively easy to pick the most appropriate viscosities.

More specifically, for low η_{lc} of 10^{21} Pa s (Figure 4.7a, and b) the S_{Hmax} orientations vary too much spatially. As a result, the model with η_{lm} of 10^{22} Pa s (Figure 4.7a) predicts S_{Hmax} orientations which differ by about 70º from the very accurate measurements at 61.4ºN, 2.5ºE (Visund) which is unacceptable. By increasing η_{lm} to 10^{23} Pa s (Figure 4.7b) the discrepancy between observations and measurements in Visund is less pronounced. However, east of the Viking Graben (around 61ºN, 4ºE) this model differs from the S_{Hmax} measurements by more than 30º. In large, for η_{lc} of 10^{21} Pa s the model with an increased η_{lm} of 10^{23} Pa s seems to be more appropriate than the model with η_{lm} of 10^{22} Pa s as the spatial stress changes seem to occur over reasonable distances. Yet, both models do not achieve a satisfactory fit to the observed S_{Hmax} orientations.

An increased η_{lc} of 10^{22} Pa s (Figure 4.7c, d, e, f) greatly improves the model match. Especially, the model with a η_{lm} of 10^{23} Pa s (Figure 4.7e) fits the S_{Hmax} data almost perfectly and is described in the previous section (best-fitting North Sea model). For the same η_{lc} but with $\eta_{lm} = 10^{22}$ Pa s (Figure 4.7d) the fit is still better than for any model with η_{lc} of 10^{21} Pa s but the modeled S_{Hmax} orientations in the northern North Sea miss the observations by ≈20°. By further decreasing η_{lm} to 10^{21} Pa s (Figure 4.7c) the fit gets even worse and is very similar to the model with $\eta_{lc} = 10^{21}$ Pa s and $\eta_{lm} = 10^{22}$ Pa s (Figure 4.7a). The similarity between the results of these two models, which are almost identical except for the interchanged η_{lc} and η_{lm}, suggests that the sequence of the viscosity-layering is irrelevant. By increasing η_{lm} from the best-fitting model to 10^{24} Pa s (Figure 4.7f) the model roughly catches the spatial stress variations but shows slight discrepancies, e.g. at 61°N, 4°E and the spatial stress changes seem to occur over too long distances suggesting that the viscosities are too high.

For an even higher η_{lc} of 10^{23} Pa s (Figure 4.7g, h and i) the model nicely fits the S_{Hmax} observations, assuming that $\eta_{lm} = 10^{22}$ Pa s. In fact, the predictions of this model are almost identical to the best-fitting model, which confirms that the sequence of the viscosity-layering is irrelevant, i.e. as long as one viscoelastic layer has a viscosity of 10^{22} Pa s and the other viscoelastic layer has a viscosity of 10^{23} Pa s the model perfectly mimics the observed stress field. For a higher η_{lm} of 10^{23} Pa s in combination with $\eta_{lc} = 10^{23}$ Pa s (Figure 4.7h) the model is unable to fully catch the observed spatial stress variations because the stresses do not vary enough spatially. For an even higher η_{lm} of 10^{24} Pa s (Figure 4.7i) the model predicts an almost constant WNW striking S_{Hmax} orientation throughout the northern North Sea which clearly does not reflect the measurements.

Most previous studies of glacial rebound (e.g. Wu et al., 1999) considered a purely elastic lithosphere, ignoring the possibility of permanent intra-lithospheric deformation. This is a good assumption for the purpose of modeling uplift data, because permanent deformation within the lithosphere is much smaller than below the lithosphere, which makes uplift data insensitive to intra-lithospheric viscous processes. To test the validity of this assumption for the purpose of modeling stress changes resulting from lithospheric flexure in Fennoscandia, I ran a model with extremely high viscosities ($\eta_{lm} = \eta_{lc} = 10^{26}$ Pa s) so the modeled lithosphere behaves essentially purely elastic. The resulting stress orientations (shown in Figure 4.8) achieve a very poor fit to the stress observations. For example, in the northern North Sea the modeled S_{Hmax} orientations are almost perpendicular to the measured orientations. This means that models with a purely elastic lithosphere, while being able to match uplift data, are inadequate to study stress changes associated with lithospheric flexure resulting from glacial loading and unloading.

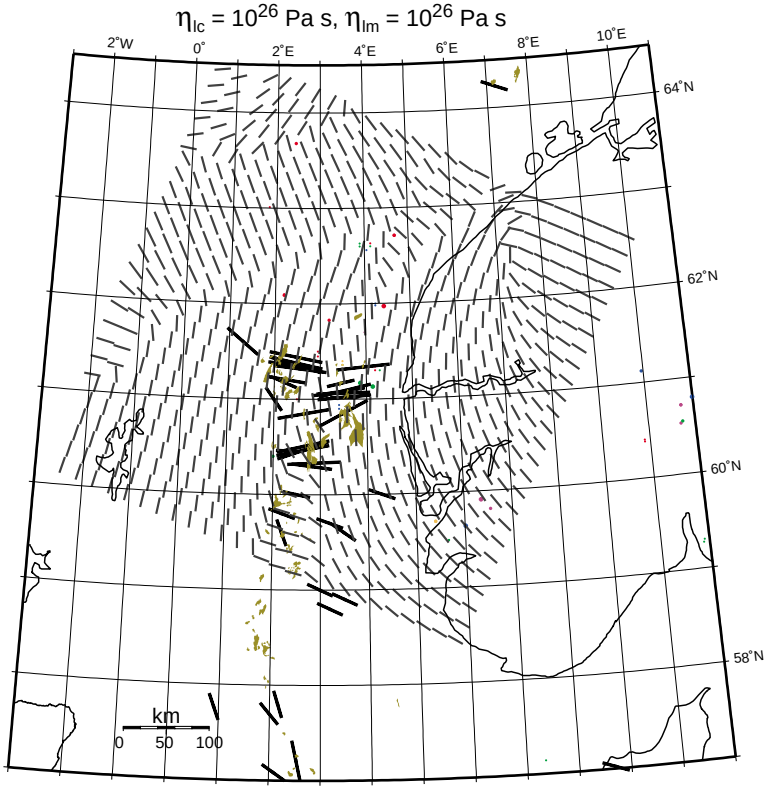

Figure 4.8: Modeled S_{Hmax} orientation for the North Sea model with a purely elastic lithosphere. The grey lines show the modeled results of S_{Hmax} which can be compared to the borehole measurements (black lines). The model shows a very poor fit to the observations.

The previously described models assumed that the upper crust is underlain by two viscoelastic layers (lower crust, and lithospheric mantle). I wanted to test whether a satisfactory fit could be achieved with just one viscoelastic layer, by omitting the lithospheric mantle. Figure 4.9a shows that the model with a single viscoelastic layer and a viscosity of 10^{22} Pa s achieves a relatively poor fit. It mismatches most of the S_{Hmax} orientations in the northern North Sea by 25º or more. Also, the measured WNW-striking S_{Hmax} in the vicinity of the Frigg field (60ºN, 2ºE) can not be explained with this model. An increased viscosity of 10^{23} Pa s (Figure 4.9b) leads to a more convincing result which matches most of the S_{Hmax} measurements within 15º. However, none of the models with a one viscoelastic layer is able to accomplish the almost perfect fit of the best-fitting model which includes two viscoelastic layers.

Figure 4.9: (next page) Modeled S_{Hmax} orientation for North Sea models with only one viscoelastic layer below the upper crust. The grey lines show the modeled results of S_{Hmax} which can be compared to the borehole measurements (black lines). The models show that a reasonable fit can be achieved but a second viscoelastic layer significantly improves the results.

a)

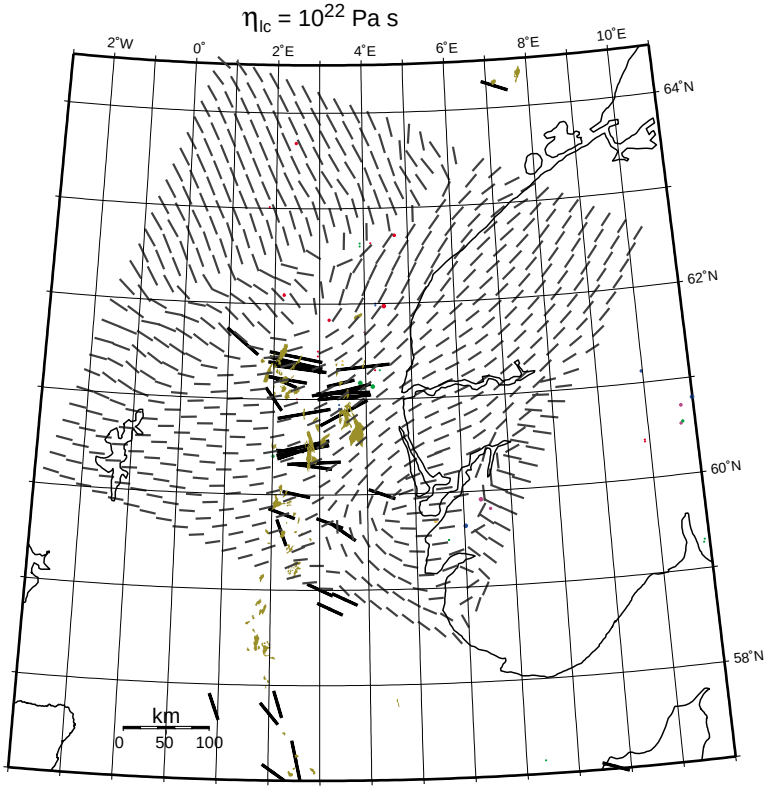
η_{lc} = 10^{22} Pa s
2°W
0°
2°E
4°E
6°E
8°E
10°E
64°N
62°N
60°N
58°N
km
0 50 100

b)

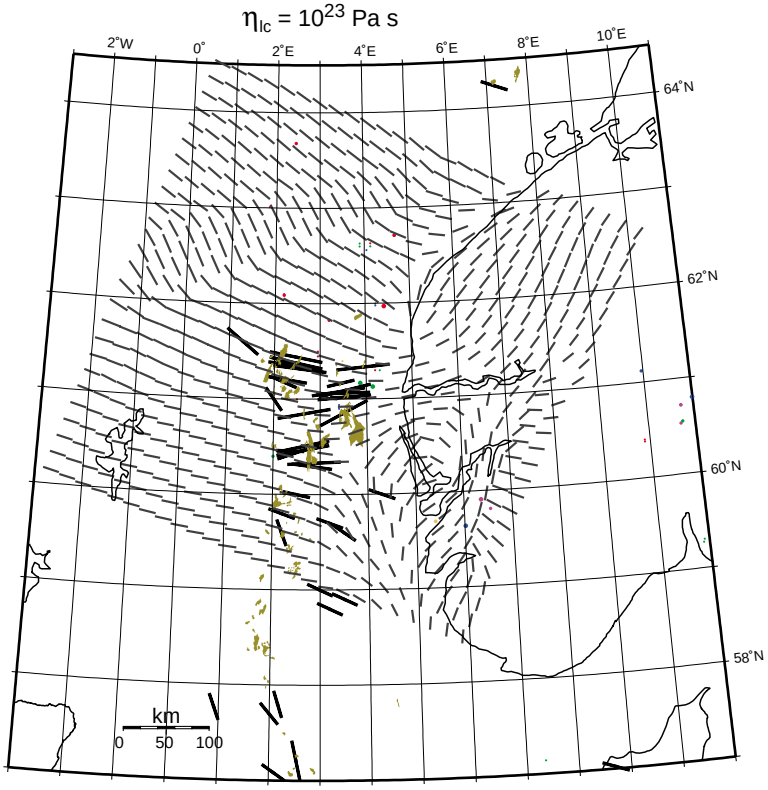
η_{lc} = 10^{23} Pa s
2°W
0°
2°E
4°E
6°E
8°E
10°E
64°N
62°N
60°N
58°N
km
0 50 100

In conclusion, by studying a wide range of lower crustal and lithospheric mantle viscosities, we obtain the best fit with the stress observations for $\eta_{lc} = 10^{22}$ Pa s and $\eta_{lm} = 10^{23}$ Pa s (or vice versa). These values correspond to the findings of Strehlau and Meissner (1987) for a wet, Variscan continental crust and agree well with lithospheric viscosity values of the western United States (Flesch et al., 2000). A model with only one viscoelastic layer achieves an acceptable fit for a viscosity of 10^{23} Pa s but the inclusion of a second viscoelastic layer improves the model results significantly. Lastly, the large misfit of the purely elastic model shows that viscoelastic behavior within the lithosphere is crucial in modeling stress changes associated with glacial loading and unloading.

Influence of chosen ice sheet evolution

As a next step, I will use the best-fitting viscosity model from the previous section to test a variety of ice sheet evolutions. The "reference" ice model that I have considered so far is the most plausible ice model but in order to understand the influence of the chosen ice history it is important to test a number of alternative ice evolutions. In addition to the reference ice model, I will test five alternative ice histories with the following characteristics (see Figure 4.10): Alternative ice model 1 is similar to the reference model but neglects the maximum ice stage between 110,000 years ago and 20,000 years ago. Ice model 2 differs from the reference model in that one million years ago the ice sheet also grows to its maximum extent and remains in this state for 200,000 years. Ice model 3 includes all the interglacials during the Weichselian cold period (starting 110,000 years ago) based on Lundqvist (1986), and during the last 15,000 years the ice sheet melts back completely before advancing to the 11,000 years and 10,000 years extents. Ice model 4 considers only the Weichselian glaciation and ignores the previous Pleistocene glaciations. According to Shackleton et al. (1984) oxygen isotope curves from deep sea drilling show a characteristic cold period duration of 10^5 years during the Pleistocene. Accordingly, I tested ice model 5 which includes pre-Weichselian ice loading cycles with a periodicity of 10^5 years. I have already used ice model 5 in Chapter 3 to test the influence of the chosen ice history on the two-dimensional northern North Sea model.

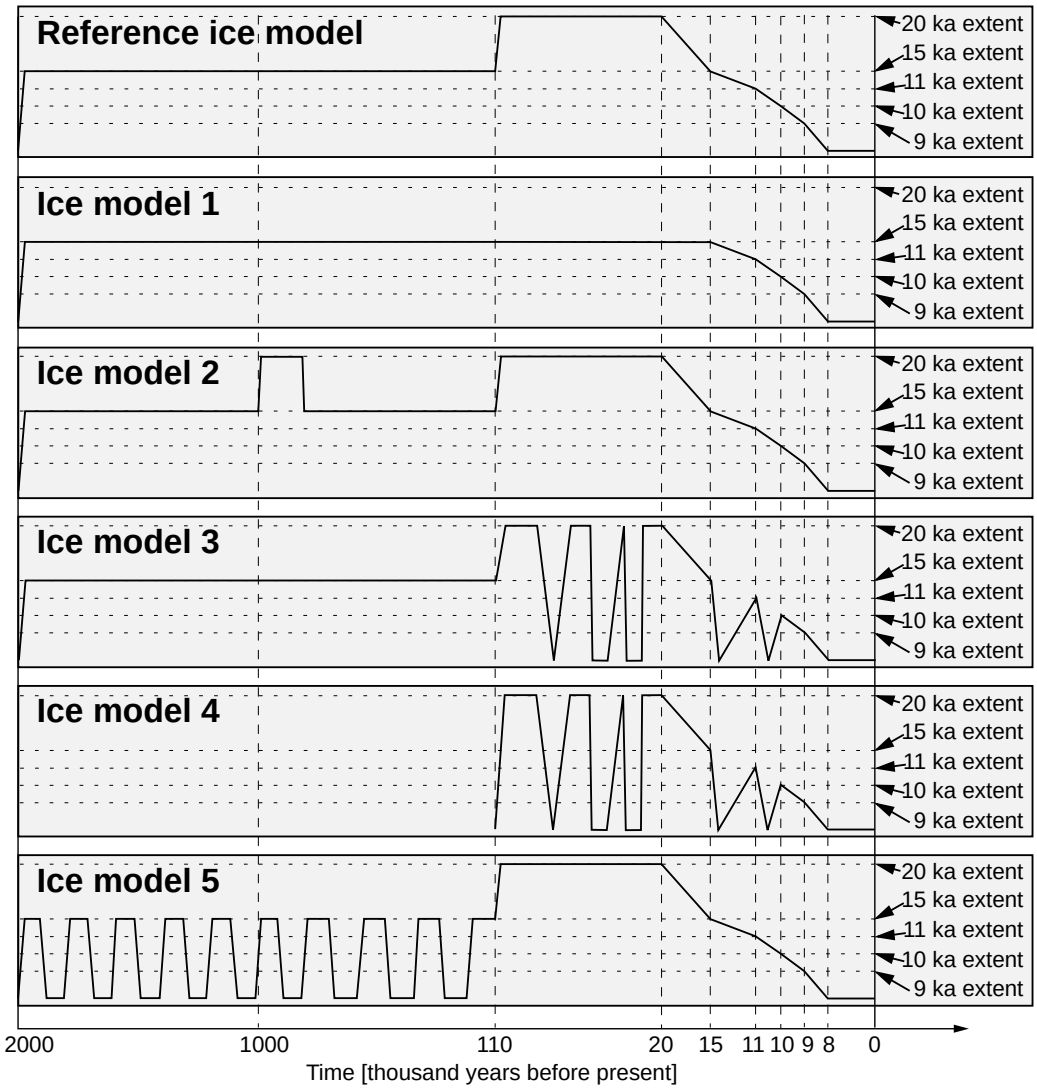

Figure 4.10: Temporal change of ice extent for different ice models.

a)

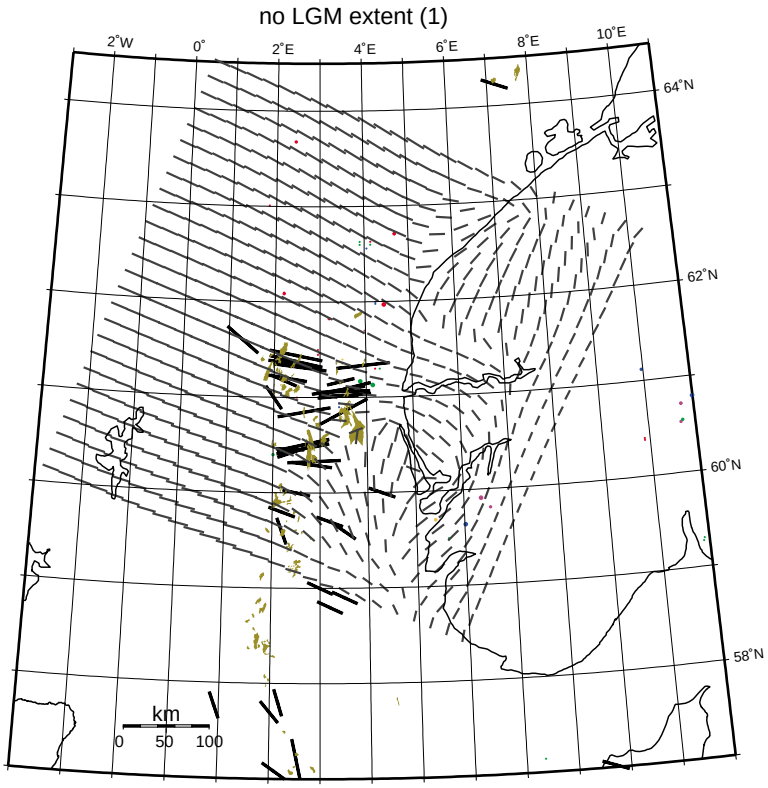
no LGM extent (1)
2°W
0°
2°E
4°E
6°E
8°E
10°E
64°N
62°N
60°N
58°N
km
0
50
100

b)

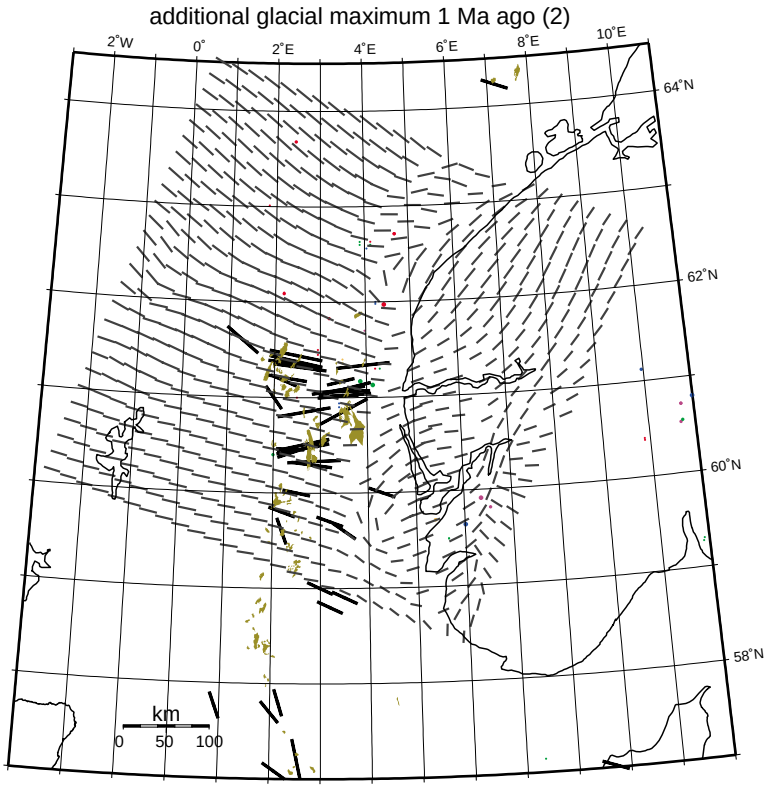
additional glacial maximum 1 Ma ago (2)
2°W
0°
2°E
4°E
6°E
8°E
10°E
64°N
62°N
60°N
58°N
km
0
50
100

c)

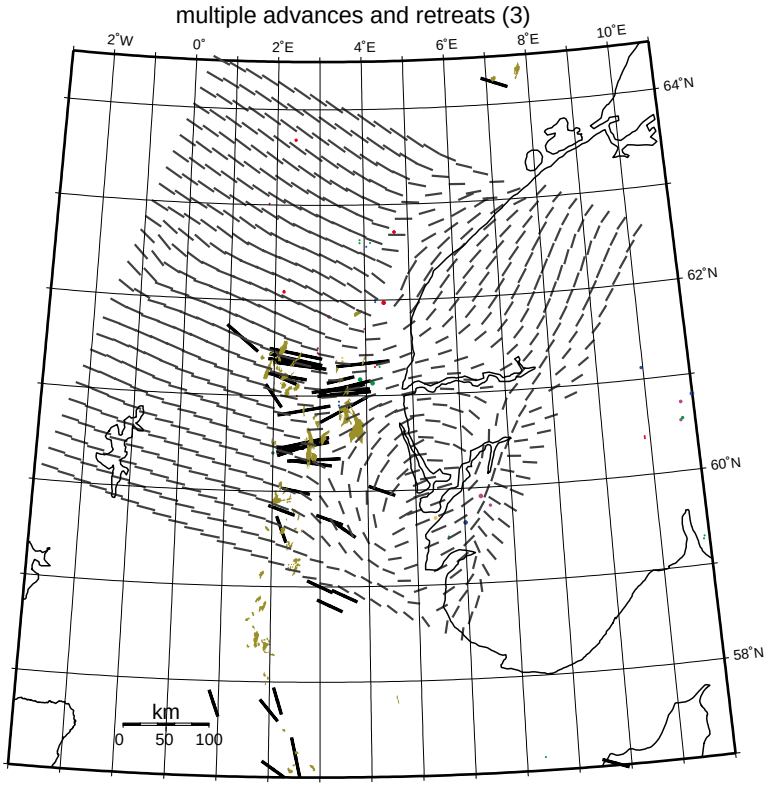
multiple advances and retreats (3)
2°W
0°
2°E
4°E
6°E
8°E
10°E
64°N
62°N
60°N
58°N
km
0
50
100

d)

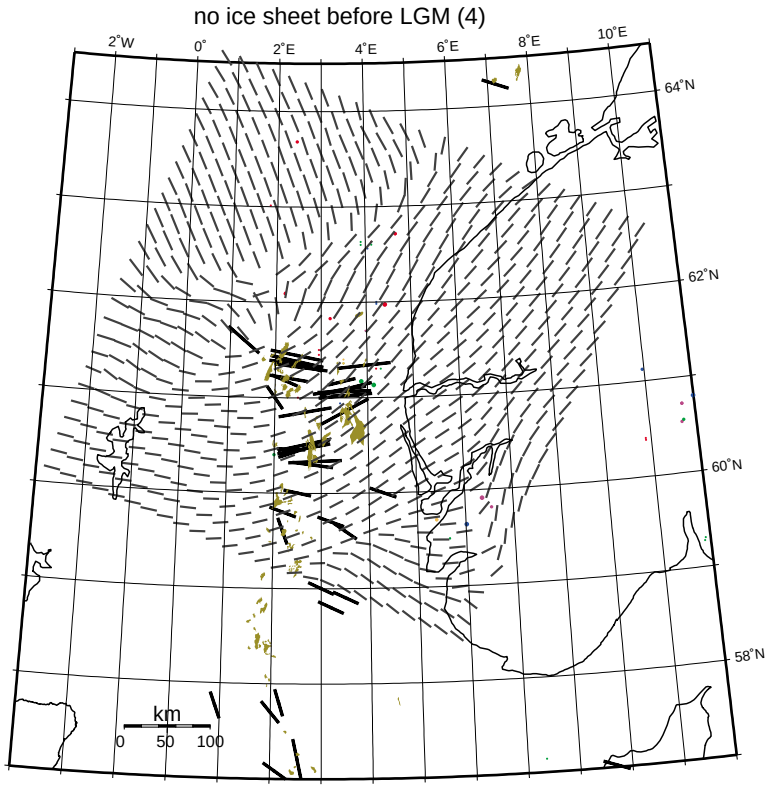
no ice sheet before LGM (4)
2°W
0°
2°E
4°E
6°E
8°E
10°E
64°N
62°N
60°N
58°N
km
0
50
100

e)

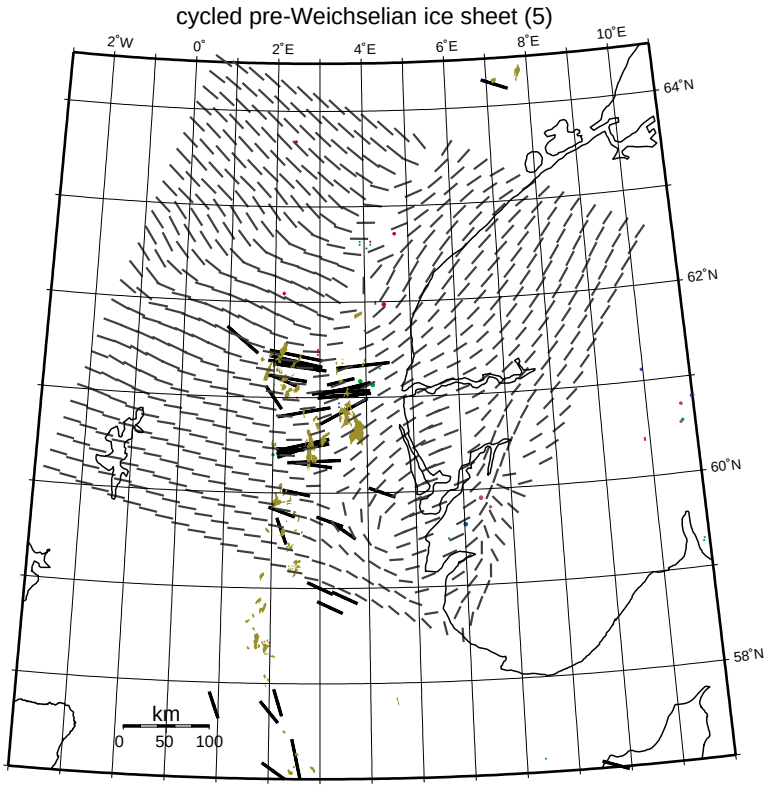

Figure 4.11: (also previous pages) Modeled S_{Hmax} orientation for North Sea models with varying ice sheet evolutions. The grey lines show the modeled results of S_{Hmax} which can be compared to the borehole measurements (black lines).

Figure 4.11 shows the results of the North Sea model with different ice histories. By assuming that the ice sheet never reached its maximum extent for a significant duration (ice model 1) the model roughly fits the data (Figure 4.11a) but modeled S_{Hmax} orientations in the northern North Sea deviate up to 20º from the measurements. In comparison, ice model 2 (Figure 4.11b) achieves a slightly better fit but still does not reproduce the observed stress field appropriately, i.e. around 61ºN, 3.5ºE the modeled S_{Hmax} orientation is ESE but the observations shows a ENE striking S_{Hmax}. As ice models 1 and 2 obtain worse results than the reference ice model, we can put bounds on the plausible duration of the maximum ice extent. On one hand, the ice sheet must have reached its maximum extent for several tens of thousands of years or else ice model 1 would achieve a better fit. On the other hand, the ice sheet could not have remained at its maximum stage for longer than approximately 200,000 years or else ice model 2 would achieve a better fit than the reference ice model.

The results of ice model 3 (Figure 4.11c) match the observations very well. In fact, they are hardly distinguishable from the best-fitting model (using the reference ice model) which implies that the fast growth and retreat cycles during the Weichselian, as considered

by ice model 3, hardly affect the present-day model predictions. Ice model 4 gives a very poor fit to the S_{Hmax} observations (Figure 4.11d), i.e. in the area of interest, the modeled S_{Hmax} orientations are rotated counterclockwise by up to 40° from the observations. Accordingly, we conclude that the ice sheet must have remained at the 15,000 years extent during large portions of the Pleistocene or else ice model 4 could also achieve an acceptable fit. Ice model 5 tests the importance of the 15,000 years extent by loading the ice sheet in cycles throughout the pre-Weichselian Pleistocene. Figure 4.11e shows that ice model 5 achieves almost the same fit to the measured S_{Hmax} orientations like the reference ice model. Thus, exact pre-Weichselian variations of the ice sheet are irrelevant for the purpose of modeling the present-day stress field in the North Sea as long as the ice sheet remains in its 15,000 years extent for an accumulated time of ≈1 Million years (as in ice model 5) or possibly even less.

The model results and their dependence on different ice histories is governed by the characteristic relaxation times of the viscoelastic layers. According to Nadai (1963) the characteristic relaxation time (τ) assuming Maxwell viscoelasticity is defined as $3\eta/E$ (the exact definition varies between authors). Using Nadai's definition our best-fitting North Sea model has a characteristic lower crustal relaxation time (τ_{lc}) of 13,400 years and the lithospheric mantle has a relaxation time (τ_{lm}) of 95,000 years.

These relaxation times explain why the relatively short term Weichselian ice sheet fluctuations in ice model 3 hardly affect the model results because none of the viscoelastic layers has enough time to undergo considerable viscous deformation. Conversely, the results of ice model 2 strongly differ from the findings of the reference ice model because the additional maximum ice extent lasted for more than twice the τ_{lm}. However, ice model 1 shows that not loading the ice sheet to its maximum extent results in a relatively poor fit as well. So the best fit is achieved by loading the maximum ice extent for longer than τ_{lc} but not more than τ_{lm}. Ice model 5 gives results analogous to the reference ice model because the pre-Weichselian ice sheet has an accumulated existence of 1 Ma which is much longer than τ_{lm}. In other words, it does not matter whether the pre-Weichselian ice sheet has an accumulated existence of 1 Ma (ice model 5) or 2 Ma (reference ice model) because most of the viscous response occurs in ≈100,000 years.

In conclusion, to model the present-day stress field in the North Sea, a model of glacial loading and unloading has to include a pre-Weichselian ice sheet in the 15ka extent which lasts at least for the relaxation time of the highest viscosity layer. At some point in its history the ice sheet must have grown to its maximum extent and remained there for longer than τ_{lc} but less than τ_{lm}. The short term ice fluctuations on the order of several thousand years do not significantly influence the results.

Influence of chosen initial stress state (ridge push)

As mentioned in the introduction (Section 4.2), the stress field in northwestern Europe is believed to be the result mainly of ridge push. Gölke et al. (1996) suggested that the generally northwest-striking S_{Hmax} observations offshore Norway result from ridge push and its interaction with a heterogeneous crustal structure. To test how a possible influence of ridge push would affect our predictions of S_{Hmax} orientations, we used the best-fitting North Sea model but instead of starting with an isotropic stress state according to Equation 4.2, we prestressed the upper crust such that it was critically stressed according to the Mohr Coulomb failure criterion, as described in Equation 4.1. The finding of Parsons and Richter (1980) that the available net force from ridge push (F_R) approaches $\approx 3 \times 10^{12}$ Nm^{-1} at a sufficiently large distance from the ridge serves as an additional constraint of the initial stress state. For our model this means that F_R has to satisfy the following condition (according to England and Houseman, 1986):

$$\mathbf{F_R} = \int_{\mathbf{uc}} (\sigma_1 - \sigma_3)\mathbf{dz} \qquad \text{Eqn. 4.4}$$

As the differential stress (σ_1-σ_3) is increasing monotonically with depth, Equation 4.4 can be linearized, so

$$\mathbf{F_R} = \frac{1}{2}(\sigma_{1\mathbf{uc}} - \sigma_{3\mathbf{uc}})\mathbf{T_{uc}} \qquad \text{Eqn. 4.5}$$

where T_{uc} is the thickness of the upper crust, and σ_{1uc} and σ_{3uc} are the effective stresses at the bottom of the upper crust. By adding the Mohr Coulomb criterion as an additional constraint, σ_{3uc} can be calculated for a given F_R, and μ with Equation 4.6:

$$\sigma_{3\mathbf{uc}} = \frac{2\mathbf{F_R}}{\mathbf{T_{uc}}([\sqrt{\mu^2 + 1} + \mu]^2 - 1)} \qquad \text{Eqn. 4.6}$$

Equation 4.6 yields that for $F_R = 3 \times 10^{12}$ Nm^{-1}, $\mu = 0.6$, $T_{uc} = 20$ km, and our chosen upper crustal density of 2700 kg/m^3, $S_3/S_v = 0.64$ and $S_1/S_v = 1.2$ assuming a hydrostatic pore pressure throughout the upper crust. We ran a model analogous to the best-fitting North Sea model but using the initial stress state as described above, and with the initial S_1 striking parallel to the southwest edge of the model (roughly perpendicular to the coast line). The results of this model in terms of S_{Hmax} orientations are shown in Figure 4.12.

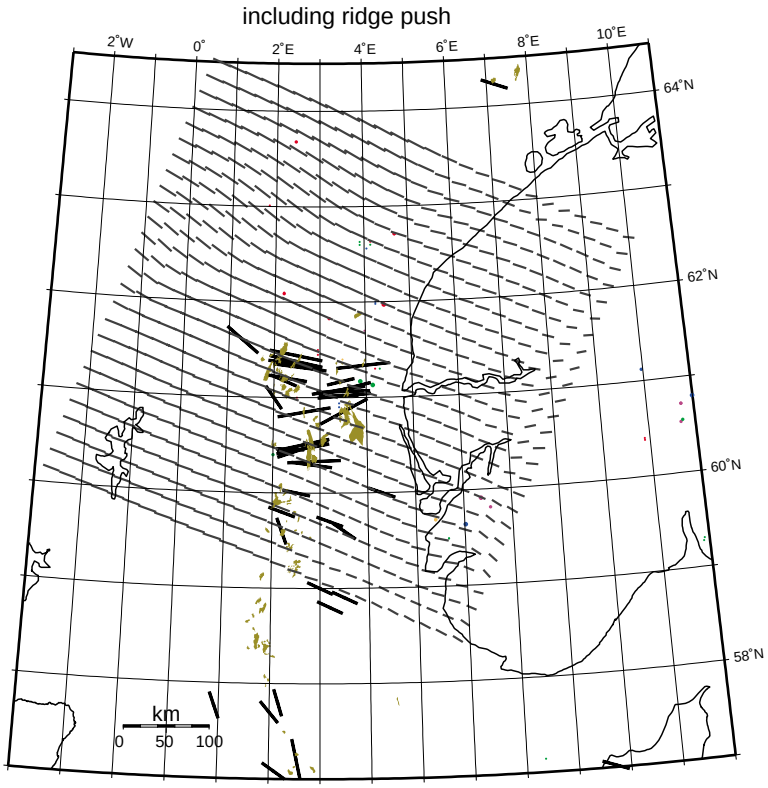

Figure 4.12: Modeled S_{Hmax} orientation for the North Sea model assuming that ridge push significantly influences the stress field in the North Sea. The grey lines show the modeled results of S_{Hmax} which can be compared to the borehole measurements (black lines).

By including ridge push, the predicted S_{Hmax} orientations hardly vary laterally which is in contrast to the measurements. The mismatch between this model and the S_{Hmax} measurements suggests that ridge push might not be a significant stress contributor in the northern North Sea, or at least in the area with the best coverage of S_{Hmax} measurements.

Our method of including ridge push makes two critical assumptions: First, we assume that the entire net force created by ridge push is stored in the upper crust, i.e. no differential stress exists in the lower crust or the lithospheric mantle. However, for high enough strain rates on the order of 10^{-14} s^{-1} even the ductile parts of the lithosphere can carry an appreciable amount of differential stress (e.g. Carter and Tsenn, 1987). As a consequence of this first assumption, our approach tends to overestimate the importance of ridge push in creating differential stress in the upper crust. Second, by simply adding the ridge push stresses to the initial stress state we are ignoring the fact that ridge push is a renewable stress source (Bott and Kusznir, 1984). This second assumption tends to underestimate the contribution of ridge push to the upper crustal stress state. As the errors associated with the

two assumptions have opposite signs they tend to eliminate each other.

So why does the stress field in the northern North Sea seem to be unaffected by ridge push? There are several possible explanations. For example, a relatively weak formation below the northern North Sea might decouple the overlying units from the ridge push forces. This is very unlikely, as such a layer has never been encountered by any of the numerous wells in the area. Further, the so called "spreading stresses" which result from the density contrast between the light continental crust and the denser oceanic crust (Artyushkov, 1973), might mask the ridge push stresses in the northern North Sea by reducing the margin perpendicular stress. Lastly, by modeling the interaction between ridge push and the heterogeneous crustal structure Gölke and Coblentz (1996) predict that ridge push leads to a very small horizontal stress anisotropy in most of the area that is covered by our North Sea model. So, maybe the crustal structure "deflects" the ridge push force such that it does not cause any horizontal stress anisotropy in the northern North Sea and thus the stress observations fully reflect the stress perturbation caused by glacial loading and unloading.

4.3.3 Modeling the in-situ stress field on the Mid-Norwegian Margin (the 'Mid-Norway model')

The previous sections showed that observed stresses in the northern North Sea can be explained with the bending of the lithosphere as a result of growing and retreat of the Fennoscandian ice shield. In order to obtain a best fit to the stress observations, we calibrated the model by adjusting the viscosity structure of the lithosphere and testing a variety of ice models. Assuming that the viscosity structure is more or less constant along the Norwegian coast, we should now be able to use the viscosities obtained from the North Sea model to match the stress observations on the Mid-Norwegian Margin equally well. In other words, we can use the Mid-Norway model as a 'blind test' for the model parameters that we obtained from calibrating the North Sea model.

The spatial extent of the Mid-Norway model is displayed in Figure 4.2 and corresponds to an area of 398,000 km^2. The model measures 648.5 km in the northwest-southeast direction and 613.4 km in the northeast-southwest direction and each element is 25.94 km by 24.54 km in size. The number of elements, their extent with depth, and the lithospheric rheology is identical to the best-fitting North Sea model (Figure 4.3 and Table 4.1) with $\eta_{lc} = 10^{22}$ Pa s, and $\eta_{lm} = 10^{23}$ Pa s. Like the North Sea model, the area of interest of the Mid-Norway model as outlined in Figure 4.2 is surrounded by a 300 km wide zone made of 5,400 elements to avoid boundary effects.

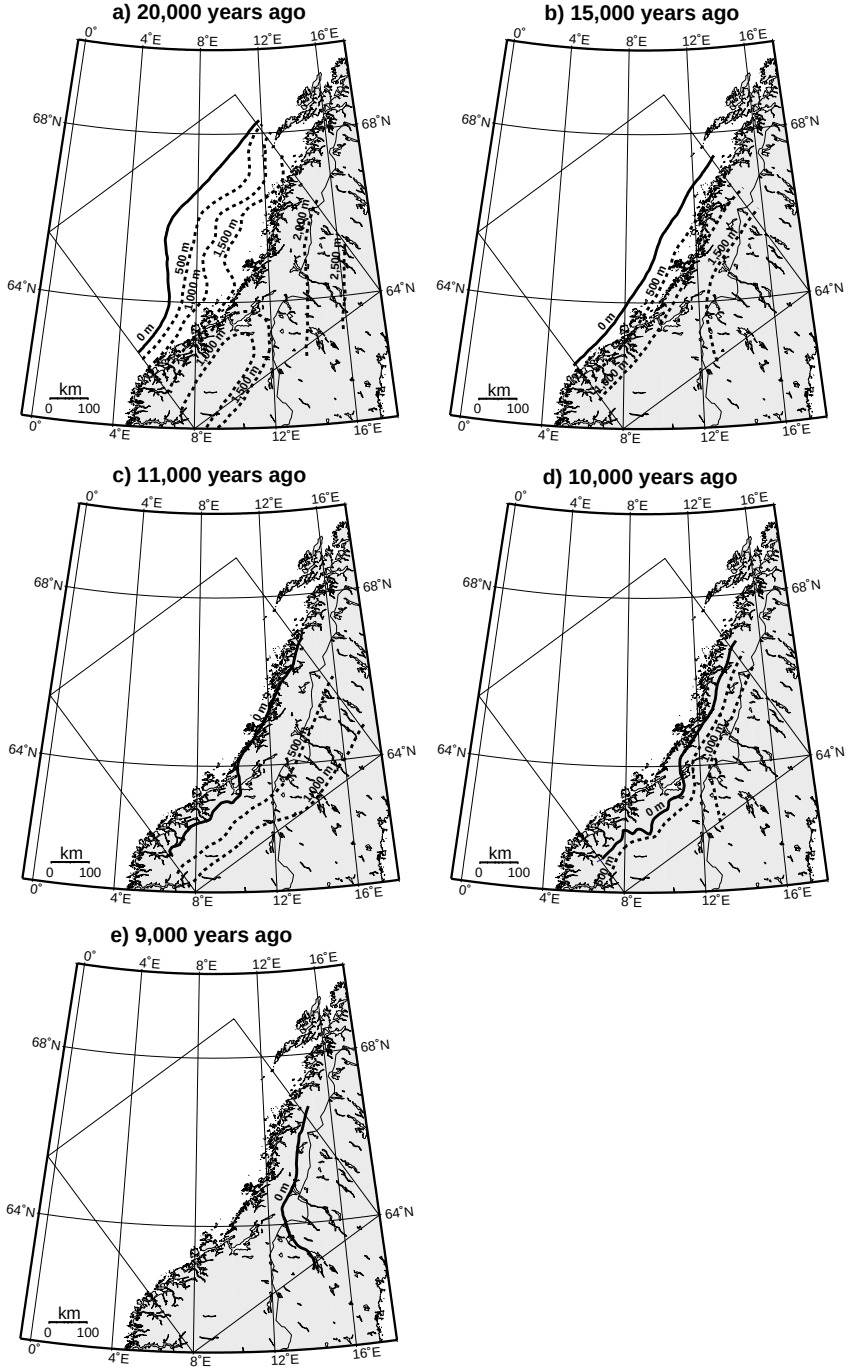

Figure 4.13: Extent and thickness of the modeled ice sheet for different stages of the Mid-Norway model. Figure 4.13a shows the maximum ice sheet extent that existed 20,000 years ago. The ice extent at 15,000 years ago (Figure 4.13b) is the reference ice extent that is representative for most of the ice sheet's existence during the Pleistocene.

Similar to the North Sea model, we used published information on ice shield extents and thicknesses for different ice stages to include the ice sheet in the Mid-Norway model

(Figure 4.13). As the Mid-Norway model is closer to the former center of the Fennoscandian ice sheet, the completion of ice melting occurred as late as 8,000 years ago. Consequently, we had to add an additional ice stage for 9,000 years ago (Figure 4.13e). Otherwise the modeled ice evolution is similar to the "reference" ice evolution of the North Sea model. Overall, the Fennoscandian ice sheet has a much simpler geometry in Mid-Norway than in the North Sea area. Even at its maximum extent the ice margin strikes more or less parallel to the Mid-Norwegian coast line (Figure 4.13a).

Results of the "blind test" Mid-Norway model

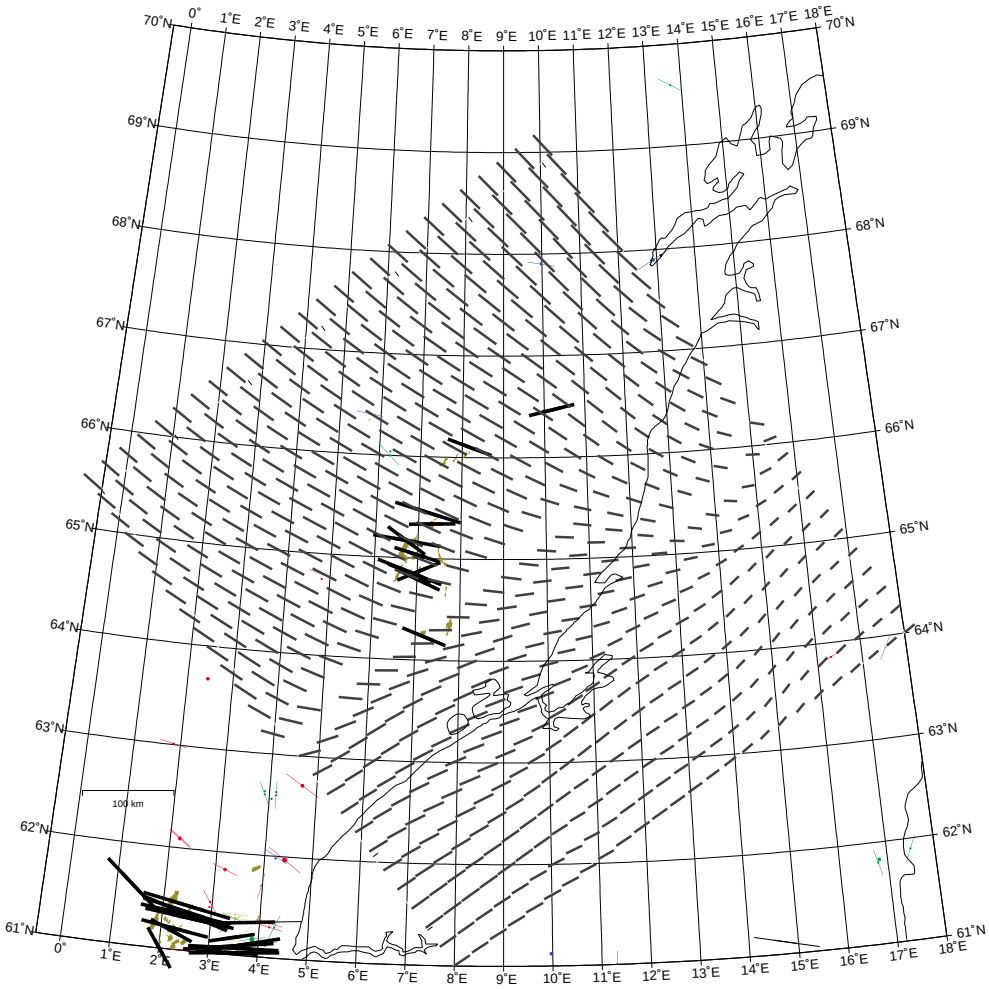

Figure 4.14: Modeled S_{Hmax} orientation for the Mid-Norway model with the same lithospheric and asthenospheric viscosities as the best-fit North Sea model. The grey lines show the modeled results of S_{Hmax} which can be compared to the borehole measurements (black lines) and roughly to the earthquakes (colored lines). The model fits most of the observations, suggesting that deglaciation causes the observed spatial stress variations and that the model rheology roughly represents the lithosphere.

Figure 4.14 compares the modeled S_{Hmax} orientations of the "blind test" Mid-Norway model (with the same parameters as the best-fitting North Sea model) to the observations. Like the North-Sea model, the model of Mid-Norway predicts S_{Hmax} orientations perpendicular to the coastline at distances > 100 km from the coast, and closer to the coast S_{Hmax} tends to be more aligned with the coastline. However, north of 65ºN S_{Hmax} is almost perpendicular even in proximity of the coast, because the area covered by the migrating ice front is much larger than further south where the ice front does not vary much.

Most of the S_{Hmax} orientations from boreholes are located around 65ºN and 7ºE because the majority of the hydrocarbon reservoirs in Mid-Norway known to date are restricted to this area. These wells show that S_{Hmax} orientations lie between 100º and 120º, and the model matches these observations extremely well. Even further to the north, at 66ºN and 8ºE the model predicts S_{Hmax} exactly as observed. The model deviates from the measurement at 66.5ºN-10ºE and gives only a poor fit to the measurement at 64.2ºN-7.2ºE. Possible explanations for these misfits are bad data quality as previously discussed, the stress field can be locally perturbed due to slip on faults, or the lithosphere-asthenosphere rheology is not identical to the North Sea. Since, the number of S_{Hmax} observations from boreholes is limited we also included earthquake data in Figure 4.14. Earthquakes give only a rough estimate for S_{Hmax} orientations since focal plane mechanisms reflect the strain field rather than the stress field associated with the earthquake. Also, the depth resolution for earthquakes offshore Norway is poor (Bungum, 1991) which is problematic since S_{Hmax} orientations might vary with depth. Nevertheless, model and earthquakes agree that S_{Hmax} strikes ≈ 110º at 65ºN - 5ºE and at 66ºN - 6ºE. Moreover, the two earthquakes around 64ºN - 17ºE confirm that S_{Hmax} rotates to a northeast-striking direction in this area which is predicted by the model. In conclusion, the Mid-Norway model mostly fits the available S_{Hmax} measurements with some local deviations.

Figure 4.15 shows the fit of the Mid-Norway model to the observed S_{hmin}/S_v values. Observations and model agree that S_{hmin}/S_v is close to unity at a large distance from the coast which was also the case for the North Sea model, and that S_{hmin}/S_v decreases towards the coast. However, it is unclear where exactly this transition from high to low S_{hmin}/S_v occurs. The observations suggest that at 65ºN S_{hmin}/S_v starts to drop at 7.5ºE. For the same latitude the model predicts high S_{hmin}/S_v to as far east as 9ºE. Possible explanations for this discrepancy are a insufficient description of the ice sheet evolution, local variations in crustal structure, or simply flawed data. Clearly, the match of S_{hmin}/S_v predictions to the observations in Mid-Norway is inferior to the North Sea model's match. Nevertheless, the Mid-Norway model and observations agree that S_{hmin}/S_v drops towards the coast.

a)

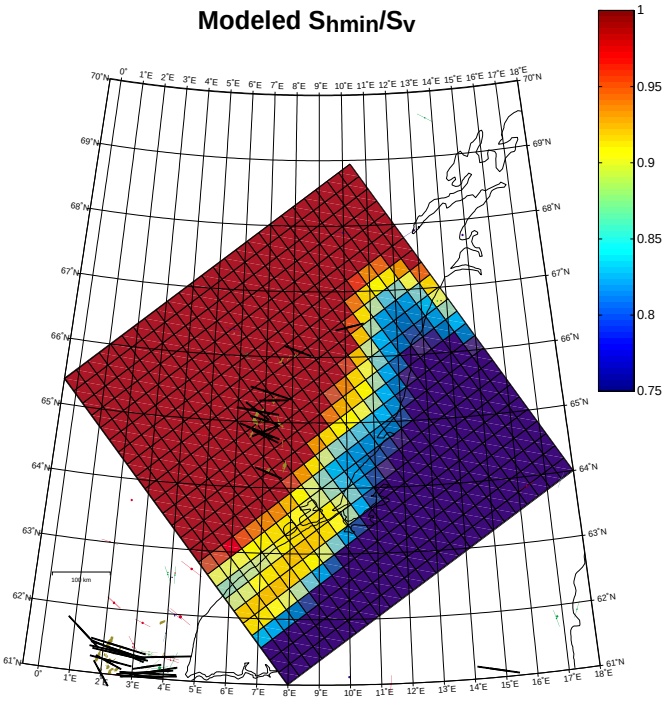

b)

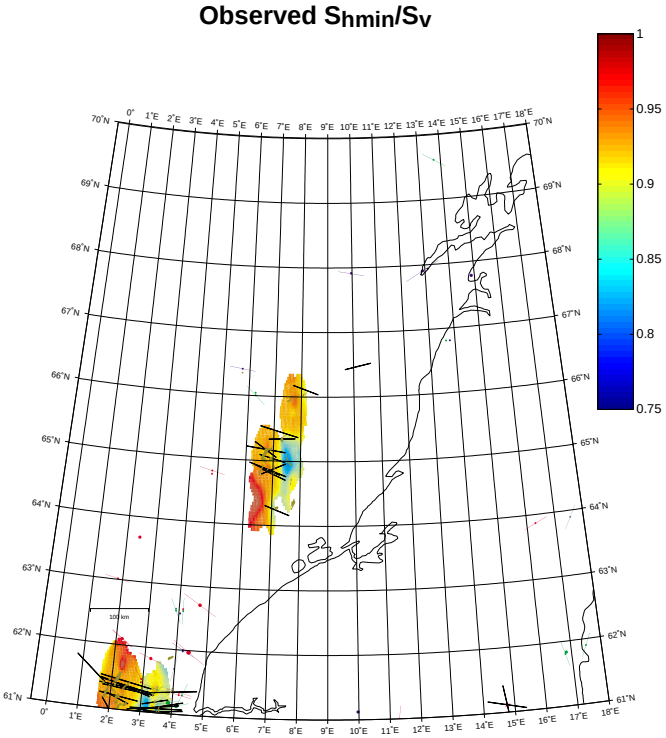

Figure 4.15: Comparison of modeled and observed S_{hmin}/S_v. Figure 4.15a shows the modeled S_{hmin}/S_v for the blind-test model at a depth of 3000 m. Figure 4.15b shows observed S_{hmin}/S_v from leak off tests for comparison. Both, the model and the observations show a drop of Shmin/Sv towards the coast. However, the modeled S_{hmin}-drop is closer to the coast than observed.

Influence of chosen lower crust and lithospheric mantle viscosities

With the blind-test Mid-Norway model we were assuming that the lithospheric viscosities are constant along the Norwegian coast. By testing different lithospheric viscosity profiles, we will now test whether this was a good assumption. The range of tested viscosities corresponds to the North Sea models discussed in the section on the influence of chosen viscosities on page 75, including the model with a purely elastic lithosphere. We left out the two models ignoring the lithospheric mantle because the stress measurements in Mid-Norway do not resolve the stress field well enough to constrain any possible differences in modeled S_{Hmax} orientations.

a)

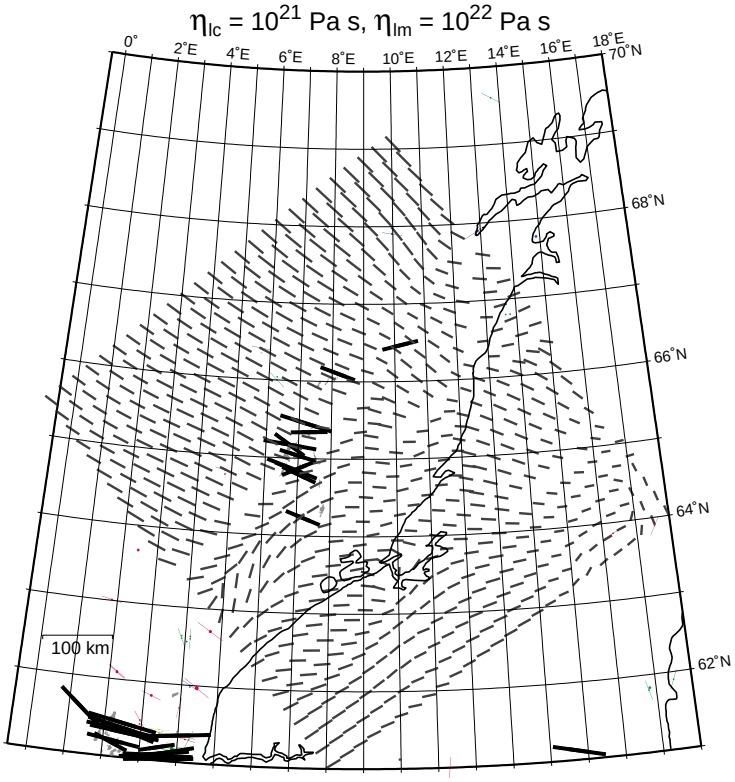

Figure 4.16: (including next pages) Modeled S_{Hmax} orientation for the Mid-Norway models with varying viscosities. The grey lines show the modeled results of S_{Hmax} which can be compared to the borehole measurements (black lines). For all these models we assumed the "reference" ice evolution as described in Section 4.3.2.

b)

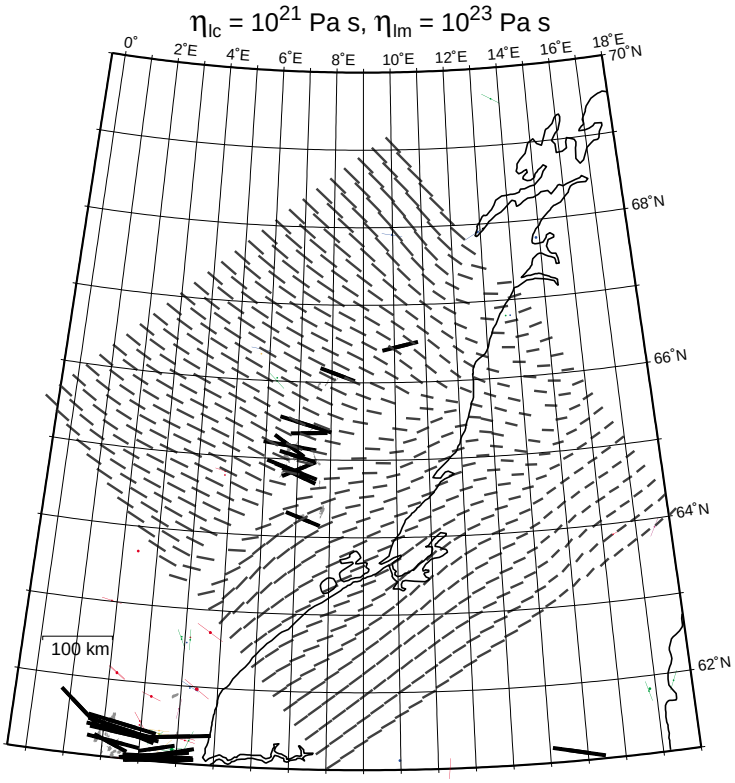
$\eta_{lc} = 10^{21}$ Pa s, $\eta_{lm} = 10^{23}$ Pa s
0°
2°E
4°E
6°E
8°E
10°E
12°E
14°E
16°E
18°E
70°N
68°N
66°N
64°N
62°N
100 km

c)

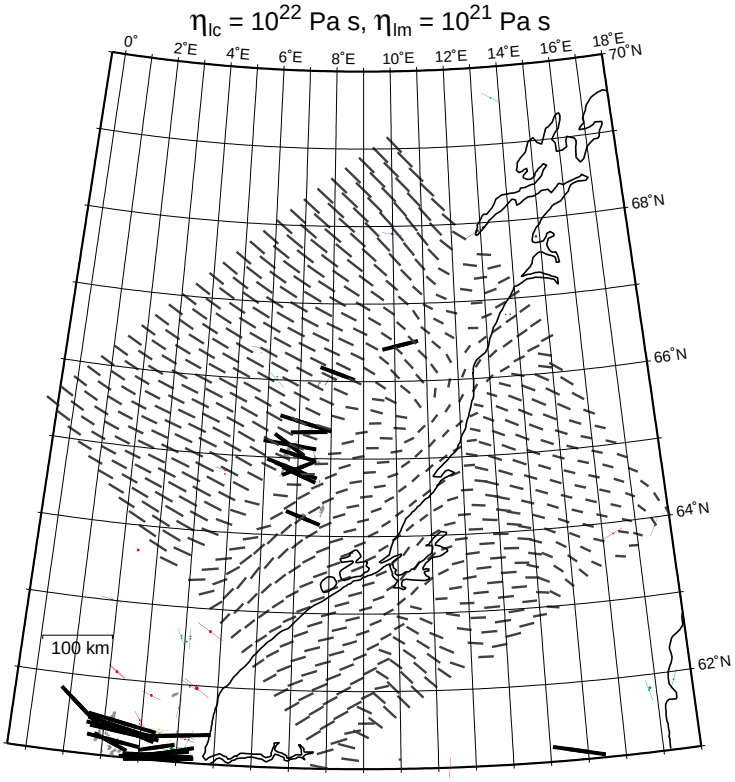
$\eta_{lc} = 10^{22}$ Pa s, $\eta_{lm} = 10^{21}$ Pa s
0°
2°E
4°E
6°E
8°E
10°E
12°E
14°E
16°E
18°E
70°N
68°N
66°N
64°N
62°N
100 km

d)

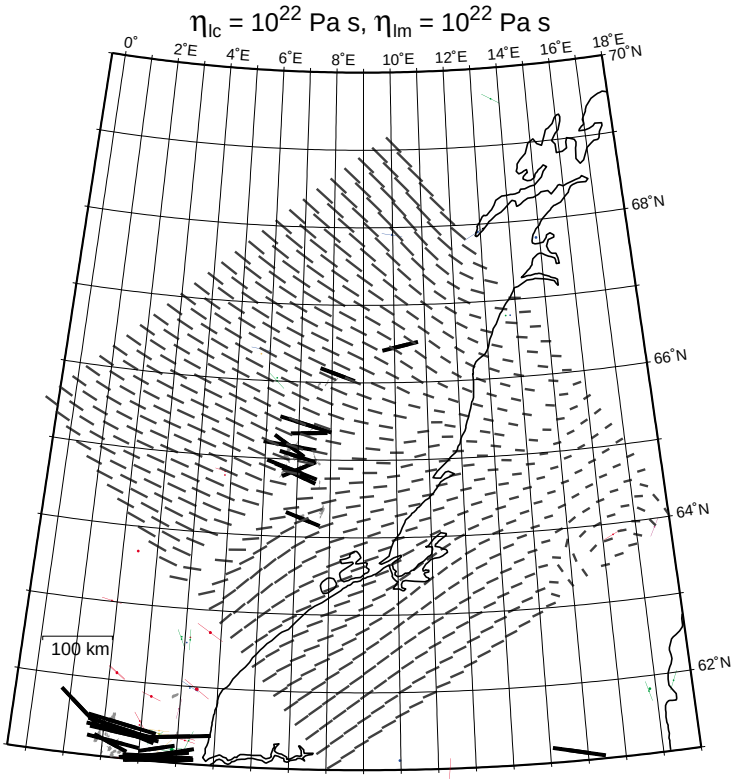
$\eta_{lc} = 10^{22}$ Pa s, $\eta_{lm} = 10^{22}$ Pa s
0°
2°E
4°E
6°E
8°E
10°E
12°E
14°E
16°E
18°E
70°N
68°N
66°N
64°N
62°N
100 km

e)

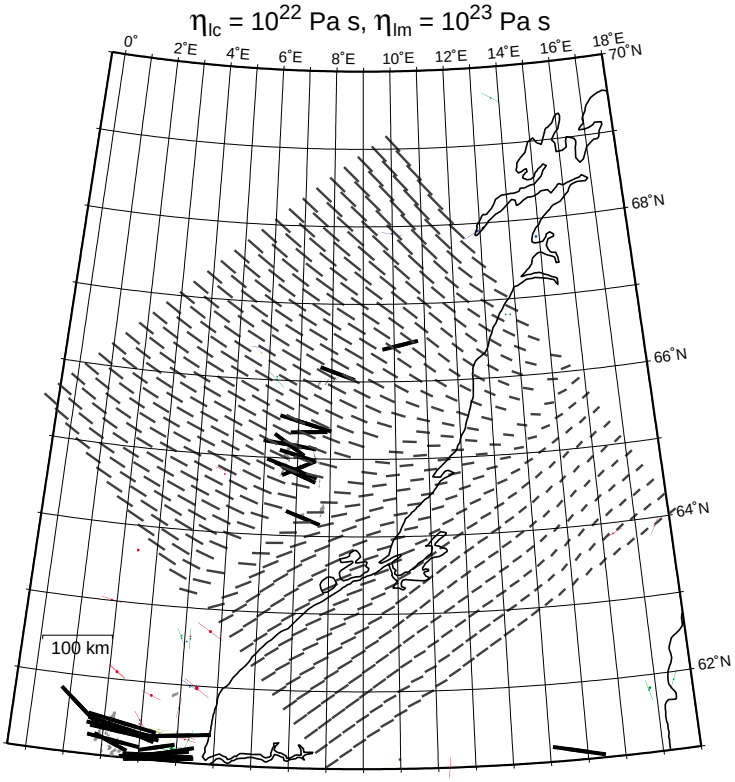
$\eta_{lc} = 10^{22}$ Pa s, $\eta_{lm} = 10^{23}$ Pa s
0°
2°E
4°E
6°E
8°E
10°E
12°E
14°E
16°E
18°E
70°N
68°N
66°N
64°N
62°N
100 km

f)

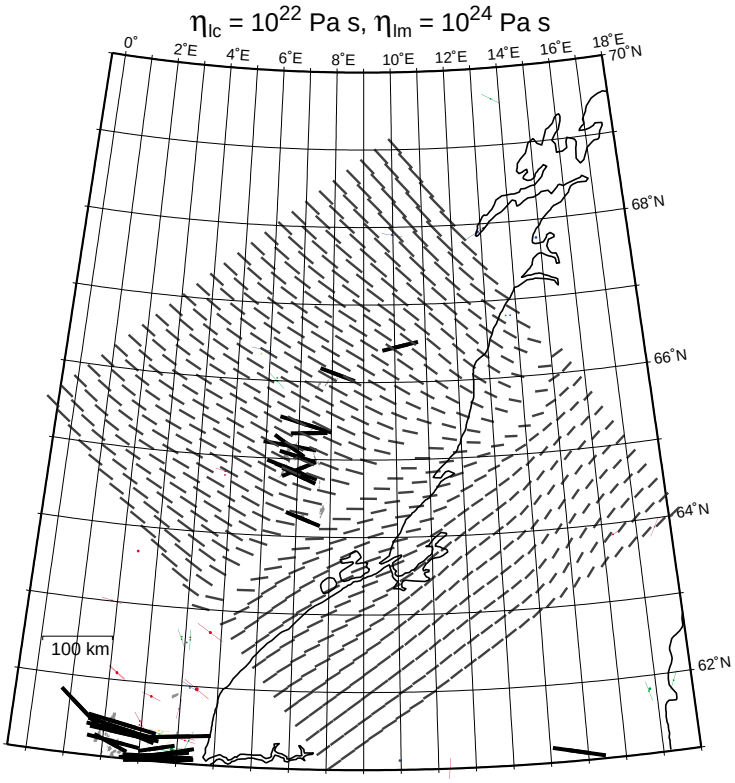
$\eta_{lc} = 10^{22}$ Pa s, $\eta_{lm} = 10^{24}$ Pa s
0°
2°E
4°E
6°E
8°E
10°E
12°E
14°E
16°E
18°E
70°N
68°N
66°N
64°N
62°N
100 km

g)

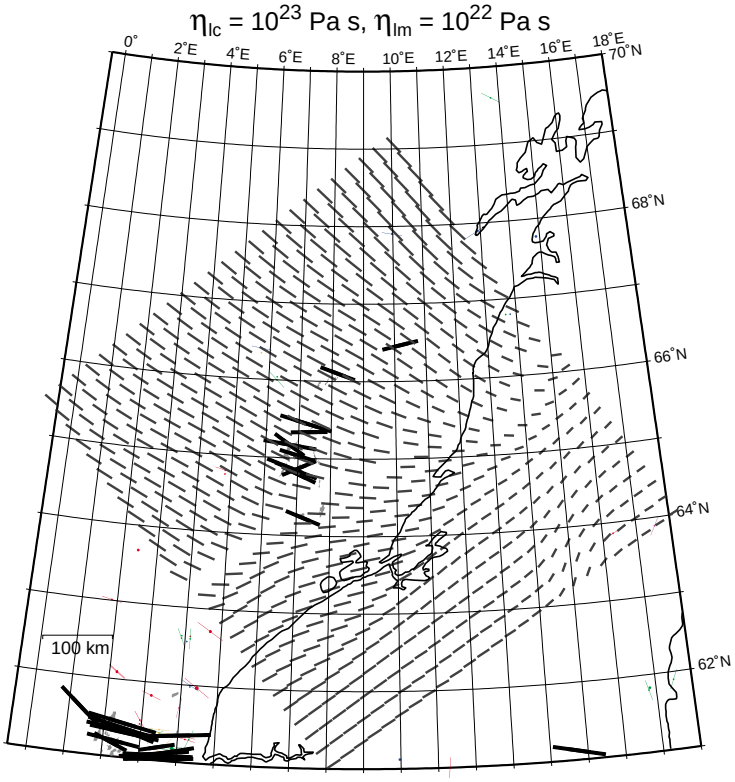
$\eta_{lc} = 10^{23}$ Pa s, $\eta_{lm} = 10^{22}$ Pa s
0°
2°E
4°E
6°E
8°E
10°E
12°E
14°E
16°E
18°E
70°N
68°N
66°N
64°N
62°N
100 km

h)

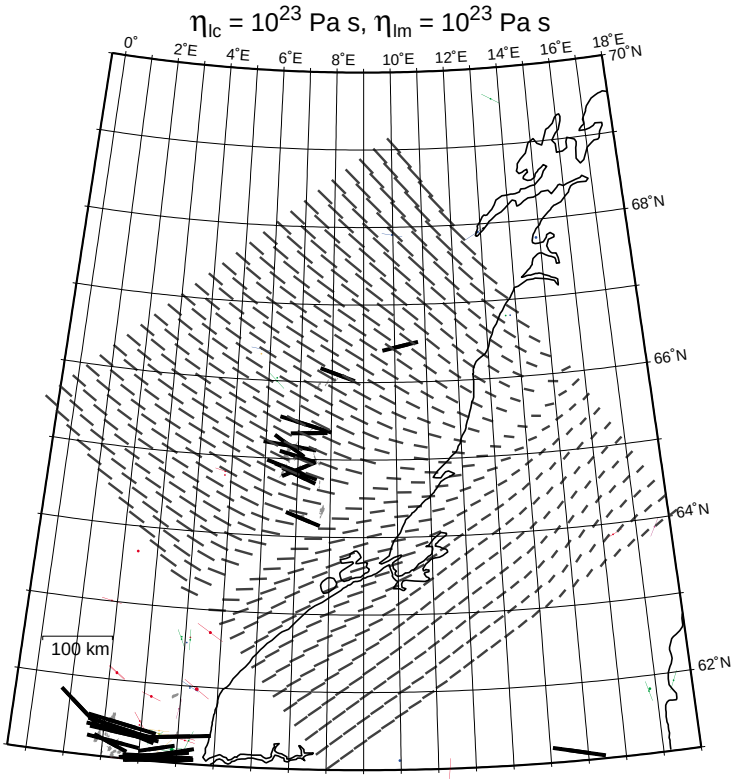
$\eta_{lc} = 10^{23}$ Pa s, $\eta_{lm} = 10^{23}$ Pa s
0°
2°E
4°E
6°E
8°E
10°E
12°E
14°E
16°E
18°E
70°N
68°N
66°N
64°N
62°N
100 km

i)

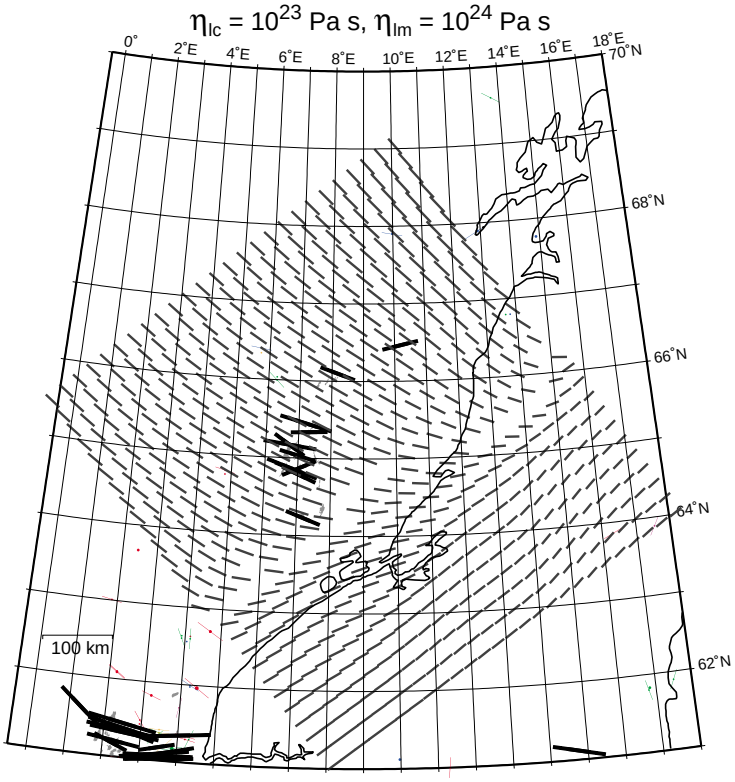
$\eta_{lc} = 10^{23}$ Pa s, $\eta_{lm} = 10^{24}$ Pa s
0°
2°E
4°E
6°E
8°E
10°E
12°E
14°E
16°E
18°E
70°N
68°N
66°N
64°N
62°N
100 km

Compared to the North Sea models, chosen lithospheric viscosities do not significantly affect the modeled S_{Hmax} orientations in Mid-Norway. All tested Mid-Norway models show an almost constant WNW-striking S_{Hmax} orientation in the northwestern half of the model and in all the models this orientation rotates clockwise to a more northwest-striking S_{Hmax} at the northern model corner (around 68ºN, 10ºE). As a result, all models match the consistently WNW-striking S_{Hmax} measurements in the area around 65ºN, 7ºE. Furthermore, the models agree that in the southern corner of the model S_{Hmax} strikes to the northeast. The reason for the more uniform behavior of the Mid-Norway models is the relatively simple ice sheet geometry in this area which does not allow much variation of the modeled stresses.

The main difference between the models presented in Figure 4.16 is the location of the roughly northeast-trending transition zone from northwest or WNW striking S_{Hmax} predictions to east or northeast-striking directions closer to the coast and on land. For example, in the model with the lowest viscosities (Figure 4.16a) this transition occurs exactly at the location of the hydrocarbon reservoirs around 65ºN, 7ºE where the southeasternmost oil fields have a predicted ENE-striking S_{Hmax} direction. With increasing viscosities this transition zone is shifted towards the coast and becomes less pronounced. Accordingly, the blind-test model (Figure 4.16e) predicts consistent WNW-striking S_{Hmax} orientations in the vicinity of the main hydrocarbon fields (at 65ºN, 7ºE) and the transition to northeast-striking S_{Hmax} predictions is located near the coast. For models with higher viscosities than the blind test model, the transition zone is pushed even closer to the coast. For example, the model with $\eta_{lc} = 10^{23}$ Pa s and $\eta_{lm} = 10^{24}$ Pa s (Figure 4.16i) predicts a WNW-striking S_{Hmax} orientation near the breakout measurement at 64.3ºN, 7.5ºE where models with lower viscosities suggest east-west or even northeast-trending S_{Hmax} orientations. Consequently, the model shown in Figure 4.16i achieves a better fit to the S_{Hmax} observations than any other Mid-Norway model because it matches the breakout measurement at 64.3ºN, 7.5ºE. If this single breakout measurement can be trusted, it would suggest that the lithospheric viscosities in Mid-Norway are higher than in the North Sea. According to Dragoni et al. (1993) heat flow is relatively high in southwestern Fennoscandia (southern Sweden, and southern Norway) and decreases towards the northeast (northern Finland). They suggest that this heat flow transition causes a lateral change in lithospheric strength (higher strength towards the northeast), which would to a first order confirm our possible finding of higher lithospheric viscosities in Mid-Norway.

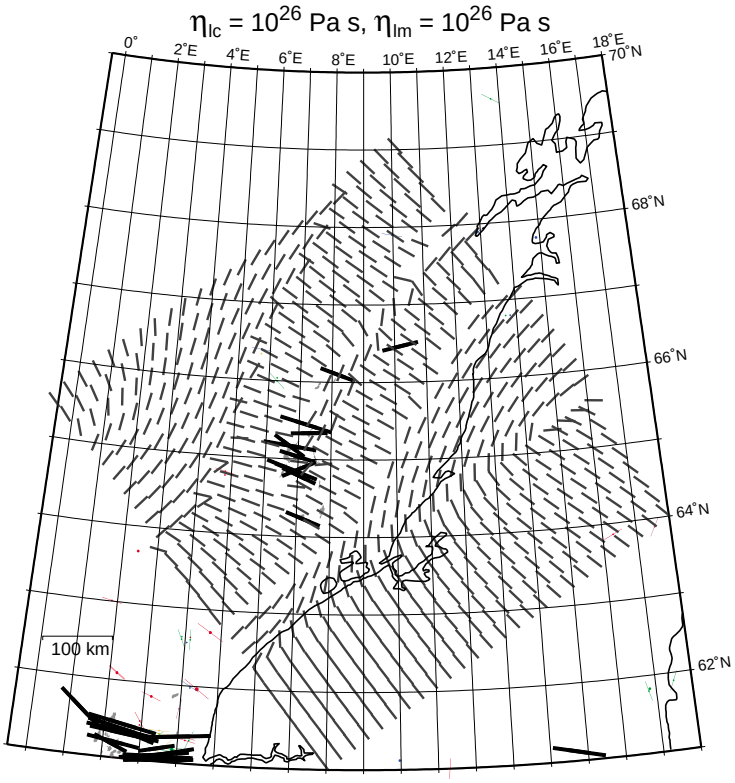

Figure 4.17: Modeled S_{Hmax} orientation for the Mid-Norway model with a purely elastic lithosphere. The grey lines show the modeled results of S_{Hmax} which can be compared to the borehole measurements (black lines). The model shows an acceptable fit to the observations.

Despite the fact that the North Sea model with a purely elastic lithosphere gave a very poor fit to the S_{Hmax} observations (Figure 4.8), I ran a similar model for Mid Norway (Figure 4.17). This model matches the observations to a first order by explaining some of the WNW-striking S_{Hmax} orientations at 65ºN, 7ºE. However, in the same area the model also predicts that S_{Hmax} rotates by almost 90º which is not observed. According to this model, the predicted present-day stress perturbations due to deglaciation are very small so the modeled magnitude of S_{Hmax} is almost equal to S_{hmin} which explains the strong spatial changes of the predicted S_{Hmax} orientations. But, the existence of strike-slip faulting earthquakes in the area suggests an appreciable horizontal stress anisotropy, so a purely elastic lithosphere model does not seem to work in Mid-Norway either.

In summary, the viscosities of the best-fitting North Sea model also work in Mid-Norway, but increasing the viscosities by an order of magnitude leads to a better fit. Thus, the models suggest a transition to higher lithospheric viscosities from the North Sea towards Mid-Norway which would agree with heat flow observations. As with the North

Sea model, it is necessary to include viscoelastic behavior within the lithosphere to obtain satisfactory stress predictions.

Influence of chosen ice sheet evolution

Now I will test how the stress predictions of the Mid-Norway model depend on the chosen ice model, similar to the section on chosen ice evolution for the North Sea model on page 84. According to the results of the previous section, I will use $\eta_{lc} = 10^{23}$ Pa s, and $\eta_{lm} = 10^{24}$ Pa s (the best-fitting Mid-Norway model) in order to test the ice models shown in Figure 4.10.

a)

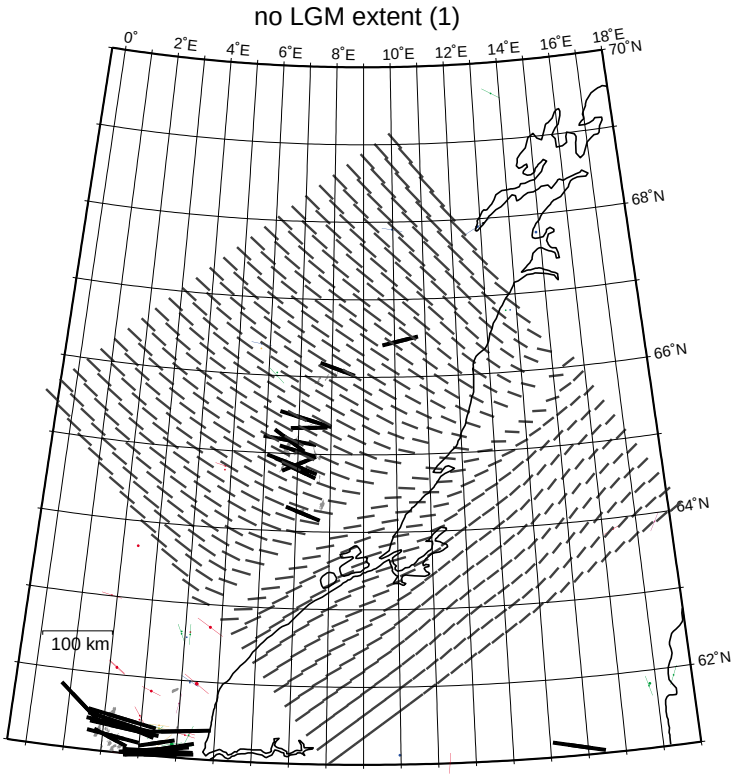

Figure 4.18: (and next pages) Modeled S_{Hmax} orientation for Mid-Norway models with varying ice sheet evolutions. The grey lines show the modeled results of S_{Hmax} which can be compared to the borehole measurements (black lines).

b)

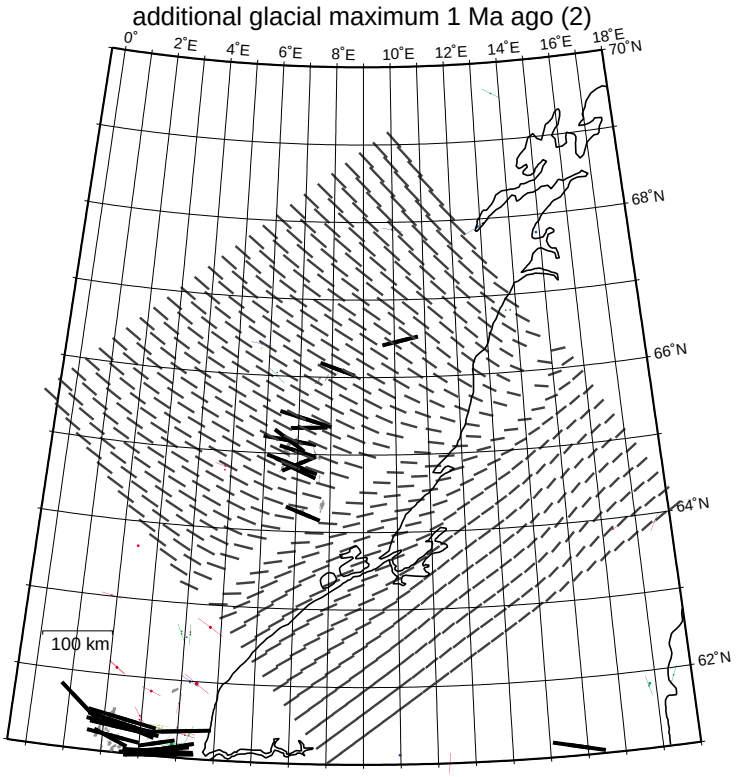
additional glacial maximum 1 Ma ago (2)
0°
2°E
4°E
6°E
8°E
10°E
12°E
14°E
16°E
18°E
70°N
68°N
66°N
64°N
62°N
100 km

c)

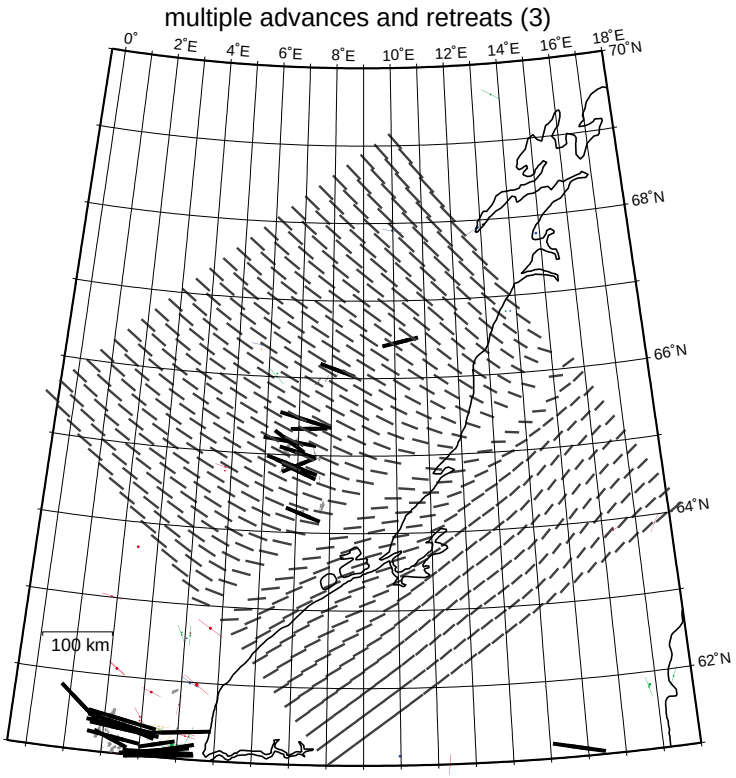
multiple advances and retreats (3)
0°
2°E
4°E
6°E
8°E
10°E
12°E
14°E
16°E
18°E
70°N
68°N
66°N
64°N
62°N
100 km

d)

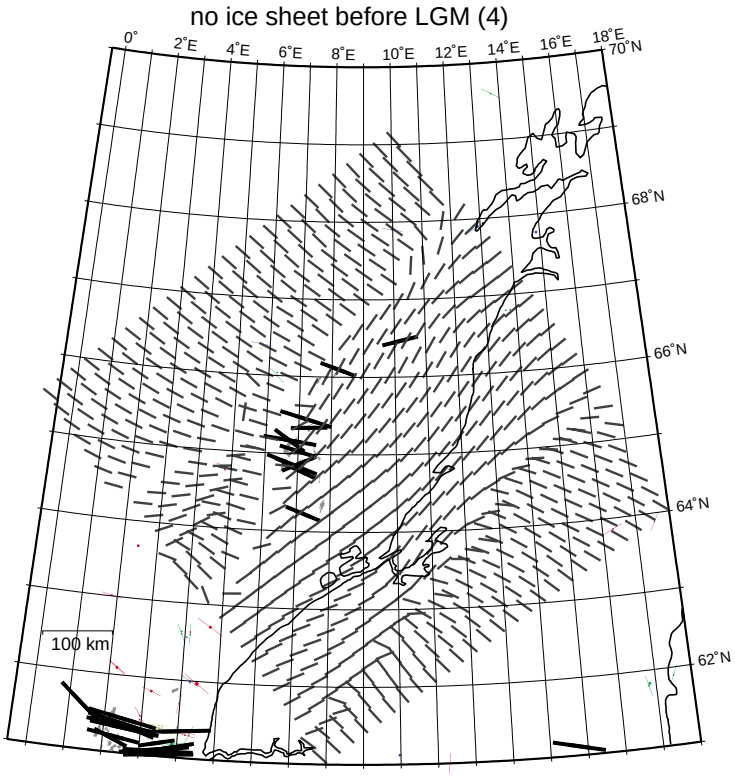
no ice sheet before LGM (4)
0°
2°E
4°E
6°E
8°E
10°E
12°E
14°E
16°E
18°E
70°N
68°N
66°N
64°N
62°N
100 km

e)

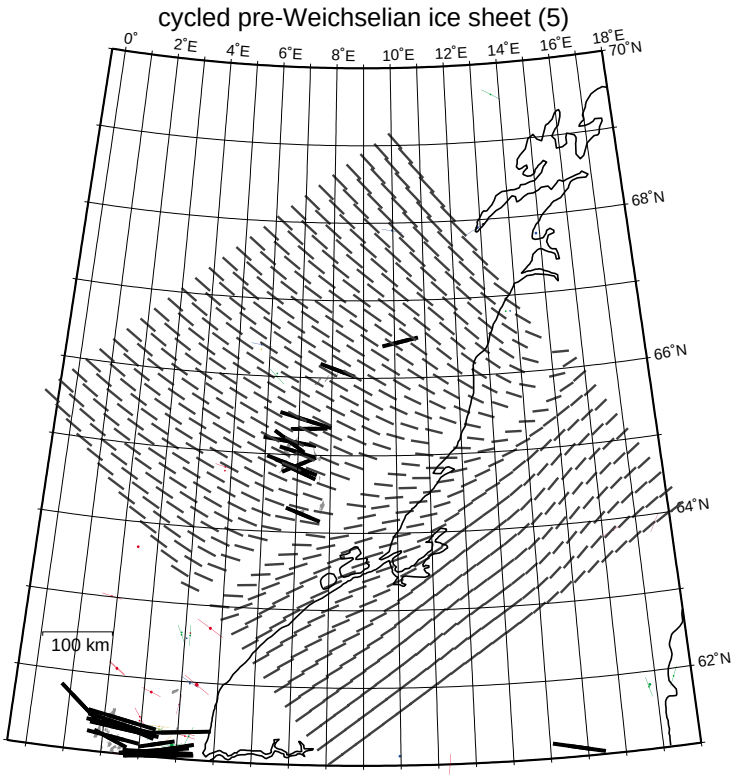
cycled pre-Weichselian ice sheet (5)
0°
2°E
4°E
6°E
8°E
10°E
12°E
14°E
16°E
18°E
70°N
68°N
66°N
64°N
62°N
100 km

The results shown in Figure 4.18 demonstrate that the Mid-Norway model fits the stress orientation data largely independent of the chosen ice model. For example, ice model 1 (Figure 4.18a) is almost indistinguishable from the results of the reference ice model (Figure 4.16i). Except for ice model 4 (Figure 4.18d), all other ice evolutions achieve a fit comparable to ice model 1 with some very minor variations.

Similar to the North Sea model, the behavior of the Mid-Norway model strongly depends on the characteristic relaxation times of the viscoelastic layers. For the best-fitting viscosities of the Mid-Norway model ($\eta_{lc} = 10^{23}$ Pa s, $\eta_{lm} = 10^{24}$ Pa s) the relaxation times are τ_{lc} = 134,000 years and τ_{lm} = 950,000 years. In contrast to ice model 4, the other ice models load the 15 ka extent for at least 1 million years which allows both viscoelastic layers to respond viscously. As a result, all these models yield almost identical results. Ice model 4 however gives a poor fit to the observations, because the viscoelastic layers have not responded viscously to the 15 ka extent. With the exception of ice model 2, the duration of the 20 ka extent is irrelevant as this extent existed for less than 134,000 years (τ_{lc}). By loading the 20 ka extent for longer than τ_{lc} (ice model 2, Figure 4.18b) the model achieves a slightly worse fit to the breakout measurement at 64.3ºN, 7.2ºE suggesting that the 20 ka extent existed for less than τ_{lc} (134,000 years). However, this interpretation is certainly pushing the capabilities of the stress data to constrain the models in Mid-Norway.

Nevertheless, the Mid-Norway model confirms the findings of the North Sea model that the ice sheet along the Norwegian coast must have existed in its 15 ka extent for an accumulated time of at least ≈1 million years. The models suggest that the 20 ka extent could not have lasted for longer than ≈100,000 years but its duration must have exceeded τ_{lc} of the North Sea (≈10,000 years). Both models agree that the short term fluctuations of the ice sheet do not affect the stress predictions.

Influence of chosen initial stress state (ridge push)

To test the influence of plate tectonic forces (ridge push) on the stress field in Mid-Norway, we used the methodology outlined on page 90 to prestress the Mid-Norway model prior to ice loading. We assumed that the ridge push direction is striking to the northwest (parallel to the model boundaries). The initial stress magnitudes are similar to the North Sea model as described on page 90 and the resulting S_{Hmax} orientations are displayed in Figure 4.19.

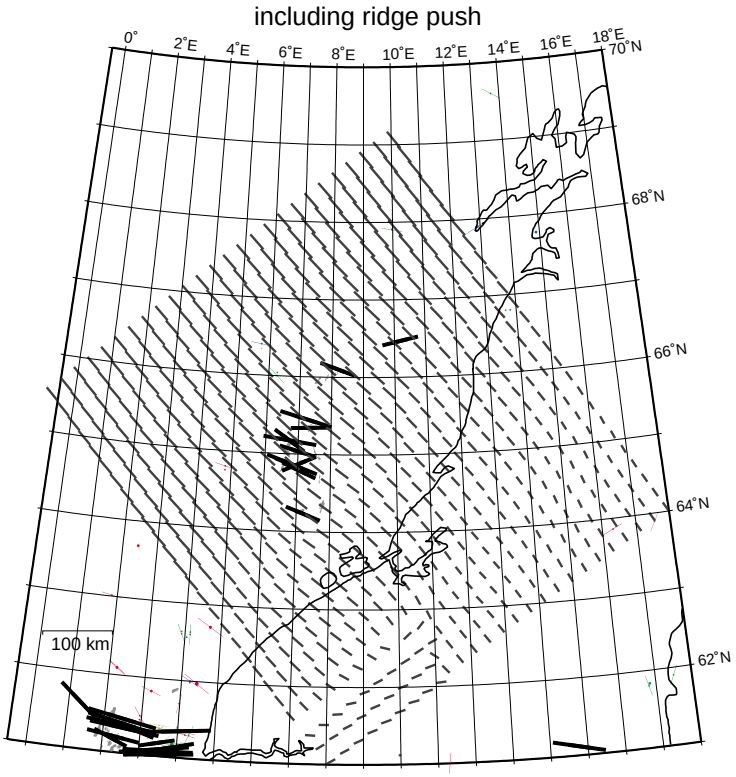

Figure 4.19: Modeled S_{Hmax} orientation for the Mid-Norway model assuming that ridge push significantly influences the stress field along the Mid-Norwegian margin. The grey lines show the modeled results of S_{Hmax} which can be compared to the borehole measurements (black lines).

Not surprisingly, the modeled S_{Hmax} orientations hardly vary across Mid-Norway which agrees with the S_{Hmax} data showing not much spatial variation. However, the modeled orientations are rotated clockwise relative to the measurements which leads to a consistent misfit of approximately 15 degrees. Of course, by applying the initial S_{Hmax} in a slightly rotated orientation we probably would be able to achieve a better fit to the S_{Hmax} observations.

The scarce data coverage on the Mid-Norwegian margin does not allow us to rule out a possible influence of ridge push on the observed stress field. The observed stress orientations might possibly result from ridge push. Conversely, just because the measured S_{Hmax} orientations are roughly parallel to the regional ridge push orientation does not prove that ridge push in fact causes these orientations as several authors have concluded (e.g. Lindholm et al., 1995; Fejerskov, 1996). As our models in previous sections show, the observed stress directions in Mid-Norway can just as well be explained in the absence of ridge push, by simply accounting for glacial loading and unloading. Similar to the North Sea model,

the observed stress field might result from a combination between ridge push and glacial loading and unloading. The model of Gölke and Coblentz (1996) suggests that the interaction between a heterogeneous crustal structure below Mid-Norway, and ridge push leads to a horizontally close to isotropic stress field (similar to the northern North Sea). As a result, any stress perturbation (glacial loading) can easily influence the orientation of S_{Hmax} leading to the observed WNW-striking S_{Hmax} orientation on the Mid-Norwegian margin.

4.3.4 Comparison of model results to uplift rates

So far, we exclusively checked our models against stress measurements which has worked remarkably well in constraining and validating the models. Traditionally, glacial rebound models have been constrained with uplift data (e.g. Fjeldskaar, 1997). In our case, uplift data can be used as an additional way to test the model results. Ekman (1996) compiled a map of apparent uplift rates in Fennoscandia from sea level records, lake level records, and high-precision levelling as shown in Figure 4.20.

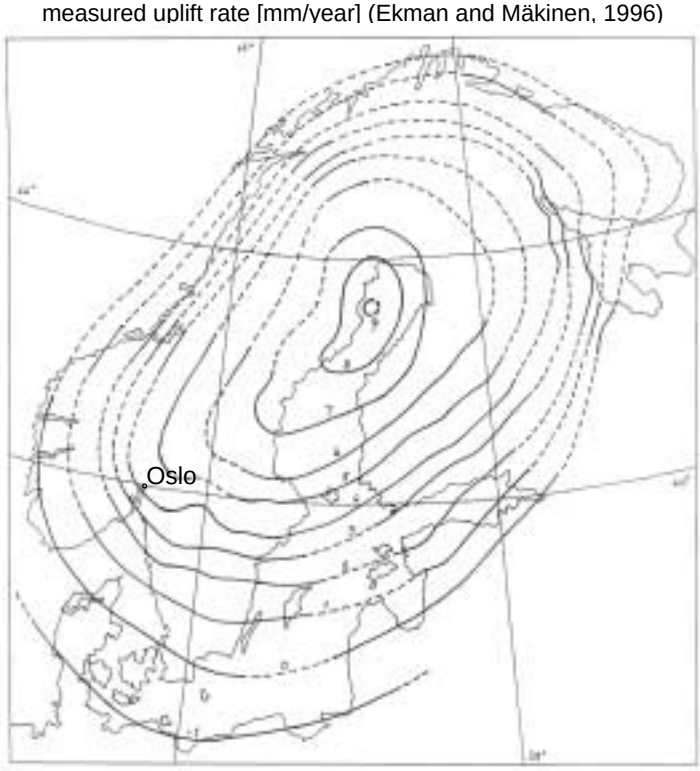

Figure 4.20: Map of apparent uplift rates in Fennoscandia (Ekman, 1996). The map is based on the compilation of sea level recordings, lake level recordings, and high-precision leveling between 1892 and 1991. The shown values are apparent uplift rates (relative to sea level).

Measured uplift rates are highest in the northern Gulf of Bothnia where they reach more than 9 mm/year. In the area of our North Sea model, the apparent uplift rate is negligible along the coastline and only slowly increases further inland to reach values between 2-3 mm/year at the eastern boundary of our model. In Mid-Norway the coastline undergoes an uplift of 2 mm/year and further inland the uplift rate increases rapidly.

Our finite element models do not directly provide the apparent uplift rate for a certain location. Instead, the models give the total vertical displacement at the end of each calculation step. So, in order to calculate present uplift rates from our model results, we need to calculate the difference between the vertical displacement at the beginning and at the end of the last calculation step and normalize it by the duration of the last step. This procedure provides the absolute present uplift rate (relative to the geoid), so in order to compare it to the apparent uplift (relative to sea level) as displayed in Figure 4.20 we need to apply a eustatic correction which accounts for the world-wide sea level rise. Accordingly, we need to subtract 1.15 mm/year (Nakiboglu and Lambeck, 1991) from our predicted absolute uplift rates, in order to obtain apparent uplift rates.

Figure 4.21 shows the apparent uplift rates calculated by the best-fitting North Sea model. Along the coastline the North Sea model predicts an uplift rate of 0 to 1 mm/year. According to the measurements, the isoline for zero uplift is located ≈20 km east of the coastline where the modeled uplift rate is close to 1 mm/year. Further inland, near the eastern end of the biggest Fjords, the modeled uplift rates are slightly higher than 1 mm/year which is confirmed by the measurements. The North Sea model reaches a maximum uplift rate of ≈2 mm/year near its easternmost end which is located about halfway between Oslo and the Norwegian west coast at a latitude of 61°N. Measured uplift rates at this location are on the order of 2 mm/year.

Thus, the North Sea model matches most of the observed uplift values within the error bounds. Except, near the coast the modeled uplift rates are slightly too high. This mismatch might be due to a discrepancy between the modeled ice sheet and the actual ice front profile. Also, the local, post-glacial sea level change might differ from the global estimate which we used to calculate the modeled apparent uplift rates. Furthermore, the estimate of the global eustatic sea level change strongly depends on the assumed earth model (e.g. Wolf, 1992) and is therefore subject to an error of at least ±0.5 mm/year.

a)

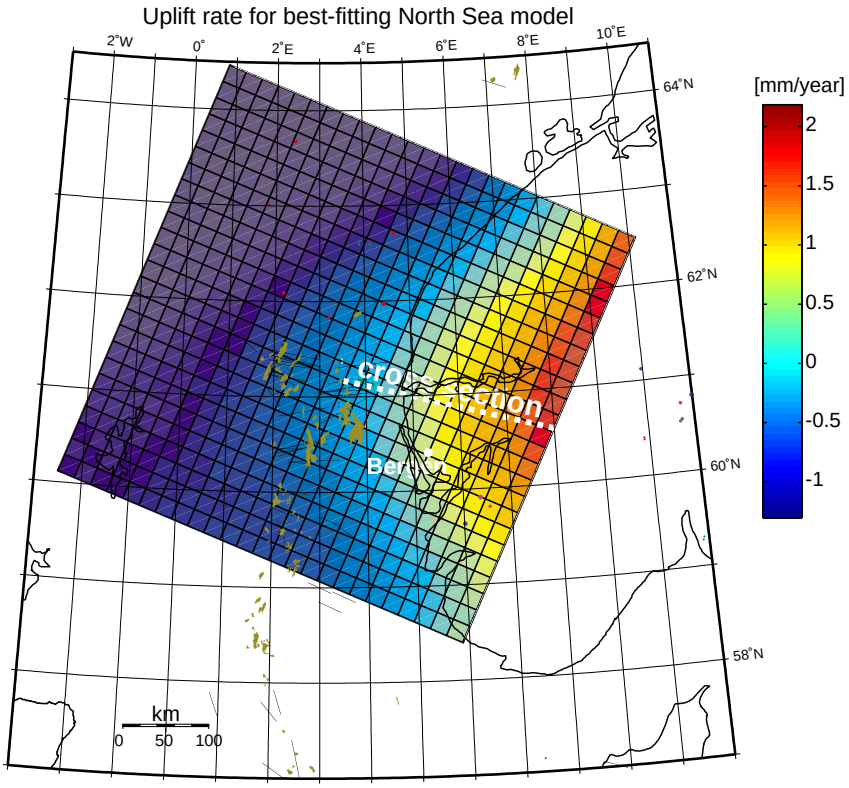

b)

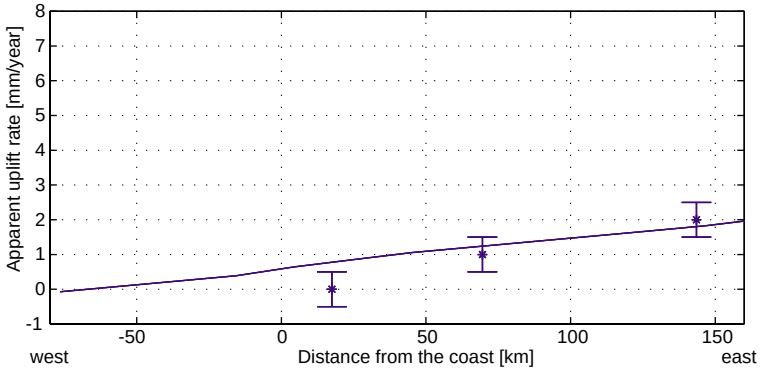

Figure 4.21: Modeled uplift from the best-fitting North Sea model. a) Predicted present-day apparent uplift rates (corrected for eustatic sea level changes). b) Apparent uplift rates along the cross section shown in Figure 4.21a compared to the measurements from Figure 4.20.

a)

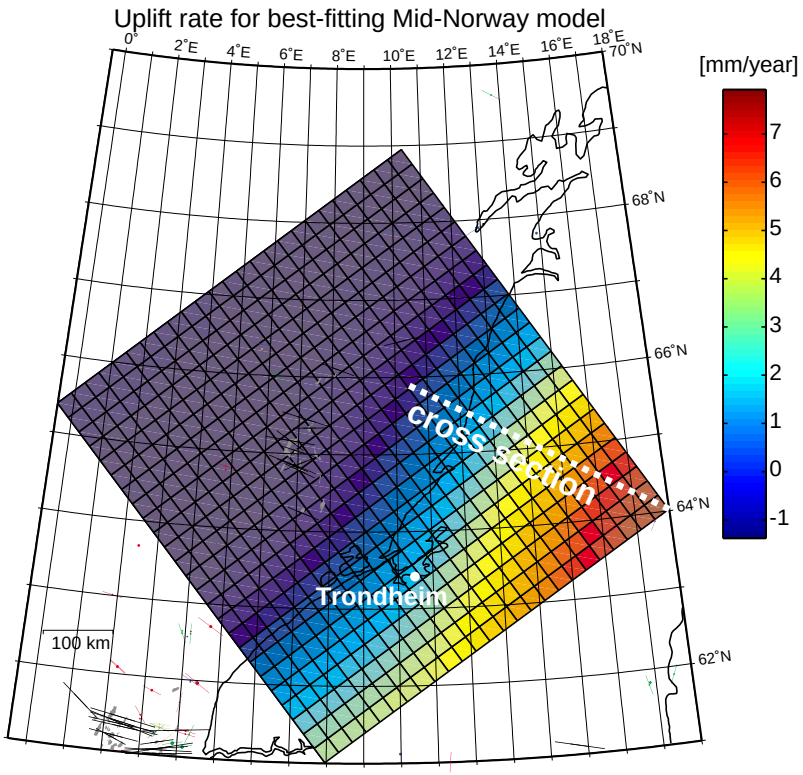

b)

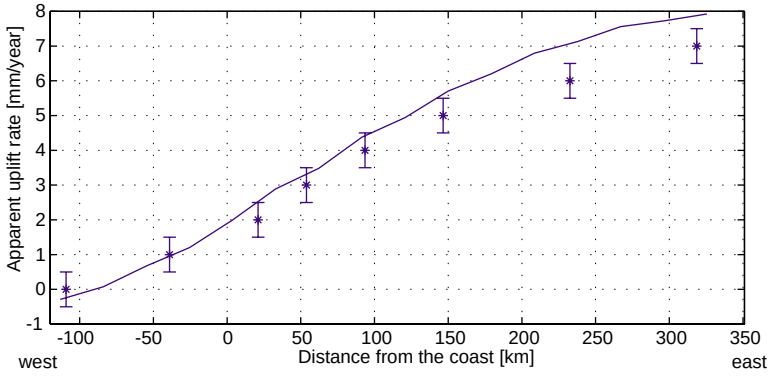

Figure 4.22: Modeled uplift from the Mid-Norway model. a) Predicted present-day apparent uplift rates (corrected for eustatic sea level changes). b) Apparent uplift rates along the cross section shown in Figure 4.22a compared to measurements from Figure 4.20.

Similar to the North Sea model, the Mid-Norway model mostly reproduces the uplift rate data within the error bounds (0.5 mm/year). Uplift rates reach much higher values than in the North Sea model, because the Mid-Norway model is located near the center of the Fennoscandian ice sheet. Along the coastline the Mid-Norway model (Figure 4.22) predicts uplift rates between 1 and 2 mm/year where measured values show an apparent uplift of 2

mm/year. The easternmost part of the Mid-Norway model uplifts at a rate of almost 8 mm/year and is located about three quarters along the way from the Norwegian coast to the Swedish coast which coincides with the location of the measured 7 mm/year isoline. Measured uplift rates in the offshore are exactly as predicted by the model even though these “measurements” are interpolations between uplift observations in western Norway and the Lofoten island chain.

Overall, the Mid-Norway model matches the measured uplift rates but slightly overpredicts uplift rates at the easternmost corner of the modeled area. This mismatch can be due to the already mentioned error sources (incorrect eustatic correction, oversimplified ice profile geometry) but might also result from model boundary effects.

So far, we have considered present-day uplift information. Radiocarbon dating of marine terraces, beach ridges, and the transition between lacustrine and marine sediments in lake basins can be used to construct shore displacement curves (showing elevation relative to sea level as a function of time). By comparing shore displacement curves from different locations, diagrams of shoreline tilt versus time can be constructed. Shoreline tilt information has the advantage that the eustatic sea level changes are eliminated. Kaland (1984) used dated core from dammed lakes of different heights to construct the shoreline tilt data shown in Figure 4.23. The analyzed lakes are scattered along a coast-normal cross section, located roughly 20 km north of Bergen. The solid line in Figure 4.23 shows the model-predicted shoreline tilt for the same area, based on the results of the best-fitting North Sea model. With the exception of the data point at 9500 years before present, the model nicely agrees with the data.

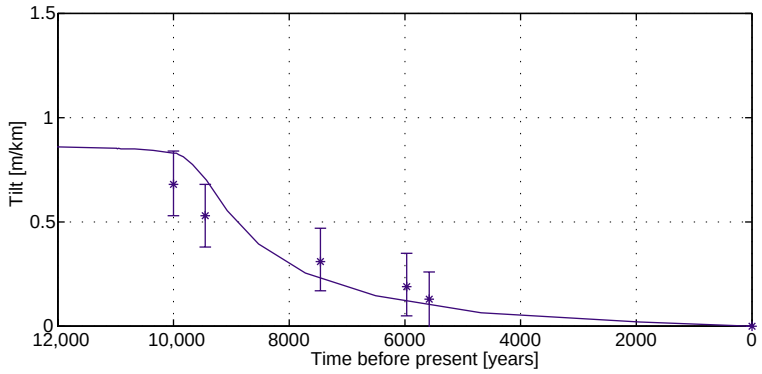

Figure 4.23: Modeled shoreline tilt ≈20 km north of Bergen compared to shoreline tilt measurements (Kaland, 1984).

Kjemperud (1986), constructed similar shoreline tilt data for the Trondheimfjord area and Figure 4.24 shows the comparison with our predictions from the Mid-Norway model. The model achieves an almost perfect match for the entire post-glacial period (later than

8000 years before present), but underestimates the shoreline tilt between 10,000 and 9000 years before present. The post-glacial model response is mainly affected by the chosen model rheologies but the ice geometry has only a minor influence. Thus, the comparison between model results and shoreline tilt data shows that the model includes appropriate rheologies. The under-predicted tilt at 10,000 years before present might suggest a over-simplified geometry of the modeled ice sheet.

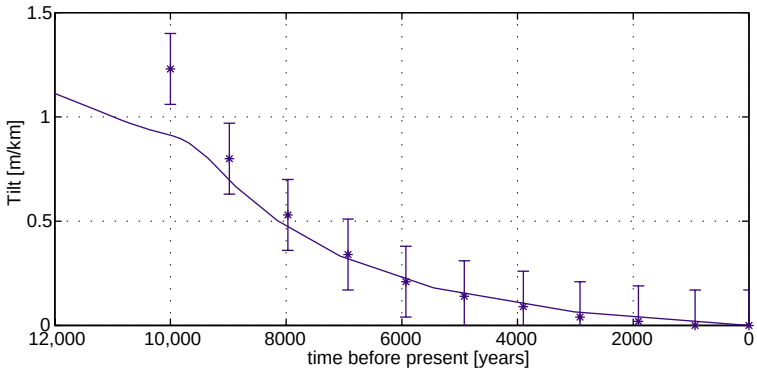

Figure 4.24: Modeled shoreline tilt in the Trondheimfjord area compared to shoreline tilt measurements (Kjemperud, 1986).

We have shown that both models match the observed apparent uplift rates within an acceptable error bound, and achieve an almost perfect fit with shoreline tilt data. At the same time, both models explain the majority of stress measurements throughout the entire area of investigation. The consistency of our model results with all available data from a variety of sources strongly supports the validity of our models.

4.4 Discussion

Clearly, the models presented include many assumptions such as ice sheet extents, ice sheet thicknesses, lithospheric structure, and rheologies. Ice sheet extents are fairly well known from mapping of submarine moraines and other morphological features (Andersen, 1981). Ice thicknesses are usually harder to constrain because they have to rely on ice flow models or scratch marks along Fjord walls (Mangerud, 1979) which only give the ice thickness near the perimeter of the ice sheet. Fortunately, our models are located near the ice sheet front so the ice thicknesses in our models are fairly well constrained. The lithospheric structure in the investigated areas is not flat-layered as assumed in the models. In fact, the Mid-Norwegian Margin was subjected to magmatic underplating (Mjelde et al., 1997), and the North Sea underwent rifting during Permo-Triassic and Jurassic-early Cretaceous times (e.g. Færseth et al., 1995). Regarding rheology, lab tests show that ductile behavior of rock

at conditions comparable to the lower crust and upper mantle is best described by power creep laws (e.g. Kirby, 1983; Carter and Tsenn, 1987). Our models use linearized viscoelasticity and therefore only approximate the real rheologies of the lower crust and the upper mantle. As previously mentioned, we chose simple lithospheric structures and rheologies because we tried to keep the models as straightforward as possible.

Despite all these simplifications, and by only including glacial loading and unloading as the unique source of deviatoric stress our models are able to roughly explain the observed stresses, i.e. S_{Hmax} orientations and S_{hmin} magnitudes, in both areas investigated. This suggests that ice loading and associated lithospheric flexure is a major stress contributor offshore Norway and that the model setup is not overly simplified. Prior to this study, spreading of the Mid-Atlantic ridge (ridge push) was assumed to be the most important stress source along the Norwegian passive margin (e.g. Lindholm et al., 1995), because observed S_{Hmax} orientations roughly align with the direction of plate motion. However, this study shows that lithospheric bending due to glacial loading and subsequent unloading matches the same observations, and furthermore explains local variations of the stress field, such as the rotation of S_{Hmax} in proximity of the coast, which can not be caused by ridge push. Importantly, we constrained our models with stress observations from the uppermost 5 km of the lithosphere. Consequently, our findings only apply to this depth range, i.e. ridge push might be important at greater depth but is masked by glacial bending stresses near the surface.

An important part of our models was the calibration process, which provided rough estimates of lithospheric viscosities. The North Sea model, as well as the Mid-Norway model show that the observed stresses can only be explained by including viscoelastic deformation within the lithosphere. In the North Sea the lithosphere must have viscosities between 10^{22} Pa s and 10^{23} Pa s, whereas viscosities on the Mid-Norwegian margin are probably slightly higher. The lithospheric viscosities can be related to characteristic strain rates at which the lithosphere deforms under constant loading conditions, such as plate tectonic forces, by dividing the characteristic differential stress by the viscosity. Assuming a differential stress between 1 and 10 MPa and a viscosity of 10^{23} Pa s (as obtained from our North Sea model calibration), the corresponding strain rate falls between 10^{-16} and 10^{-17} s^{-1}. Plate tectonic reconstructions and VLBI measurements suggest that the intraplate lithosphere globally deforms at strain rates $\leq 10^{-17}$ s^{-1} (Zoback and Townend, 2000). According to these considerations, our viscosity estimates for the North Sea are at the low end of allowable values. Due to an elevated heat flow (Dragoni et al., 1993) and the proximity to the continental margin, the lithospheric viscosity in the North Sea might be lower than the global intraplate average, which might explain this slight discrepancy with the

global strain rate predictions. Further north, on the Mid-Norwegian margin our models suggest viscosities between 10^{23} and 10^{24} Pa s, corresponding to strain rates of 10^{-17} to 10^{-18} s^{-1} which is compatible with the global strain rate estimates.

Furthermore, our estimates of lithospheric viscosities are compatible with estimates for the western United States by Flesch et al. (2000) and also agree with viscosity estimates from the linearization of power law behavior from lab tests (Strehlau and Meissner, 1987). The consistency of our models with such findings as well as the good match to stress and uplift data reinforce the validity of our models and thus the importance of glaciation on the stress field offshore Norway.

Having identified lithospheric bending due to the Fennoscandian ice shield as a major stress source along the Norwegian margin enables us to determine typical features of spatial stress variations. As in previous studies with two-dimensional models (e.g. Chapter 3) we show that deglaciation-related lithospheric bending increases horizontal stresses away from the former ice sheet and decreases horizontal stresses underneath the ice sheet in proximity of the ice front. This spatial stress change is caused by the interaction of bending stresses and the time-dependent response of the lower crust and the upper mantle. Near the coast, lithospheric bending due to ice sheet growth increased horizontal stresses at shallow depth but caused a stress decrease at the base of the lithosphere. In response to this stress decrease, the ductile portion of the lithosphere was extending irreversibly while near the surface the lithosphere was still in compression. Subsequent, ice melting caused the near surface compression to decrease near the coast. Had there been no permanent deformation in the ductile part of the lithosphere the near surface compression would simply disappear, but the ductile lithosphere transfers the accumulated extension to shallow depth, leading to decreased present-day horizontal stresses near the surface. Conversely, further offshore the lower lithosphere underwent irreversible compression which resulted in the observed horizontal stress increase. The three-dimensional models map out this transition from high to low horizontal stresses towards the coast in much more detail than the previous two-dimensional models and it is much easier to directly compare the modeled results with stress data (e.g. Figure 4.5).

Acknowledgments

We would like to thank Norsk Hydro for generously providing the data and financial support for this study.

Chapter 5

IMPACT OF GLACIALLY-INDUCED STRESS CHANGES ON HYDROCARBON EXPLORATION OFFSHORE NORWAY

This chapter will be published with Mark D. Zoback as co-author in an AAPG special issue.

5.1 Abstract

Three-dimensional models of lithospheric bending associated with glacial loading and unloading provided the evolution of the stress field in the Norwegian offshore areas. In this study, we have used this knowledge of temporal and lateral stress changes in the Norwegian sector of the North Sea, and on the Mid-Norwegian margin to estimate pore pressure changes due to the poroelastic response to glacially related stress changes. The locations of modeled overpressure coincide with areas of observed overpressures which shows that the glacially-induced stress changes had an impact on the reservoir pore pressure. However, the magnitude of the modeled overpressure is smaller than observed overpressures, which suggests that additional mechanisms, such as rapid sedimentation, also contribute to the observed overpressures. The temporally changing stress field leads to frequent reactivations of reservoir faults during the course of the Pleistocene glaciations, especially during Weichselian interglacials. As a result, hydrocarbon fields in the Norwegian offshore areas might have been exposed to multiple periods of extensive fault leakage.

5.2 Introduction

Extensive numerical modeling has shown that lithospheric bending due to the Pleistocene glaciations is the major source of lateral stress variations in the northern North Sea and on the Mid-Norwegian margin (Grollimund and Zoback, in prep.). The modeled stress variations mimic the observed orientations of the maximum horizontal stress (S_{Hmax}) as well as stress magnitudes, obtained from leak off test in more than 400 wells. In this study, we utilize the modeled stress information to estimate the impact of the Pleistocene glaciations on pore pressure changes, and on the leaking potential of major reservoir faults. The previously mentioned model results allow us to track stress changes with time and we can estimate the impact of these temporal stress changes on selected hydrocarbon reservoirs.

Hydrocarbon reservoirs along the Norwegian coast could have been affected by a number of processes related to the Plio-Pleistocene cold period. Uplift related to glacial processes can tilt hydrocarbon reservoirs and might cause leakage by changing the reservoir's spill point (Riis, 1992). Sales (1992) suggests that rapid subsidence and sedimentation due to glacial erosion of the onshore areas affects hydrocarbon reservoirs by maximizing the seal integrity.

In this study, we will investigate the effect of glaciation/deglaciation induced stress changes on pore pressure, and the effect of the temporally changing stress state on the

leaking behavior of reservoir faults. According to Engelder and Fischer (1994) pore pressure and stress are closely related via poroelastic processes. An induced horizontal stress increase due to lithospheric bending resulting from deglaciation, as observed in the Tampen Spur area west of the Viking Graben can cause a pore pressure increase which might explain the high overpressures observed in this area. The temporally changing stress field associated with ice growths and retreats can affect reservoir leakage by activating reservoir faults. According to a study by Wiprut and Zoback (2000) this process is responsible for current leakage in the Visund field.

5.3 The evolution of stress magnitudes

The models of lithospheric flexure due to glacial loading and loading show that the present-day stress field is the result of a long history during which stress magnitudes underwent repeated changes. In this section, we will illustrate the important components of the "stress path" which are responsible for the stress patterns observed today.

Figure 5.1 shows the temporal changes of the ratio of the maximum horizontal stress normalized by the vertical stress (S_{Hmax}/S_v), and similarly for the minimum horizontal stress (S_{hmin}/S_v) at a depth of 3000 m. The illustrated stress path is based on a model of lithospheric flexure for the northern North Sea and western Norway. Initial ice loading decreases the horizontal stress magnitudes in the vicinity of the ice front as a result of lithospheric flexure. A forebulge starts to form about 150 km off the Norwegian coast and consequently S_{Hmax}/S_v is slightly elevated to a value of 1.1. The ice covered onshore areas experience a horizontal stress increase as a result of the bent lithosphere (see Figure 3.4b). The above described stress pattern results from the immediate, elastic response to ice loading.

With time, the viscoelastic deformation significantly alters the horizontal stress magnitudes. 110,000 years ago, the forebulge has moved towards the coast and its shape is more pronounced which is evidenced by high horizontal stresses ($S_{Hmax}/S_v \approx 1.3$, $S_{hmin}/S_v \approx 1.1$) located no more than 100 km off the Norwegian coast. On land, the horizontal stress magnitudes are lower than immediately after ice emplacement because the viscoelastic lower lithosphere is extending under the weight of the overlying ice sheet. The lateral transition from high to low stress magnitudes (where $S_{Hmax}/S_v = S_{hmin}/S_v = 1$) is now closely tracing the ice front.

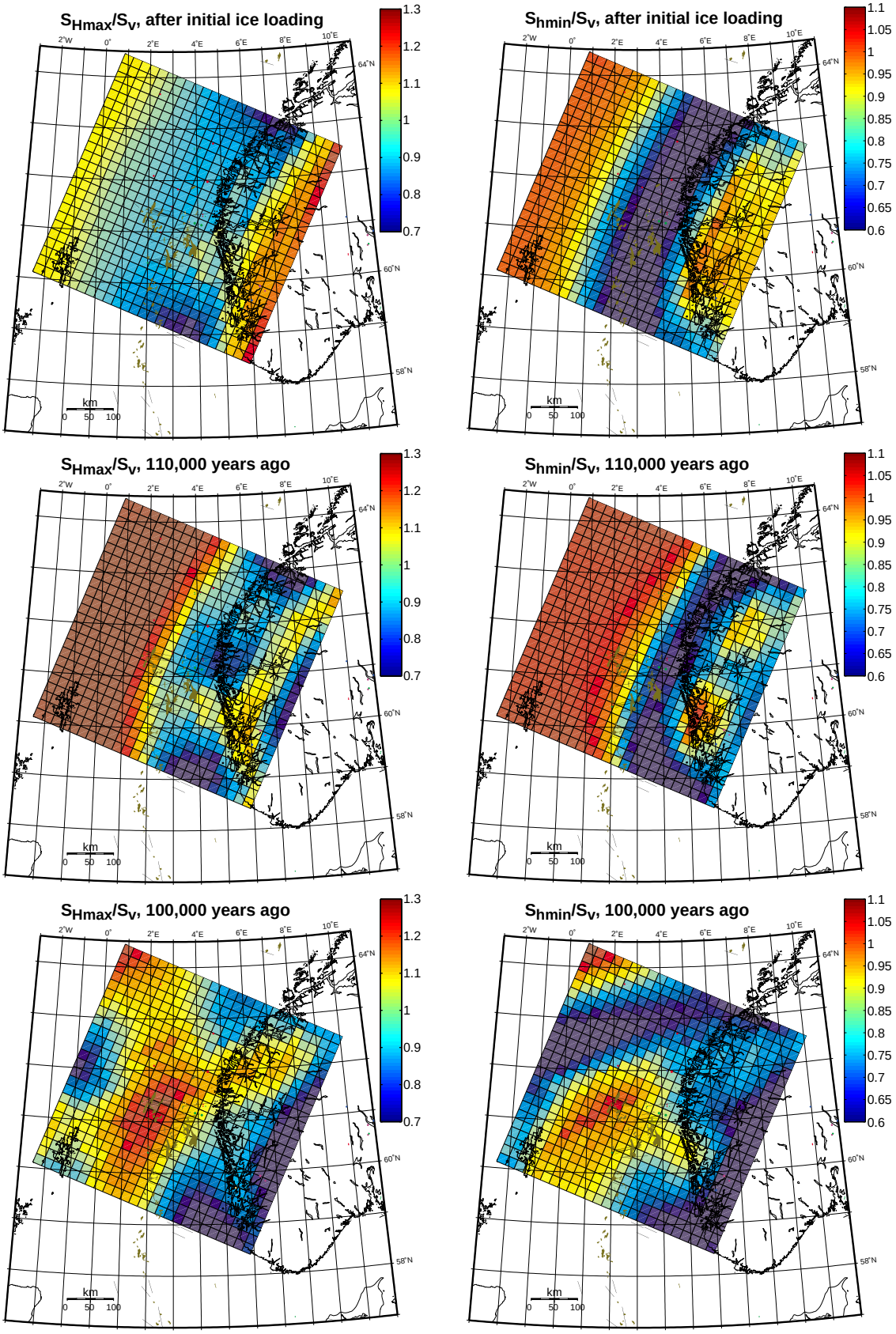
S_{Hmax}/S_V, after initial ice loading
S_{hmin}/S_V, after initial ice loading
S_{Hmax}/S_V, 110,000 years ago
S_{hmin}/S_V, 110,000 years ago
S_{Hmax}/S_V, 100,000 years ago
S_{hmin}/S_V, 100,000 years ago
2°W 0° 2°E 4°E 6°E 8°E 10°E
64°N 60°N 58°N
km
0 50 100
1.3 1.2 1.1 1 0.9 0.8 0.7
1.1 1.05 1 0.95 0.9 0.85 0.8 0.75 0.7 0.65 0.6

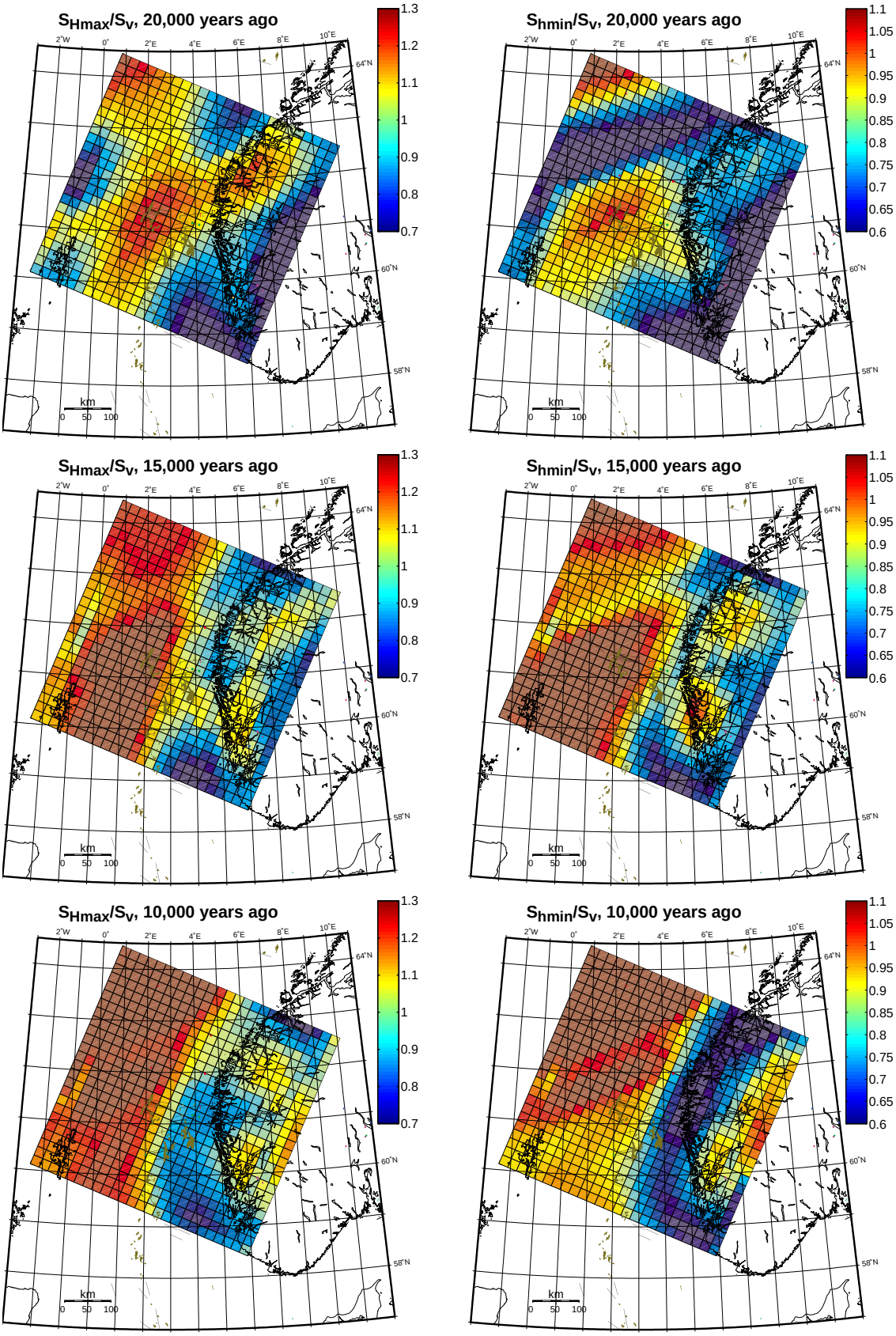
S_{Hmax}/S_V, 20,000 years ago
S_{hmin}/S_V, 20,000 years ago
S_{Hmax}/S_V, 15,000 years ago
S_{hmin}/S_V, 15,000 years ago
S_{Hmax}/S_V, 10,000 years ago
S_{hmin}/S_V, 10,000 years ago
2°W 0° 2°E 4°E 6°E 8°E 10°E
64°N 60°N 58°N
km
0 50 100
1.3 1.2 1.1 1 0.9 0.8 0.7
1.1 1.05 1 0.95 0.9 0.85 0.8 0.75 0.7 0.65 0.6

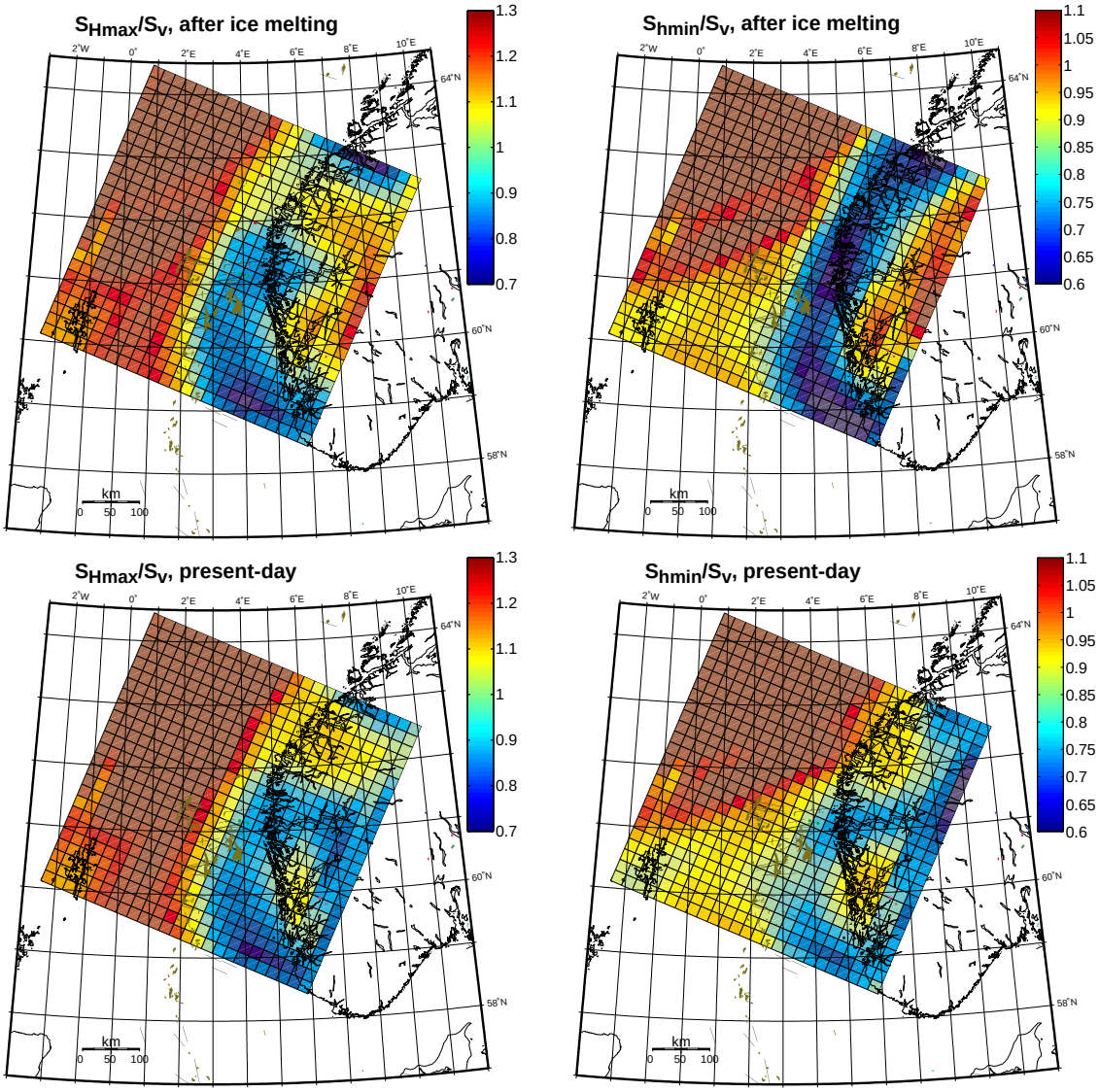

Figure 5.1: Temporal evolution of S_{Hmax}/S_v and S_{hmin}/S_v. The figure shows the spatial and temporal changes of S_{Hmax}/S_v, and S_{hmin}/S_v for the best-fitting North Sea model at a depth of 3000 m.

Between 110,000 years ago and 100,000 years ago, the ice sheet grew to its maximum (Weichselian) extent. The resulting horizontal stress magnitudes are a mixture between the long-term "imprint" of the pre Weichselian ice sheet and the elastic response to the newly grown Weichselian ice sheet. A zone of low S_{hmin}/S_v values forms near the new ice front, roughly between 62ºN and 63ºN, but S_{Hmax}/S_v still tends to be higher in the former forebulge. A laterally confined zone of high horizontal stress magnitudes forms with the Tampen Spur in its center. In this zone, compressional bending underneath the large ice sheet adds constructively to the already existing high stresses due to the previous forebulge. Closer to the center of the large ice sheet, bending of the lithosphere is negligible, so the

horizontal stresses do not change much. However, S_v increases drastically due to the overlying ice mass which causes the S_{Hmax}/S_v and S_{hmin}/S_v ratios to drop significantly. For example, S_{Hmax}/S_v reaches values below 0.7 in southwestern Norway.

The modeled Weichselian ice sheet lasts only for 80,000 years. Thus, viscoelastic processes do not have enough time to significantly alter the lithosphere which explains why stress magnitudes remain almost unchanged between 100,000 and 20,000 years ago. After the ice sheet's melt back to the 15,000 years extent, the stress magnitudes largely return to their pre-Weichselian (110,000 years ago) values. However, the comparison of horizontal stress magnitudes between 110,000 and 15,000 years ago reveals that S_{Hmax} and S_{hmin} were permanently reduced outside the large ice sheet's perimeter. Conversely, areas that were ice covered experienced a permanent S_{Hmax} and S_{hmin} increase if located within ≈150 km from the ice front (e.g. Troll).

The continuing retreat of the ice sheet to its 10,000 years extent leads to a relatively simple stress pattern, exhibiting low horizontal stresses near the coast and high stresses almost everywhere else. The ice front of the 10,000 years extent was located between 20 and 50 km inland from the current coast line and caused decreasing horizontal stress magnitudes along the coast, and in near-coastal offshore areas. These areas were already exposed to relatively low horizontal stresses 15,000 years ago, so the effect of the 10,000 years ice extent was even more pronounced. At distances of approximately 100 km inland of the present-day coastline, lithospheric flexure due to the 10,000 years ice extent caused compression and as a result increased the horizontal stresses drastically.

Between 10,000 years ago and the completion of ice melting, the horizontal stresses remained more or less unchanged. However, in areas that were still covered by ice at the 10,000 years stage (e.g. 60.5ºN, 8ºE) the S_{Hmax}/S_v, and S_{hmin}/S_v ratios increased significantly because the disappearing ice lowered S_v. Consequently, S_{Hmax} and S_{hmin}, were higher than the vertical stress after ice melting which corresponds to a thrust faulting stress state. In northern Norway, and in northern Sweden, there is ample evidence for active thrust faulting, immediately following deglaciation (e.g. Olesen, 1988; Lagerbäck, 1990). These fault scarps were found at distances between 100 km 200 km from the current coastline. Our North Sea model predicts post-glacial, thrust faulting stress states at comparable distances from the coast.

Post-glacial lithospheric rebound reduces these high horizontal stresses in the onshore areas and leads to the stress patterns as discussed in previous sections. The present-day stress magnitudes are an artifact of the pre-Weichselian ice sheet with a limited influence of the large, Weichselian ice sheet.

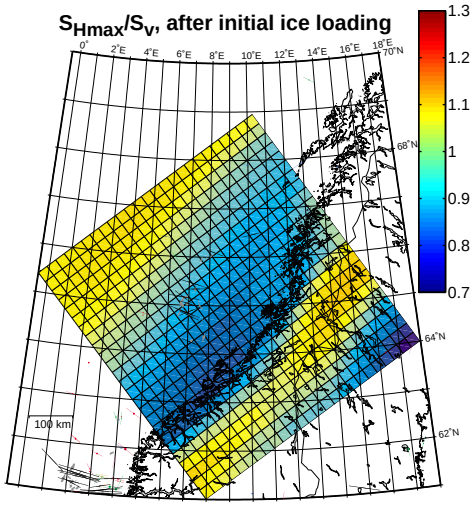
S_{Hmax}/S_V, after initial ice loading
1.3
1.2
1.1
1
0.9
0.8
0.7
70°N
68°N
64°N
62°N
100 km

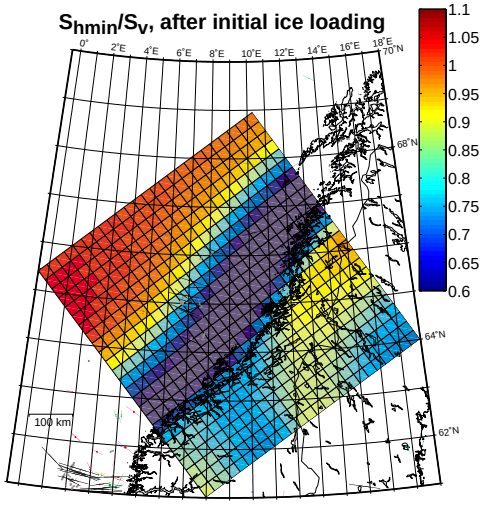
S_{hmin}/S_V, after initial ice loading
1.1
1.05
1
0.95
0.9
0.85
0.8
0.75
0.7
0.65
0.6
70°N
68°N
64°N
62°N
100 km

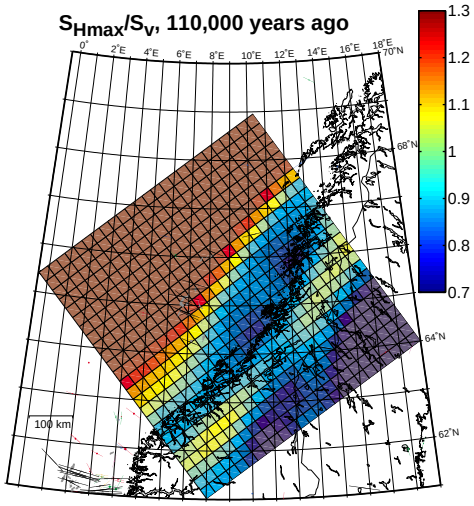
S_{Hmax}/S_V, 110,000 years ago
1.3
1.2
1.1
1
0.9
0.8
0.7
70°N
68°N
64°N
62°N
100 km

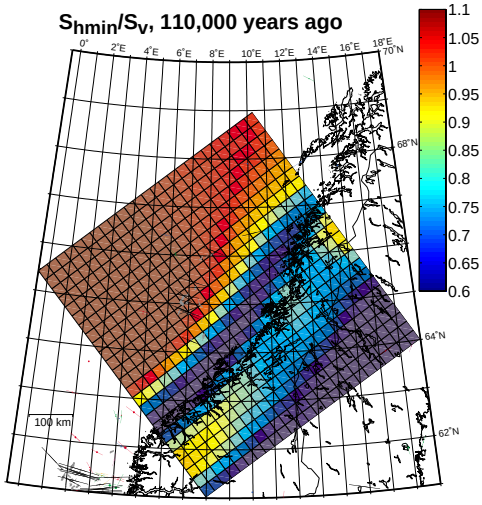
S_{hmin}/S_V, 110,000 years ago
1.1
1.05
1
0.95
0.9
0.85
0.8
0.75
0.7
0.65
0.6
70°N
68°N
64°N
62°N
100 km

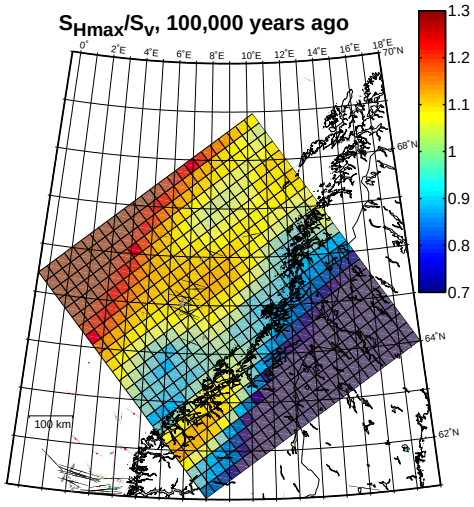
S_{Hmax}/S_V, 100,000 years ago
1.3
1.2
1.1
1
0.9
0.8
0.7
70°N
68°N
64°N
62°N
100 km

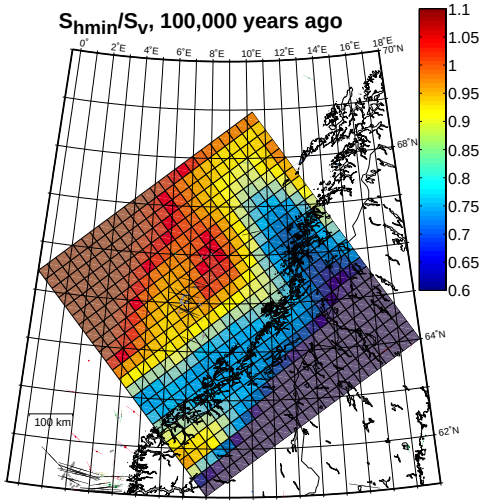
S_{hmin}/S_V, 100,000 years ago
1.1
1.05
1
0.95
0.9
0.85
0.8
0.75
0.7
0.65
0.6
70°N
68°N
64°N
62°N
100 km

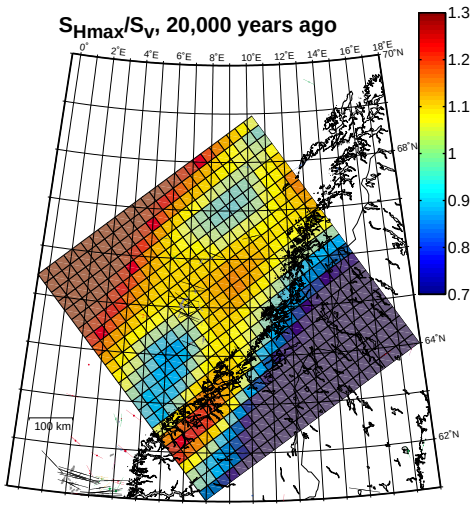
S_{Hmax}/S_V, 20,000 years ago
1.3
1.2
1.1
1
0.9
0.8
0.7
0° 2°E 4°E 6°E 8°E 10°E 12°E 14°E 16°E 18°E
70°N
68°N
64°N
62°N
100 km

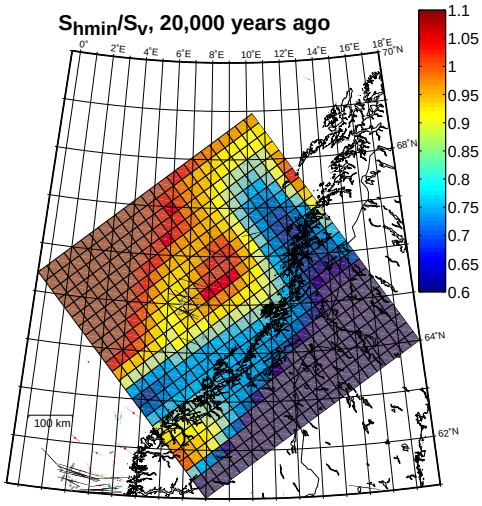
S_{hmin}/S_V, 20,000 years ago
1.1
1.05
1
0.95
0.9
0.85
0.8
0.75
0.7
0.65
0.6
0° 2°E 4°E 6°E 8°E 10°E 12°E 14°E 16°E 18°E
70°N
68°N
64°N
62°N
100 km

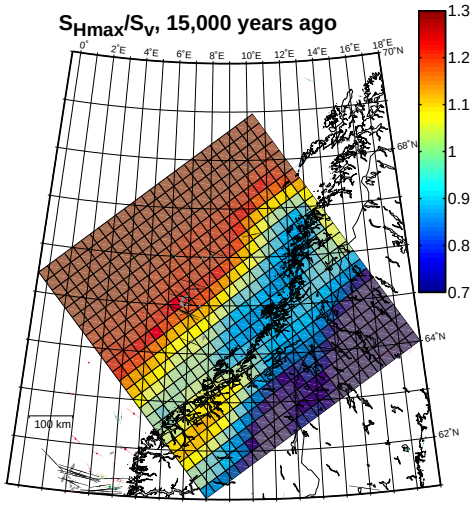
S_{Hmax}/S_V, 15,000 years ago
1.3
1.2
1.1
1
0.9
0.8
0.7
0° 2°E 4°E 6°E 8°E 10°E 12°E 14°E 16°E 18°E
70°N
68°N
64°N
62°N
100 km

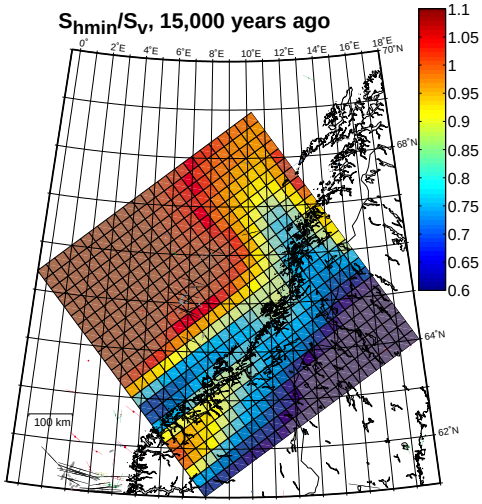
S_{hmin}/S_V, 15,000 years ago
1.1
1.05
1
0.95
0.9
0.85
0.8
0.75
0.7
0.65
0.6
0° 2°E 4°E 6°E 8°E 10°E 12°E 14°E 16°E 18°E
70°N
68°N
64°N
62°N
100 km

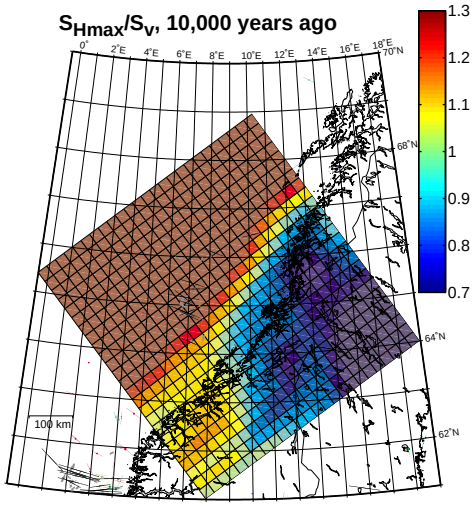
S_{Hmax}/S_V, 10,000 years ago
1.3
1.2
1.1
1
0.9
0.8
0.7
0° 2°E 4°E 6°E 8°E 10°E 12°E 14°E 16°E 18°E
70°N
68°N
64°N
62°N
100 km

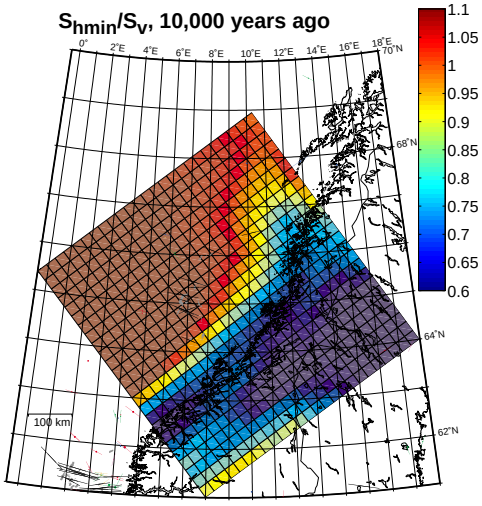
S_{hmin}/S_V, 10,000 years ago
1.1
1.05
1
0.95
0.9
0.85
0.8
0.75
0.7
0.65
0.6
0° 2°E 4°E 6°E 8°E 10°E 12°E 14°E 16°E 18°E
70°N
68°N
64°N
62°N
100 km

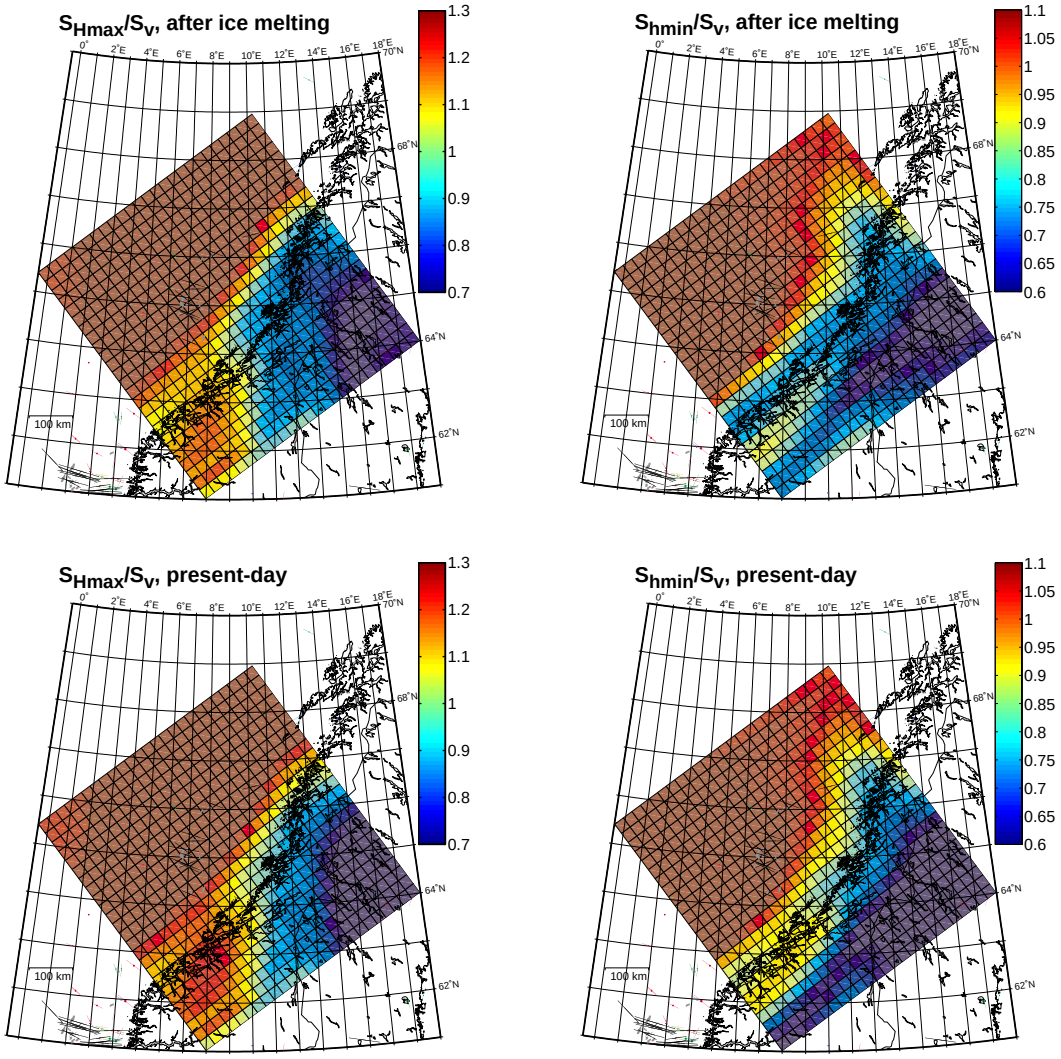

Figure 5.2: Temporal evolution of S_{Hmax}/S_v and S_{hmin}/S_v. The figure shows the spatial and temporal changes of S_{Hmax}/S_v, and S_{hmin}/S_v for the blind-test Mid Norway model at a depth of 3000 m.

Figure 5.2 shows the evolution of stress magnitudes for the Mid-Norwegian margin at a depth of 3000 m. Initial loading of the pre-Weichselian ice sheet causes an approximately 100 km-wide zone of decreased horizontal stresses following the ice front (comparable to the North Sea). The peripheral forebulge forms to the northwest of the Mid Norwegian hydrocarbon fields (Halten Terrace). Subsequent lithospheric relaxation during the pre-Weichselian glacial period lets the forebulge migrate eastward, leading to a gradual increase of horizontal stresses in the vicinity of the Halten Terrace until 110,000 years ago S_{hmin} exceeds the vertical stress (i.e. $S_{hmin}/S_v > 1$) and S_{Hmax}/S_v is above 1.3.

The advance of the large Weichselian ice sheet reduces the S_{Hmax}/S_v and S_{hmin}/S_v ratios on the Halten Terrace, mainly by increasing S_v. The zone of low horizontal stresses along the coast becomes less pronounced because the large ice sheet bends the lithosphere between the ice front and the current coast line such that horizontal stress magnitudes increase. In the easternmost part of the model the horizontal stress ratios drop significantly because the immense weight of the overlying ice sheet increases S_v.

During the existence of the Weichselian ice sheet, the lithosphere does not undergo significant viscous deformation. Thus, the stress pattern shows only minor changes between 100,000 years ago and 20,000 years ago. Accordingly, 15,000 years ago the stress conditions roughly return to the pre-Weichselian state (110,000 years ago). After 15,000 years ago, the disappearing ice sheet hardly affected the horizontal stress ratios.

At present-day, the modeled horizontal stresses are elevated in almost all the Mid-Norwegian offshore areas. The easternmost part of the Mid-Norway model shows drastically reduced horizontal stresses. These are mainly due to the large spatial gradient in ice thickness of the Weichselian ice sheet which reached a thickness of more than 2500 meters within the modeled area. As a result of this "steep" ice sheet, the rebounding lithosphere shows a strong "updoming" behavior where inland areas uplift much faster than the coastal provinces. This effect causes near surface extension which explains the low horizontal stresses.

5.4 Predicted pore pressure changes

We can estimate the pore pressure change in the northern North Sea due to glacial loading and unloading resulting from the poroelastic response to stress changes by multiplying the change in the first stress invariant ($\Delta\sigma_m$) by Skempton's coefficient (B), where B varies between 0 and 1. For B=1 the change in P_p is equal to $\Delta\sigma_m$ and for B=0 any change in $\Delta\sigma_m$ doesn't affect the pore pressure. For our calculations we assume B=0.8, which is an upper bound for realistic values of B and typical for shales. Reservoir sands with high porosities typically have B-values of ≈0.5. We chose a relatively high B-value since we wanted to get an upper bound on how deglaciation influences the pore pressure.

Figure 5.3: (next page) Overpressure in the North Sea. The figure compares predicted overpressure (a) to measured overpressure (b) for the Norwegian sector of the North Sea at a depth of 3000 m. To a first order the patterns of predicted and observed overpressure agree. The absolute scale of measured overpressure is confidential.

a)

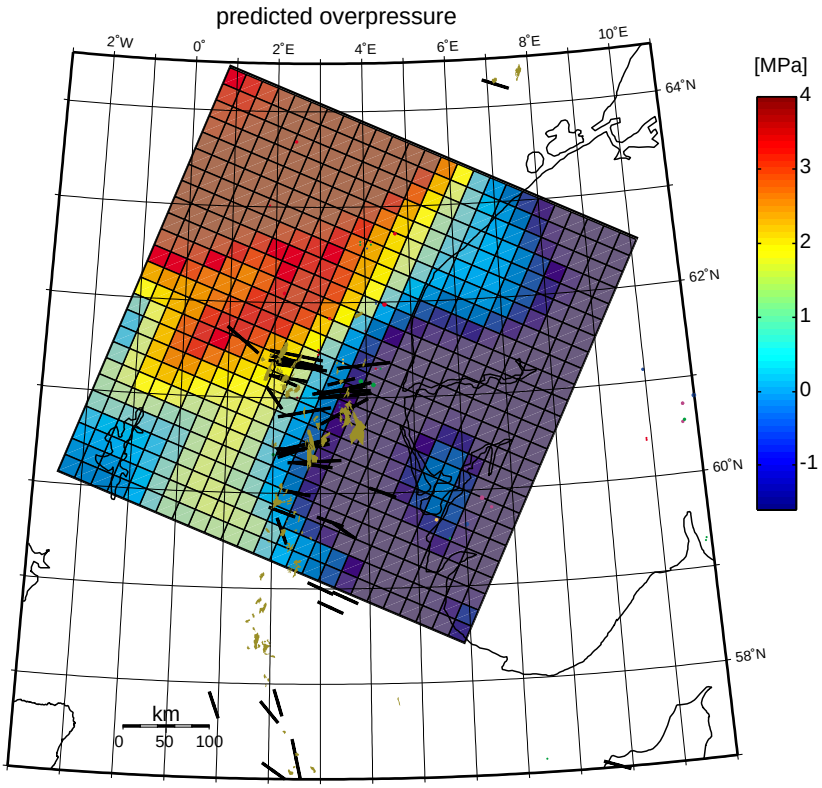
predicted overpressure
2°W
0°
2°E
4°E
6°E
8°E
10°E
64°N
62°N
60°N
58°N
[MPa]
4
3
2
1
0
-1
km
0
50
100

b)

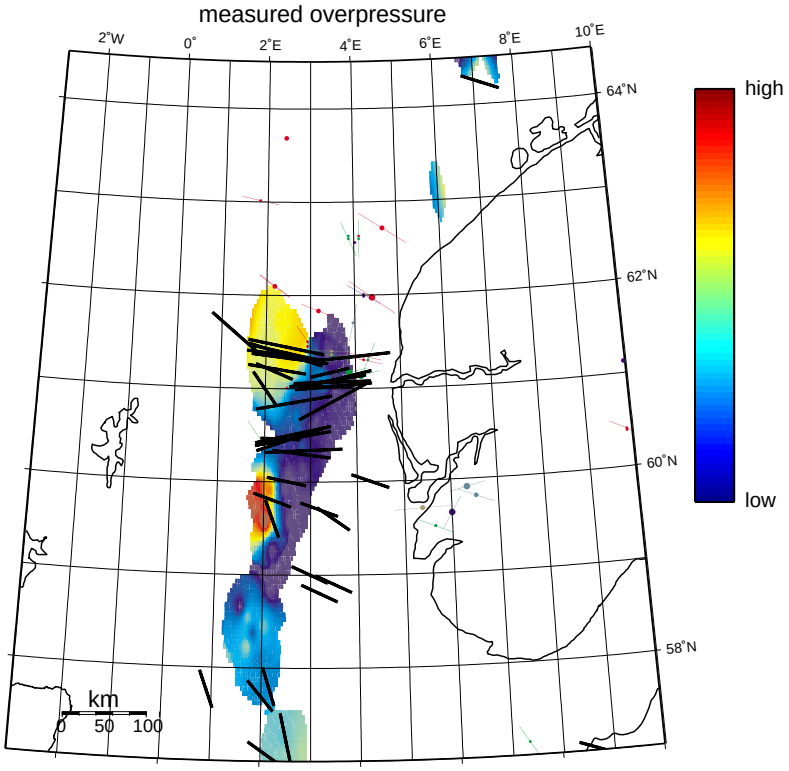
measured overpressure
2°W
0°
2°E
4°E
6°E
8°E
10°E
64°N
62°N
60°N
58°N
high
low
km
0
50
100

a)

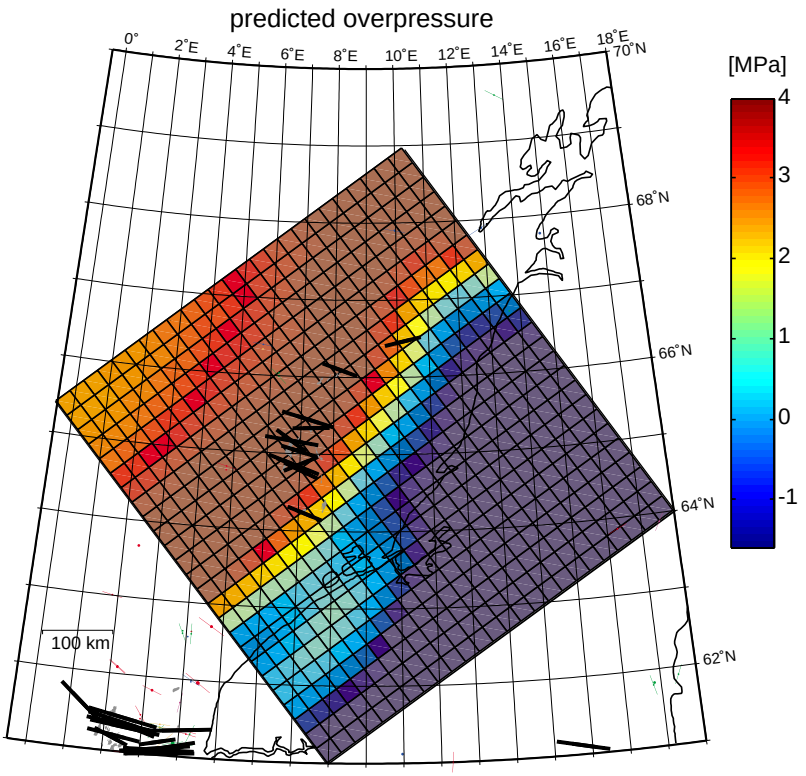
predicted overpressure
0°
2°E
4°E
6°E
8°E
10°E
12°E
14°E
16°E
18°E
70°N
68°N
66°N
64°N
62°N
[MPa]
4
3
2
1
0
-1
100 km

b)

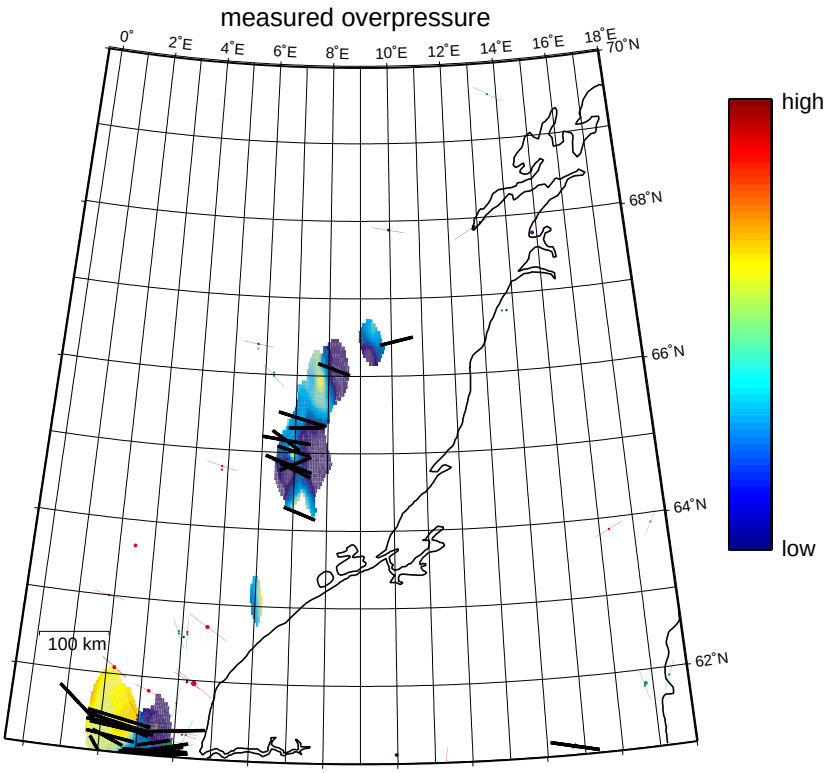
measured overpressure
0°
2°E
4°E
6°E
8°E
10°E
12°E
14°E
16°E
18°E
70°N
68°N
66°N
64°N
62°N
high
low
100 km

Figure 5.4: (previous page) Overpressure in Mid-Norway. Comparison of predicted overpressure and measured overpressure on the Mid-Norwegian margin at a depth of 3000 m. There is no evident correlation between predicted and observed overpressure in this area. The absolute scale of measured overpressure is confidential.

Figure 5.3 compares the estimated pore pressure to measured overpressures in the Norwegian Sector of the North Sea, and Figure 5.4 does a similar comparison for the Mid-Norwegian margin. Figure 5.3 shows that the spatial pattern of predicted overpressure in the North Sea roughly agrees with the observed overpressures. In the vicinity of the Tampen Spur (≈61.5ºN, 2ºE) the model predicts overpressures on the order of 2 to 3 MPa and the observations show moderate to high overpressures in this area. Closer to the coast, around 61ºN and 4ºE, no overpressure is suggested either by the model or by the measurements. Further south, at a latitude of 60ºN, the model matches the observed transition from overpressured units west of 2.5ºE to hydrostatic pore pressures closer to the coast. Even though the model achieves an acceptable match to the spatial distribution of measured overpressures, the magnitude of the predicted pore pressure increase is negligible (no more than 3 MPa). This finding agrees with the two-dimensional model in Chapter 3 which gave a maximum overpressure of 3.5 MPa. However, observed overpressures are much more severe and often exceed 15 MPa at a depth of 3000 m below sea level. Thus, the three-dimensional North Sea model confirms the finding from Section 3.5 that additional sources of overpressure, such as under-compaction, are more important than the poroelastic response to bending stresses due to glacial loading and unloading.

On the Mid-Norwegian margin (Figure 5.4) the model predicts an approximately 100 km-wide zone of overpressures reaching values of ≈4 MPa and most of the hydrocarbon discoveries in Mid-Norway are located within this zone. According to the model, the overpressure decreases towards the coast where the pore pressure is predicted to be close to hydrostatic. It is impossible to check these predicted, spatial variations with measured pore pressures because the measurements cover only a relatively small area. But, even within this area the measurements suggest a complicated pattern of spatial pore pressure variations that is not predicted by the model. As the model only suggests a maximum pore pressure change of ≈4 MPa the measured variations are probably due to a different source of overpressure (such as under-compaction).

In conclusion, poroelastic pore pressure changes due to glacial loading and unloading are only a secondary source of overpressure in the Norwegian offshore areas leading to a maximum overpressure of ≈4 MPa. Nevertheless, in the North Sea the model is able to roughly predict the spatial variations of overpressure with a transition from overpressured reservoirs far offshore, to hydrostatic pore pressures in proximity of the coast.

5.5 Predicted sealing/leaking behavior of faults

In this section, we will use the knowledge of temporal stress changes to predict whether faults offshore Norway were sealing or leaking in the past. Our analysis is based on the findings of Barton et al. (1995) who suggested that critically stressed faults (i.e., capable of slipping in the current stress field) are permeable whereas not critically stressed faults are impermeable. Wiprut and Zoback (2000) showed that this concept can be used to asses the current sealing/leaking potential of reservoir-bounding faults in the Visund field.

To characterize a fault's sealing/leaking behavior during the past, we calculate the pore pressure change required to make the fault critically stressed (ΔPp_{crit}). The lower ΔPp_{crit}, the more likely it is for a fault to be leaking, i.e. small pore pressure changes can activate fault slip. We calculate ΔPp_{crit} for a certain fault with the following methodology: First we determine the fault normal vector (n) for a given dip azimuth (θ) and dip angle (ϕ) according to Equation 5.1 assuming a right-handed coordinate system:

$$\mathbf{n} = \begin{bmatrix} -\sin\theta\sin\phi \\ -\cos\theta\cos\phi \\ \cos\phi \end{bmatrix} \qquad \text{Eqn. 5.1}$$

Then we calculate the fault's traction vector (t) for every model time step by simply multiplying the stress tensor (in the geographic coordinate system) by n. The resolved normal stress (t_n) and the resolved shear stress (t_s) on the fault plane can be easily determined:

$$\mathbf{t_n} = \mathbf{t} \cdot \mathbf{n} \qquad \text{Eqn. 5.2}$$

$$\mathbf{t_s} = |\mathbf{t} - \mathbf{n}\mathbf{t_n}| \qquad \text{Eqn. 5.3}$$

And finally, the Mohr-Coulomb criterion yields the following relationship for frictional sliding in the absence of cohesion:

$$\Delta\mathbf{Pp_{crit}} = \mathbf{t_n} - \mathbf{Pp} - \frac{\mathbf{t_s}}{\tan\mu} \qquad \text{Eqn. 5.4}$$

We used the stress results obtained from the North Sea model along with fault orientations from some representative faults in the Visund, Fram, and Oseberg fields (see Figure 2.3 for locations). We have tested different ice models, incorporating Weichselian interglacials (ice model 3), and pre-Weichselian climate variations (ice model 5). The predicted present-day stresses were unaffected by these interglacials but they might play an important role for fault reactivation. For this reason, we present our fault analysis for both ice models. The fault orientations are obtained from depth-converted seismic data (pers. com. D. Wiprut) and are summarized in Table 5.1.

Table 5.1: Fault orientations used in the sealing/leaking analysis

Field	Fault	θ	ϕ
Visund	A north	102	21
Visund	A central	95	35
Visund	EW-3	68	21
Fram	F6	107	59
Fram	F7	278	54
Fram	Fkr 2	307	53
Oseberg	F43	226	39
Oseberg	F63	235	56
Oseberg	F217	265	44
Oseberg	F275	289	43

These fault orientations are average values that are representative for large parts of the analyzed faults at the modeled depth of 3000 m. As we only consider averaged fault orientations, our fault analysis does not reveal the exact location of potential leakage. Instead, the goal is to roughly estimate the potential for leakage in the chosen hydrocarbon fields during the past using some examples of representative fault orientations.

Importantly, our models calculated stress by assuming a hydrostatic pore pressure throughout the entire model duration. Realistically, P_p might have changed due to many possible mechanisms such as under-compaction, and hydrocarbon maturation. The changing P_p might have triggered active faulting which could have caused leaking and in turn affected P_p. For these reasons, a realistic fault analysis should be based on a model which consists of a mechanical module (such as our models) and a flow model accounting for P_p changing processes. The two modules would have to be coupled, i.e. changes in stress affect the pore pressure and vice versa. Such a coupled model would be very ambitious and is certainly above the scope of this project. Consequently, our predictions of time-varying ΔPp_{crit} are only very rough estimations. The most valuable information that

can be gained from our analysis is probably the relative change of ΔPp_{crit} with changing ice sheet extents, whereas provided absolute ΔPp_{crit} values for a specific time are meaningless.

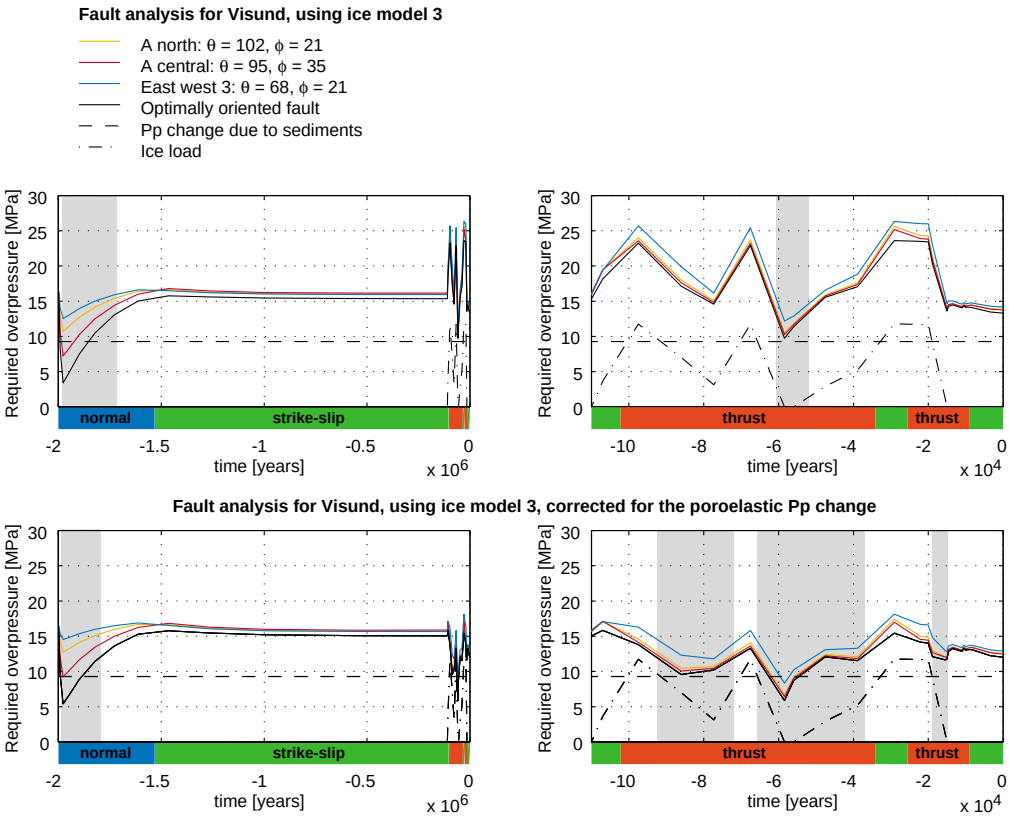

Figure 5.5: Calculated ΔPp_{crit} for Visund, assuming ice model 3. The left panels show the entire model duration. The panels on the right only display the last 110,000 years. In contrast to the upper panels, the lower panels calculate ΔPp_{crit} by including the poroelastic response of P_p to stress changes since the onset of glaciation. The dashed line shows the estimated P_p-change resulting from under-compaction. The dash-dotted line illustrates the ice loaded in the area. The grey shaded areas illustrate periods when active fault slip was feasible.

We will present all results of the fault analysis in the manner of Figure 5.5. The two upper panels plot ΔPp_{crit} as a function of time, analyzing three faults in the Visund field (colored lines) and a hypothetical, optimally-oriented fault (black line). The upper left panel covers the entire model duration while the upper right panel zooms in on the last 110,000 years, including the Weichselian glaciations. An estimate of the possible influence of under-compaction (due to rapid Pleistocene sedimentation) on the pore pressure is shown with the dashed black line. We calculated this estimate by multiplying the overburden of the unconsolidated sediments by Skempton's coefficient. The density and thickness of the poorly consolidated Hordaland Group are obtained from drilling information and we assume B = 0.6. Our method of calculating an under-compaction driven

P_p-increase gives an upper bound, because we are assuming that $\Delta\sigma_m \approx \Delta S_v$ which implies that either Poisson's ratio is close to 0.5, or creep deformation within the reservoir is fast (relative to drainage). Lastly, the dash-dotted line shows the overburden stress due to the overlying ice sheet, and the color bar below the time axis shows the varying stress regimes (blue = normal faulting, green = strike-slip faulting, red = thrust faulting).

The two lower panels are identical to the upper panels but ΔPp_{crit} is corrected for a poroelastic pore pressure change. In other words, instead of using Equation 5.4 we calculated ΔPp_{crit} with Equation 5.5 which additionally includes the $B\Delta\sigma_m$ term.

$$\Delta \mathbf{Pp_{crit}} = \mathbf{t_n} - \mathbf{Pp} - \mathbf{B}\Delta\sigma_{\mathbf{m}} - \frac{\mathbf{t_s}}{\tan\mu} \qquad \text{Eqn. 5.5}$$

The grey shaded areas mark time periods when ΔPp_{crit} was below the present-day value for an optimally oriented fault. During these periods active fault slip was feasible.

Fault analysis in Visund

As mentioned earlier our absolute predictions of ΔPp_{crit} are unreliable so we need a means of calibrating our analysis. According to Wiprut and Zoback (2000), faults in Visund are very close to being critically stressed in the current stress field and there is evidence for gas leakage above the A central fault (Figure 5.6). Most faults in Visund are dipping no more than 35º, so the field is most susceptible to leakage under thrust-faulting conditions. Possible episodes of fault slip-related leakage might have occurred on all the studied faults in Visund during the interglacial at 60,000 years before present, because ΔPp_{crit} was below the present-day value. Also, the initial loading of the ice sheet at the onset of the Pleistocene drastically reduced ΔPp_{crit} which might have promoted a phase of leakage in the Visund field. The A central fault generally has the most favorable orientation for leakage, because it is almost optimally oriented for reverse faulting with the prevailing, WNW-striking S_{Hmax} orientation. Conversely, EW-3 strikes almost parallel to S_{Hmax} and therefore tends to be less prone to active fault slip. However, the differences in ΔPp_{crit} between the analyzed faults during the last 110,000 years are minute. The poroelastic correction (lower panels in Figure 5.5) damps the ΔPp_{crit} oscillations and slightly lowers the absolute values of ΔPp_{crit}. More specifically, the required overpressure for leakage is mostly below the present-day level during the Weichselian cold period, suggesting a higher tendency for leakage. At the 60,000 years bp interglacial ΔPp_{crit} even drops below the under-compaction pore pressure line (dashed black line), implying that under-compaction in combination with glacial loading and unloading alone could have caused leakage on all the studied fault

orientations..

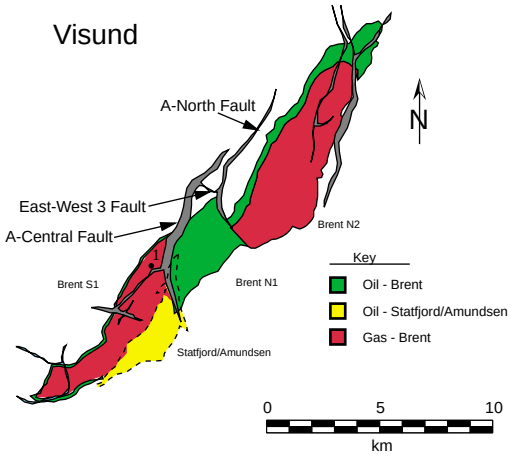

Figure 5.6: Structural map of the Visund field showing the major faults and the reservoir extent.

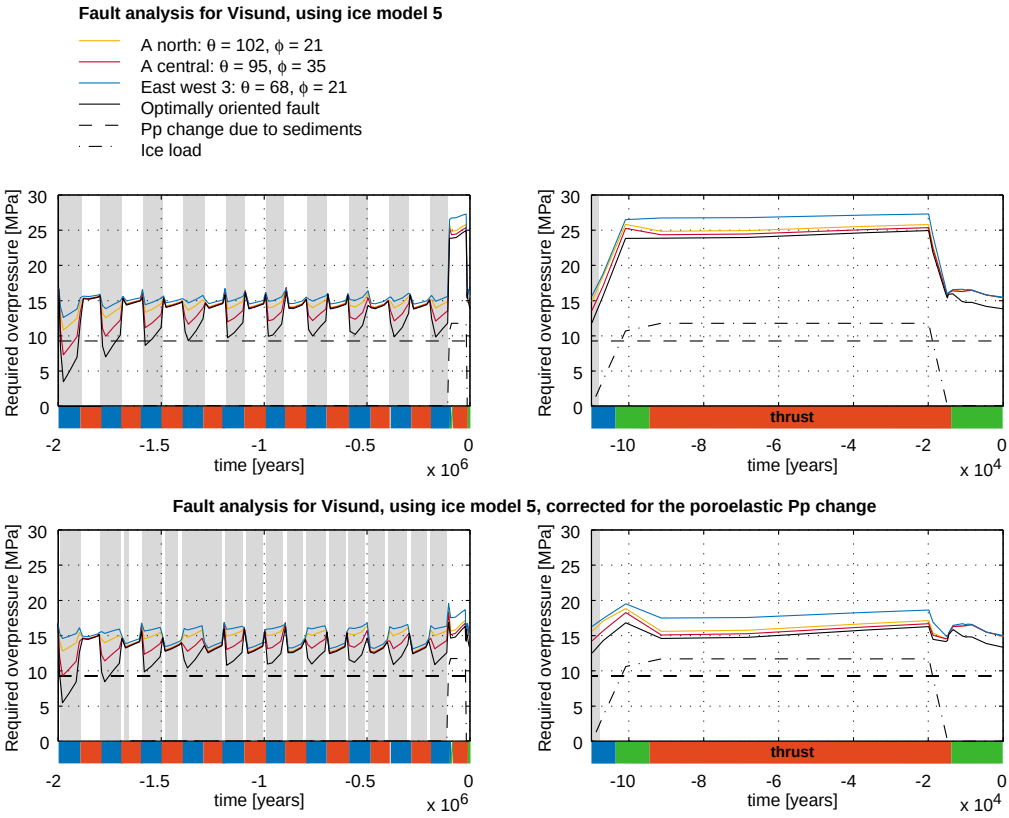

Figure 5.7: Calculated ΔPp_{crit} for Visund, assuming ice model 5 with a varying, pre-Weichselian ice sheet. The left panels show the entire model duration. The panels on the right only display the last 110,000 years. In contrast to the upper panels, the lower panels calculate ΔPp_{crit} by including the poroelastic response of P_p to stress changes since the onset of glaciation. The dashed line shows the estimated P_p-change resulting

from under-compaction. The dash-dotted line illustrates the ice loaded in the area. The grey shaded areas illustrate periods when active fault slip was feasible.

By using ice model 5, we can more closely investigate the influence of the pre-Weichselian ice fluctuations on leakage in the Visund field (Figure 5.7). Initial ice loading, 2 million years ago causes ΔPp_{crit} to drop considerably and subsequent ice melting restores the stress conditions on the faults to the initial state. Succeeding ice cycles cause a repeating pattern of dropping and increasing ΔPp_{crit}, which suggests that fault slip occurred during ice advances while ice melting halted possible fault movements. The A central fault was most susceptible to reactivation during pre-Weichselian cold periods, with ΔPp_{crit} being close to the under-compaction caused P_p-change (dashed line). The Weichselian ice growth causes an opposite effect, in that the advancing ice sheet moves the faults away from failure because the Weichselian ice sheet actually covered the Visund field. As a result, the stress state in Visund was affected by the direct overburden of the ice sheet, which tends to prevent failure (e.g. Johnston, 1987). Conversely, the pre-Weichselian ice sheet never crossed the Viking Graben and therefore only indirectly influences the Visund field by changing the stress field as a result of lithospheric flexure which led to a lowered ΔPp_{crit}. The poroelastic correction mostly affects the stress state during the Weichselian glaciation when ΔPp_{crit} does not increase as much as without the poroelastic correction.

In conclusion, considering that parts of the A central fault are currently leaking, it is likely that leakage on this fault occurred whenever the ice sheet grew to its 15 ka extent (pre-Weichselian) and possibly during Weichselian interglacials. Throughout the entire pre-Weichselian Pleistocene, the A central fault was most likely to be critically stressed whereas the A north and the EW-3 faults were less susceptible to reactivation. During the Weichselian interglacials the A north and the A central could have been reactivated as they both were well-oriented for reverse faulting.

Fault analysis in Fram

In contrast to Visund, the Fram field shows no clear evidence for current leakage due to active fault slip. Faults in Fram dip more steeply than in Visund making them more susceptible for reactivation under normal faulting or strike-slip faulting conditions. Some seismic cross sections might suggest gas chimneys above north-south trending faults but the evidence is inconclusive (pers. com. D. Wiprut). As shown in Chapter 2, Fram has a lower pore pressure than Visund which is one of the main reasons why the current leaking potential is reduced. Figure 5.9 shows that the under-compaction driven P_p-change is less than 5 MPa which might partly explain the low observed pore pressure. Assuming that faults in Fram are currently sealing, ice model 3 (Figure 5.9) suggests that leakage could

have occurred during the long interglacial at 60,000 years before present. At that time, fault orientations similar to F7, and Fkr 2 (Figure 5.8) were more likely to be reactivated under the reverse faulting conditions than the more steeply dipping F6 fault. The pre-Weichselian ice sheet exposed Fram to normal faulting which drastically reduced ΔPp_{crit} on most faults as they are almost perfectly oriented for normal faulting.

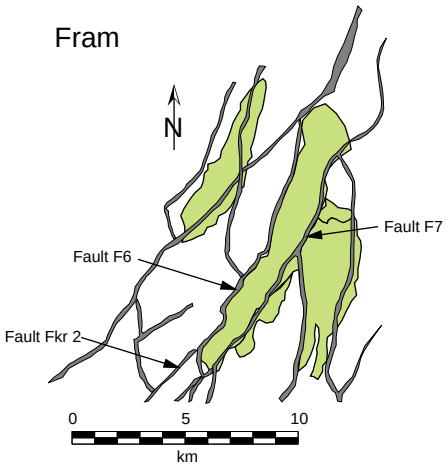

Figure 5.8: Structural map of the Fram field showing the major faults and the reservoir extent.

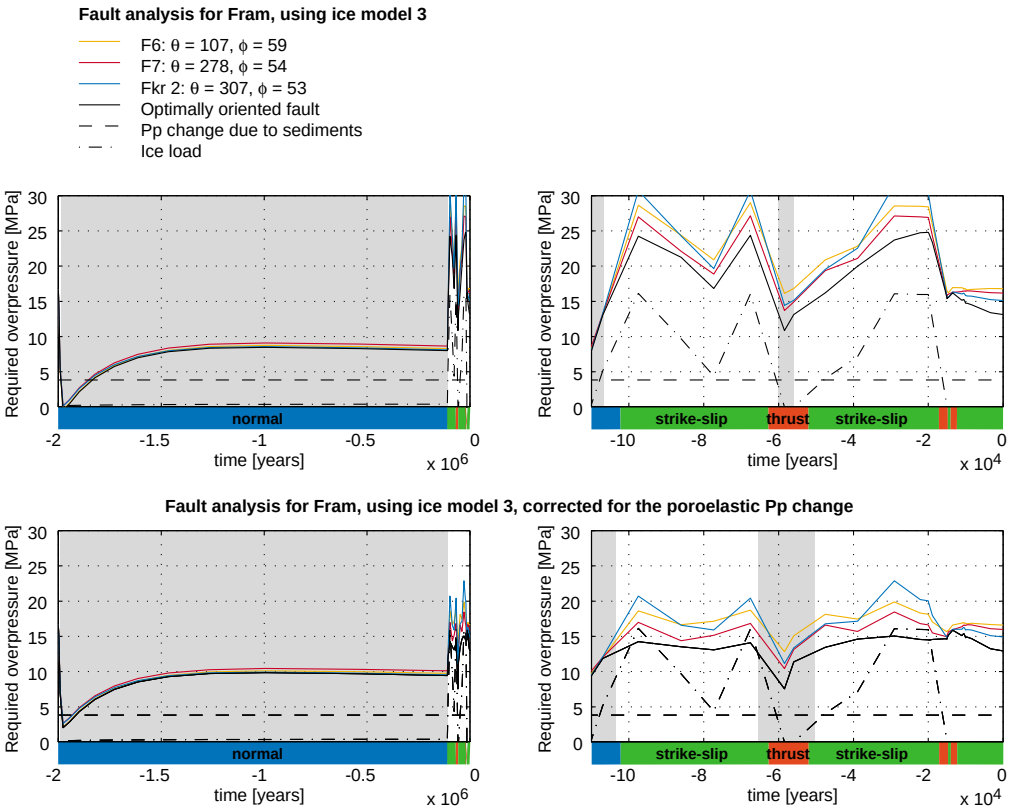

Figure 5.9: Calculated ΔPp_{crit} for Fram, assuming ice model 3 with a constant, pre-Weichselian ice sheet. The left panels show the entire model duration. The panels on the right only display the last 110,000 years. In contrast to the upper panels, the lower panels calculate ΔPp_{crit} by including the poroelastic response of P_p to stress changes since the onset of glaciation. The dashed line shows the estimated P_p-change resulting from under-compaction. The dash-dotted line illustrates the ice loaded in the area. The grey shaded areas illustrate periods when active fault slip was feasible.

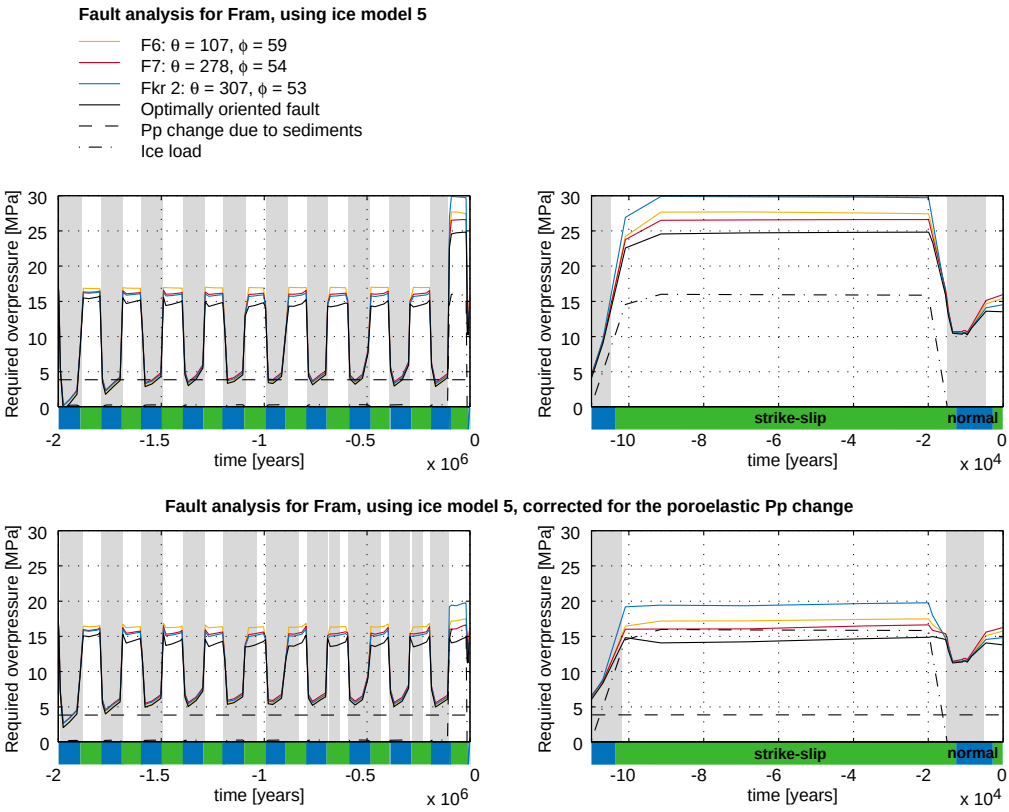

Figure 5.10: Calculated ΔPp_{crit} for Fram, assuming ice model 5 with a varying, pre-Weichselian ice sheet. The left panels show the entire model duration. The panels on the right only display the last 110,000 years. In contrast to the upper panels, the lower panels calculate ΔPp_{crit} by including the poroelastic response of P_p to stress changes since the onset of glaciation. The dashed line shows the estimated P_p-change resulting from under-compaction. The dash-dotted line illustrates the ice loaded in the area. The grey shaded areas illustrate periods when active fault slip was feasible.

Ice model 5 shows that ΔPp_{crit} repeatedly drops below the current value if pre-Weichselian ice variations are included therefore suggesting that there might have been several periods of fault reactivation as a result of ice growth to the 15 ka extent. During these normal faulting periods, most of the major Faults in Fram would have been activated as all are close to being optimally oriented for normal faulting. The under-compaction related P_p-change (dashed line) would have created sufficient overpressure, to cause leakage on all important faults. Similar to the predictions for Visund, ΔPp_{crit} was very high during the maximum ice sheet extents, which confirms earlier findings that the existence of the maximum ice extent serves to prevent leakage. By considering the poroelastic correction the ΔPp_{crit}-increasing effect of the maximum ice sheet is reduced.

In conclusion, severe leakage might have occurred on all major, NNE-striking faults during pre-Weichselian glaciations. The large Weichselian ice sheet prevented active fault

slip, but Weichselian interglacials might have reactivated fault F7, Fkr 2 and other faults with similar orientations.

Fault analysis in Oseberg

Lastly, we are going to apply our fault analysis method to the Oseberg field. Oseberg shows absolutely no evidence of current fault leakage (pers. com. D. Wiprut). The low present-day leakage potential in Oseberg (i.e. high ΔPp_{crit}) results from the combination between low P_p, and lower horizontal stresses than in Visund or Fram (see Chapter 2). Nevertheless, due to the large variety of fault orientations in Oseberg, ranging from relatively shallow dipping fault segments to steeply dipping normal faults, past leakage events are very likely. In fact, Figure 5.12 shows that for most faults ΔPp_{crit} was lower than the expected overpressure from under-compaction during the pre-Weichselian glaciation. This suggests that the pre-Weichselian glaciation caused extensive leakage on the roughly north-south trending, major faults, while the north-west trending faults (e.g. F43) were inactive. The growth of the maximum ice sheet, starting 110,000 years ago, terminated the phase of leakage but Weichselian interglacials (e.g. 60,000 years ago) might have reactivated the north-south trending faults under reverse-faulting conditions. The inclusion of the poroelastic correction, decreases ΔPp_{crit} during the Weichselian glaciations. The predictions for ΔPp_{crit} before 110,000 years ago are almost unaffected by the correction.

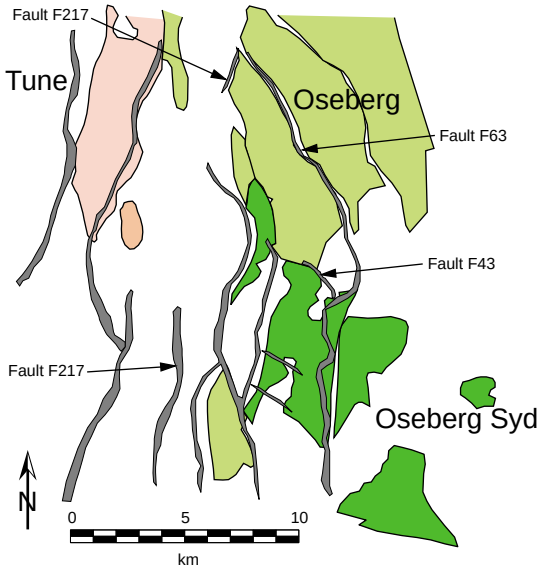

Figure 5.11: Structural map of the Oseberg field showing the major faults and the reservoir extent.

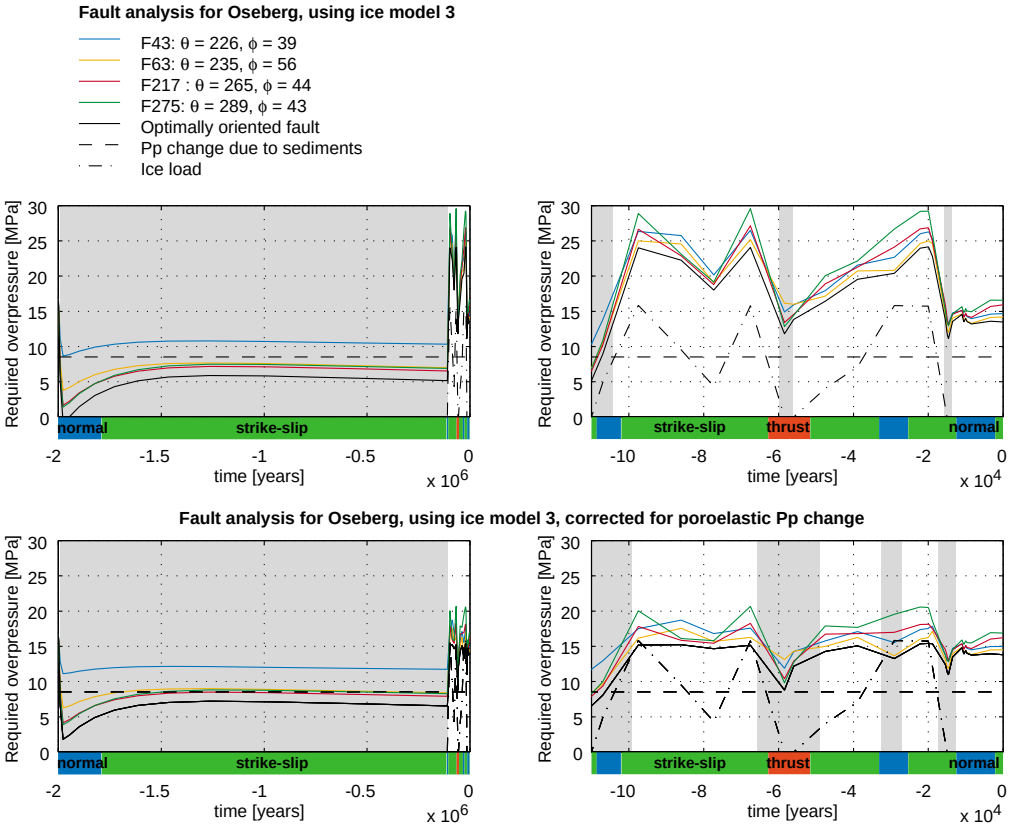

Figure 5.12: Calculated ΔPp_{crit} for Oseberg, assuming ice model 3 with a varying, pre-Weichselian ice sheet. The left panels show the entire model duration. The panels on the right only display the last 110,000 years. In contrast to the upper panels, the lower panels calculate ΔPp_{crit} by including the poroelastic response of P_p to stress changes since the onset of glaciation. The dashed line shows the estimated P_p-change resulting from under-compaction. The dash-dotted line illustrates the ice loaded in the area. The grey shaded areas illustrate periods when active fault slip was feasible.

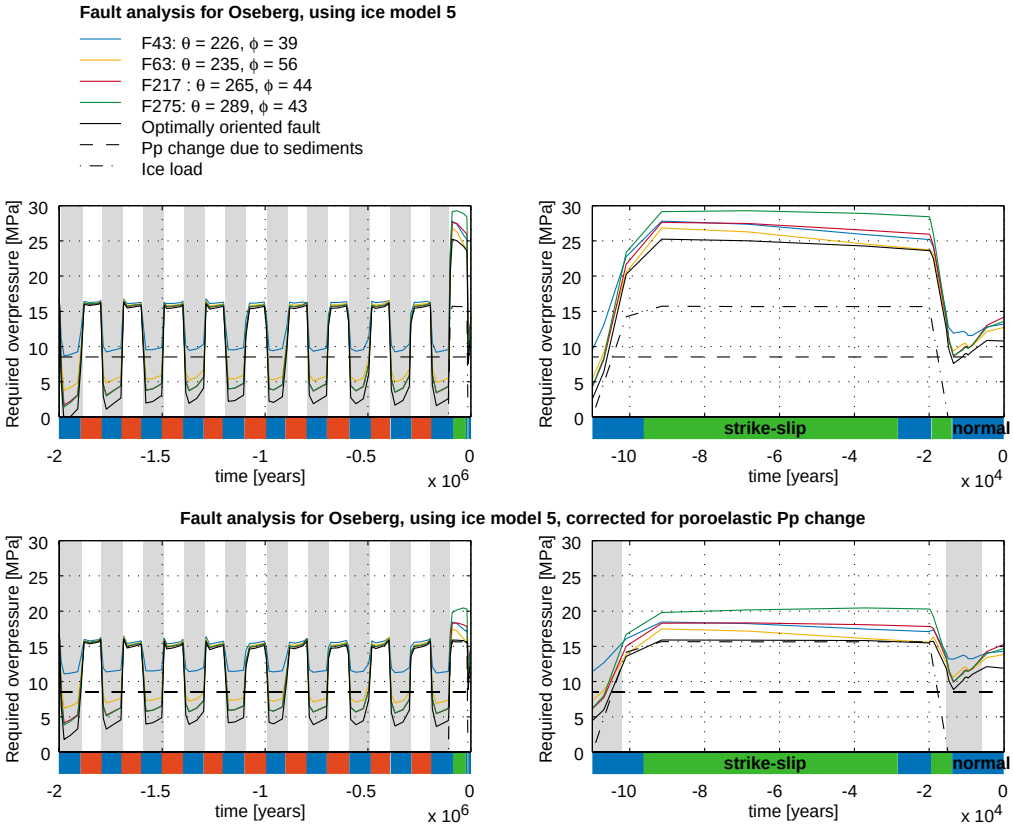

Figure 5.13: Calculated ΔPp_{crit} for Oseberg, assuming ice model 5 with a varying, pre-Weichselian ice sheet. The left panels show the entire model duration. The panels on the right only display the last 110,000 years. In contrast to the upper panels, the lower panels calculate ΔPp_{crit} by including the poroelastic response of P_p to stress changes since the onset of glaciation. The dashed line shows the estimated P_p-change resulting from under-compaction. The dash-dotted line illustrates the ice loaded in the area. The grey shaded areas illustrate periods when active fault slip was feasible.

Ice model 5 (Figure 5.13) shows that pre-Weichselian glaciations strongly affected the potential for leakage in Oseberg. The associated ΔPp_{crit} variations are on the order of 10 MPa or more. Again the roughly north-south trending faults seem to have been most favorably oriented, under the syn-glacial normal faulting stress state. According to ice model 5, the large ice sheet suppressed active faulting on all faults, which agrees with the findings of Visund and Fram.

In conclusion, even if there is no evidence for current faulting in Oseberg, this analysis suggests that extensive faulting/leakage occurred during the pre-Weichselian glaciations and possibly during interglacials between the maximum ice extents. The north-south trending faults would have been the most prominent migration pathways.

The discrepancy between predicted leakage during the past, but no indications for present-day leakage suggest that Oseberg is being recharged with hydrocarbons on a

relatively short time scale (≈10,000 years or less). In other words, present-day indications for leakage, like a missing gas cap, only resemble the last couple of thousand years of the reservoir's evolution. If leakage stopped more than approximately 10,000 years ago, as is probably the case in Oseberg, all previous signs of leakage have disappeared because the reservoir has already been recharged.

5.6 Conclusions

We used the knowledge of temporal stress changes resulting from glacial loading and unloading cycles to compare the current leaking potential to possible phases of leakage in the past. At this point it is impossible to prove or disprove our estimates of past leakage but we can provide a rough idea on how the Pleistocene glaciations might have affected the permeability of reservoir faults offshore Norway. The analysis suggests that all the investigated hydrocarbon reservoirs have been exposed to fault leakage as a result of either glacial loading or unloading during their past. The smaller pre-Weichselian ice sheets served to promote leakage because it increased the horizontal stress anisotropy within the reservoir due to lithospheric flexure while the vertical stress remained unchanged. The growth of the maximum ice extent prevented leakage throughout the northern North Sea, as the weight of the overlying ice sheet served to stabilize faults, by increasing the isotropic part of the stress tensor. Conversely, during Weichselian interglacials the stress state changed such that leakage was promoted in all the studied hydrocarbon fields.

Acknowledgments

We would like to thank Norsk Hydro for generously providing the data and financial support for this study and David Wiprut for very helpful information on current leakage in the Visund, Fram and Oseberg fields.

Chapter 6

DID DEGLACIATION TRIGGER INTRAPLATE SEISMICITY IN THE NEW MADRID SEISMIC ZONE?

Parts of this chapter were submitted with Mark D. Zoback as co-author to Geology

6.1 Abstract

We have investigated the interaction between large-scale plate driving forces, lithospheric structure and the stresses induced by bending of the lithosphere as a result of glacial loading and unloading in the New Madrid seismic zone and surrounding regions. The modeling shows that the removal of the Laurentide ice sheet that covered large parts of the northern United States until ~20,000 years ago changed the stress field in the vicinity of New Madrid and caused seismic strain rates to increase by about 3 orders of magnitude. The modeling predicts that the high rate of seismic energy release observed during late Holocene time is likely to remain essentially constant for the next few thousand years.

6.2 Introduction

While most earthquakes occur on plate boundaries, the infrequent occurrence of large intraplate earthquakes can have devastating consequences as their magnitudes can be comparable to those of plate boundary events (Johnston, 1996). The New Madrid seismic zone (NMSZ) experienced three major earthquakes in 1811-1812, and paleo-liquefaction data suggest that very large, New Madrid type events have occurred every 200-900 years at least during the past 1200 years (Kelson et al., 1996; Tuttle, 1999). These prehistoric events, along with the 1811-1812 earthquakes, must have had moment magnitudes of 7.5, or larger, to have been big enough to cause the severe liquefaction observed over large areas (Tuttle, 1999). However, extensive seismic reflection data in the NMSZ show relatively small cumulative fault offsets in the post-Cretaceous Mississippi embayment sediments (e.g., Hamilton and Zoback, 1981) which implies that the level of seismicity observed in late Holocene time could not have lasted much longer (Schweig and Ellis, 1994). Further, on the basis of seismic reflection and trench data, Van Arsdale (2000) concludes that slip rates on the Reelfoot fault during the Holocene are at least four orders of magnitude higher than during the Pleistocene. Thus, in both the Reelfoot fault area and throughout the NMSZ there appears to have been an anomalously high rate of seismicity in the Holocene that is not characteristic of the region over longer time periods.

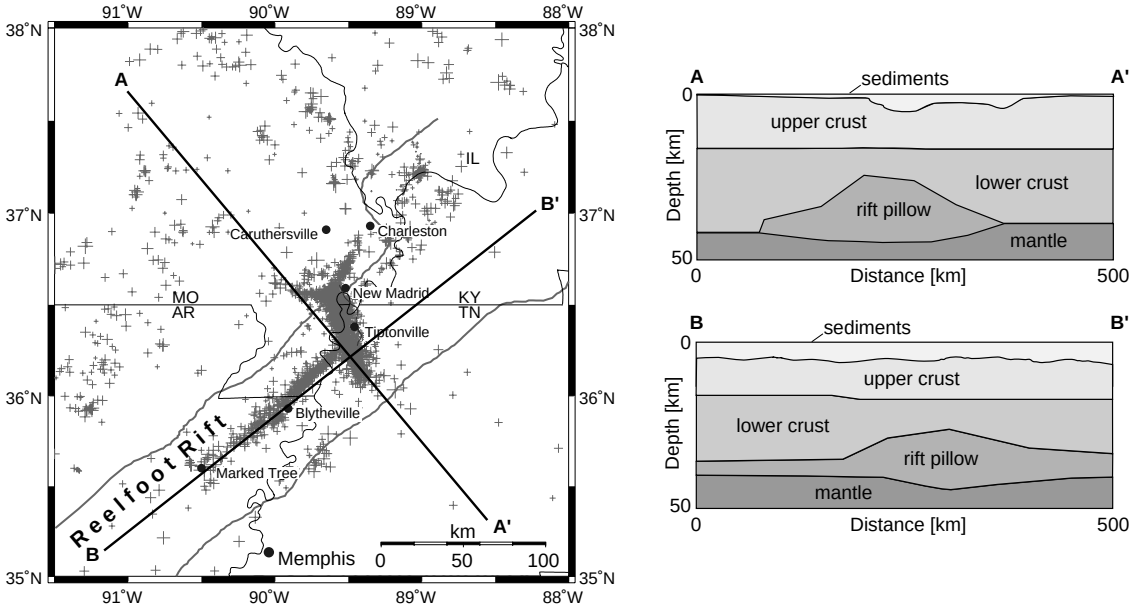

Figure 6.1: Map of the NMSZ and Crustal heterogeneities below the area. The map shows recent background seismicity and the extent of the Reelfoot rift. The two cross sections show crustal heterogeneities based on seismic and gravity data (Stuart et al., 1997) and Mooney et al. (1983) illustrating a lower crustal mafic pillow in the area of most intense seismicity.

The NMSZ is broadly associated with an ancient intraplate rift zone principally active during latest Precambrian and/or early Paleozoic time (e.g., McKeown, 1982). Geological and geophysical data indicate an episode of Cretaceous magmatic activity (Zoback et al., 1980; Hildenbrand, 1985). As a result, crustal structure in the NMSZ is quite anomalous with respect to the surrounding region (Figure 6.1). Aeromagnetic data provide evidence for the existence of the large mafic intrusions at the boundaries of the failed rift (Hildenbrand, 1985), and seismic refraction and gravity studies reveal an anomalously dense “rift pillow” with high velocities at the base of the crust beneath the rift (Mooney et al., 1983, Stuart et al., 1997).

In the context of this anomalous crustal structure, a number of hypotheses have been proposed to explain the spatial concentration of seismicity in the NMSZ. Grana and Richardson (1996) propose a stress concentration due to the rift pillow as possibly the reason for increased seismicity in the area. Liu and Zoback (1997) proposed that the high rate of seismicity results from high ductile strain rates in the lower crust and upper mantle due to locally elevated heat flow. Stuart et al. (1997) suggest the existence of a weak subhorizontal detachment fault in the lower crust directly above the rift pillow as the cause of a stress concentration leading to the observed seismicity. Unfortunately, each of these

hypotheses fails to explain the sudden seismicity increase during the Holocene.

In this paper we investigate the possible influence of deglaciation on the onset of increased seismicity. The temporal coincidence between melting of the Laurentide ice sheet (between 19,000 and 8,000 years ago), and the onset of increased seismicity in the NMSZ is striking. James and Bent (1994) demonstrated that deglaciation significantly changes strain rates, even several hundred kilometers away from the ice sheet front. However, using a simplified circular geometry for the ice sheet and linear superposition of calculated deglaciation-related stress changes using a homogeneous elastic lithosphere and assumed tectonic stresses, they concluded that deglaciation did not promote seismicity. More recently, Wu and Johnston (2000) (who also considered a homogenous elastic lithosphere) consider a more realistic ice sheet geometry. They predict seismicity in the NMSZ to have begun about 200 years ago, although the region in which it is predicted to have occurred is not localized to the New Madrid area.

In this study, we utilize a three-dimensional finite element model to incorporate more realistic lithospheric rheologies and explore the coupled interaction between the large-scale plate driving forces, the stress perturbations caused by deglaciation, and heterogeneous lithospheric properties. The aim of this study is not to accurately predict seismicity on a selected fault, such as the Reelfoot fault, nor to give a general description of seismicity in the eastern United States. Rather, we attempt here to examine whether deglaciation could be a possible candidate for triggering Holocene seismicity in the region of the NMSZ and if so, what conditions, in terms of lithospheric structure, far-field stress state, and ice sheet evolution are required for this to occur.

6.3 The model

We use a three-dimensional finite element model that covers most of the eastern United States corresponding to an area of 6,250,000 km^2 (Figure 6.2). The boundaries are chosen such that the model includes the most important features of the Laurentide ice shield, and the NMSZ is located far from the model boundaries. The model consists of 15,625 trilinear “brick” elements each measuring 100 km horizontally and 3 km in depth. Strain within an element changes linearly in all three directions. Both the lower crust and the lithospheric mantle behave according to linear “Maxwell” viscoelasticity. The 75 km-thick lithosphere is underlain by a viscous asthenosphere which effectively behaves like a fluid substratum accounting for isostasy (similar to the method described in Chapter 4).

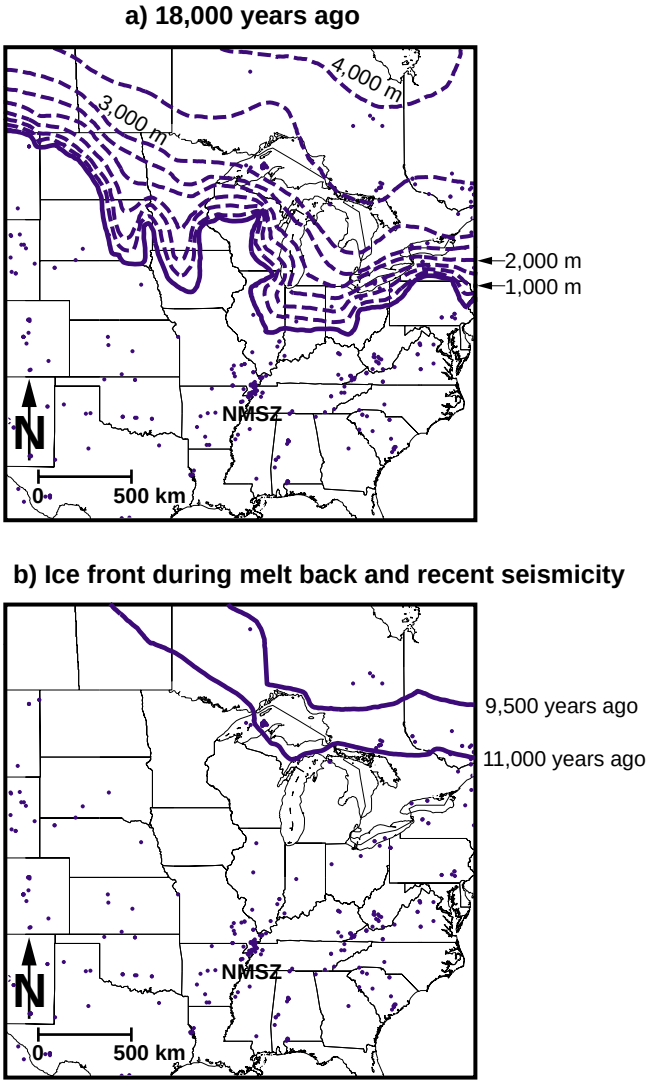

Figure 6.2: The portion of the eastern United States and southeastern Canada that has been modeled. a) The size and thickness of the Laurentide ice sheet during its maximum Wisconsin extent which lasted until approximately 18,000 years ago. The dots are recorded earthquakes larger than magnitude 2, for the last 50 years. b) shows the extents of the ice sheet during its melt back phase.

We include the effect of the ice sheet by applying vertical loads on every surface element, corresponding to the respective ice thickness. The time evolution of the modeled ice sheet is as follows: The entire duration of our model is 5×10^6 yr. We allow 4×10^6 yr for the lithosphere to reach equilibrium with the applied tectonic stresses and body forces before ice loading begins.

We have tested different ice histories, to study the dependence of the modeled seismicity on the chosen ice evolution. In the “reference” ice evolution the ice sheet starts

to grow 1 million years ago and reaches its maximum extent 10,000 years after the onset of ice growth. Subsequently, the ice sheet remains unchanged until 18,000 years ago (Figure 6.2a). The final retreat of the ice sheet follows the description of Denton and Hughes (1981); Tushingham and Peltier (1991), by melting back to the 11,000 years extent, then to the 9,500 years extent (Figure 6.2b). At 8000 years before present the ice sheet has completely melted away. Due to the viscoelastic response of the asthenosphere, lower crust, and lithospheric mantle deformation continues until present-day. Later, in Section 6.4.3, we will also investigate the influence of interglacials on the modeled seismicity in the NMSZ.

We model the lithosphere utilizing a rheologically layered structure in the manner of e.g. Klemann and Wolf (1998), accounting for viscoelasticity within the lithosphere. Chapter 4 shows that viscoelasticity within the lithosphere is crucial in modeling deglaciation-related stress changes. The average viscosity structure of the lower crust ($\eta=10^{22}$ Pa s) and lithospheric mantle ($\eta=10^{23}$ Pa s) are those of Strehlau and Meissner (1987) which agree with the findings by Flesch et al. (2000) and are consistent with the findings of Chapters 3 and 4. The viscosity of the asthenosphere is taken from Cathles (1975). Our model neglects rheological stratifications below the asthenospheric mantle as modeling of deglaciation-induced stress changes appear to be insensitive to them (e.g. Wu, 1997).

As the exact rheological structure of the anomalous lithosphere in the NMSZ is not known, we have considered three different models illustrated in Figure 6.3. Model 1 (Figure 6.3a) considers a thinned upper crust, possibly resulting from rifting as suggested by Braile et al. (1986) and implied by positive gravity anomalies (Hildenbrand et al., 1996). The upper crust is thinned by 9 km over a 300 km wide zone that is comparable to the average width of the Mississippi embayment. Alternatively, in Model 2 the crust has a constant thickness but the lithospheric mantle contains a zone with a one order-of-magnitude lower viscosity (10^{22} Pa s) below the NMSZ (Figure 6.3b). This viscosity decrease might be due to a slightly elevated heat flow, as suggested by Liu and Zoback (1997). The horizontal extent of the low-viscosity lithospheric mantle is the same as the area of anomalously weak crust in Model 1. Model 3 is similar to Model 2, but the low-viscosity zone in the lithospheric mantle is limited to 300 km by 300 km (Figure 6.3c) and might be the result of mantle depletion associated with the emplacement of the rift pillow and/or a residual thermal dome associated with the passage of the Bermuda hot-spot during mid-Cretaceous times as suggested by Cox and Van Arsdale (1997).

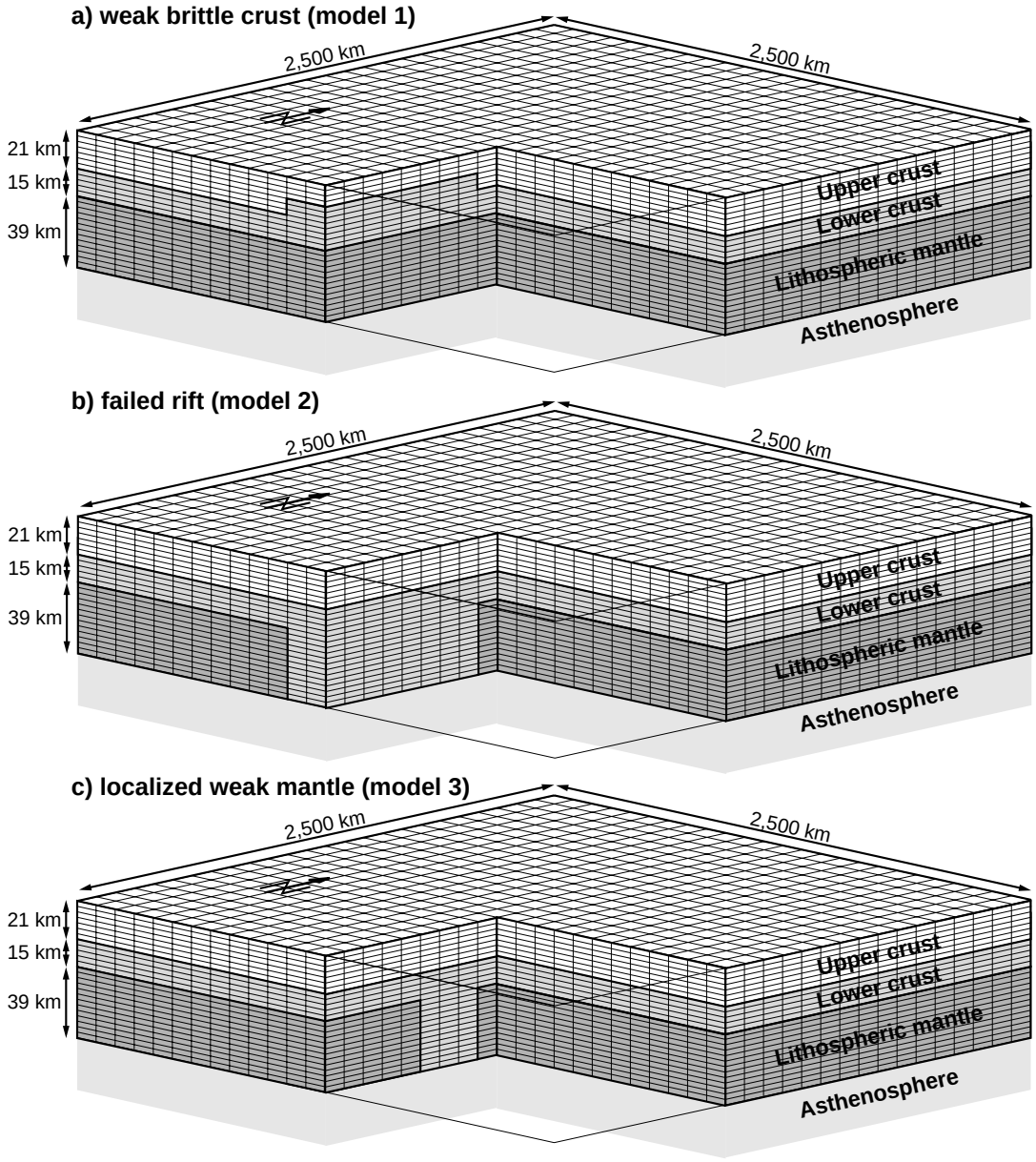

Figure 6.3: The three different lithospheric models tested. For all the models we assume a lithospheric thickness of 75 km. The model extends for 2,500 km on each side and consists of 15,625 8-node elements. Each element measures 100 km horizontally and 3 km with depth. The nature of the heterogeneities in each model are explained in the text.

All of our models incorporate a 21 km thick elastic-plastic upper crust which behaves elastically to the point of failure (as defined by the Mohr-Coulomb criterion) and is perfectly plastic once frictional failure occurs. As failure according to the Mohr-Coulomb criterion depends on both the deviatoric and hydrostatic parts of the stress tensor, we have included body forces resulting from gravity in the model which is also necessary for

isostatic adjustments.

We assume that the brittle crust is in a state of frictional failure equilibrium as defined by the Mohr-Coulomb criterion using laboratory-derived values of friction and hydrostatic pore pressure (e.g., Brace and Kohlstedt, 1980). Townend and Zoback (2000) summarize the direct observational data that support these assumptions in intraplate areas. In the upper crust, we assume a strike-slip stress state such that $S_{Hmax}>S_v>S_{hmin}$ and S_{Hmax} ($S_{Hmax}=S_1$) acts in an east-west direction (Zoback and Zoback, 1989). Accordingly, we assume that the north south stress, S_{hmin} ($S_{hmin}=S_3$) is lower than S_v (Figure 6.4a). To focus on the deformation induced by the ice loading and unloading, we set the initial horizontal stresses in the lower crust and lithospheric mantle to be equal to the vertical stress, i.e. viscously relaxed. In reality, there is likely to be some differential stress in the lower crust and upper mantle accounting for an extremely low rate of steady-state intraplate deformation. On the boundaries of the model we apply forces necessary to balance the initial stress state throughout the lithosphere (Figure 6.4b). As the initial S_{Hmax} strikes east-west, the applied forces in the east-west direction are higher than in north-south direction and the difference between the applied forces normalized over the model width is equal to 3.85×10^{12} Nm^{-1}, comparable to the estimate of the available net force from ridge push (Parsons and Richter, 1980).

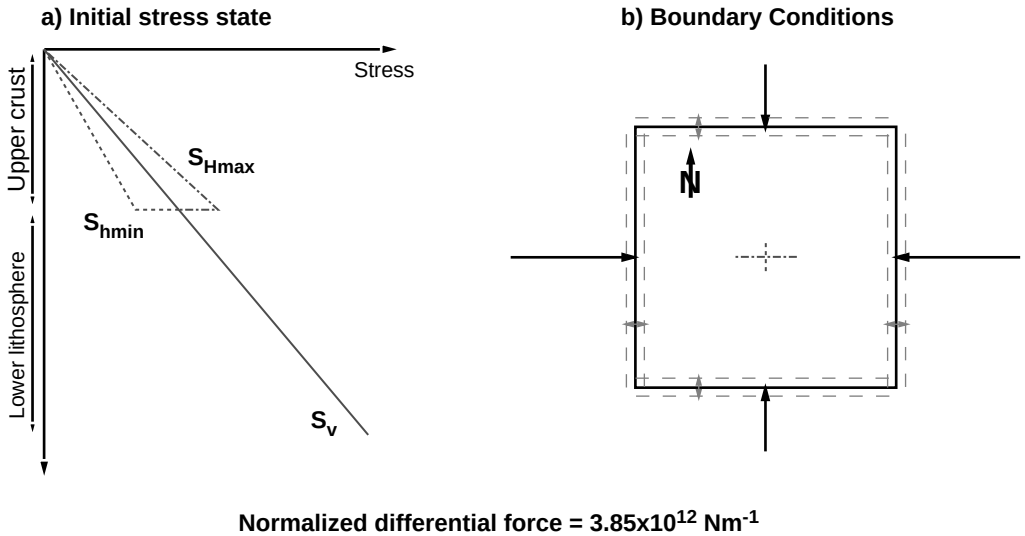

Figure 6.4: Initial stress state and boundary conditions. a) Initially the upper crust is at failure equilibrium with a strike-slip faulting stress state. In the lower crust, and in the upper mantle the initial stress state is isotropic. b) The boundaries are subjected to horizontal net forces which account for plate driving forces. The difference between the forces in north-south and east-west direction corresponds to the net force available from ridge push.

More specifically, we used Equation 4.6, assuming $F_R = 3.85x10^{12}$ Nm^{-1} and calculated the resulting σ_{hmin} throughout the upper crust.(assuming a hydrostatic pore pressure). Once, σ_{hmin} is determined, the required σ_{Hmax} for the upper crust follows from Equation 4.1 (using the Mohr-Coulomb criterion). As mentioned above the lower crust, and the lithospheric mantle are exposed to an initially isotropic stress state according to Equation 4.2. The resulting stress state along with the rheological parameters of the models are given in Table 6. 1.

Table 6.1: Rheological parameters and initial stress state of the New Madrid models

	Upper crust	Lower crust	Lithospheric mantle
ρ (kg/m^3)	2700	3000	3000
E (GPa)	60	80	100
ν	0.25	0.25	0.25
η (Pa s)	∞	varies	varies
μ	0.6	-	-
C_0 (MPa)	0.01	-	-
S_v	$\int \rho_{(z)} \mathbf{g} \mathbf{dz}$	$\int \rho_{(z)} \mathbf{g} \mathbf{dz}$	$\int \rho_{(z)} \mathbf{g} \mathbf{dz}$
S_{Hmax}	1.35 S_v	S_v	S_v
S_{hmin}	0.69 S_v	S_v	S_v

We implement this initial stress state in the manner of the Norway models as described in Chapter 4. In other words, we prestress the lithosphere and add the tectonic contribution to the stress tensor, such that the application of gravity results in the initial stress state as described in Table 6. 1. The force necessary to balance this stress state at the north and south boundaries can be calculated with Equation 5.1.

$$\mathbf{F_{NS}} = \mathbf{l} \int_{\mathbf{lithosphere}} \sigma_{\mathbf{NS(z)}} \mathbf{dz} \qquad \text{Eqn. 5.1}$$

where l is the model width (2500 km) and σ_{NS} is the effective stress in the north-south direction. As we assume a strike-slip faulting initial stress state, σ_{NS} is equal to σ_{hmin}. The applied force on the east and west boundaries (F_{EW}) is obtained in a similar fashion but by using σ_{Hmax} instead of σ_{hmin}.

To quantify the seismicity that is predicted by these models, we consider the seismic strain rate in the brittle crust during the Holocene and compare it to the seismic strain rate prior to deglaciation. The method by which the seismic strain rate is computed is as follows: Each model consists of more than 100 time increments to incorporate time-varying ice sheet geometries and to account for the time-dependent lithosphere and asthenosphere rheologies. The length of the time increments is variable (depending on how much time-dependent deformation is occurring) but is between 10^2 and 10^3 years for the period of interest here. At the beginning of each time step, we predict the stress state at the end of the step by considering the elastic response. If the predicted stress state is in excess of the failure state we lower the shear stress to the Mohr-Coulomb level and compute the corresponding strain release to accomplish this. Lowering the stress state of a "failing element", affects the stress equilibrium of the model. Therefore, equilibrium iterations are necessary to account for this non-linear behavior.

As a result of the procedure outlined above, we obtain a brittle (seismic) strain for each time increment. This brittle strain, normalized by the length of the time increment in the calculations yields an effective seismic strain rate for the brittle crust. For reference, Anderson (1986) estimated the background seismic strain rate for the Central and eastern United States (outside the NMSZ) to be on the order of 10^{-12} to 10^{-11} yr^{-1} whereas Johnston (1994) estimated values between 10^{-12} to 10^{-10} yr^{-1}.

6.4 Model results

The model results will be presented in three sections: Section 6.4.1 investigates the importance of the chosen lithospheric structure. Later, in Section 6.4.2 we will study the influence of different lithospheric viscosities, and Section 6.4.3 explores the impact of the chosen ice sheet history on the modeled seismicity. We will present all model results in two ways: First, we show the spatial distribution of the predicted, present-day seismic strain rate to check whether the model concentrates seismicity in the NMSZ. Second, we monitor the seismic strain rate in the NMSZ temporally which allows the comparison to paleoseismic findings.

6.4.1 Different implications of the structural heterogeneity

As mentioned in Section 6.3, the exact rheological structure of the lithosphere below the NMSZ is unknown. Consequently, we tested the three different lithospheric structures shown in Figure 6.3., assuming a lower crustal viscosity of 10^{22} Pa s, and a lithospheric mantle viscosity of 10^{23} Pa s. All models tested in this section use the reference ice history

as described in Section 6.3.

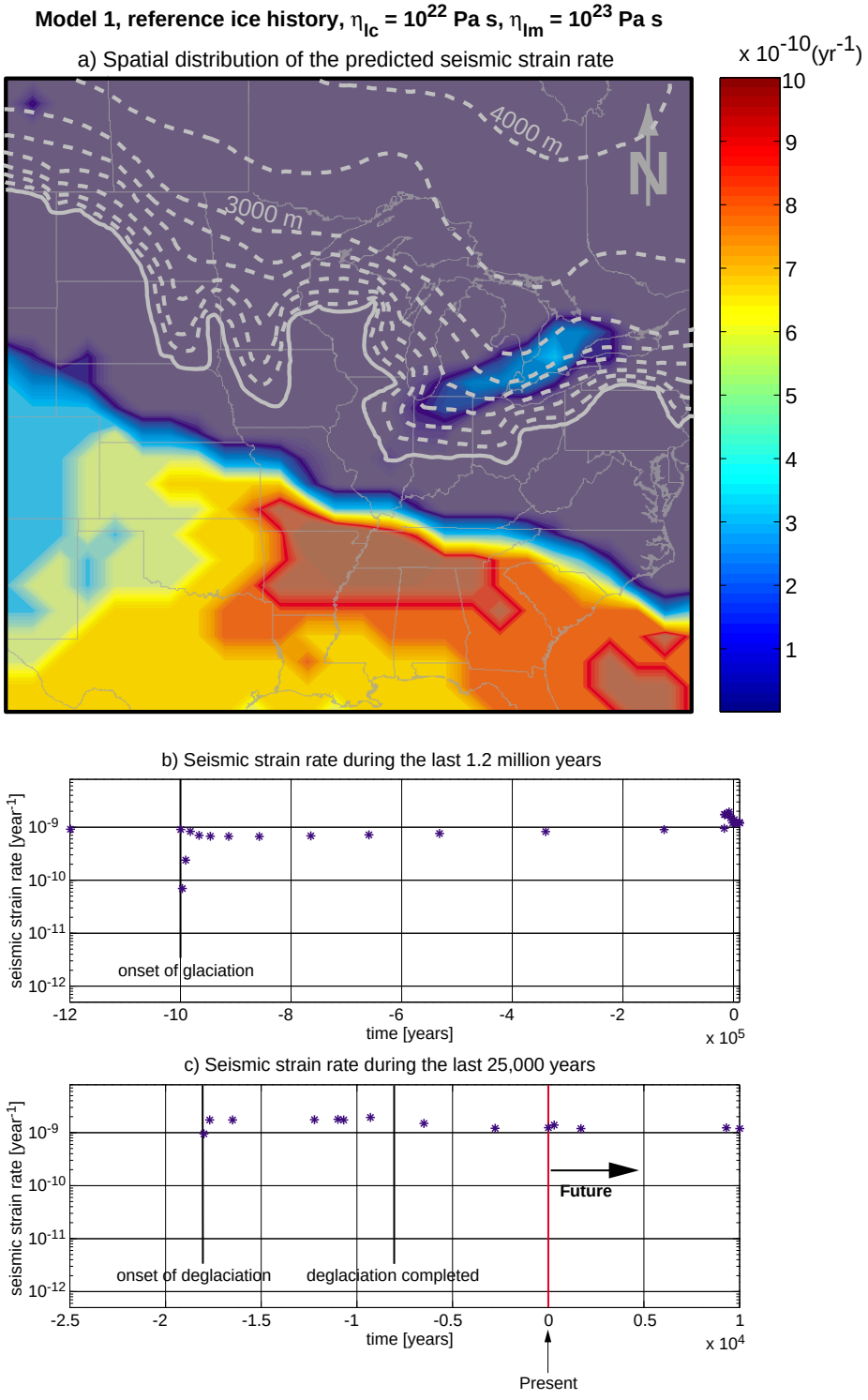

Figure 6.5: a) Predicted present-day seismic strain rates for Model 1 at a depth of 12,000 m. A zone of increased seismicity is centered around the NMSZ. The highest present-day strain rates are 10^{-9} year^{-1}, almost 3 orders of magnitude higher than the background seismic strain rate of 10^{-12} year^{-1} (Anderson, 1986). b) Seismic strain in

the NMSZ at a depth of 12,000 m for the entire glacial period. c) Seismic strain rate for the last 25,000 years and 10,000 years into the future.

Model 1 (weak brittle crust)

In Model 1, the upper crust below the NMSZ is thinned by 9 km, resulting in an upper crustal thickness of 15 km (instead of 21 km everywhere else). The zone in which the upper crust is thinned, extends from the NMSZ all the way to the southern model boundary, and measures 300 km across.

Model 1 predicts a zone of increased seismicity in the vicinity of the NMSZ (Figure 6.5a) where the seismic strain rate reaches 10^{-9} year^{-1} which is up to 3 orders of magnitude higher than the estimate for the background seismicity in the eastern United States (Anderson, 1986; Johnston, 1994). However, according to Model 1 increased seismic strain rates are not limited to the immediate surroundings of the NMSZ, but instead cover large portions of the southern United States. In fact, this model suggests that present-day seismic strain rates are elevated in all areas located at a distance of roughly 300 km or greater from the southernmost ice front as shown in Figure 6.5a.

Figure 6.5b shows that the seismic strain rate in the NMSZ has been more or less constant throughout the past. Before the onset of glaciation, the seismic strain rate was close to its present-day level of 10^{-9} year^{-1}. Glaciation caused a temporary drop by a little more than one order of magnitude. Shortly after the completion of ice loading, the seismic strain rate recovered to the pre-glaciation level and then remained unchanged for the rest of the glacial period. More recently, the starting deglaciation doubled the seismic strain rate to $\approx 2 \times 10^{-9}$ year^{-1} (Figure 6.5c) but immediately after deglaciation was complete, the seismic strain rate returned to the present-day prediction of 10^{-9} year^{-1}. Had the strain rates been at such a high level throughout the past, seismic cross sections in the area should show significant fault offset which is not observed (Hamilton and Zoback, 1981). As a result, the maxium allowable long-term seismic strain rate in the NMSZ must have been close to Anderson's estimate of $\approx 10^{-12}$ s^{-1} which implies that the weak brittle crust model gives unrealistic results.

In conclusion, Model 1 predicts a high present-day seismic activity in the NMSZ but in contrast to the observations (Figure 6.1 and Figure 6.2) Model 1 does not restrict high seismicity to the NMSZ. By suggesting a permanently high seismic strain rate, Model 1 is in contrast with paleoseismic findings which suggest a significant seismicity increase during the Holocene. The permanently high seismicity, suggested by this model, results from the concentration of seismic strain in the thinned upper crust. The ice sheet's effect on seismicity in the NMSZ is barely able to overshadow the background seismicity resulting from the weakened upper crust.

Model 2 (weak mantle)

In Model 2 the upper crust has a constant thickness of 21 km. The heterogeneity is included by lowering the lithospheric mantle viscosity by one order of magnitude relative to the surroundings. Such a decrease in viscosity could be the result of a slightly elevated heat flow along the ancient rift. The spatial extent of the anomalous lithospheric mantle corresponds to the extent of the weakened upper crust in Model 1.

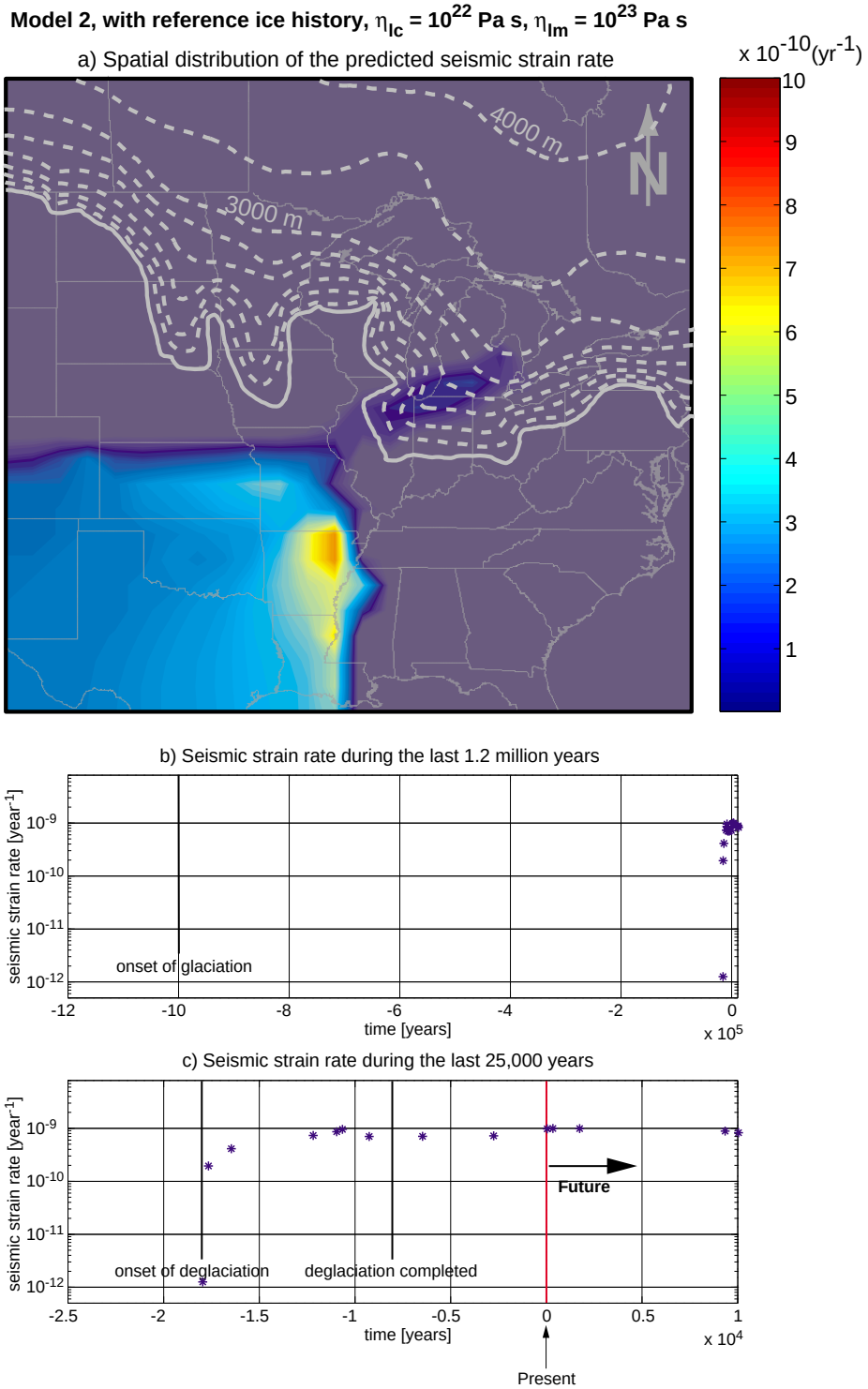

Figure 6.6: a) Predicted present-day seismic strain rates for Model 2 at a depth of 12,000 m. A zone of increased seismicity is located just west of the NMSZ. The highest present-day strain rates are close to 10^{-9} year^{-1}, almost 3 orders of magnitude higher than the background seismic strain rate of 10^{-12} year^{-1} (Anderson, 1986). b) Seismic strain just west of the NMSZ at a depth of 12,000 m for the entire glacial period. c) Seismic strain rate for the last 25,000 years and 10,000 years into the future.

In contrast to Model 1, this model strongly localizes the current seismicity in a relatively small zone, just west of the NMSZ (Figure 6.6a), and the southwestern corner of the model shows a slightly elevated seismic strain rate of approximately $3x10^{-10}$ $year^{-1}$. However, in all other areas seismicity is absent. As the NMSZ itself is not exposed to any modeled seismicity, Figure 6.6b and c show the temporal evolution of seismic strain rate in the area of highest seismicity (≈100 km west of the NMSZ). Model 2 predicts that no seismicity occurred either before or during glaciation. Subsequent ice melting caused a rapid acceleration of the seismic strain rate by three orders of magnitude to the current value of almost 10^{-9} $year^{-1}$.

In conclusion, Model 2 achieves a better fit to the observations than Model 1 by predicting a significant increase of seismicity after the onset of ice melting. Also, Model 2 constrains the increased seismicity to a relatively small area which agrees well with the spatially limited occurrence of seismicity in the NMSZ. However, the modeled zone of increased seismicity is offset from the NMSZ by approximately 100 km.

Model 3 (localized weak mantle)

Lastly, we tested a model which is similar to Model 2, but the zone of decreased lithospheric mantle viscosity is limited to the south, measuring 300 km by 300 km. The cross sections shown in Figure 6.1 support the assumption made by this model, that the lithospheric anomaly below the NMSZ does not extend far towards the south (as assumed by Model 2).

The seismicity predictions of Model 3 are roughly identical with the findings of Model 2 (Figure 6.7a). However, Model 3 locates the peak seismicity in the direct vicinity of the NMSZ which is clearly more realistic than the predictions of Model 2. Figure 6.7b and c display seismic strain rate as a function of time at a depth of 12 km in the NMSZ. No seismicity is observed either before or during glaciation because the boundary conditions maintain the upper crust at frictional yield but without exceeding the failure envelope. Deglaciation causes an acceleration in seismic strain rate to more than 10^{-9} yr^{-1}, almost three orders of magnitude higher than the background seismic strain rate. Importantly, the increased seismic strain rate of 10^{-9} yr^{-1} is almost constant during the Holocene and remains at a very high level for at least the next 10,000 years.

In conclusion, Model 3 achieves the most accurate prediction of seismicity, by concentrating present-day seismicity near the NMSZ, while the surrounding areas are essentially aseismic. Furthermore, Model 3 suggests that seismicity in the NMSZ was absent before the onset of deglaciation, which matches paleoseismic observations. Thus, for the remainder of Chapter 6, we will focus on Model 3.

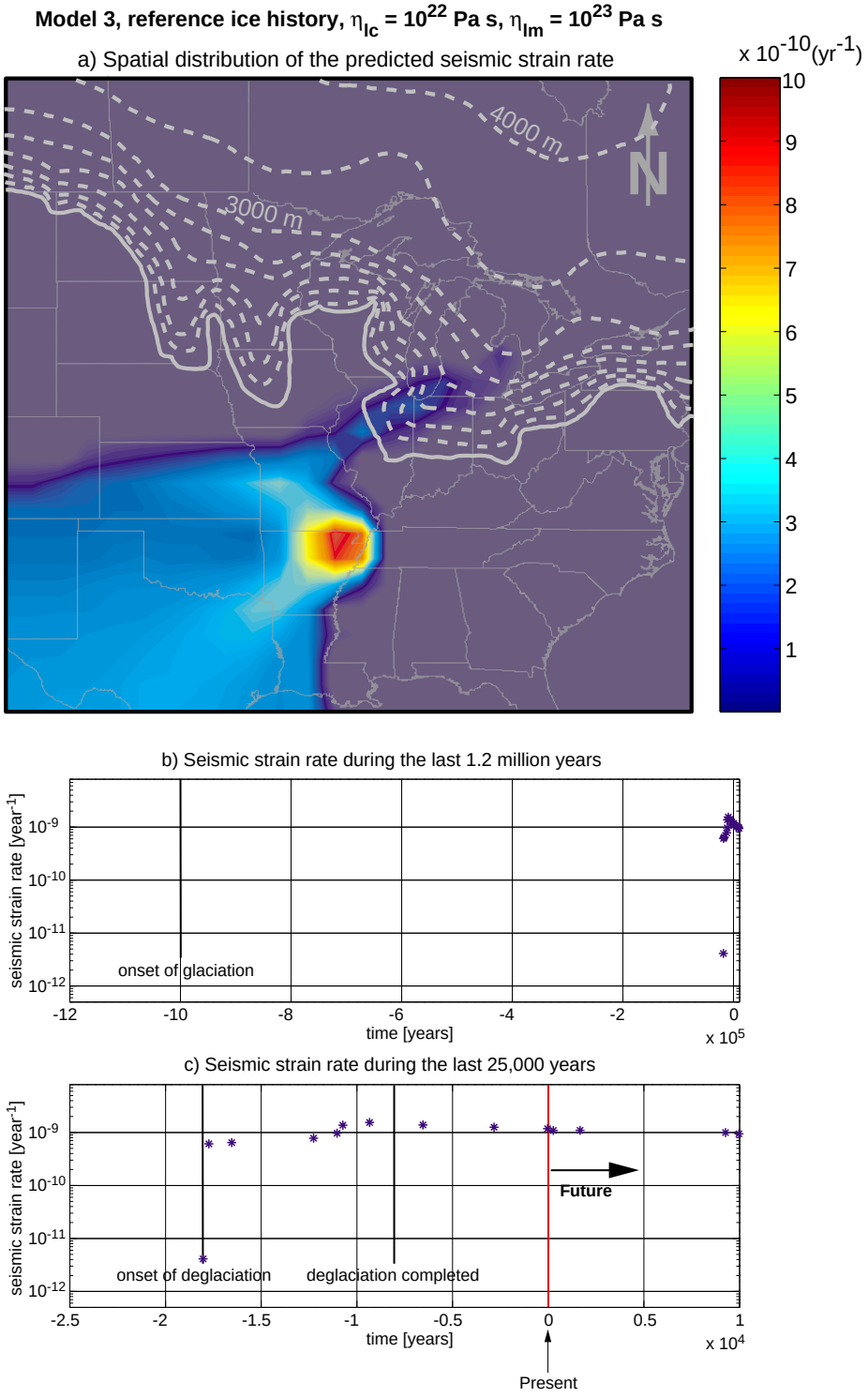

Figure 6.7: a) Predicted present-day seismic strain rates for Model 3 at a depth of 12,000 m. A zone of increased seismicity is located at the NMSZ. The highest present-day strain rates are close to 10^{-9} year^{-1}, almost 3 orders of magnitude higher than the background seismic strain rate of 10^{-12} year^{-1} (Anderson, 1986). b) Seismic strain in the NMSZ at a depth of 12,000 m for the entire glacial period. c) Seismic strain rate for the last 25,000 years and 10,000 years into the future.

6.4.2 The influence of the chosen lithospheric viscosities

In the previous section we have established that the model with a localized weak lithospheric mantle (Model 3) gives the most convincing seismicity predictions, both spatially and temporally. So far, we assumed that $\eta_{lc} = 10^{22}$ Pa s, and $\eta_{lm} = 10^{23}$ Pa s (reference viscosities).In this section, we will vary the lithospheric viscosities to investigate the influence of the chosen viscosities on the predicted seismicity.

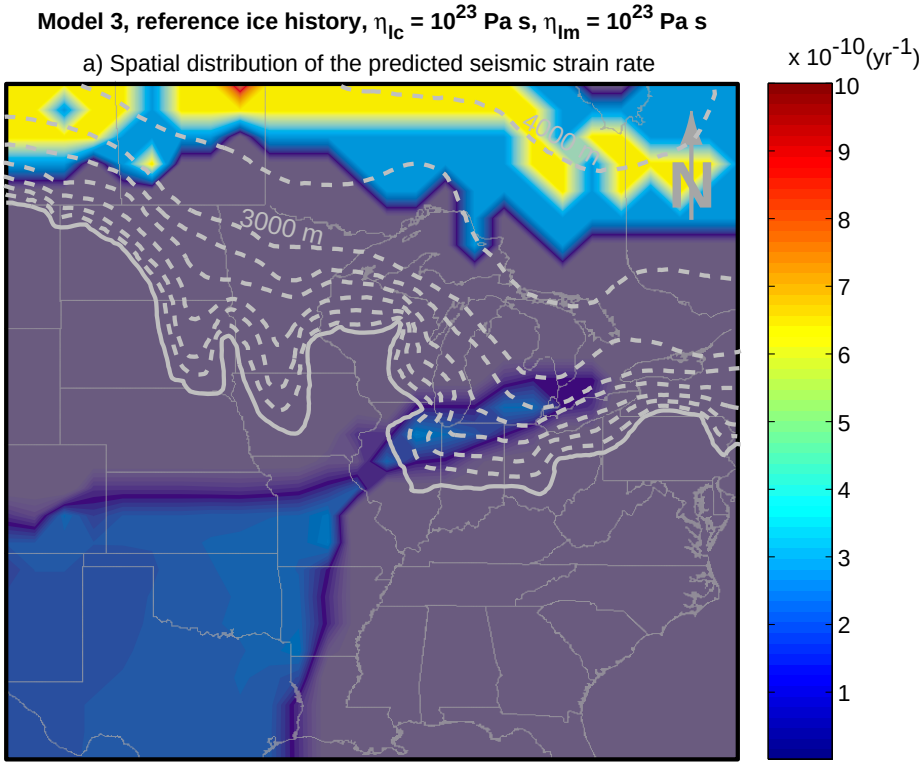

Figure 6.8: Predicted present-day seismic strain rates for Model 3 at a depth of 12,000 m, with an increased lower crustal viscosities. No seismicity is predicted for the NMSZ either during the past or at present.

Figure 6.8 shows the modeled present-day seismic strain rate if the lower crustal viscosity is one order of magnitude higher than in the model presented in Figure 6.7. Most importantly, the model with an increased η_{lc} predicts no seismicity in the NMSZ, either at present or throughout the past. Obviously, by predicting no seismicity in the NMSZ this model is in strong contrast with the experienced seismic events which suggests that the lower crustal viscosity in the NMSZ is not 10^{23} Pa s but closer to 10^{22} Pa s. Interestingly, the increased η_{lc} causes a zone of seismicity in southern Canada, striking roughly parallel to the ice sheet front. According to Figure 6.2, there is evidence for some seismic activity in this area.

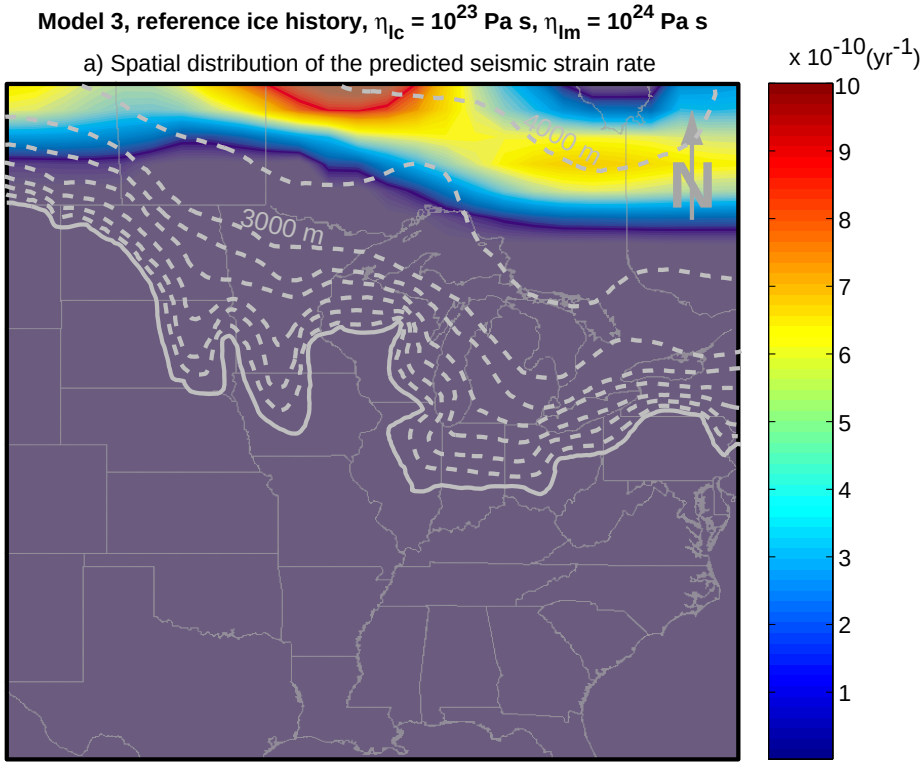

Figure 6.9: Predicted present-day seismic strain rates for Model 3 at a depth of 12,000 m, with increased lower crustal and lithospheric mantle viscosities. No seismicity is predicted for the NMSZ either during the past or at present.

If I increase η_{lc} and η_{lm} by one order of magnitude relative to the reference viscosities, the model predicts no deglaciation-related seismicity throughout the entire United States (Figure 6.9). However, similar to the model presented in Figure 6.8 a zone of increased seismicity is expected in southern Canada but the model presented in Figure 6.9 defines the extent of this zone more clearly. It roughly strikes parallel to the ice sheet front and has an approximate width of 500 km. The exact location of this increased seismicity zone is probably not very accurate as it might be affected by model boundary effects, especially at the northwestern corner of the model.

Lastly, we tested a model with lowered viscosities (η_{lc} = $5x10^{21}$ Pa s, η_{lm} = $5x10^{22}$ Pa s) and the results are shown in Figure 6.10. According to this model, lowered viscosities cause a zone of increased seismicity around the NMSZ and the seismic strain rate reaches almost $5x10^{-9}$ $year^{-1}$. Compared to the model with the reference viscosities (Figure 6.7), the area of increased seismicity is much larger and covers almost the entire area south of the former ice margin. Furthermore, this model suggests that the majority of the United States exhibits seismic strain rates on the order of 10^{-9} $year^{-1}$ or more, which is at least one order of magnitude above the estimates of Anderson (1986) and Johnston (1994).

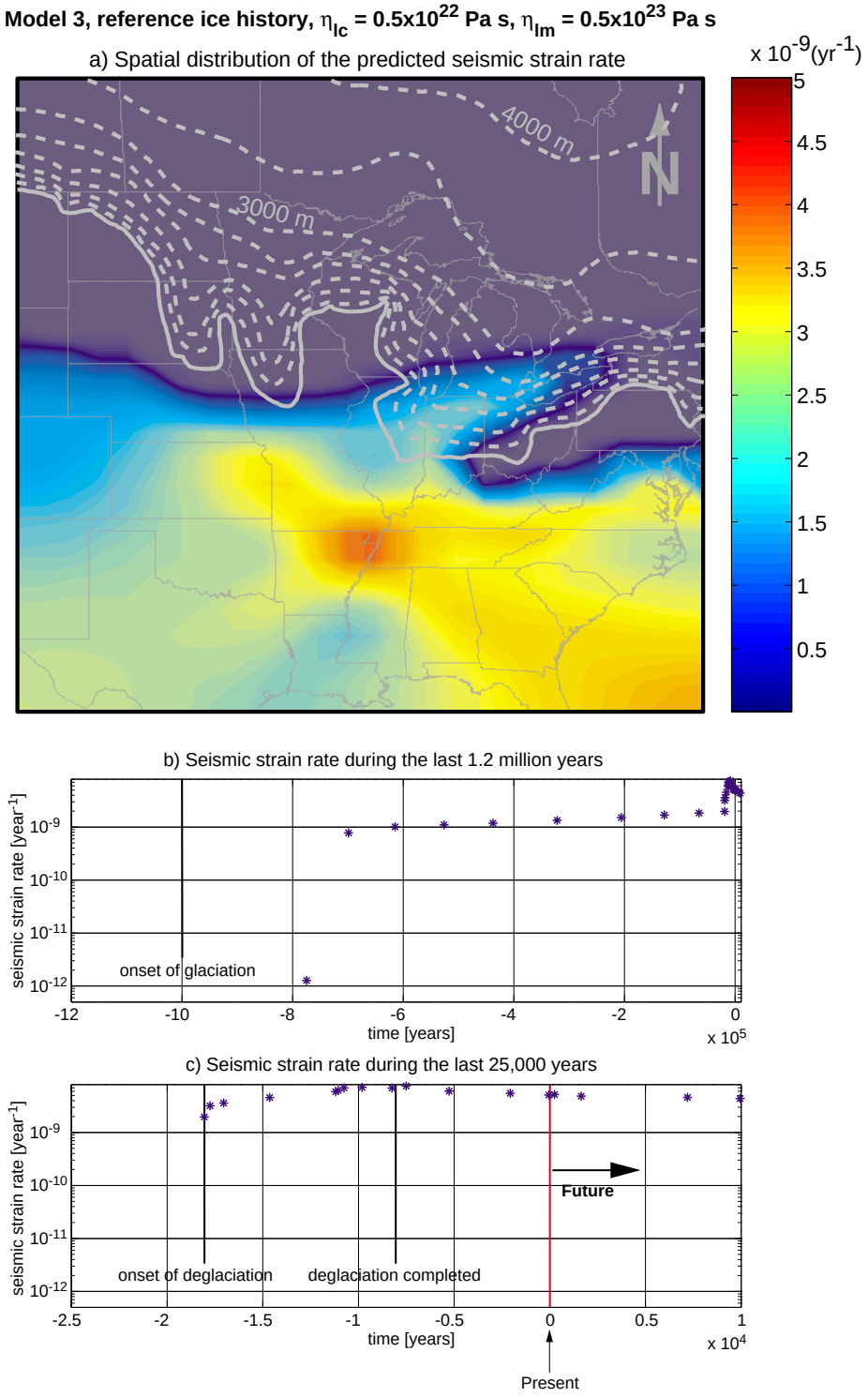

Figure 6.10: Predicted present-day seismic strain rates for Model 3 at a depth of 12,000 m, with increased lower crustal and lithospheric mantle viscosities. A zone of increased seismicity is located at the NMSZ. The highest present-day strain rates are close to 5x10^{-9} year^{-1}, more than 3 orders of magnitude higher than the background seismic strain rate of 10^{-12} year^{-1} (Anderson, 1986). b) Seismic strain in the NMSZ at a depth of 12,000 m for the entire glacial period. c) Seismic strain rate for the last 25,000 years

and 10,000 years into the future.

Figure 6.10b shows that the lowered viscosities cause seismicity to start approximately 200,000 years after the onset of glaciation. Subsequently, the seismic strain rates remain high throughout the ice sheet's existence. Deglaciation increases the seismic strain rate by half an order of magnitude. According to this model, the NMSZ should show a substantial cumulative fault offset in the NMSZ as seismicity should have been present for almost 1 million years. However, as mentioned in Section 6.2 cumulative fault offsets in the NMSZ are small and hence lowered viscosities provide unrealistic predictions.

In conclusion, the model using the reference viscosities ($\eta_{lc} = 10^{22}$ Pa s, and $\eta_{lm} = 10^{23}$ Pa s) gives the best predictions of seismic strain rate, both spatially and temporally. In order to concentrate seismicity around the NMSZ a viscosity of less than 10^{23} Pa s is required. However, if the entire lithosphere has a viscosity of less than 10^{23} Pa s the predicted seismicity is too high. The increased occurrence of earthquakes in southern Canada might suggest a tendency towards higher lithospheric viscosities to the north. Earthquakes outside the NMSZ could also be associated with additional zones of structural weakness which are not included in our model (as discussed later in Section 6.6).

6.4.3 The influence of interglacials

The reference ice model, used in previous sections, ignores the existence of interglacials. Realistically, the ice sheet went through multiple cycles of growth and retreat during the Pleistocene. The ice sheet's melt back history is complicated and involves many surges and subsequent melt-downs (e.g. Marshall, 1998). To investigate the importance of interglacials on the modeled seismicity, we tested three alternative ice models. These alternative ice models, along with the previously used "reference" ice model are displayed in Figure 6.11. The first alternative ice evolution (ice model 1) is similar to the reference ice evolution but the ice sheet disappears for 20,000 years in order to account for the Eemian interglacial. The second alternative ice evolution (ice model 2) corresponds to ice model 1, but the Eemian interglacial lasts for 40,000 years. Finally, ice model 3 includes multiple cycles of ice growth and retreat with a periodicity of 100,000 years (similar to ice model 5 in Chapter 4) based on climate estimates from oxygen isotopes (Shackleton et al., 1984). Additionally, ice model 3 includes three complete melt-downs during the last 18,000 years before present.

All models presented in this section include the structural heterogeneity below the NMSZ in the manner of Model 3 (localized weak mantle), and use the best-fitting lithospheric viscosities obtained from Section 6.4.2 ($\eta_{lc} = 10^{22}$ Pa s, $\eta_{lm} = 10^{23}$ Pa s).

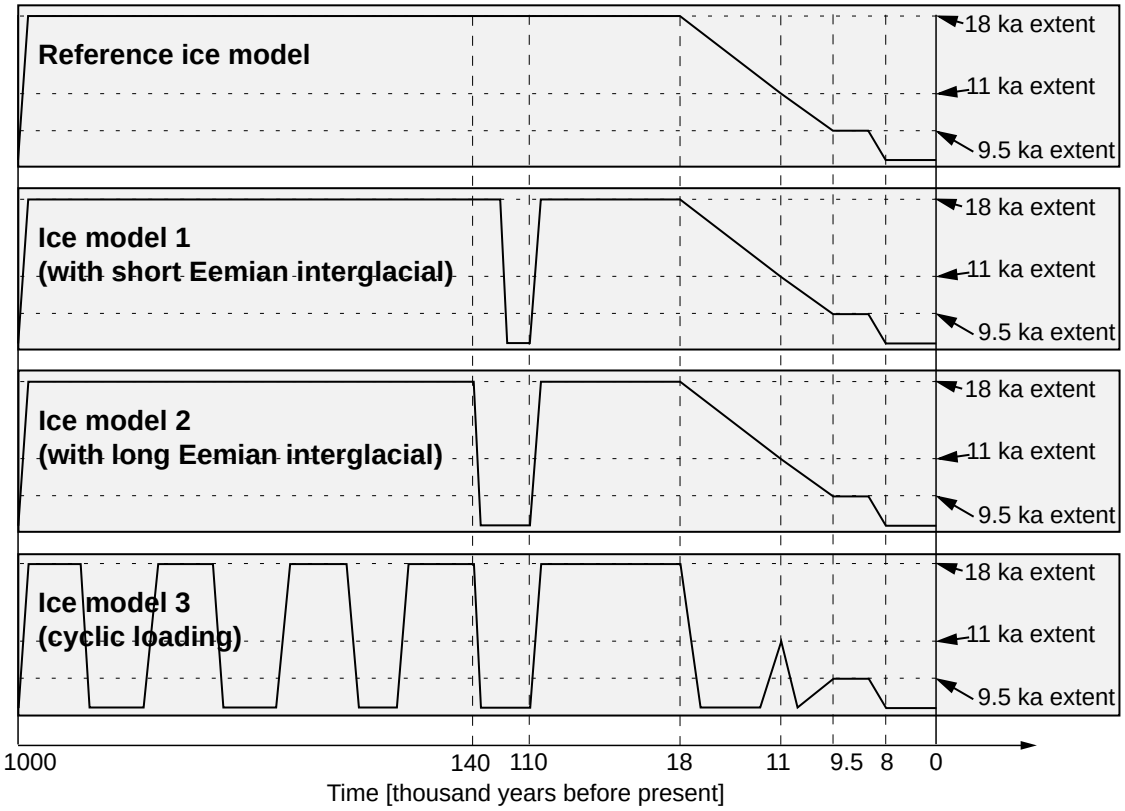

Figure 6.11: Temporal change of ice extent for different ice models.

Ice model 1 (with short Eemian interglacial)

By including a relatively short Eemian interglacial, the resulting present-day seismicity (Figure 6.12a) is identical to the predictions of the reference ice model (Figure 6.7a). Figure 6.12b shows that the Eemian interglacial caused a seismic strain rate acceleration to approximately half of the present-day level but the subsequent ice advance suppressed seismicity again. The seismic response to the last deglaciation, starting 18,000 years ago, is very similar to the reference ice model, thereby suggesting that a short Eemian interglacial has no big effect on post-glacial seismicity in the NMSZ. With or without a short Eemian interglacial, the model predicts present-day seismic strain rates on the order of 10^{-9} $year^{-1}$ around the NMSZ, whereas seismicity is low or absent everywhere else. Ice model 1 also agrees with the reference model in that seismicity will remain at present-day levels for at least the next 10,000 years.

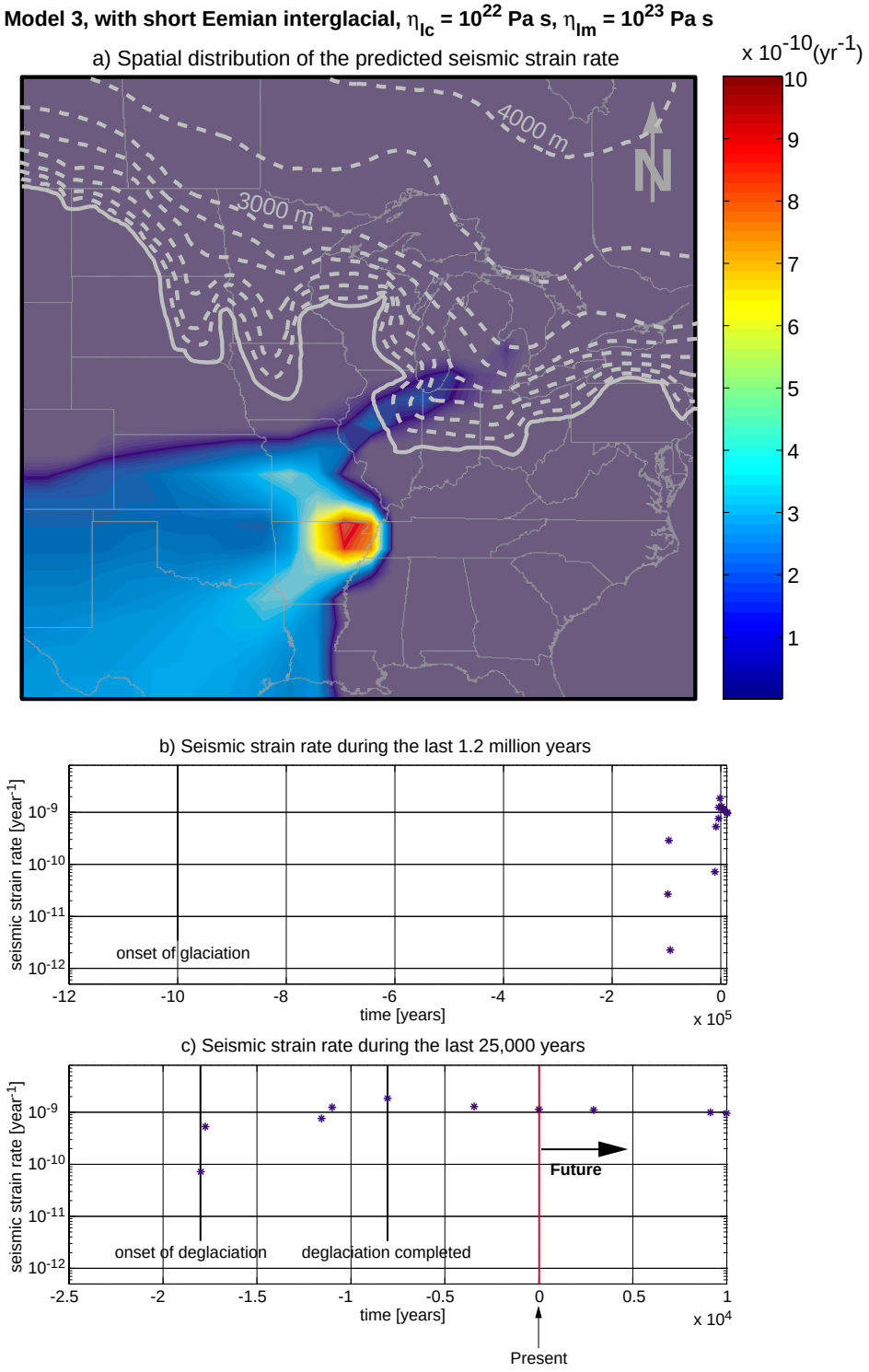

Figure 6.12: Predicted present-day seismic strain rates for ice model 1 at a depth of 12,000 m. A zone of increased seismicity is located at the NMSZ. The highest present-day strain rates are close to 10^{-9} year^{-1}, about 3 orders of magnitude higher than the background seismic strain rate of 10^{-12} year^{-1} (Anderson, 1986). b) Seismic strain in the NMSZ at a depth of 12,000 m for the entire glacial period. c) Seismic strain rate for the last 25,000 years and 10,000 years into the future.

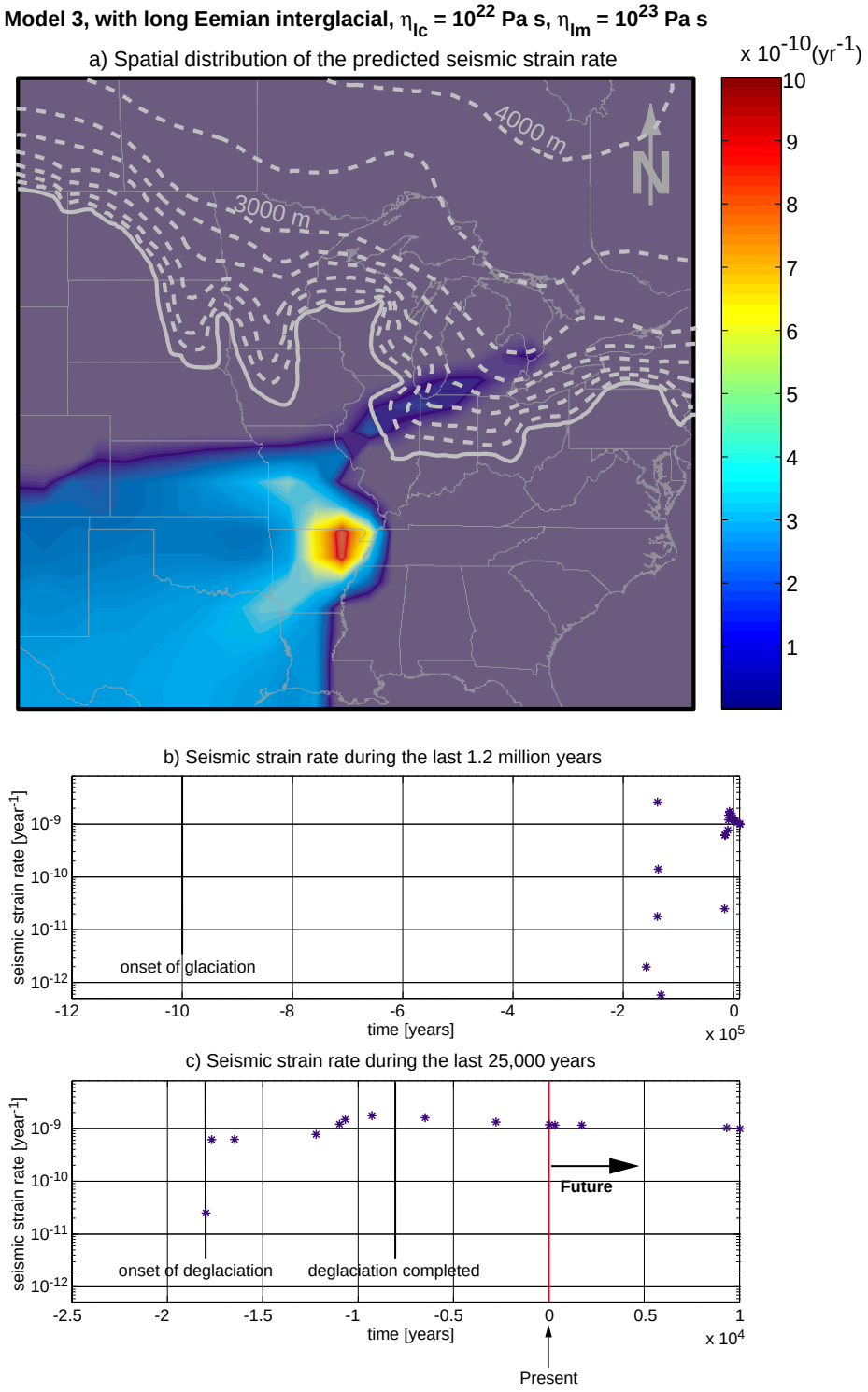

Figure 6.13: Predicted present-day seismic strain rates for ice model 2 at a depth of 12,000 m. A zone of increased seismicity is located near the NMSZ. The highest present-day strain rates are close to 10^{-9} year^{-1}, about 3 orders of magnitude higher than the background seismic strain rate of 10^{-12} year^{-1} (Anderson, 1986). b) Seismic strain just west of the NMSZ at a depth of 12,000 m for the entire glacial period. c) Seismic strain rate for the last 25,000 years and 10,000 years into the future.

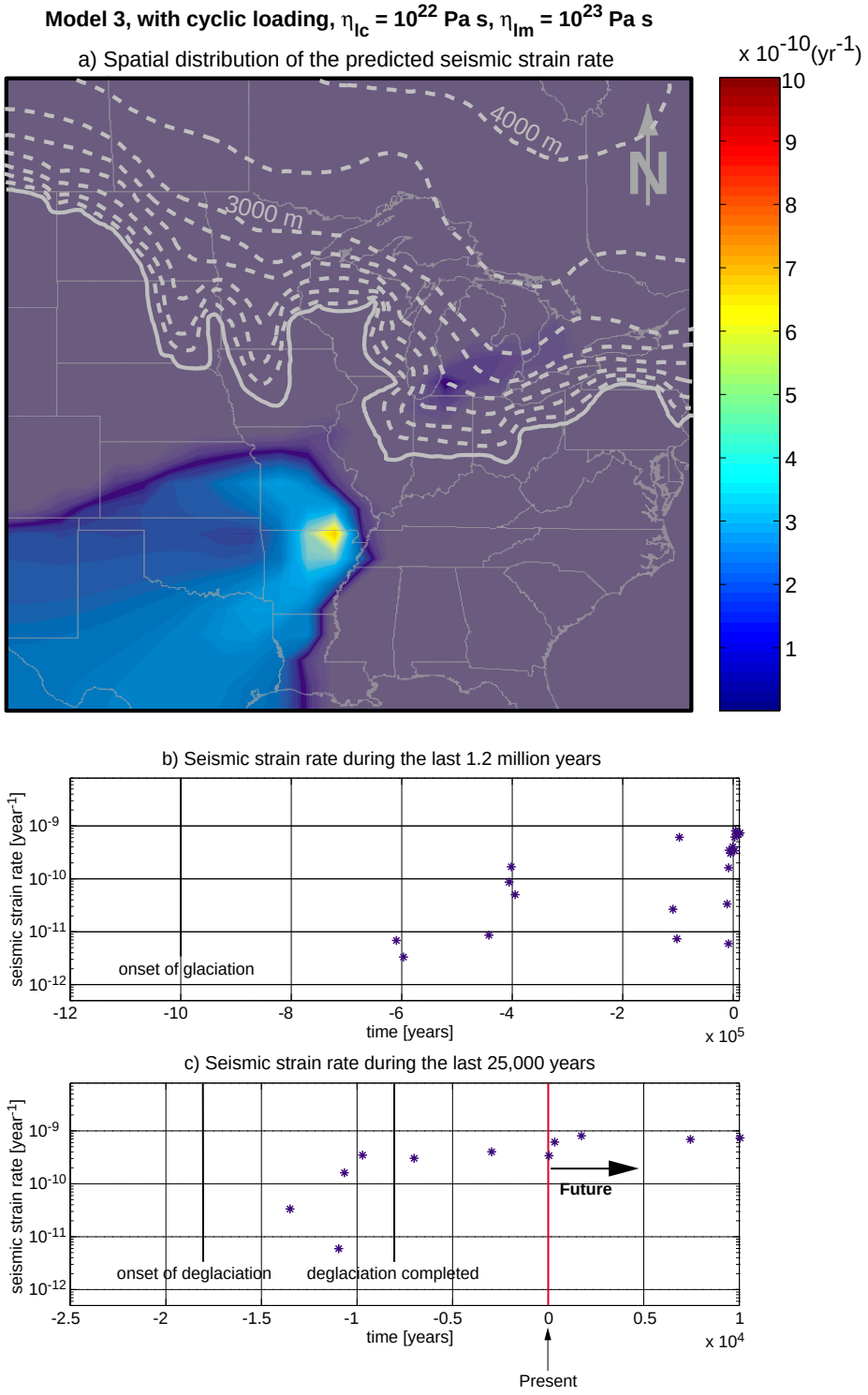

Figure 6.14: Predicted present-day seismic strain rates for ice model 3 at a depth of 12,000 m. A zone of increased seismicity is located west of the NMSZ. The highest present-day strain rates are about 7×10^{-10} year^{-1}, close to 3 orders of magnitude higher than the background seismic strain rate of 10^{-12} year^{-1} (Anderson, 1986). b) Seismic strain just west of the NMSZ at a depth of 12,000 m for the entire glacial period. c) Seismic strain rate for the last 25,000 years and 10,000 years into the future.

Ice model 2 (with long Eemian interglacial)

A prolonged Eemian interglacial of 40,000 years, has a more significant effect on the predicted seismicity (Figure 6.13). The peak of present-day seismicity is offset by ≈100 km to the west of the NMSZ. In the NMSZ itself, the present-day seismic strain rate is reduced to $6x10^{-10}$ $year^{-1}$. Figure 6.13b and c show the temporal evolution of the seismic strain rate in the area of peak present-day seismicity, just west of the NMSZ. The long Eemian interglacial caused an acceleration of seismicity to $3x10^{-9}$ $year^{-1}$ which is almost 3 times the modeled present-day value. The seismic response to the final ice melting is comparable to the predictions of ice model 1 for the NMSZ.

By concluding that the longer Eemian interglacial moves the peak of present-day seismicity slightly to the west (by ≈100 km), we are certainly pushing the resolution limit of our model, considering that the horizontal element size is 100 km. Also, the fact that seismicity during the Eemian interglacial is higher than after the last deglaciation might be due to the fact that the modeled ice sheet melts almost instantaneously during the Eemian interglacial, whereas the final melting considers the 11,000 years, and 9,500 years extents.

Ice model 3 (with cyclic ice loading)

Lastly, ice model 3 considers several interglacials throughout the modeled period (see Figure 6.11). This model locates the peak present-day seismicity ≈100 km west of the NMSZ where the seismic strain rate reaches a value of $7x10^{-10}$ $year^{-1}$(as shown in Figure 6.14a). The comparison with ice model 1 and ice model 2 suggests that the accumulated time of interglacials affects the location of the modeled present-day seismicity, i.e. a long duration of interglacials tends to shift the seismicity peak towards the west of the NMSZ.

Figure 6.14b shows that the first interglacial, ending 800,000 years ago, triggered no seismicity. Consecutive interglacials had an increasing impact on seismicity and the final deglaciation accelerated the seismic strain rate to almost 10^{-9} $year^{-1}$. There are two possible explanations for the increasing influence of interglacials on seismicity: Each interglacial might contribute to the stress state such that the subsequent interglacials cause higher seismicity. Alternatively, the stress state in the upper crust might slowly change as a result of ductile (viscoelastic) processes in the lower crust, and in the lithospheric mantle in response to the increasing accumulated duration of ice loading. In the latter case, the interglacials simply reflect the current potential of the stress state to produce seismicity, and this potential increases with time. The fact that the reference ice model (neglecting interglacials) produces a comparable amount of Holocene seismicity favors the latter possibility, suggesting that the main cause of seismicity following deglaciation are permanent deformation processes underneath the upper crust. Thus, seismicity after

deglaciation is mainly governed by the accumulated duration of interglacials, rather than the number of interglacials.

In conclusion, the studied ice models agree that deglaciation causes an acceleration of the seismic strain rate to $\approx 10^{-9}$ year^{-1} in the vicinity of the NMSZ, whereas most of the other modeled areas are aseismic at present. Increasing duration of interglacials moves the zone of predicted peak-seismicity approximately 100 km to the west of the NMSZ. All models suggest that seismicity remains at its current level at least for the next 10,000 years.

6.5 The change of seismicity with time

So far, I have focused on the model predictions for seismicity in the New Madrid area. In addition to the NMSZ, other areas in the eastern United States and in Canada are commonly associated with paleoseismic events following deglaciation. For example, the Charlevoix area in Quebec has been subjected to seismic events during the Holocene (e.g. Shilts et al., 1992). Further south, in the Wabash Valley, bordering Indiana and Illinois, Obermeier et al. (1991) suggest several large seismic events with magnitudes larger than 6. The largest of these events is interpreted to have occurred between 7500 and 1500 years ago. Tuttle et al. (1999) also find numerous evidence for Holocene, paleoseismic events in the southern half of Illinois and in southeastern Missouri.

Deglaciation seems to have triggered seismicity near or underneath the former ice sheet. Later on, the area of increased seismicity migrated towards the south, affecting southern Missouri, Illinois, and Indiana and finally reached the NMSZ. We have analyzed our model results in a time sequence, starting after the onset of deglaciation, in order to compare the above mentioned paleoseismological findings with our model.

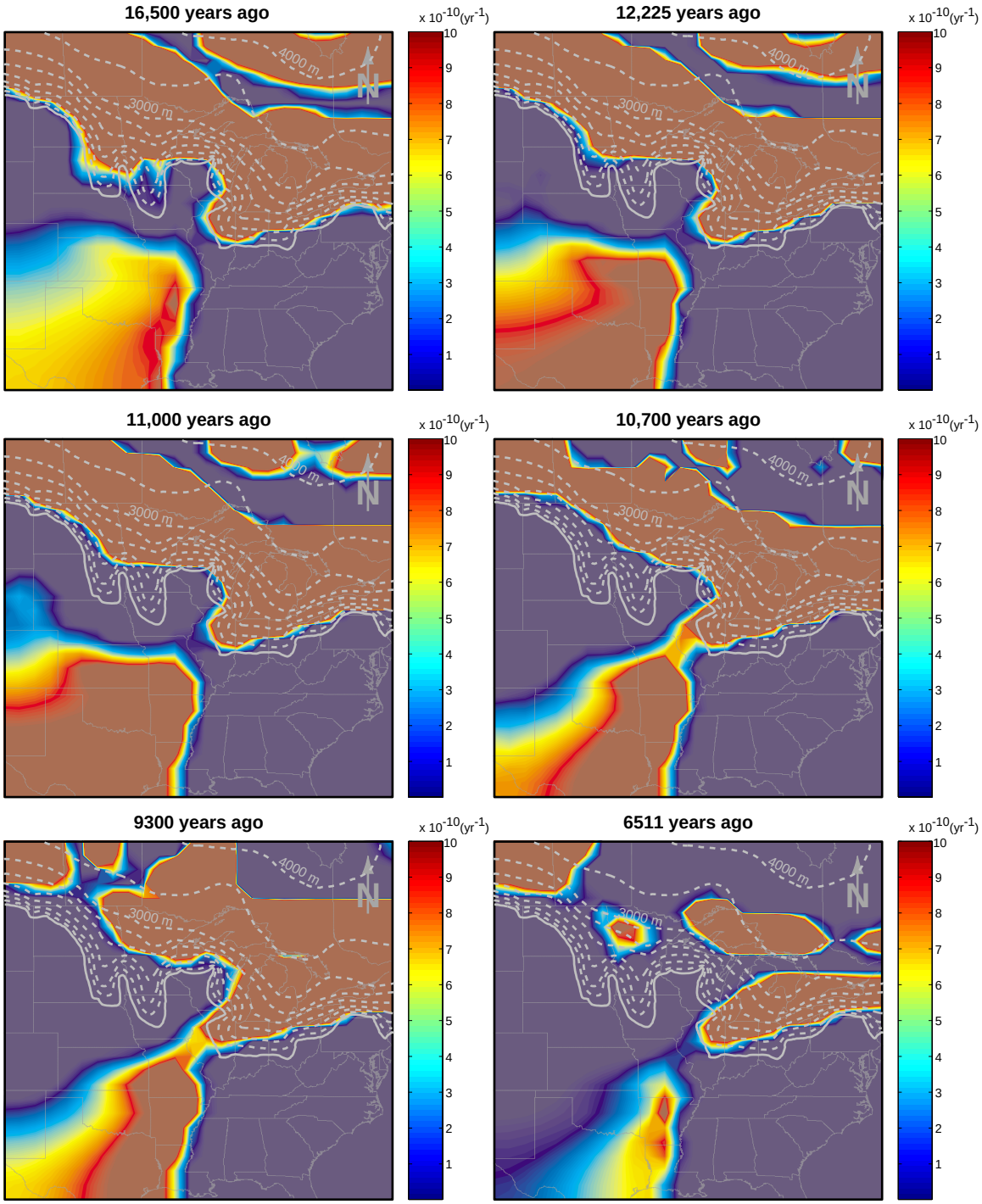
16,500 years ago
12,225 years ago
11,000 years ago
10,700 years ago
9300 years ago
6511 years ago
4000 m
3000 m
N
x 10^-10 (yr^-1)
10
9
8
7
6
5
4
3
2
1

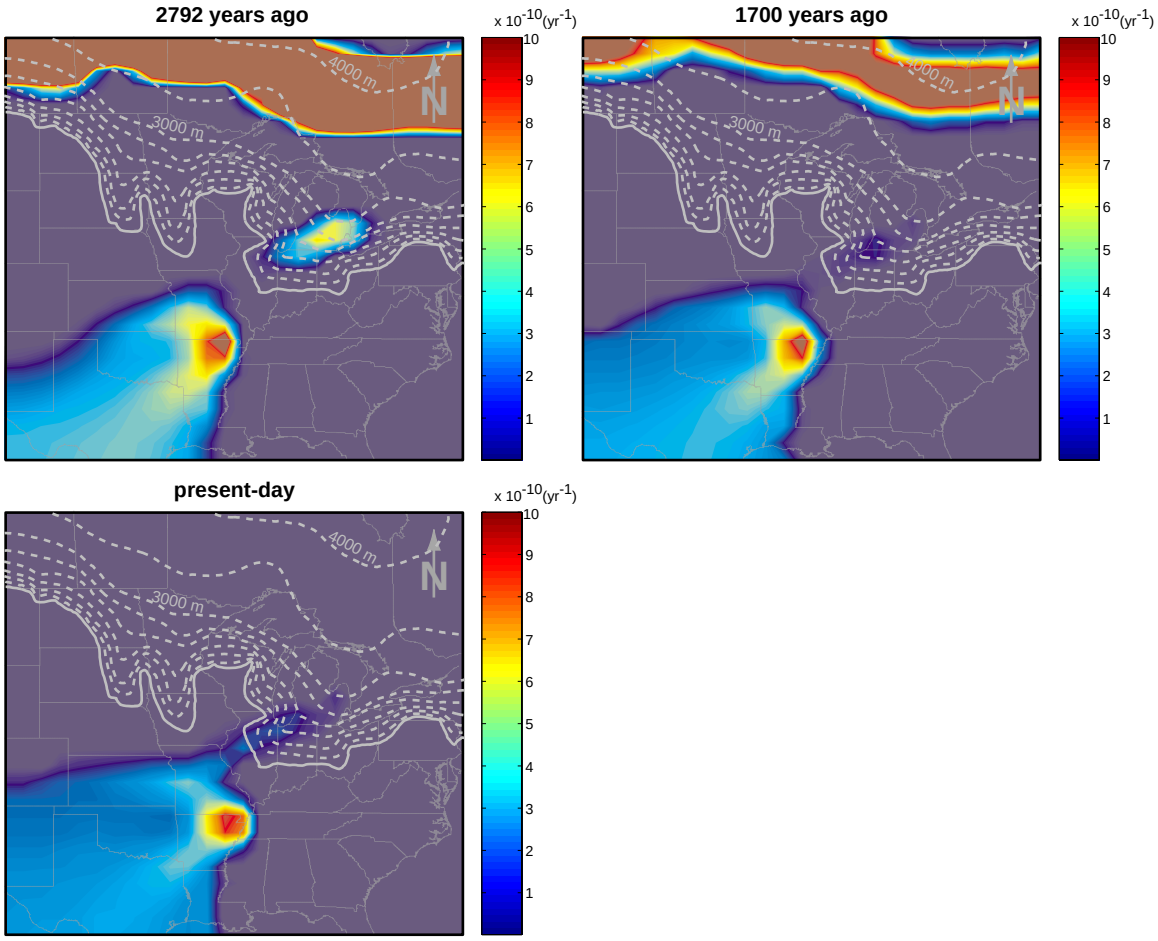

Figure 6.15: Seismicity as a function of time. The figure shows the temporal evolution of the predicted seismicity at a depth of 12,000 m, obtained from Model 3, with the reference viscosities ($\eta_{lc} = 10^{22}$ Pa s, and $\eta_{lm} = 10^{23}$ Pa s), and the reference ice history.

Figure 6.15 displays the results of Model 3 (localized weak mantle), assuming the reference ice history, and the best-fitting viscosities ($\eta_{lc} = 10^{22}$ Pa s, and $\eta_{lm} = 10^{23}$ Pa s). According to this model, the onset of ice melting causes a large zone of increased seismicity, which roughly follows the perimeter of the largest ice extent. This zone remains unchanged until the ice sheet has completely disappeared (8500 years ago). Later, this ice sheet front-parallel zone starts to migrate towards the north until it completely disappears sometimes between 1700 years ago and present-day.

Another seismic area develops in the southwestern quadrant of the model, immediately after the onset of ice melting (e.g. 16,500 years ago). With continuing deglaciation, seismicity in this zone becomes more pronounced. 11,000 years ago most of the southwestern quadrant is exposed to seismic strain rates of 10^{-9} year^{-1} or more. After

deglaciation is finished (e.g. 6511 years ago), increased seismic strain rates are focused to a relatively small, north-south trending zone just to the west of the NMSZ. Subsequently, high seismic strain rates start to concentrate just slightly offset to the west of the NMSZ.

The increased seismicity in the ice sheet-parallel zone, just after the onset of deglaciation, is due to the S_v reduction as a result of the disappearing ice mass. The horizontal stresses only drop by about 1/3 of the change in S_v which eventually leads to a reverse faulting stress state and later to failure. Johnston (1987) used this effect to explain why ice covered areas, such as Greenland, show no seismicity, but deglaciation usually is followed by a short phase of predominantly reverse-faulting seismicity underneath the former ice front. In other words, deglaciation relieves the seismicity which was suppressed during the ice sheet's existence. The paleoseismic activity in the Charlevoix area, in Canada, is most likely due to this effect.

The paleoseismic observation of southward migrating seismicity through southern Illinois towards the NMSZ can not be directly seen in the model results. The model suggests that seismicity starts to focus around the NMSZ about 3000 years ago, but before there was no modeled seismicity in the southern half of Illinois, contradicting paleoseismic findings. Instead the model suggests high seismic strain rates in the states of Missouri and Arkansas.

A possible reasons for this discrepancy, is the fact that the modeled, quadratic zone of weakness in the upper mantle is overly simplified. In reality, the strike of the structural heterogeneity in the New Madrid area (Reelfoot Rift) strikes from southwest to northeast and probably extends further to the northeast than the modeled heterogeneity (as suggested by gravity data, Hildenbrand et al., 1996). If the modeled heterogeneity extended further to the northeast, including the Wabash Valley, the modeled seismicity might be deflected to the east (increased seismicity in southern Illinois and Indiana instead of southern Missouri) and might therefore match the paleoseismic observations.

6.6 Discussion

Almost all the tested models predict a significant increase in seismic strain rate following deglaciation within ~100 km of the NMSZ and that it will remain at late Holocene levels for thousands of years into the future. Model 3 gives the most convincing results as it predicts an increase of seismic strain rate in Holocene time of three orders of magnitude over the background seismic strain rate in the vicinity of the NMSZ. Also, the zone of weakness in Model 3 is coincident with the region of anomalous structure (Figure 6.1).

Model 3, using the reference ice evolution (Figure 6.7) predicts a present-day seismicity of 10^{-9} year^{-1} over an area of approximately 25,000 km^2. Most of the alternative models give comparable results. For comparison, Anderson (1986) calculated seismic strain rates for the NMSZ from converting recurrence estimates of 11 experts and obtained an average seismic strain rate of $7x10^{-9}$ year^{-1} (with an uncertainty of one to two orders of magnitude) over and area of 20,000 km^2. Thus, our results fit Anderson's analysis within the uncertainties.

Overall, the perturbation caused by ice loading is to suppress seismicity whereas ice melting enhances seismic strain release. Lithospheric bending associated with loading of the ice sheet causes the north-south stress in the lower lithosphere to increase beneath the NMSZ. As a result, the lower part of the lithosphere undergoes permanent north-south shortening and east-west extension. This is transmitted to the upper crust such that S_{Hmax} (S_1) decreases and S_{hmin} (S_3) increases slightly, which decreases the differential stress in the upper crust and inhibits brittle failure. Subsequent to the ice loading 1 million years ago, tectonic driving forces bring the stress state back to failure equilibrium until melting of the ice occurs and causes the converse effects to ice loading - the lower lithosphere deforms in such a way that upper crustal stress in the east-west stress direction increases more than the north south stress. This promotes brittle failure and causes the observed Holocene seismicity. The zone of weakness in the models serves to concentrate the seismic strain rate in the region of the NMSZ. The high level of modeled Holocene seismicity in the NMSZ following deglaciation is caused by a shear stress increase of about 2.5 MPa. If the stress state was more than 2.5 MPa from failure before the onset of deglaciation, Holocene seismicity would not develop. Thus, the capability of the model to regain failure equilibrium during the existence of the ice sheet, i.e. inclusion of tectonic force boundary conditions, is an important aspect of our approach.

Taking into account the interaction between a single fault and a weak lower crust using a model analogous to those considered here, Kenner and Segall (submitted) show that the Holocene increase in seismic strain rate in the NMSZ can be associated with seismic bursts that reoccur every several hundred years. They also demonstrate that the general types of models presented here can produce relatively frequent earthquakes and yet still be associated with the low rates of strain accumulation ($<10^{-7}$ yr^{-1}) as implied by recent GPS measurements in the NMSZ (Newman et al., 1999; Kerkela et al., 1998).

The simple models considered can not be used to estimate seismic strain rates throughout the eastern United States, in part because they only include lithospheric heterogeneities in the NMSZ. To date, we have neglected the existence of several other potential zones of weakness such as the Midcontinent Rift System (e.g., Hildenbrand et al.,

1996) and have also ignored variations of regional stress states as well as other possible sources of stress in the region. Furthermore, the geometry of the modeled zone of weakness is very simple, ignoring the elongated southwest-northeast trending shape. As mentioned in Section 6.5, by including a more appropriate heterogeneity, the models might be able to better explain the occurrence of earthquakes north of the NMSZ, which occurred between 7500 and 1500 years ago.

Finally, our analysis is based on models with a relatively large element size (100 km laterally), and the way in which we include the structural heterogeneities below the NMSZ is relatively crude. Furthermore, the boundaries of the model are close to the area of interest (NMSZ) and might additionally affect the model results. Consequently, the modeled seismic strain rates are only rough estimates. A more accurate analysis would necessitate more detailed models requiring super-computing capabilities. Despite these uncertainties, our models show that deglaciation is a plausible mechanism for triggering seismicity in the NMSZ.

6.7 Conclusions

By directly incorporating far field stresses and heterogeneous lithospheric structure, we have demonstrated that bending of the lithosphere associated with glacial unloading has had a significant effect in central U.S. near the New Madrid seismic zone. We suggest, therefore, that the 1811-1812 earthquake sequence, and the previous large earthquakes throughout the Holocene, have been triggered by retreat of the Laurentide ice shield. Although the model with a concentrated zone of weakness in the upper mantle gives the most convincing results, most of the models tested produce a localized increase of seismicity near the New Madrid region during the Holocene. All of the models tested predict that seismic strain rates for the next few thousand years will be comparable to the high rates of the past several thousand years. This implies high seismic hazard for this anomalous intraplate region.

Acknowledgments

We thank Arch Johnston, George Thompson, Tom Hanks, Joan Gomberg, and Martitia Tuttle for useful comments regarding early versions of this manuscript.

Appendix A

ANALYTICAL MODEL OF VISCOELASTIC BENDING OF THE LITHOSPHERE UNDER DISTRIBUTED PRESSURE

According to Nadai (1963), if the lithosphere is a "Maxwell" viscoelastic layer with thickness T underlain by a fluid substratum accounting for isostasy the time dependent flexural deflection $w_{(x,t)}$ as a result of a distributed load $P_{(x,t)}$ can be described with the following equation:

$$\mathbf{D}\frac{\partial^4}{\partial \mathbf{x}}(\mathbf{w}') = -\mathbf{k}\left(\mathbf{w}' + \frac{\mathbf{w}}{\tau}\right) + \mathbf{P}' + \frac{\mathbf{P}}{\tau} \tag{A1}$$

where the flexural rigidity is $D=ET^3/9$ for $\nu=0.5$, τ is the relaxation time, $k = g(\rho_a-\rho_w)$ is the density restoring factor if the lithosphere is covered by water. In case of a dry surface $k = g\rho_a$. w' and P' are the time differentiations of w and P.

The solution to A1 for a periodic load is

$$\mathbf{w}(\mathbf{x}, \mathbf{t}) = \frac{\mathbf{P}_0}{\mathbf{k}}\sum_{\mathbf{n}=1}^{\infty}\varphi_{\mathbf{n}}(\mathbf{t})\mathbf{C}_{\mathbf{n}}\cos\frac{\mathbf{n}\pi\mathbf{x}}{\mathbf{a}} \tag{A2}$$

If the load has a constant thickness h_{ice} a half width c and the load center is located at distance a from the origin (x=0) then

$$\mathbf{C}_{\mathbf{n}} = \frac{-1^{\mathbf{n}}}{\mathbf{n}}\sin\frac{\mathbf{n}\pi\mathbf{c}}{\mathbf{a}} \tag{A3}$$

and

$$\mathbf{P}_0 = \frac{2}{\pi}\rho_{\mathbf{ice}}\mathbf{h}_{\mathbf{ice}}\mathbf{g} \tag{A4}$$

and φ_n for an exponentially growing load

$$\varphi_{\mathbf{n}}(\mathbf{t}) = \frac{\left\{(\mathbf{t}_\mathbf{p}-\tau)\left(1-\mathbf{e}^{-\frac{\mathbf{t}}{\mathbf{t}_\mathbf{p}}}\right)-(\mathbf{t}_\mathbf{n}-\tau)\left(1-\mathbf{e}^{-\frac{\mathbf{t}}{\mathbf{t}_\mathbf{n}}}\right)\right\}}{\mathbf{t}_\mathbf{p}-\mathbf{t}_\mathbf{n}} \tag{A5}$$

t_n is the characteristic time for each Fourier term

$$\mathbf{t}_{\mathbf{n}} = \left\{1+\left(\frac{\mathbf{D}}{\mathbf{k}}\right)\left(\frac{\mathbf{n}\pi}{\mathbf{a}}\right)^4\right\}\tau \tag{A6}$$

and t_p determines how fast the load is applied. Values much smaller than unity correspond to an instantaneous growth. The flexural stress can be calculated with

$$\mathbf{S_{xx}(x, z, t)} = \frac{4\mathbf{EzP}_0}{3\mathbf{k}} \sum_{\mathbf{n}=1}^{\infty} \left(\frac{\mathbf{n}\pi}{\mathbf{a}}\right)^2 \mathbf{f_n(t)C_n} \cos\frac{\mathbf{n}\pi\mathbf{x}}{\mathbf{a}} \tag{A7}$$

where z is depth and

$$\mathbf{f_n(t)} = \frac{\tau}{(\mathbf{t_p} - \mathbf{t_n})\left(\mathbf{e}^{-\frac{1}{\mathbf{t_p}}} - \mathbf{e}^{-\frac{\mathbf{t}}{\mathbf{t_n}}}\right)} \tag{A8}$$

Because the applied load is periodic, i.e. another ice sheet exists at x=-a, the solutions are governed by the boundary condition dw/dx = 0 at x=0.

Appendix B

LIST OF SYMBOLS

S_{Hmax}	Maximum horizontal stress, [MPa]
S_{hmin}	Minimum horizontal stress, [MPa]
S_v	Vertical stress, [MPa]
S_1	Maximum principal stress, [MPa]
S_2	Intermediate principal stress, [MPa]
S_3	Least principal stress, [MPa]
σ	Effective stress ($S-P_p$), [MPa]
P_p	Pore pressure, [MPa]
ΔPp_{crit}	Required pore pressure change for a fault to be critically stressed, [MPa]
A	Area surrounding a bottom node of the model, [m^2]
$F_{isostatic}$	Force applied to account for isostasy, [N]
F_R	Net force from ridge push, [N/m^{-1}]
F_{NS}	Applied boundary force in north-south direction, [N]
F_{EW}	Applied boundary force in east-west direction, [N]
T	Effective elastic thickness of the lithosphere, [m]
$T_{lithosphere}$	Thickness of the lithosphere, [m]
h_{ice}	Thickness of the ice sheet, [m]
c	Half width of the ice sheet, [m]
a	Distance of ice center from x=0, [m]
k	Density restoring factor, [N/m^3]
l	Model width, [m]
T_{uc}	Thickness of upper crust, [m]
u_z	Vertical displacement, [m]
τ	Maxwell relaxation time, [a]
ρ	Density, [kg/m^3]
ρ_a	Asthenospheric density, [kg/m^3]
ρ_{ice}	Density of ice, [kg/m^3]

ρ_w	Density of water, [kg/m^3]
E	Young's modulus, [GPa]
ν	Poisson's ratio
η	Viscosity, [Pa s]
η_{lc}	Lower crustal viscosity, [Pa s]
η_{lm}	Lithospheric mantle viscosity, [Pa s]
σ_m	First stress invariant ($1/3\sigma_{ii}$), [MPa]
B	Skempton's coefficient ($\Delta P_p/\Delta\sigma_m$)
n	plane normal vector
θ	Fault dip azimuth, [degrees]
ϕ	Fault dip angle, [degrees]
t	traction vector, [MPa]
t_n	Resolved normal stress on the fault plane, [MPa]
t_s	Resolved shear stress on the fault plane, [MPa]

REFERENCES

Adams, J., 1989. Crustal stresses in eastern Canada. In: Gregersen, S. and Basham P.W., eds., Earthquakes at North-Atlantic Passive Margins: Neotectonics and Postglacial Rebound. Kluwer, p. 289-297.

Amelung, F., and Wolf, D., 1994. Viscoelastic perturbations of the earth: significance of the incremental gravitational force in models of glacial isostasy. Geophysical Journal International, v. 117, p. 864-879.

Andersen, B.G., 1981. Late Weichselian Ice Sheets in Eurasia and Greenland. In: Denton, G.H., Hughes, T.J. (Eds.), The Last Great Ice Sheets. Wiley, New York, p. 1-65.

Anderson, E.M., 1951. The Dynamics of Faulting and Dyke Formation with Applications to Britain: Oliver and Boyd, Edinburgh.

Anderson, J.G., 1986. Seismic strain rates in the central and eastern United States. Bulletin of the Seismological Society of America, v. 76, p. 273-290.

Anundsen, K., and Fjeldskaar, W., 1983. Observed and theoretical Late Weichselian shore-level changes related to glacier oscillationsat Yrkje, south-west Norway. In: Schroeder-Lanz, H. (Editor), Late- and Postglacial Oscillations of Glaciers: Glacial and Periglacial Forms. Balkema, Rotterdam, p. 133-170.

Artyushkov, E.V., 1973. Stresses in the lithosphere caused by crustal thickness inhomogeneities. Journal of Geophysical Research, v. 78, p. 7675-7708.

Barton, C.A., Zoback, M.D., and Moos, D, 1995. Fluid flow along potentially active faults in crystalline rock. Geology, v.23, p. 683-686.

Borgerud, L., and Svare, E., 1995. In-situ stress field on the Norwegian margin, 620-670 north. Workshop on Rock Stresses in the North Sea, Trondheim, Norway, Feb. 13-14 (1995).

Bott, M.H.P., and Kusznir, N., 1984. The origin of tectonic stress in the lithosphere. Tectonophysics, v. 105, p. 1-13.

Brace, W.F., and Kohlstedt, W.F., 1980. Limits on lithospheric stress imposed by laboratory experiments. Journal of Geophysical Research, v. 85, p. 6248-6252.

Braile, L.W., Hinze, L.W., Keller, G.R., Lidiak, G.R., and Sexton, J.L., 1986. Tectonic development of the New Madrid rift complex, Mississippi embayment, North America. Tectonophysics, v. 131, p. 1-21.

Breuer, D., and Wolf, D., 1995. Deglacial land emergence in Svalbard: evidence of lateral inhomogeneity in the upper mantle. Geophysical Journal International, v. 121, no. 3, p. 775-788.

Brudy, M., 1998. Determination of the state of stress by analysis of drilling-induced frac-

tures - results from the northern North Sea: paper SPE 47236 presented at the 1998 SPE Annual Technical Conference and Exhibition, Trondheim, Jul. 8-10.

Bungum, H., 1989. Earthquake occurrence and seismotectonics in Norway and surrounding areas. In: Gregersen, S., Basham, P.W. (Eds.), Earthquakes at North-Atlantic Passive Margins: Neotectonics and Postglacial Rebound. Kluwer Academic Publishers, Dordrecht, p. 501-519.

Bungum, H., Alsaker, A., Kvamme, L.B., and Hansen, R.A., 1991. Seismicity and seismotectonics of Norway and nearby continental shelf areas. Journal of Geophysical Research, v. 96, no. B2, p. 2249-2265.

Byerlee, J. D., 1978. Friction of rocks. Pure and Applied Geophysics, v. 116, p. 615-629.

Caillet, G., Sejourne, C., Grauls, D., and Arnaud, J., 1991. The hydrodynamics of the Snorre Field area, offshore Norway: Terra Nova, v. 3, p. 180-194.

Carter, N.L., and Tsenn, M.C., 1987. Flow properties of continental lithosphere. Tectonophysics, v. 136, p. 27-63.

Cathles, L.M., 1975. The viscosity of the earth's mantle. Princeton University Press, Princeton, 386 p.

Cox, R.T., and Van Arsdale, R.B., 1997. Hotspot origin of the Mississippi embayment and its possible impact on contemporary seismicity. Engineering Geology, v. 46, p. 201-216.

Denton, G.H., and Hughes, T., 1981. The last great ice sheet. John Wiley and Sons, New York, 484 p.

Doré, A.G., 1992. The base Tertiary surface of southern Norway and the northern North Sea. Norsk Geologisk Tidsskrift, v. 72, p. 259-265.

Dragoni, M., Pasquale, V., Verdoya, M., and Chiozzi, P., 1993. Rheological consequences of the lithospheric thermal structure in the Fennoscandian Shield. Global and Planetary Change, v. 8, p. 113-126.

Ekman, M., 1996. A consistent map of the postglacial uplift of Fennoscandiaé Terra Nova, v. 8, no. 2, p. 158-165.

Ekman, M., and Mäkinen, J., 1996. Recent postglacial rebound, gravity change and mantle flow in Fennoscandia. Geophysical Journal International, v. 126, p. 229-234.

Engelder, T. and Fischer, M.P., 1994. Influence of poroelastic behavior on the magnitude of minimum horizontal stress, S_h, in overpressured parts of sedimentary basins. Geology, v.22, p. 949-952.

England, P.C., and Houseman, G.A., 1986. Finite strain calculations of continental deformation; 2, comparison with the India-Asia collision zone. Journal of Geophysical Research, v. 91, p. 3664-3676.

Færseth, R.B., Gabrielsen, R.H., and Hurich, C.A., 1995. Influence of basement in structuring of the North Sea basin, offshore southwest Norway. Norsk Geologisk Tidsskrift, v. 75, p. 105-119.

Fejerskov, M., 1996. Determination of in-situ rock stresses related to petroleum activities on the Norwegian continental shelf. PhD thesis, Norwegian University of Science and Technology, Trondheim, Norway.

Fejerskov, M., and Lindholm, C.D., 2000. Crustal stress in and around Norway: an evaluation of stress-generating mechanisms. In: Nøttvedt, A., eds., Dynamics of the Norwegian Margin. Geological Society Special Publication, no. 167, p. 451-467.

Fjeldskaar, W., and Cathles, L., 1991. Rheology of mantle and lithosphere inferred from post-glacial uplift in Fennoscandia. In: Sabadini, R., Lambeck, K., and Boschi, E. (Eds.), Glacial Isostasy, Sea-level and Mantle Rheology. Kluwer, Dordrecht, p. 1-19.

Fjeldskaar, W., 1997. Flexural rigidity of Fennoscandia inferred from the postglacial uplift. Tectonics, v. 16, no. 4, p. 596-608.

Flesch, L.M., Holt, W.E., Haines, A.J., and Shen-Tu, B., 2000. Dynamics of the Pacific-North American plate boundary in the western United States: Science, v. 287, p. 834-836.

Forsyth, D., and Uyeda, S., 1975. On the relative importance of the driving forces of plate motion. Geophys. J. R. Astr. Soc., v. 43, p. 163-200.

Gaarenstroom, L., Tromp, R.A.J., de Jong, M.C., and Brandenburg, A.M., 1993. Overpressures in the Central North Sea: implications for trap integrity and drilling safety. In: Parker, J.R., ed., Petroleum Geology of Northwest Europe. Proceedings of the 4th Conference, p. 1305-1313.

Gölke, M., 1996. Patterns of stress in sedimentary basins and the dynamics of pull-apart basin formation. Ph.D. Thesis, Vrije Universiteit. Amsterdam, Netherlands.

Gölke, M., and Brudy, M., 1996. Orientation of crustal stresses in the North Sea and Barents Sea inferred from borehole breakouts. Tectonophysics, v. 266, p. 25-32.

Gölke, M, 1996. Finite-element modelling of stress patterns along the mid-Norwegian continental margin, 62 degrees to 68 degrees N. Tectonophysics, v. 266, p. 33-53.

Gölke, M, and Coblentz, D., 1996. Origin of the European regional stress field, v. 266, p. 11-24.

Grana, J.P., and Richardson, R.M., 1996. Tectonic stress within the New Madrid seismic zone. Journal of Geophysical Research, v. 101, p. 5445-5458.

Gregersen, S., Korhonen, H., and Husebye, E.S., 1991. Fennoscandian dynamics: Present-day earthquake activity. Tectonophysics, v. 189, p. 333-344.

Grollimund, B., Zoback, M.D., and Arnesen, L., 1998. Flexurally-induced stresses in the

northern North Sea: preliminary comparison between observation and theory, SRB annual Report, 68.

Grollimund, B., Zoback, M.D., Wiprut, D.J., Arnesen, L., in press. Regional synthesis of stress orientation, pore pressure and least principle stress data in the Norwegian sector of the North Sea. Petroleum Geoscience.

Grünthal, G., Stromeyer, D., 1992. The recent crustal stress field in Central Europe - trajectories and finite element modeling. Journal of Geophysical Research, v. 97, no. 8, p. 11,805-11,820.

Hamilton, R.M., and Zoback, M.D., 1981. Tectonic features of the New Madrid seismic zone from seismic reflection profiles. U.S. Geological Survey Professional Paper, 1236-F, p. 55-82.

Hansen, S., 1996. Quantification of net uplift and erosion on the Norwegian Shelf south of 66ºN from sonic transit times of shale. Norsk Geologisk Tidsskrift, v. 76, p. 245-252.

Hasegawa, H.S., and Basham, P.W., 1989. Spatial correlation between seismicity and postglacial rebound in Eastern Canada. In: Gregersen, S. and Basham P.W., eds., Earthquakes at North-Atlantic Passive Margins: Neotectonics and Postglacial Rebound. Kluwer, p. 483-500.

Hildenbrand, T.G., 1985. Rift Structure of the Northern Mississippi Embayment From the Analysis of Gravity and Magnetic Data. Journal of Geophysical Research, v. 90, p. 12,607-12,622.

Hildenbrand, T.G., Griscom, A., Van Schmus, W.R., and Stuart, W.R., 1996. Quantitative investigations of the Missouri gravity low: A possible expression of a large, Late Precambrian batholith intersecting the New Madrid seismic zone. Journal of Geophysical Research, v. 101, p. 21,921-21,942.

Hoppe, G., 1974. The glacial history of the Shetland Islands: Progress in geomorphology, Inst. Brit. Geogr., p. 197-210.

Jaeger, J.C., and Cook, N.G.W., 1979. Fundamentals of Rock Mechanics. Chapman and Hall, London.

James, T.S., and Bent, A.L., 1994. A comparison of eastern North American seismic strain-rates to glacial rebound strain-rates. Geophysical Research Letters, v. 21, p. 2127-2130.

Johnston, A.C., 1987. Suppression of earthquakes by large continental ice sheets. Nature, v. 330, no. 3, p. 467-469.

Johnston, A.C., 1994. Seismotectonic interpretations and conclusions from the stable continental region seismicity database. In: The earthquakes of stable continental regions, Electric Power Research Institute, v. 1, p. 4-1-4-102.

Johnston, A.C., 1996. Seismic movement assessment of earthquakes in stable continental

regions; III, New Madrid 1811-1812, Charleston 1886 and Lisbon 1755. Geophysical Journal International, v. 126, p. 314-344.

Johnston, A.C., and Schweig, E.S., 1996. The enigma of the New Madrid earthquakes of 1811-1812. Annual Review of Earth and Planetary Sciences, v. 24, p. 339-364.

Johnston, P., Wu, P., and Lambeck, K., 1998. Dependence of horizontal stress magnitude on load dimension in glacial rebound models. Geophysical Journal International, v. 132, p. 41-60.

Jorgensen, T., and Bratli, R.K., 1995. In-situ stress determination and evaluation at the Tampen Spur area. In: Workshop on rock stress in the North Sea, Trondheim, Norway, p. 240-249.

Kaland, P.E., 1984. Holocene shore displacement and shorelines in Hordaland, western Norway. Boreas, v. 13, p. 203-242.

Kenner, S.J., and Segall, P., submitted to Science. The mechanics of intraplate earthquake generations with application to the New Madrid seismic zone.

Kerkela, S., Murray, M.H., Liu, L., and Zoback, M.D., 1998. Strain accumulation in the New Madrid seismic zone from GPS data. EOS Transactions AGU, v. 79, Fall Meeting Supplement, F210.

Kirby, S.H., 1983. Rheology of the lithosphere. Rev. Geophys. Space Phys., v. 21, p. 1458-1487.

Kjemperud, A., 1986. Late Weichselian and Holocene shoreline displacement in the Trondheimsfjord area, central Norway. Boreas, v. 15, p. 61-82.

Klemann, V., and Wolf, D., 1998. Modelling of stresses in the Fennoscandian lithosphere induced by Pleistocene glaciations. Tectonophysics, v. 294, p. 291-303.

Lagerbäck, R., 1990. Late Quaternary faulting and paleoseismicity in northern Fennoscandia, with particular reference to the Lansjärv area, northern Sweden. Geologiska Föreningens i Stockholm Förhandlingar, v. 112, no. 4, p. 333-354.

Lambeck, K., Johnston, P., and Nakada, M., 1990. Holocene glacial rebound and sea-level change in NW Europe. Geophysical Journal International, v. 103, p. 451-468.

Lindholm, C.D., Bungum, H., Villagram, M., and Hicks, E., 1995. Crustal Stress and Tectonics in Norwegian Regions Determined from Earthquake Focal Mechanisms. In: Workshop on rock stress in the North Sea, Trondheim, Norway, p. 77-91.

Lister, C.R.B., 1975. Gravitational drive on oceanic plates caused by thermal contraction. Nature, v. 257, p. 663-665.

Liu, L., and Zoback, M.D., 1997. Lithospheric Strength and Intraplate Seismicity in the New Madrid Seismic Zone. Tectonics, v. 16, p. 585-595.

Lundqvist, J., 1986. Stratigraphy of the central area of the Scandinavian glaciation. Quater-

nary Science Reviews, v. 5, p. 251-268.

Lundqvist, J., 1986. Late Weichselian glaciation and deglaciation in Scandinavia. Quaternary Science Reviews, v. 5, p. 269-292.

Mangerud, J., Larsen, E., Longva, O., and Sonstegaard, E., 1979. Glacial History of Western Norway 15,000-10,000 B.P. Boreas, v. 8, no. 2, p. 179-187.

Marshall, S.J., 1998. Dynamics of the Pleistocene Ice Sheets. In: P. Wu (Ed.), Dynamics of the Ice Age Earth; a modern perspective, GeoResearch Forum, v. 3-4, Trans Tech Publications, Switzerland, p. 217-248.

McConnell, R.K., 1968. Viscosity of the mantle from relaxation time spectra of isostatic adjustment. Journal of Geophysical Research, v. 73, p. 7089-7105.

McGarr, A., 1988. On the state of lithospheric stress in the absence of applied tectonic forces. Journal of Geophysical Research, v. 93, no. B11, p. 13,609-13,617.

McKeown, F., 1982. Overview and discussion. U.S. Geological Survey Professional Paper, v. 1236, p. 1-14.

Mjelde, R., Kodaira, S., Shimamura, H., Kanazawa, T., Shiobara, H., Berg, E.W., and Riise, O., 1997. Crustal structure of the central part of the Vøring Basin, mid-Norway margin, from ocean bottom seismographs. Tectonophysics, v. 277, p. 235-257.

Mooney, W.D., Andrews, M.C., Ginzburg, A., Peters, D.A., and Hamilton, R.M., 1983. Crustal structure of the northern Mississippi Embayment and a comparison with other continental rift zones. Tectonophysics, v. 94, p. 327-348.

Moos, D., and Zoback,M.D., 1990. Utilization of observations of wellbore failure to constrain the orientation and magnitude of crustal stresses: application to continental, deep sea drilling project, and ocean drilling program boreholes. Journal of Geophysical Research, v. 95, p. 9305-9325.

Muir Wood, R., 1989. Extraordinary deglaciation reverse faulting in northern Fennoscandia. In: Gregersen, S., Basham, P.W. (Eds.), Earthquakes at North-Atlantic Passive Margins: Neotectonics and Postglacial Rebound. Kluwer Academic Publishers, Dordrecht, p. 141-173.

Müller, B., Zoback, M.L., Fuchs, K., Mastin, L., Gregersen, S., Pavoni, N., Stephansson, O., and Ljunggren, C., 1992. Regional Patterns of Tectonic Stress in Europe. Journal of Geophysical Research, v. 97, no. B8, p. 11,783-11,803.

Nadai, A., 1963. Theory of Flow and Fracture of Solids. McGraw-Hill, New York.

Nakiboglu, S.M., and Lambeck, K., 1991. Secular sea-level change, in Glacial Isostasy. In: Sabadini, R., Lambeck, K., Boschi, E. (Eds.), Sea level and Mantle Rheology. Kluwer Academic Publishers, Dordrecht, p. 237-258.

Nansen, F., 1921. The strandflat and isostasy. Avh. Nor. Vid. Akad. Oslo, v. 11, p. 1-313.

Newman, A., Stein, S., Weber, J., Engeln, J., Mao, A., and Dixon, T., 1999. Slow deformation and lower seismic hazard in the New Madrid seismic zone. Science, v. 284, p. 619-621.

Obermeier, S.F., Bleuer, N.R., Munson, C.A., Munson, P.J., Martin, W.S., McWilliams, K.M., Tabaczynski, D.A., Odum, J.K., Rubin, M., and Eggert, D.L., 1991. Evidence of stron earthquake shaking in the lower Wabash Valley from prehistoric liquefaction features. Science, v. 251, p. 1061-1063.

Olesen, O., 1988. The Stuoragurra Fault; evidence of neotectonics in the Precambrian of Finnmark, northern Norway. Norsk Geologisk Tidsskrift, v. 68, no. 2, p. 107-118.

Parsons, B., Richter, F.M., 1980. A relation between the driving force and geoid anomaly associated with mid-ocean ridges. Earth and Planetary Science Letters, v. 51, no. 2, p. 445-450.

Peltier, W.R., 1974. The impulse response of a Maxwell earth. Rev. Geophys. Space Phys., v. 12, p. 649-669.

Peltier, W.R., 1976. Glacial-isostatic adjustment-II. The inverse problem. Geophys. J. R. astr. Soc. v. 46, p. 669-705.

Plumb, R. A., Hickman, S.H., 1985. Stress-induced borehole elongation: A comparison between the four-arm dipmeter and the borehole televiewer in the Auburn geothermal well. Journal of Geophysical Research, v. 90, p. 5513-5521.

Riis, F., 1992. Dating and measuring of erosion, uplift and subsidence in Norway and the Norwegian shelf in glacial periods. Norsk Geologisk Tidsskrift, v. 72, p. 325-331.

Sales, J.K., 1992. Uplift and subsidence of northwestern Europe: possible causes and influence on hydrocarbon productivity. Norsk Geologisk Tidsskrift, v. 72, p. 253-258.

Schweig, E.S., Ellis, M.A., 1994. Reconciling short recurrence intervals with minor deformation in the New Madrid Seismic zone. Science, v. 264, p. 1308-1311.

Shackleton, N.J., Backman, J., Zimmerman, H., Kent, D.V., Hall, M.A., Roberts, D.G., Schnitker, D., Baldauf, J.G., Desprairies, A., Homrighausen, R., Huddlestun, P., Keene, J.B., Kaltenback, A.J., Krumsiek, K.A.O., Morton, A.C., Murray, J.W., and Westberg-Smith, J., 1984. Oxygen isotope calibration of the onset of ice-rafting and history of glaciation in the North Atlantic region. Nature, v. 307, p. 620-623.

Shilts, W.W., Rappol, M., and Blais, A., 1992. Evidence of late and postglacial seismic activity in the Témiscouata - Madawaska Valley, Quebec - New Brunswick, Canada. Can. J. Earth Sci., v. 29, p. 1043-1069.

Stein, S., Sleep, N., Geller, R., Wang, S., and Kroeger, G., 1979. Earthquakes along the passive margin of eastern Canada. Geophys. Res. Letters, v. 5, p. 537-540.

Stein, S., Cloetingh, S., Sleep, N.H., and Wortel, R., 1989. Passive Margin Earthquakes,

Stresses and Rheology: Earthquakes at North-Atlantic Passive Margins. In: Gregersen, S. and Basham P.W., eds., Neotectonics and Postglacial Rebound. Kluwer, p. 231-259.

Stephansson, O., 1988. Ridge push and glacial rebound as rock stress generators in Fennoscandia. Bull. Geol. Inst. Univ. Uppsala. v. 14, p. 39-48.

Strehlau, J., and Meissner, R., 1987. Estimation of crustal viscosities and shear stresses from an extrapolation of experimental steady state flow data. In: Fuchs, K., Froidevaux C. (Eds.), Composition, Structure and Dynamics of the Lithosphere-Asthenosphere System. AGU, GSA, p. 69-87.

Stuart, W.D., Hildenbrand, T.G., and Simpson, R.W., 1997. Stressing of the New Madrid Seismic Zone by a lower crust detachment fault. Journal of Geophysical Research, v. 102, p. 27,623-27,633.

Townend, J., and Zoback, M.D., 2000. How faulting keeps the crust strong. Geology, v. 28, p. 399-402.

Turcotte, D.L., and Schubert, G., 1982. Geodynamics. John Wiley & Sons, New York City, 450 p.

Tushingham, A.M., and Peltier, W.R., 1991. Ice-3G: A new global model of late Pleistocene deglaciation based upon geophysical predictions of post-glacial relative sea level change. Journal of Geophysical Research, v. 96, p. 4497-4523.

Tuttle, M., Chester, J., Lafferty, R., Dyer-Williams, K., and Cande, R., 1999. Paleoseismology study northwest of the New Madrid seismic zone. Report prepared for U.S. Nuclear Regulatioory Commission, Division of Engineering Technology, Washington DC, 96 p.

Tuttle, M.P., and Schweig, E.S., 1995. Archeological and pedological evidence for large prehistoric earthquakes in the New Madrid seismic zone, central United States. Geology, v. 23, p. 253-256.

Van Arsdale, R., 2000. Displacement history and slip rate on the Reelfoot fault of the New Madrid seismic zone. Engineering Geology, v. 55, p. 219-226.

Walcott, R.I., 1970. Isostatic response to loading of the crust in Canada. Can. J. Earth. Sci. v. 7, p. 716-727.

Wiprut, D.J., and Zoback, M.D., 1998. High horizontal stress in the visund field, Norwegian North Sea: consequences for borehole stability and sand production: paper SPE 47244 presented at the 1998 SPE Annual Technical Conference and Exhibition, Trondheim, Jul. 8-10.

Wiprut, D., and Zoback, M.D., 2000. Fault reactivation and fluid flow along a previously dormant normalt fault in the northern North Sea. Geology, v. 28, no. 7, p. 595-598.

Wiprut, D.J., and Zoback, M.D., 2000. The potential for hydrocarbon leakage from reser-

voir-bounding faults in the Visund, Tune, Oseberg Syd, and Fram oil and gas fields, Norway, paper E3, SRB annual report, Vol. 75.

Wolf, D., 1986. A method of calculating lithosphere thickness from observations of deglacial land uplift and tilt. J. Geophys., v. 60, no. 1, p. 28-32.

Wolf, D., 1987. An upper bound on lithospheric thickness from glacio-isostatic adjustment in Fennoscandia. J. Geophys., v. 61, no. 3, p. 141-149.

Wolf, D., 1993. The changing role of the lithosphere in models of glacial isostasy: a historical review. Global and Planetary Change, v. 8, p. 95-106.

Wu, P., 1997. Effect of viscosity structure on fault potential and stress orientations in eastern Canada. Geophysical Journal International, v. 130, p. 365-382.

Wu, P., Johnston, P., and Lambeck, K., 1999. Postglacial rebound and fault instability in Fennoscandia. Geophysical Journal International, v. 139, p. 657-670.

Wu, P., and Johnston, P., 2000. Can deglaciation trigger earthquakes in N. America?. Geophysical Research Letters, v. 27, p. 1323-1326.

Zoback, M.D., Hamilton, R.M., Crone, A.J., Russ, D.P., McKeown, F.A., and Brockman, S.R., 1980. Recurrent intraplate tectonism in the New Madrid seismic zone. Science, v. 209, p. 971-976.

Zoback, M.D., and Healy, J.H., 1992. In Situ Stress Measurements to 3.5 km depth in the Cajon Pass Scientific Research Borehole: Implications for the Mechanics of Crustal Faulting. Journal of Geophysical Research, v. 97, p. 5039-5057.

Zoback, M.D., and Townend, J., 2000. Implications of hydrostatic pore pressures and high crustal strength for the deformation of intraplate lithosphere. Special Edition of Tectonophysics, in press.

Zoback, M.L., and Zoback, M.D., 1989. Tectonic stress field of the continental United States: Geophysical Framework of the Continental United States. Geological Society of America, p. 523-539.

Zoback, M.L., 1992. First- and Second-Order Patterns of Stress in the Lithosphere: The World Stress Map Project. Journal of Geophysical Research, v. 97, no. B8, p. 11,703-11,728.